Influence of Initial Imperfections on Buckling of Fibre Reinforced Polymer Plates Produced by Vacuum Assisted Resin Transfer Molding

Anna Kaskovitš 4514262

A.Kaskovits-1@student.tudelft.nl

Delft, 2018

1

CONTENTS

ABSTRACT

The increasing use of Fibre Reinforced Polymers produced by Vacuum Assisted Resin Transfer Molding in civil infrastructure applications leads to the need for an appropriate research data. The VARTM produced structural elements are not limited in dimensions and material properties and typically are slender structures parts of which are susceptible to plate buckling. The latest standards - CUR96 Vezelversterkte kunststoffen in bouwkundige en civieltechnische draagconstructies and JRC Prospect for New Guidance in the Design of FRP – are for a large part based on the research data of pultruded profiles and in terms of design for buckling, focus on the flange / web interaction. The goal of this thesis is to investigate the effect of initial out of plane deformations on buckling of FRP plates produced by VARTM.

Literature study includes a detailed overview of the currently available analytical models and design procedures for plate buckling, and a summary of the research dedicated to study of the effect of initial imperfections on buckling behaviour of FRP structural elements. Although the limiting values for initial out of plane deformations are provided, they are not included directly in the design procedures given in standards, referring designer to determine the influence of the imperfections either from tests or numerically. From experimental and finite element analysis studies it seems that the suggested limiting values of the initial imperfections are unrealistically large.

The first step of this research was to determine the shape of the imperfection that has the largest effect on plate's structural behaviour. The effect of the shape and amplitude of the initial out of plane deformation was studied with geometrically nonlinear finite element analysis using Abaqus software. Four different shapes (first two buckling modes, one halfwave over the whole length of the plate, wrinkle imperfections) and four amplitudes of imperfections were considered with the maximum being the limiting value suggested in standards. The effects of material layup, plate thickness and aspect ratio were investigated. It was found that an imperfect plate does not buckle, meaning there no sudden growth of out of plane deformations and thus no bifurcation point in the load – deflection diagram, which leads to difficulty of determining the critical buckling load. A couple of methods to approximate the critical load were considered, however, none of them are useful when it comes to larger amplitudes of imperfections.

Since it was impossible to quantify the influence of initial imperfections in terms of critical buckling load, another failure criterion had to be chosen. Three possibilities were considered: serviceability limit strain, Hashin progressive failure and delamination. It was shown that delamination would not be critical compared to the Hashin progressive failure criterion. By varying plate's thickness several values of plate slenderness were obtained and the corresponding failure loads determined. Based on the results buckling curves were derived showing the relation between plate slenderness and compressive load reduction due to buckling.

Lastly, a numerical example is presented that demonstrates the application of the three methods for design for local buckling of a profile: JRC/Kollar, CUR96 and buckling curves.

The general conclusion is that for thin plates the critical load criterion gives quite conservative results, as thin plates have "postbuckling" capacity. This "postbuckling" capacity is (almost) independent of the amplitude of imperfection. In case of thick plates, it was shown that failure occurs below the critical load and depends on the amplitude of initial imperfection.

1. INTRODUCTION

1.1 MOTIVATION AND BACKGROUND RELEVANCE

Fibre Reinforced Polymers (FRP) properties such as very high strength-to-weight ratio and low maintenance make it a very attractive material to use in infrastructure applications. Usually pultruded profiles with hollow, I-shape, and channel sections are used in bridge construction. However, next to pultrusion, Vacuum Assisted Resin Transfer Moulding (VARTM) is becoming one of the most used manufacturing processes for FRP in civil engineering. Typically, large monocoque structures are produced in this manner. Quality of the final product produced by VARTM is largely dependent on skill and experience of workers as the placement of fibres is done manually. Due to high slenderness and initial imperfections introduced during manufacturing these structures are susceptible to buckling.

Some of the structures in which buckling might be critical are listed next. In all of these examples, the critical parts can be regarded as plates under longitudinal compression:

- composite bridge decks; two types of instability can be identified: "wrinkling" of the top face of the deck due to longitudinal compressive stresses, which results from the deck bending and buckling of the web at the supports and under wheel loading;
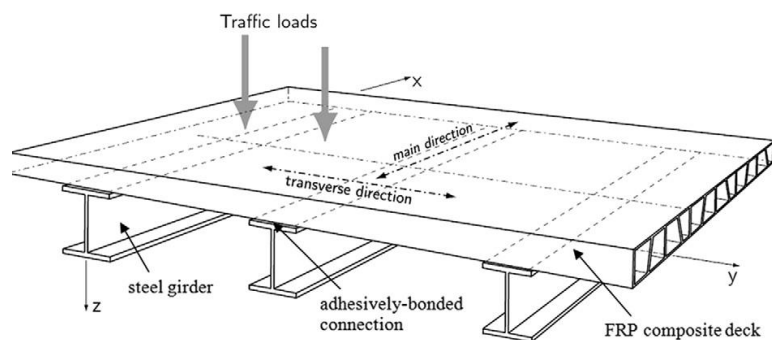
Figure 1.1.1 Composite bridge deck [31] p.46

- bridge superstructure; in the structural system as shown in the figure 1.1.2 due to bending of the bridge, tensile forces are developing in the tie and compressive forces in the chord, which is a hollow profile with thin walls and is susceptible to local buckling;
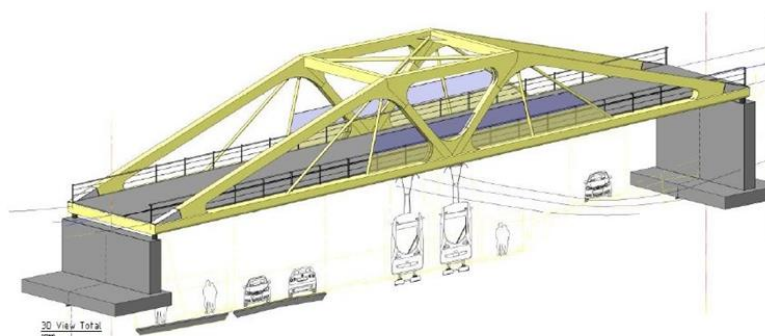
Figure 1.1.2 Paradis bridge [32] p.19

- bridge tower structure; due to global bending of the whole structure the parts of the cross section are locally compressed giving rise to buckling;

Figure 1.1.3 Landmark tower [32] p.74

Current design standards for FRP structures are still in development and are largely based on experimental data of pultruded profiles. Design procedures for local buckling that are available in the existing codes do not account for influence of initial imperfections but focus on the interaction between webs and flanges. Therefore, there is a great need for research data on VARTM-produced structural elements and on the influence of initial imperfections on buckling behaviour of plates.

Both pultrusion and VARTM are cost effective processes for production of FRP elements. Pultrusion is a continuous process in which fibres are lead into a resin bath for wetting, then pulled through a heated die where it is formed into the intended shape. After curing in the die the profiles are ready to be cut into desired lengths. VARTM is a closed mould process in which the placement of the fibres is done manually. After the fibres are placed in the mould, the resin inlet tubes are placed followed by a vacuum bad that is made of a transparent flexible material. The air is then sucked out and the resin starts to flow. The composite is removed from the mould after curing.

The key differences between structural elements produced by pultrusion and VARTM are:

Pultrusion	**VARTM**
• Prismatic profiles with open and closed cross-sections	• Large thin-walled elements, closed cross-section profiles
• Constant cross-section and layup over the whole length of the profile	• Freedom in geometry and layup over the length of the element
• In general, thicker plates; variation between the thickness within the cross-section is small	• Large variations of material properties and dimensions in the cross-section
	• Better dimensional tolerances

For the design of the elements produced by VARTM this means that the difference in thickness of webs and flanges - t_w; t_f - and various ratios of longitudinal and transverse elastic moduli E_x/E_y of a plate (flange or web), as well as difference in material properties – E_x; E_y; v_{xy} - of webs and flanges have to be accounted for. The analytical models that have been developed for pultruded profiles often leave out one or more of these considerations, simplifying the design procedure.

1.2 OBJECTIVE AND RESEARCH QUESTIONS

The objectives of this research are to clarify the design recommendations for buckling given in the two latest standards for FRP: CUR96 Vezelversterkte kunststoffen in bouwkundige en civieltechnische draagconstructies and JRC Prospect for New Guidance in the Design of FRP and to quantify the influence of initial geometric imperfections on the structural behaviour of FRP plates.

The main research question to be answered is:

- How do initial out of plane deformations influence the structural behaviour of Fibre Reinforced Polymer plates produced by Vacuum Assisted Resin Transfer Molding?

The key questions to be addressed are:

- What is the effect of shape and magnitude of imperfection?

- How much does the presence of initial imperfections degrade the load carrying capacity?

- Do the limiting values given in standards make sense in terms of design for buckling?

The methodology used in this project include literature research, which includes an overview of present design guidance and research papers on buckling of FRP plates, and finite element analysis. Linear, geometrically nonlinear and materially nonlinear analyses were used.

2. LITERATURE STUDY

The two topics that are the main focus of this literature study are the analytical models and the role of initial geometric imperfections in buckling of FRP plates and profiles. The goal is to answer the following questions:

- What are the applicability and limitations of the analytical models currently available in standards and literature?
- What is the role of boundary conditions and web / flange interaction?
- How are initial geometric imperfections considered in standards?
- What is the significance of buckling modes interaction?
- What is the effect of initial geometric imperfections on buckling behaviour of plates?

2.1 ANALYTICAL MODELS

Buckling of plates can be approached in two ways. A plate can be considered as a separate element with certain standard boundary conditions – simply supported, clamped, etc. Another way to look at plate buckling is to consider a plate as a part of an assembly, namely a profile. In latter case the local buckling (buckling of flanges or webs) of profiles is considered. The second approach is more practical for designers because in practice idealized boundary conditions can rarely be seen. The currently available analytical models for buckling of FRP profiles consider flanges and webs as separate plates and the main focus lies on the correct modelling of their boundary conditions taking into account the interaction between webs and flanges.

In this chapter an overview of analytical models dealing with buckling of FRP plates is presented, which include explicit expressions for plates with standard boundaries under uniform compression and linearly varying in-plane load, and design equations for profiles of various shapes given in the following documents: JRC Prospect for New Guidance in the Design of FRP (JRC) [1], CUR96 Vezelversterkte kunststoffen in bouwkundige en civieltechnische draagconstructies (CUR96) [2] and Stabilitätsverhalten ebener Tragwerke aus pultrudierten faserverstärkten Polymerprofilen by Heiko Trumpf [3] and the relevant background papers.

2.1.1 BUCKLING OF PLATES
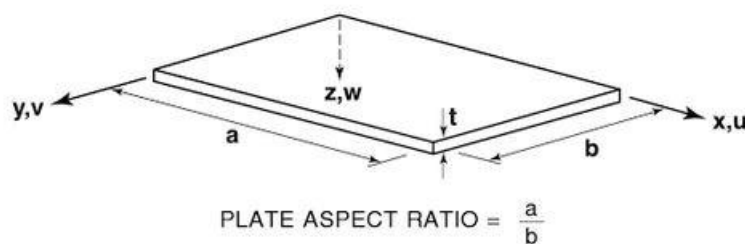
Figure 2.1.1 Perfect plate geometry [4] p. 227

Buckling of a plate is a sudden deviation from a flat state under in-plane loading (x-axis) into a state that is bowed in the normal direction (z-axis). The load under which the plate buckles is called critical buckling load. The value of this load depends on geometry of the plate and the material properties and can be determined with a linear eigenvalue analysis. What happens after the buckling load is reach can only be described by nonlinear analysis. Plates exhibit stable postbuckling behaviour, which means that a plate can still carry load after it buckles, which is illustrated in the following diagram.
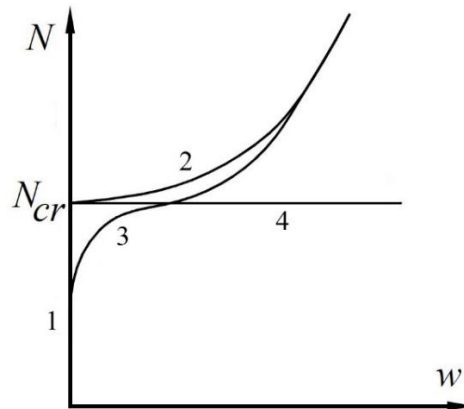
Figure 2.1.2 In-plane load versus out of plane deflection curves

Figure 2.1.2 describes the classical bifurcation behaviour. With increasing longitudinal loading, the plate deflection follows the ordinate upwards showing no out of plane deflection (1) – a plate only shortens in the load direction while remaining flat. Theoretically after the in-plane loading exceeds the critical buckling load N_{cr}, the curve might continue upwards up to the failure load. More realistically, at $N = N_{cr}$, which is called bifurcation point, assuming that the load is applied in the midplane of a perfectly flat plate, a plate will buckle and take a new shape and equilibrium state but still will be able to carry load with a reduced stiffness. This is shown by curve 2. In reality, initial imperfections in form of load eccentricities and geometric imperfections will be introduced, which will result in deviation from the curve 1-2 and postbuckling path will then look similar to the curve 3. Horizontal line 4 illustrates a neutral postbuckling behaviour, in this case a structural element (a bar) cannot carry load after the critical buckling load is reached.

2.1.2 PLATE BUCKLING DESIGN EXPRESSIONS

The equation of the deflected surface of symmetrically laminated perfectly flat plate is:

$$D_{11}\frac{\partial^4 w}{\partial x^4} + 4D_{16}\frac{\partial^4 w}{\partial x^3 \partial y} + 2(D_{12} + D_{66})\frac{\partial^4 w}{\partial x^2 \partial y^2} + 4D_{26}\frac{\partial^4 w}{\partial x \partial y^3} + D_{22}\frac{\partial^4 w}{\partial y^4} - N_x\frac{\partial^2 w}{\partial x^2} - 2N_{xy}\frac{\partial^2 w}{\partial x \partial y}$$
$$- N_y\frac{\partial^2 w}{\partial y^2} = 0$$

(2.1.1)

For symmetrical composite plate with cross-ply lamination there is no coupling between bending and twisting, which means that $D_{16} = D_{26} = 0$ and the equation becomes:

$$D_{11}\frac{\partial^4 w}{\partial x^4} + 2(D_{12} + D_{66})\frac{\partial^4 w}{\partial x^2 \partial y^2} + D_{22}\frac{\partial^4 w}{\partial y^4} - N_x\frac{\partial^2 w}{\partial x^2} - 2N_{xy}\frac{\partial^2 w}{\partial x \partial y} - N_y\frac{\partial^2 w}{\partial y^2} = 0$$

(2.1.2)

$D_{11}, D_{22}, D_{66}, D_{16}, D_{26}$ are the orthotropic plate stiffnesses defined as:

$$D_{ij} = \frac{1}{3}\sum_{k=1}^{n}(\bar{Q}_{ij})_k\left(h_k^3 - h_{k-1}^3\right)$$
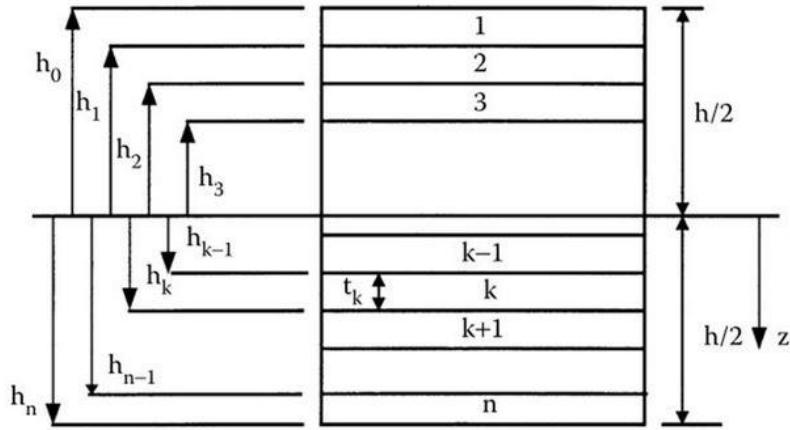
Figure 2.1.3 Laminate with n plies [5]

An exact solution of this equation is possible when the shear loading N_{xy} is equal to zero and N_x and N_y are constants.

For a plate that is loaded by uniform uniaxial loading:

$$D_{11}\frac{\partial^4 w}{\partial x^4} + 2(D_{12} + D_{66})\frac{\partial^4 w}{\partial x^2 \partial y^2} + D_{22}\frac{\partial^4 w}{\partial y^4} - N_x\frac{\partial^2 w}{\partial x^2} = 0$$

(2.1.3)

The boundary conditions for a plate simply supported at all four edges are (with respect to figure 2.1):

- at $x = 0, a$: $w = M_x = 0$;
$$M_x = -\left(D_{11}\frac{\partial^2 w}{\partial x^2} + D_{22}\frac{\partial^2 w}{\partial y^2}\right) \rightarrow w(x) = \frac{\partial^2 w}{\partial x^2} = 0$$
- at $y = 0, b$: $w = M_y = 0$
$$M_y = -\left(D_{12}\frac{\partial^2 w}{\partial x^2} + D_{22}\frac{\partial^2 w}{\partial y^2}\right) \rightarrow w(y) = \frac{\partial^2 w}{\partial y^2} = 0$$

(2.1.4)

Where M_x and M_y are bending moments.

The buckling mode may be taken in the form:

$$w(x,y) = c_{mn} \cdot \sin\frac{m\pi x}{a} \cdot \sin\frac{n\pi y}{b}$$

(2.1.5)

where c_{mn} is arbitrary amplitude coefficient.

Substituting (2.1.5) into (2.1.3) yields a fourth order ordinary differential equation which has an exact closed form solution. This equation was solved for plates with various boundary conditions under uniaxial loading; the most common cases are listed in the Table 2.1.

It can be seen that the buckling load N is a function of m, a number of half-waves in x direction of the plate (for uniaxial loading the number of half-waves in y direction is $n = 1$) and the aspect ratio $AR = a/b$. The fundamental buckling mode shape can have any number of half-waves in the direction of loading, depending on the aspect ratio and the stiffness ratio of a particular plate. For small plate aspect ratios the plate buckles into a single half-wave in x direction. As the aspect ratio increases, the number of half-waves m in the direction of the load increases. Figure 2.1.4 illustrates dependence of buckling load on aspect ratio for isotropic ($D_{11} = D_{22}$) plate. For a certain stiffness ratio there is a corresponding plate aspect ratio for which the plate buckles with a minimum in-plate loading into a certain buckled shape:

$$AR = m \cdot \sqrt[4]{\frac{D_{11}}{D_{22}}}$$

(2.1.6)

Substituting 2.1.6 into the first formula given in Table 2.1 the equation for the buckling load of a long plate with simply supported edges is derived. The design equations for the calculation of the critical buckling stress of long plates with various boundary conditions are presented in Table 2.2.

More in-depth derivations and investigations of plate equations for various loading and boundary conditions can be studied in works of S. G. Lekhnitskii [7] and A. W. Leissa [8].
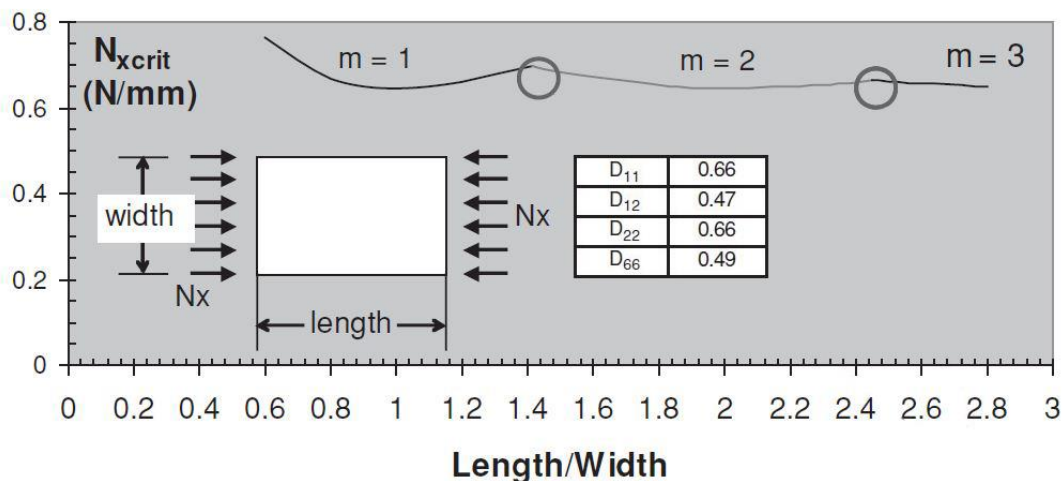
Figure 2.1.4 Dependence of aspect ratio of a plate on buckling load [6] p.129
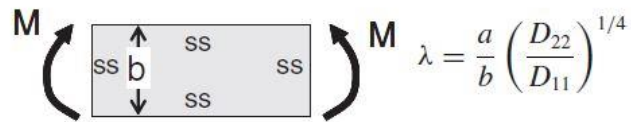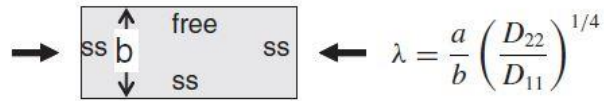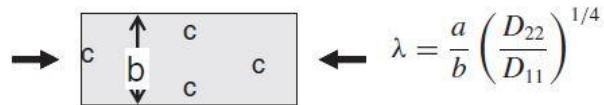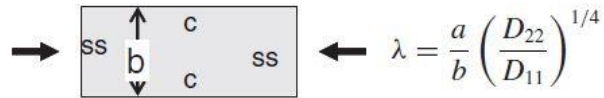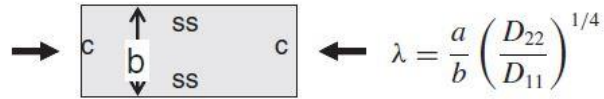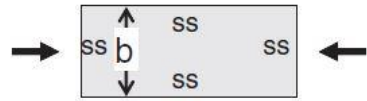
$$N_o = \frac{\pi^2 \left[D_{11} m^4 + 2(D_{12} + 2D_{66}) m^2 (AR)^2 + D_{22}(AR)^4\right]}{a^2 m^2}$$

$\lambda = \frac{a}{b}\left(\frac{D_{22}}{D_{11}}\right)^{1/4}$

$$N_o = \frac{\pi^2}{b^2}\sqrt{D_{11}D_{22}}\,(K) \quad K = \frac{4}{\lambda^2} + \frac{2(D_{12}+2D_{66})}{\sqrt{D_{11}D_{22}}} + \frac{3}{4}\lambda^2 \quad 0 < \lambda < 1.662$$

$$K = \frac{m^4 + 8\,m^2 + 1}{\lambda^2(m^2+1)} + \frac{2(D_{12}+D_{66})}{\sqrt{D_{11}D_{22}}} + \frac{\lambda^2}{m^2+1} \quad \lambda > 1.662$$

$\lambda = \frac{a}{b}\left(\frac{D_{22}}{D_{11}}\right)^{1/4}$

$$N_o = \frac{\pi^2}{b^2}\sqrt{D_{11}D_{22}}\,(K) \quad K = \frac{m^2}{\lambda^2} + \frac{2(D_{12}+2D_{66})}{\sqrt{D_{11}D_{22}}} + \frac{16\lambda^2}{3\,m^2}$$

$\lambda = \frac{a}{b}\left(\frac{D_{22}}{D_{11}}\right)^{1/4}$

$$N_o = \frac{\pi^2}{b^2}\sqrt{D_{11}D_{22}}\,(K) \quad K = \frac{4^2}{\lambda^2} + \frac{8(D_{12}+2D_{66})}{3\sqrt{D_{11}D_{22}}} + 4\lambda^2 \quad 0 < \lambda < 1.094$$

$$K = \frac{m^4 + 8\,m^2 + 1}{\lambda^2(m^2+1)} + \frac{2(D_{12}+D_{66})}{\sqrt{D_{11}D_{22}}} + \frac{\lambda^2}{m^2+1} \quad \lambda > 1.094$$

$\lambda = \frac{a}{b}\left(\frac{D_{22}}{D_{11}}\right)^{1/4}$

$$N_o = \frac{\pi^2}{b^2}\sqrt{D_{11}D_{22}}\,(K) \quad K = \frac{12}{\pi^2}\frac{D_{66}}{\sqrt{D_{11}D_{22}}} + \frac{1}{\lambda^2}$$

$\lambda = \frac{a}{b}\left(\frac{D_{22}}{D_{11}}\right)^{1/4}$

$$M_o = \frac{\pi^2}{b^2}\sqrt{D_{11}D_{22}}\,(K)$$

$$K = 0.047\pi^2 b^2 \sqrt{\left(\frac{m^2}{\lambda^2} + \frac{2(D_{12}+2D_{66})}{\sqrt{D_{11}D_{22}}} + \frac{\lambda^2}{m^2}\right)\left(\frac{m^2}{\lambda^2} + \frac{8(D_{12}+2D_{66})}{\sqrt{D_{11}D_{22}}} + 16\frac{\lambda^2}{m^2}\right)}$$

Table 2.1 Buckling load of plates with various boundary and loading conditions [6] p.146
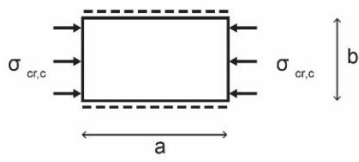
$$\sigma_{cr,c} = \frac{\pi^2}{tb^2}\left[2\sqrt{D_{11}D_{22}} + 2(D_{12} + 2D_{66})\right]$$
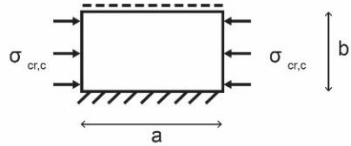
$$\sigma_{cr,c} = \frac{\pi^2}{tb^2}\left[3{,}125\sqrt{D_{11}D_{22}} + 2{,}33(D_{12} + 2D_{66})\right]$$
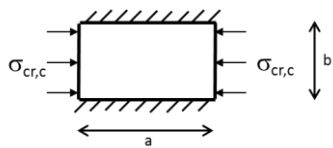
$$\sigma_{cr,c} = \frac{\pi^2}{tb^2}\left[4{,}53\sqrt{D_{11}D_{22}} + 2{,}44(D_{12} + 2D_{66})\right]$$
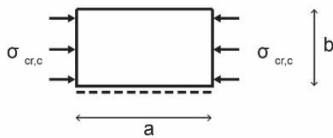
$$\sigma_{cr,c} = 12\frac{D_{66}}{tb^2}$$
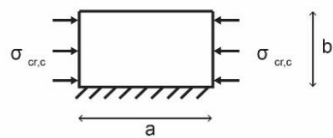
$$\sigma_{cr,c} = \frac{1}{tb^2}\sqrt{D_{11}D_{22}}\left[15{,}1K\sqrt{1-v} + 7(1-K)\right]$$
for K ≤ 1

$$\sigma_{cr,c} = \frac{1}{tb^2}\sqrt{D_{11}D_{22}}\left[15{,}1K\sqrt{1-v} + 6(K-1)(1-v)\right] \text{ for K > 1}$$
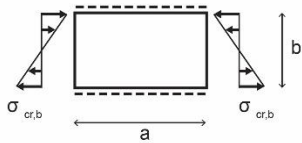
$$\sigma_{cr,b} = \frac{\pi^2}{tb^2}\left[13{,}4\sqrt{D_{11}D_{22}} + 10{,}4(D_{12} + 2D_{66})\right]$$
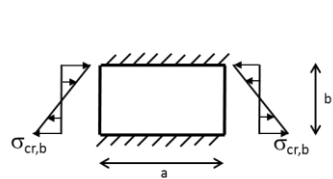
$$\sigma_{cr,b} = \frac{\pi^2}{tb^2}\left[26{,}8\sqrt{D_{11}D_{22}} + 12{,}9(D_{12} + 2D_{66})\right]$$
for K ≤ 3

$$\sigma_{cr,b} = \frac{\pi^2}{tb^2}\left[30{,}1\sqrt{D_{11}D_{22}} + 11{,}5(D_{12} + 2D_{66})\right]$$
for K > 3

———————	Free edge
▄▄ ▄▄ ▄▄ ▄▄	Simply supported edge
⁄⁄⁄⁄⁄⁄⁄⁄	Clamped edge

Table 2.2 Buckling load of long plates with various boundary and loading conditions [2] p. 75-76

Where:

a is the plate length

b is the plate width

t is the plate thickness

$$D_{11} = \frac{E_L \cdot t^3}{12 \cdot (1 - \nu_{LT} \cdot \nu_{TL})}$$

(2.1.7)

$$D_{22} = \frac{E_T \cdot t^3}{12 \cdot (1 - \nu_{LT} \cdot \nu_{TL})}$$

(2.1.8)

$$D_{12} = \nu_{LT} \cdot D_{22}$$

(2.1.9)

$$D_{66} = \frac{G_{LT} \cdot t^3}{12}$$

(2.1.10)

$$\upsilon = \frac{D_{12}}{2D_{66} + D_{12}}$$

(2.1.11)

$$K = \frac{2D_{66} + D_{12}}{\sqrt{D_{11} \cdot D_{22}}}$$

(2.1.12)

2.1.3 JRC PROSPECT FOR NEW GUIDANCE IN THE DESIGN OF FRP

DESIGN PROCEDURE

Design procedure for local instability under longitudinal compression for pultruded doubly symmetric elements is given in ANNEX C.

$N_{loc,Rd}$ is the design value of compressive force which determines the local instability of the element and can be calculated as:

$$N_{loc,Rd} = A \cdot f_{loc,d}^{axial}$$

(2.1.13)

The design value of local critical stresses is the minimum design value of critical stresses in the uniformly compressed flanges or the web: $f_{loc,d}^{axial} = \frac{\eta_c}{\gamma_M} \min \left\{ \left(f_{loc,k}^{axial} \right)_f, \left(f_{loc,k}^{axial} \right)_w \right\}$

Procedure to evaluate local critical stresses in the web and the flanges is given for I-cross section (figure 2.1.5).
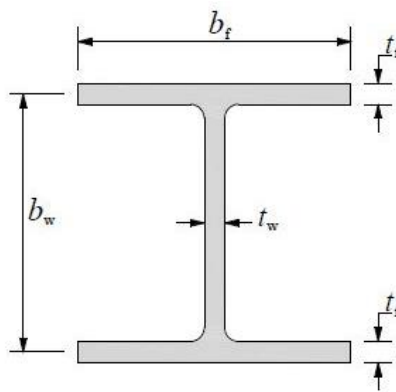
Figure 2.1.5 I-section [1] p. 151

Subscripts used:

f – flange; w – web; L- longitudinal direction; T- transversal direction.

First, the critical stresses are calculated assuming hinged connections between the flange and the web:

$$\left(f_{loc,k}^{axial} \right)_f^{SS} = 4 \cdot G_{LT} \cdot \left(\frac{t_f}{b_f} \right)^2$$

(2.1.14)

$$\left(f_{loc,k}^{axial} \right)_w^{SS} = k_c \cdot \frac{\pi^2 \cdot E_{Tc}}{12 \cdot (1 - \nu_{LT} \cdot \nu_{TL})} \cdot \left(\frac{t_w}{b_w} \right)^2 \; ; \; k_c = 2 \sqrt{\frac{E_{Lc}}{E_{Tc}}} + 4 \frac{G_{LT}}{E_{Tc}} \cdot (1 - \nu_{LT} \cdot \nu_{TL}) + 2 \cdot \nu_{LT}$$

(2.1.15)

$\left(f_{loc,k}^{axial} \right)_f^{SS}$ corresponds with the analytical solution for an orthotropic symmetrical plate that is loaded in longitudinal compression and is simply supported at three edges and has one unloaded

edge free and represents half of a flange of an I-section. $(f_{loc,k}^{axial})_w^{SS}$ is the solution for an orthotropic symmetrical plate which is simply supported at all four edges and is loaded by uniform compression and represents simplified boundary conditions for a web. k_c is called the plate buckling coefficient.

The element (web or flange) with lower critical stress will buckle first. It is then assumed that through the interaction between the flange and the web the element that has a higher critical stress will restrain the plate with lower critical buckling stress. The lower critical stress is then evaluated using expressions given in ANNEX E taking into account the interaction between the flange and the web.

In order to evaluate $(f_{loc,k}^{axial})_f$, when $(f_{loc,k}^{axial})_f^{SS} < (f_{loc,k}^{axial})_w^{SS}$, the stiffness of the rotational constraint $\tilde{k}$ exercised by the web on the flanges has to be taken into account:

$$(f_{loc,k}^{axial})_f = \frac{\sqrt{(D_{11})_f \cdot (D_{22})_f}}{t_f \cdot \left(\frac{b_f}{2}\right)^2} \cdot \left\{ K \cdot \left[15.1 \cdot \eta \cdot \sqrt{1-\rho} + 6 \cdot (1-\rho) \cdot (1-\eta)\right] + \frac{7 \cdot (1-K)}{\sqrt{1+4.12 \cdot \zeta}} \right\},$$

$$K \leq 1$$

(2.1.16)

$$(f_{loc,k}^{axial})_f = \frac{\sqrt{(D_{11})_f \cdot (D_{22})_f}}{t_f \cdot \left(\frac{b_f}{2}\right)^2} \cdot \left[15.1 \cdot \eta \cdot \sqrt{1-\rho} + 6 \cdot (1-\rho) \cdot (K-\eta)\right], K > 1$$

(2.1.17)

$$\zeta = \frac{(D_{22})_f}{\tilde{k} \cdot \frac{b_f}{2}}$$

(2.1.18)

$$\rho = \frac{(D_{12})_f}{2 \cdot (D_{66})_f + (D_{12})_f}$$

(2.1.19)

$$\eta = \frac{1}{\sqrt{1 + (7.22 - 3.55 \cdot \rho) \cdot \zeta}}$$

(2.1.20)

$$K = \frac{2 \cdot (D_{66})_f + (D_{12})_f}{\sqrt{(D_{11})_f \cdot (D_{22})_f}}$$

(2.1.21)

$$\tilde{k} = \frac{(D_{22})_w}{b_w} \cdot \left[1 - \frac{t_f \cdot (f_{loc,k}^{axial})_f^{SS} \cdot \frac{1}{(E_{Lc})_f \cdot t_f}}{t_w \cdot (f_{loc,k}^{axial})_w^{SS} \cdot \frac{1}{(E_{Lc})_w \cdot t_w}}\right] \geq 0$$

(2.1.22)

The expression to evaluate $(f_{loc,k}^{axial})_w$, in case $(f_{loc,k}^{axial})_w^{SS} < (f_{loc,k}^{axial})_f^{SS}$ takes into account the torsional stiffness GI_t of the constraint given by the flanges:

$$(f_{loc,k}^{axial})_w = \frac{\pi^2}{t_w \cdot b_w^2}$$
$$\cdot \left\{ 2 \cdot \sqrt{1 + 4.139 \cdot \xi'} \cdot \sqrt{(D_{11})_w \cdot (D_{22})_w} + (2 + 0.62 \cdot \xi'^2) \right.$$
$$\left. \cdot [(D_{12})_w + 2 \cdot (D_{66})_w] \right\}$$

(2.1.23)

$$\xi' = \frac{1}{1 + 10 \cdot \zeta'}$$

(2.1.24)

$$\zeta' = \frac{(D_{22})_w \cdot b_w}{GI_t}$$

(2.1.25)

$$GI_t = 4 \cdot (D_{66})_f \cdot b_f \cdot \left[1 - \frac{t_w \cdot (f_{loc,k}^{axial})_w^{SS} \cdot \frac{1}{(E_{Lc})_w \cdot t_w}}{t_f \cdot (f_{loc,k}^{axial})_f^{SS} \cdot \frac{1}{(E_{Lc})_f \cdot t_f}} \right]$$

(2.1.26)

Design procedure for local instability under bending loading for pultruded doubly symmetric elements is given in ANNEX D.

The design value of the bending moment which determines the local instability can be determined using the following expression:

$$M_{loc,Rd} = W \cdot f_{loc,d}^{flex}$$

(2.1.27)

When the element is subjected to bending the top flange is in compression and the web is in bending, the design value of the critical stress for flexure is $f_{loc,d}^{flex} = \frac{\eta_c}{\gamma_M} \min \left\{ (f_{loc,k}^{axial})_f, (f_{loc,k}^{flex})_w \right\}$.

$(f_{loc,k}^{axial})_f$, when $(f_{loc,k}^{axial})_f^{SS} < (f_{loc,k}^{flex})_w^{SS}$, can be determined in the same way as described in the procedure for uniform compression loading, first assuming simply supported edges, and then evaluating the critical stress using expressions 2.1.16 to 2.1.22.

$(f_{loc,k}^{flex})_w$, when $(f_{loc,k}^{flex})_w^{SS} < (f_{loc,k}^{axial})_f^{SS}$ is determined using the conservative expression:

$$(f_{loc,k}^{flex})_w = (f_{loc,k}^{flex})_w^{SS} = k_f \cdot \frac{\pi^2 \cdot E_{Tc}}{12 \cdot (1 - \nu_{LT} \cdot \nu_{TL})} \cdot \left(\frac{t_w}{b_w}\right)^2 ;$$

$$k_f = 13.9 \cdot \sqrt{\frac{E_{Lc}}{E_{Tc}}} + 22.2 \cdot \frac{G_{LT}}{E_{Tc}} \cdot (1 - \nu_{LT} \cdot \nu_{TL}) + 11.1 \cdot \nu_{LT}$$

(2.1.28)

Rearranging the expression (2.1.28) will result in the Lekhnitskii's formula for a plate that is simply supported and is loaded by linearly varying load:

$$\sigma_{cr} = \frac{\pi^2}{tb^2}\left[13.9\sqrt{D_{11}D_{22}} + 11.1(D_{12} + 2D_{66})\right]$$

(2.1.29)

It is the same as reported in JRC 15.2.4 and in Table 2.2 in 2.1.2 of this report but for the constants 13.9 and 11.1. The explanation for that is found in Trajan, Sapkas and Kollar (2010) [9]. It was concluded that these coefficients (13.9 and 11.1) are a little high and 13.4 and 10.4 give better approximation.

BACKGROUND

More detailed insight into the procedures given in JRC can be gained by studying the research paper by L. P. Kollar "Local Buckling of Fiber Reinforced Plastic Composite Structural Members with Open and Closed Cross Sections" [10], which provides calculation procedures for box, I-, C-, Z- and L-sections under compression and bending loads. This report will focus on I- and box sections.

Webs and flanges of a profile are considered as separate plates with rotationally restrained edges. Two ways of restrain are possible:

- edges rotationally restrained by springs
- edges rotationally restrained by stiffeners

In the first case, the rotational spring constant k_0 is considered:

$$k_0 = \frac{c \cdot (D_{22})_{rs}}{L_{rs}}$$

(2.1.30)

Coefficient c takes into account boundary conditions of the restraining plate and L is the width of the restraining plate. However, this expression is only valid when no axial load is applied. To take the effect of axial loading into account the amplification factor is used:

$$r = \frac{1}{1 - \dfrac{t_{bu} \cdot (f_{loc,k}^{axial})_{bu}^{SS} \cdot \dfrac{1}{(E_{Lc})_{bu} \cdot t_{bu}}}{t_{rs} \cdot (f_{loc,k}^{axial})_{rs}^{SS} \cdot \dfrac{1}{(E_{Lc})_{rs} \cdot t_{rs}}}}$$

(2.1.31)

Subscript bu stands for the element that buckles, rs – the element that restrains. If $(f_{loc,k}^{axial})_f^{SS} < (f_{loc,k}^{axial})_w^{SS}$, then the flange buckles first and the web will be the restraining plate and vice versa.

The torsional spring stiffness can be written as:

$$\tilde{k} = k_0 \cdot \frac{1}{r} = \frac{c \cdot (D_{22})_{rs}}{L_{rs}} \cdot \left[1 - \frac{t_{bu} \cdot (f_{loc,k}^{axial})_{bu}^{SS} \cdot \frac{1}{(E_{Lc})_{bu} \cdot t_{bu}}}{t_{rs} \cdot (f_{loc,k}^{axial})_{rs}^{SS} \cdot \frac{1}{(E_{Lc})_{rs} \cdot t_{rs}}} \right]$$

(2.1.32)

Coefficient c depends on the edge conditions of the restraining element and is given in the Figure 2.1.6:
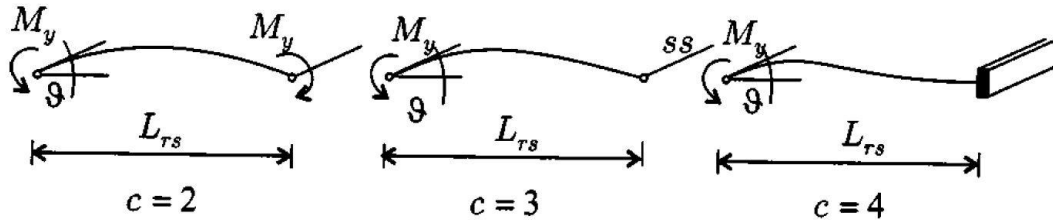
Figure 2.1.6 Coefficient c for different edge conditions [10] p. 1507

When the edges are restrained by stiffeners, the torsional stiffness is given as

$$GI_{t0} = 4 \cdot (D_{66})_{rs} \cdot L_{rs}$$

(2.1.33)

Taking into account the effect of axial loading:

$$GI_t = 4 \cdot (D_{66})_{rs} \cdot L_{rs} \cdot \left[1 - \frac{t_{bu} \cdot (f_{loc,k}^{axial})_{bu}^{SS} \cdot \frac{1}{(E_{Lc})_{bu} \cdot t_{bu}}}{t_{rs} \cdot (f_{loc,k}^{axial})_{rs}^{SS} \cdot \frac{1}{(E_{Lc})_{rs} \cdot t_{rs}}} \right]$$

(2.1.34)

In case of an I-section under the axial loading the same procedure as described by equations 2.1.14 to 2.1.26 applies. If the flange buckles first, the web is the restraining plate and the flange is the buckling plate, coefficient $c = 2$ and a factor of $1/2$ is introduced because the web restrains two "half" flanges:

$$\tilde{k} = \frac{1}{2} \cdot \frac{c \cdot (D_{22})_{rs}}{L_{rs}} \cdot \left[1 - \frac{t_{bu} \cdot (f_{loc,k}^{axial})_{bu}^{SS} \cdot \frac{1}{(E_{Lc})_{bu} \cdot t_{bu}}}{t_{rs} \cdot (f_{loc,k}^{axial})_{rs}^{SS} \cdot \frac{1}{(E_{Lc})_{rs} \cdot t_{rs}}} \right]$$

(2.1.35)

After rewriting the expression 2.1.35 it will become identical to expression 2.1.22 given in JRC.

For the situation when the web of the I-section buckles first under uniform compression and the torsional stiffness GI_t is considered, it should be noted that the expression 2.1.24 from JRC is not the same as given by Kollar:

$$\xi' = \frac{1}{1 + 0.6 \cdot \zeta'^{1.2}}$$

(2.1.36)

21

For a hollow section in compression the same general procedure applies, except in case of box members the boundary conditions for the webs are the flanges are identical. Therefore, to evaluate critical stress for both the webs and the flanges the rotational spring constant is used. Also, in a hollow section when calculating spring constant factor of $1/2$ is omitted and the expression becomes:

$$\tilde{k} = \frac{c \cdot (D_{22})_{rs}}{L_{rs}} \cdot \left[1 - \frac{t_{bu} \cdot (f_{loc,k}^{axial})_{bu}^{SS} \cdot \frac{1}{(E_{Lc})_{bu} \cdot t_{bu}}}{t_{rs} \cdot (f_{loc,k}^{axial})_{rs}^{SS} \cdot \frac{1}{(E_{Lc})_{rs} \cdot t_{rs}}} \right]$$

(2.1.37)

with $c = 2$.

Under linearly varying loading (bending) for an I-section the spring constant according to Kollar is calculated with equation 2.1.35 with $c = 4$ because when a profile is in bending, only one flange is in compression and the tensile flange stabilizes the web. The introduction of coefficient $c = 4$ will result in a different value of rotational spring constant than described in JRC.

For flanges of a hollow section in bending the spring constant is calculated using equation 2.1.37 with $c = 4$.

No closed form solution was in given for a plate with rotationally restrained edges subjected to a linearly varying normal force and therefore the webs both of I- and box sections should be calculated using the conservative expression 2.1.29.

Table 2.3 summarizes design equations proposed by Kollar for I- and hollow cross-sections under uniform compression and bending.

Table 2.4 gives a comparison of equations given in JRC and by Kollar for an I-profile in compression and in bending.

I-section		Hollow section	
Compression	Bending	Compression	Bending
$(f_{loc,k}^{axial})_f^{SS} = \dfrac{12(D_{66})_f}{t_f(b_f/2)^2}$ (spanning both columns)		$(f_{loc,k}^{axial})_f^{SS} = \dfrac{\pi^2}{t_f b_f^2}\left\{2\sqrt{(D_{11})_f(D_{22})_f} + 2[(D_{12})_f + 2(D_{66})_f]\right\}$ (spanning both columns)	
$(f_{loc,k}^{axial})_w^{SS} = \dfrac{\pi^2}{t_w b_w^2}\left\{2\sqrt{(D_{11})_w(D_{22})_w} + 2[(D_{12})_w + 2(D_{66})_w]\right\}$	$(f_{loc,k}^{flex})_w^{SS} = \dfrac{\pi^2}{t_w b_w^2}\left\{13.9\sqrt{(D_{11})_w(D_{22})_w} + 11.1[(D_{12})_w + 2(D_{66})_w]\right\}$	$(f_{loc,k}^{axial})_w^{SS} = \dfrac{\pi^2}{t_w b_w^2}\left\{2\sqrt{(D_{11})_w(D_{22})_w} + 2[(D_{12})_w + 2(D_{66})_w]\right\}$	$(f_{loc,k}^{flex})_w^{SS} = \dfrac{\pi^2}{t_w b_w^2}\left\{13.9\sqrt{(D_{11})_w(D_{22})_w} + 11.1[(D_{12})_w + 2(D_{66})_w]\right\}$
flange buckles first: $\tilde{k} = \dfrac{(D_{22})_w}{b_w}\left[1 - \dfrac{(f_{loc,k}^{axial})_f^{SS}(E_{Lc})_w}{(f_{loc,k}^{axial})_w^{SS}(E_{Lc})_f}\right]$ web buckles first: $GI_t = 4(D_{66})_f b_f\left[1 - \dfrac{(f_{loc,k}^{axial})_w^{SS}(E_{Lc})_f}{(f_{loc,k}^{axial})_f^{SS}(E_{Lc})_w}\right]$	flange buckles first: $\tilde{k} = \dfrac{2(D_{22})_w}{b_w}\left[1 - \dfrac{(f_{loc,k}^{axial})_f^{SS}(E_{Lc})_w}{(f_{loc,k}^{flex})_w^{SS}(E_{Lc})_f}\right]$ web buckles first: $GI_t = 4(D_{66})_f b_f\left[1 - \dfrac{(f_{loc,k}^{flex})_w^{SS}(E_{Lc})_f}{(f_{loc,k}^{axial})_f^{SS}(E_{Lc})_w}\right]$	flange buckles first: $\tilde{k}_w = \dfrac{2(D_{22})_w}{b_w}\left[1 - \dfrac{(f_{loc,k}^{axial})_f^{SS}(E_{Lc})_w}{(f_{loc,k}^{axial})_w^{SS}(E_{Lc})_f}\right]$ web buckles first: $\tilde{k}_f = \dfrac{2(D_{22})_f}{b_f}\left[1 - \dfrac{(f_{loc,k}^{axial})_w^{SS}(E_{Lc})_f}{(f_{loc,k}^{axial})_f^{SS}(E_{Lc})_w}\right]$	flange buckles first: $\tilde{k}_w = \dfrac{4(D_{22})_w}{b_w}\left[1 - \dfrac{(f_{loc,k}^{axial})_f^{SS}(E_{Lc})_w}{(f_{loc,k}^{flex})_w^{SS}(E_{Lc})_f}\right]$ web buckles first: $\tilde{k}_f = \dfrac{4(D_{22})_f}{b_f}\left[1 - \dfrac{(f_{loc,k}^{flex})_w^{SS}(E_{Lc})_f}{(f_{loc,k}^{axial})_f^{SS}(E_{Lc})_w}\right]$
$(f_{loc,k}^{axial})_f = \dfrac{\sqrt{(D_{11})_f(D_{22})_f}}{t_f(b_f/2)^2}\left\{K[15.1\eta\sqrt{1-\rho} + 6(1-\rho)(1-\eta)] + \dfrac{7(1-K)}{\sqrt{1+4.12\zeta}}\right\}, K \le 1$ $(f_{loc,k}^{axial})_f = \dfrac{\sqrt{(D_{11})_f(D_{22})_f}}{t_f(b_f/2)^2}[15.1\eta\sqrt{1-\rho} + 6(1-\rho)(K-\eta)], K > 1$ $\zeta = \dfrac{(D_{22})_f}{\tilde{k} b_f/2}; \; \rho = \dfrac{(D_{12})_f}{2(D_{66})_f + (D_{12})_f}; \; \eta = \dfrac{1}{\sqrt{1+(7.22-3.55\rho)\zeta}}; \; K = \dfrac{2(D_{66})_f + (D_{12})_f}{\sqrt{(D_{11})_f(D_{22})_f}}$ (spanning both columns)		$(f_{loc,k}^{axial})_f = \dfrac{\pi^2}{t_f b_f^2}\left\{2\sqrt{1+4.139\xi}\sqrt{(D_{11})_f(D_{22})_f} + (2+0.62\xi^2)[(D_{12})_f + 2(D_{66})_f]\right\}$ $\xi = \dfrac{1}{1+10\zeta}; \; \zeta = \dfrac{(D_{22})_f}{\tilde{k}_w b_f}$ (spanning both columns)	
$(f_{loc,k}^{axial})_w = \dfrac{\pi^2}{t_w b_w^2}\left\{2\sqrt{1+4.139\xi'}\sqrt{(D_{11})_w(D_{22})_w} + (2+0.62\xi'^2)[(D_{12})_w + 2(D_{66})_w]\right\}$ $\xi' = \dfrac{1}{1+0.61\zeta'^{1.2}}; \; \zeta' = \dfrac{(D_{22})_w b_w}{GI_t}$	$(f_{loc,k}^{flex})_w = \dfrac{\pi^2}{t_w b_w^2}\left\{13.9\sqrt{(D_{11})_w(D_{22})_w} + 11.1[(D_{12})_w + 2(D_{66})_w]\right\}$	$(f_{loc,k}^{axial})_w = \dfrac{\pi^2}{t_w b_w^2}\left\{2\sqrt{1+4.139\xi}\sqrt{(D_{11})_w(D_{22})_w} + (2+0.62\xi^2)[(D_{12})_w + 2(D_{66})_w]\right\}$ $\xi = \dfrac{1}{1+10\zeta}; \; \zeta = \dfrac{(D_{22})_w}{\tilde{k}_f b_w}$	$(f_{loc,k}^{flex})_w = \dfrac{\pi^2}{t_w b_w^2}\left\{13.9\sqrt{(D_{11})_w(D_{22})_w} + 11.1[(D_{12})_w + 2(D_{66})_w]\right\}$

Table 2.3 Formulas for web and flange buckling stresses of I- and hollow cross sections according to Kollar (2003)

JRC	Kollar
Compression	

$$(f_{loc,k}^{axial})_f^{SS} = \frac{12(D_{66})_f}{t_f(b_f/2)^2}; \ (f_{loc,k}^{axial})_w^{SS} = \frac{\pi^2}{t_w b_w^2}\left\{2\sqrt{(D_{11})_w(D_{22})_w} + 2[(D_{12})_w + 2(D_{66})_w]\right\}$$

flange buckles first:

$$\tilde{k} = \frac{(D_{22})_w}{b_w}\left[1 - \frac{(f_{loc,k}^{axial})_f^{SS}(E_{Lc})_w}{(f_{loc,k}^{axial})_w^{SS}(E_{Lc})_f}\right]$$

web buckles first:

$$GI_t = 4(D_{66})_f b_f\left[1 - \frac{(f_{loc,k}^{axial})_w^{SS}(E_{Lc})_f}{(f_{loc,k}^{axial})_f^{SS}(E_{Lc})_w}\right]$$

$$(f_{loc,k}^{axial})_f = \frac{\sqrt{(D_{11})_f(D_{22})_f}}{t_f(b_f/2)^2}\left\{K\left[15.1\eta\sqrt{1-\rho} + 6(1-\rho)(1-\eta)\right] + \frac{7(1-K)}{\sqrt{1+4.12\zeta}}\right\}, K \le 1$$

$$(f_{loc,k}^{axial})_f = \frac{\sqrt{(D_{11})_f(D_{22})_f}}{t_f(b_f/2)^2}\left[15.1\eta\sqrt{1-\rho} + 6(1-\rho)(K-\eta)\right], K > 1$$

$$\zeta = \frac{(D_{22})_f}{\tilde{k}b_f/2}; \ \rho = \frac{(D_{12})_f}{2(D_{66})_f + (D_{12})_f}; \ \eta = \frac{1}{\sqrt{1+(7.22-3.55\rho)\zeta}}; \ K = \frac{2(D_{66})_f + (D_{12})_f}{\sqrt{(D_{11})_f(D_{22})_f}}$$

JRC	Kollar
$$(f_{loc,k}^{axial})_w = \frac{\pi^2}{t_w b_w^2}\left\{2\sqrt{1+4.139\xi'}\sqrt{(D_{11})_w(D_{22})_w} + (2+0.62\xi'^2)[(D_{12})_w + 2(D_{66})_w]\right\}$$ $$\boldsymbol{\xi' = \frac{1}{1+10\zeta'}}; \zeta' = \frac{(D_{22})_w b_w}{GI_t}$$	$$(f_{loc,k}^{axial})_w = \frac{\pi^2}{t_w b_w^2}\left\{2\sqrt{1+4.139\xi'}\sqrt{(D_{11})_w(D_{22})_w} + (2+0.62\xi'^2)[(D_{12})_w + 2(D_{66})_w]\right\}$$ $$\boldsymbol{\xi' = \frac{1}{1+0.61\zeta'^{1.2}}}; \zeta' = \frac{(D_{22})_w b_w}{GI_t}$$
Bending	

$$(f_{loc,k}^{axial})_f^{SS} = \frac{12(D_{66})_f}{t_f(b_f/2)^2}; \ (f_{loc,k}^{flex})_w^{SS} = \frac{\pi^2}{t_w b_w^2}\left\{13.9\sqrt{(D_{11})_w(D_{22})_w} + 11.1[(D_{12})_w + 2(D_{66})_w]\right\}$$

JRC	Kollar
flange buckles first: $$\boldsymbol{\tilde{k} = \frac{(D_{22})_w}{b_w}\left[1 - \frac{(f_{loc,k}^{axial})_f^{SS}(E_{Lc})_w}{(f_{loc,k}^{flex})_w^{SS}(E_{Lc})_f}\right]}$$ web buckles first: $$GI_t = 4(D_{66})_f b_f\left[1 - \frac{(f_{loc,k}^{flex})_w^{SS}(E_{Lc})_f}{(f_{loc,k}^{axial})_f^{SS}(E_{Lc})_w}\right]$$	flange buckles first: $$\boldsymbol{\tilde{k} = \frac{2(D_{22})_w}{b_w}\left[1 - \frac{(f_{loc,k}^{axial})_f^{SS}(E_{Lc})_w}{(f_{loc,k}^{flex})_w^{SS}(E_{Lc})_f}\right]}$$ web buckles first: $$GI_t = 4(D_{66})_f b_f\left[1 - \frac{(f_{loc,k}^{flex})_w^{SS}(E_{Lc})_f}{(f_{loc,k}^{axial})_f^{SS}(E_{Lc})_w}\right]$$

$$(f_{loc,k}^{axial})_f = \frac{\sqrt{(D_{11})_f(D_{22})_f}}{t_f(b_f/2)^2}\left\{K\left[15.1\eta\sqrt{1-\rho} + 6(1-\rho)(1-\eta)\right] + \frac{7(1-K)}{\sqrt{1+4.12\zeta}}\right\}, K \le 1$$

$$(f_{loc,k}^{axial})_f = \frac{\sqrt{(D_{11})_f(D_{22})_f}}{t_f(b_f/2)^2}\left[15.1\eta\sqrt{1-\rho} + 6(1-\rho)(K-\eta)\right], K > 1$$

$$\zeta = \frac{(D_{22})_f}{\tilde{k}b_f/2}; \ \rho = \frac{(D_{12})_f}{2(D_{66})_f + (D_{12})_f}; \ \eta = \frac{1}{\sqrt{1+(7.22-3.55\rho)\zeta}}; \ K = \frac{2(D_{66})_f + (D_{12})_f}{\sqrt{(D_{11})_f(D_{22})_f}}$$

$$(f_{loc,k}^{flex})_w = \frac{\pi^2}{t_w b_w^2}\left\{13.9\sqrt{(D_{11})_w(D_{22})_w} + 11.1[(D_{12})_w + 2(D_{66})_w]\right\}$$

Table 2.4 Local buckling of an I-section according to JRC and Kollar

2.1.4 CUR96 VEZELVERSTERKTE KUNSTSTOFFEN IN BOUWKUNDIGE EN CIVIELTECHNISCHE DRAAGCONSTRUCTIES

DESIGN PROCEDURE

Annex E provides analytical formulas to determine characteristic buckling strength that accounts for wrinkling but does not account for imperfections. The given equations can be applied for I-, H- and hollow sections.

For a profile under longitudinal compression critical stress of the flange is given by the following expression:

$$f_{c,stab,k,f} = \frac{\pi^2}{12} \cdot \left(\frac{t_f}{b}\right)^2 \cdot \left[\sqrt{q} \cdot \left(2 \cdot \sqrt{E_x \cdot E_y}\right) + p \cdot \left(y \cdot v_{xy} + 2 \cdot G_{xy}\right)\right]$$

(2.1.38)

p, q are constants that are defined by the coefficient of restraint ξ; for I- and H-shaped cross sections:

$$p = 0.3 + \frac{0.004}{\xi - 0.5}; \quad q = \frac{0.025 + \frac{0.065}{\xi + 0.4}}{\theta_{corr}^2}; \quad \xi = \frac{2 \cdot b_w}{b_f}; \quad b = \frac{b_f}{2}; \quad \theta_{corr} = 1.1$$

(2.1.39)
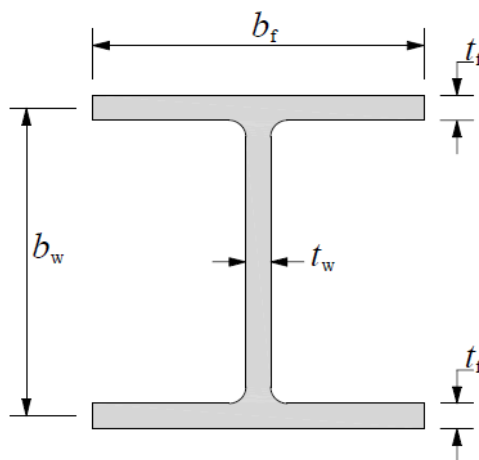
Figure 2.1.7 I-. H- sections [2] p. 151

For hollow sections:

$$p = 2.0 + \frac{0.002}{\xi - 1.3}; \quad q = 1.0 + \frac{0.08}{\xi + 0.2}; \quad \xi = \frac{b_w}{b_f}; \quad b = b_f$$

(2.1.40)
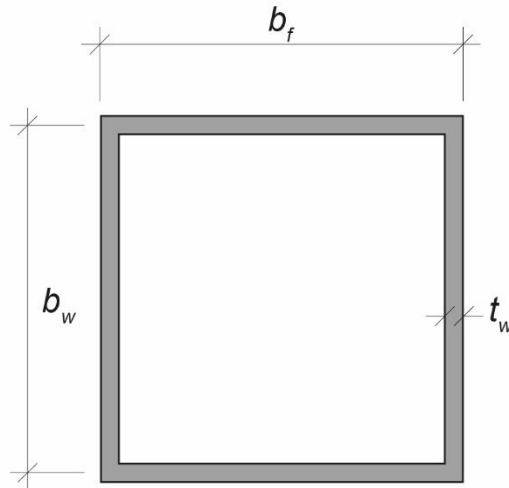
Figure 2.1.8 Hollow section [2] p. 152

Critical buckling stress of the web is calculated assuming simply supported connection to the flanges:

$$f_{c,stab,k,w} = \frac{\pi^2}{t_w \cdot b_w^2} \cdot \left(2 \cdot \sqrt{D_{11,w} \cdot D_{22,w}} + 2 \cdot \left(D_{12,w} + 2D_{66,w}\right)\right)$$

(2.1.41)

The critical stress for flanges in a profile in bending is given by expression 2.1.38.

For I- and H-shaped cross sections:

$$p = 0.3 + \frac{0.004}{\xi - 0.5}; \quad q = 0.025 + \frac{0.065}{\xi + 0.4}; \quad \xi = \frac{b_w}{b_f}; \quad b = \frac{b_f}{2}$$

(2.1.42)

For hollow sections:

$$p = 2.0 + \frac{0.002}{\xi - 1.3}; \quad q = 1.0 + \frac{0.08}{\xi + 0.2}; \quad \xi = \frac{b_w}{b_f}; \quad b = 0.85 \cdot (b_f - t_w)$$

(2.1.43)

Critical buckling stress of the web is then determined with the expression:

$$f_{b,stab,k,w} = \frac{\pi^2}{t_w \cdot b_w^2} \cdot \left(13.4 \cdot \sqrt{D_{11,w} \cdot D_{22,w}} + 10.4 \cdot \left(D_{12,w} + 2D_{66,w}\right)\right)$$

(2.1.44)

As it can be seen, the difference in calculating critical buckling stress for axial compression and bending for I- and H- sections lies in definition of coefficient of constraint ξ. For calculating critical buckling stress in the flange which is a part of profile in bending the same formula as for uniaxial compression is used. In case of bending the flange in tension supports the web, while under uniform compression both flanges will buckle. For hollow sections the flange width b is reduced in case of bending by 15% compared to case of axial compression.

BACKGROUND

It should be noted, that the equations given in CUR96 do not take into account the difference between material properties of flanges in webs. The coefficient of constraint ξ is calculated based only on geometry of the cross-section. If material properties of the webs and flanges differ, the expression for the coefficient of restraint ξ should be calculated according to the background document Step-by-Step Engineering Design Equations for Fiber-reinforced Plastic Beams for Transportation Structures [11]:

For I- and H-shaped cross sections:

$$\xi = \frac{2 \cdot b_w}{b_f} \cdot \frac{E_{T,f}}{E_{T,w}}$$

(2.1.45)

For hollow sections:

$$\xi = \frac{b_w - t_f}{b_f - t_w} \cdot \frac{E_{y,f}}{E_{y,w}}$$

(2.1.46)

The critical force is calculated depending on the loading conditions. The example is given for three-point bending:
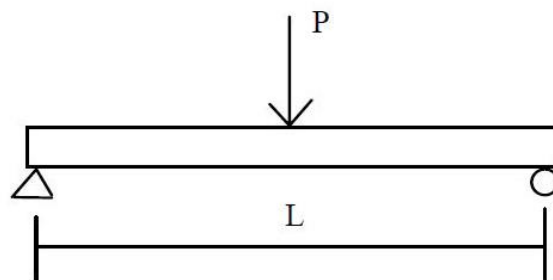
Figure 2.1.9 Three-point bending [11] p. 29

In this case the maximum moment in the midspan of the beam is given as:

$$M_{max} = \frac{P \cdot L}{4} \rightarrow P = \frac{4 \cdot M_{max}}{L}$$

(2.1.47)

From the well-known bending stress expression the moment can be expressed:

$$\sigma = \frac{M_P}{W} \rightarrow M_P = \sigma \cdot W$$

(2.1.48)

and

$$W = \frac{I}{b_w/2}$$

(2.1.49)

Substituting 2.1.48 and 2.1.49 into 2.1.47:

$$P = \frac{8 \cdot \sigma \cdot I}{b_w \cdot L}$$

(2.1.50)

Beam stiffness for I- and hollow sections can be defined by equations 2.1.51 and 2.1.52 respectively:

$$D = \frac{1}{2} \cdot E_{L,f} \cdot t_f \cdot b_w^2 \cdot b_f + \frac{1}{12} \cdot E_{L,w} \cdot t_w \cdot b_w^3 + \frac{1}{6} \cdot E_{L,f} \cdot t_f^3 \cdot b_f$$

(2.1.51)

$$D = \frac{1}{2} \cdot E_{L,f} \cdot t_f \cdot b_w^2 \cdot b_f + \frac{1}{6} \cdot E_{L,w} \cdot t_w \cdot b_w^3 + \frac{1}{6} \cdot E_{L,f} \cdot t_f^3 \cdot b_f$$

(2.1.52)

The critical force then is:

$$P_{cr}^{local} = \frac{8 \cdot D \cdot \sigma_{cr}}{E_{L,f} \cdot b_w \cdot L}$$

(2.1.53)

with σ_{cr} defined by 2.1.38.

Comparing the expression from CUR96 for the critical local buckling stress in the flange to 2.1.53 for the critical force, it can be seen that the stress expression does not take into consideration the thickness of the web because the t_w comes into calculations only when the critical force, not stress, is computed. This means that CUR96 equations for local buckling of the flange are applicable for cross-sections where thickness of the flange equals to thickness of the web.

2.1.5 STABILITÄTSVERHALTEN EBENER TRAGWERKE AUS PULTRUDIERTEN FASERVERSTÄRKTEN POLYMERPROFILEN

The design procedure proposed in this research is similar to the one that is used for checking the stability of steel plates and is developed for pultruded profiles of hollow, I- and C- cross-sections with $E_L/E_T = 2.45$ and $f_L/f_T = 2.85$.

The first step is to determine the class of the cross-section of individual parts of the profile. There are 2 cross-sectional classes defined:

- class 3: cross-sections of this class reach the strength limit in the most unfavourable fibre and further stressing is not stressing is employed;
- class 4: to determine the resistance of cross-sections of class 4 the local buckling of compressed parts has to be taken into account.

Maximum values of width-to-thickness ratios are given for the class 3 in tables 5.1 and 5.2 in [3]. If these values are exceeded, then the cross-section belongs to class 4.

The plate buckling factor $k_{\sigma x}$ is determined next. The plate buckling factor depends on the boundary conditions and loading conditions. In case of pultruded profiles two types of plates are considered: plates that are simply supported at the two edges (webs) and plates that are simply supported at one edge (flange of an open section). Values of $k_{\sigma x}$ are calculated for the two types of plates and 13 load cases, which include pure compression, pure bending and various combinations of compression combined with bending and are given in tables 3.1 to 3.3.

Once the plate buckling is known, critical plate buckling stress can be calculated with the expression:

$$\sigma_{crx,p} = k_{\sigma x} \cdot \frac{\pi^2 \sqrt{E_{cL} \cdot E_{cT}}}{12 \cdot (1 - \nu_{LT} \cdot \nu_{TL})} \cdot \left(\frac{t}{b}\right)^2$$

(2.1.54)

The buckling stress of a plate (flange, web) is given as $f_{ux\,i} = \chi_p \cdot f_{cx}$; χ_p is a reduction factor and can be determined from buckling curves or using the following expression:

$$\chi_p = \frac{1}{\Phi + \sqrt{\Phi^2 - \bar{\lambda}_p^\gamma}} \leq 0$$

(2.1.55)

$\chi_p = 1{,}0$ for sections of class 4 and the resistance is calculated using the full area of the section.

Shape function is defined as $\Phi = 0.5 \cdot \left(1 + \alpha_p \cdot \left(\bar{\lambda}_p - \bar{\lambda}_{p,0}\right) + \bar{\lambda}_p^\gamma\right)$

Parameter $\bar{\lambda}_p$ is plate slenderness and is a square root of ratio of compressive strength and critical buckling load:

$$\bar{\lambda}_p = \sqrt{\frac{f_{cx}}{\sigma_{crx,p}}}$$

(2.1.56)

Parameters α_p – imperfection factor, $\bar{\lambda}_{p,0}$ – length of horizontal plateau in the buckling curve diagram and γ – restraint coefficient are determined experimentally and numerically.

For webs:

$\gamma = 2$; $\bar{\lambda}_{p,0} = 0.37$; $\alpha_p = 1.15$

and flanges:

$\gamma = 1$; $\bar{\lambda}_{p,0} = 0.37$; $\alpha_p = 1.0$

$f_{ux\,2} = max(f_{ux\,i})$ is the capacity of the strongest part of the profile. The effective widths are given in tables 5.3 and 5.4;

$$A_{eff\,i} = A_i \cdot \frac{f_{ux\,i}}{f_{ux\,2}}$$

(2.1.57)

And the resistance of the cross-section can then be calculated based on the effective cross-section.

This model takes the influence of initial geometrical imperfections into account by incorporating the imperfection factor α_p. However, this influence is applied to the ultimate load, not the buckling load. For the critical buckling stress this model assumes simply supported boundary conditions between webs and flanges, giving a conservative estimation of the buckling strength.

2.2 IMPERFECTIONS

The imperfections of FRP structural elements can be divided in two groups: internal and external. Internal imperfections, or material imperfections, are the imperfections that occur in the material itself. Some examples are voids, local waviness of fabrics, initial delamination. External imperfections have to do with the deviations of the intended geometry of the considered element: flatness and straightness of the element or variations in thickness, or load and support eccentricities. This study focuses on the geometric imperfections of plates and profiles.

The analytical models for local buckling in standards focus on the web/flange interaction. This chapter will describe the effect of initial imperfections on buckling behaviour of plates, how the initial imperfections are implemented in the standards in the design equations, and what limiting values of geometric imperfections found in literature.

2.2.1 EFFECT OF INITIAL IMPERFECTIONS
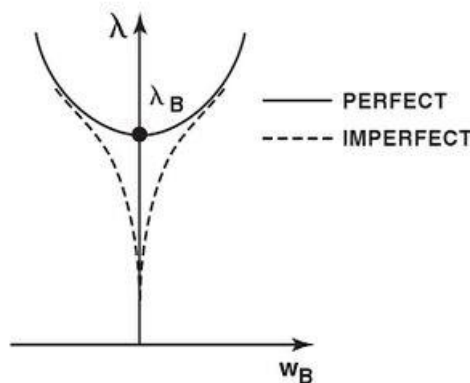
Figure 2.2.1 Perfect and imperfect plate buckling [4] p. 22

For the symmetric stable postbuckling behaviour, which is characteristic for plates, effects of initial imperfections result in a path deviation from the postbuckling curve of a perfect structure in a manner shown in the figure 2.2.1. The degree of deviation of the imperfect postbuckling path depends on the magnitude and nature of the initial imperfection. The most detrimental geometric imperfection is assumed to be the one in a shape of a buckling mode of a perfect plate. The most noticeable effect of initial imperfections occurs around the load values where buckling of a perfect plate occurs. The larger the imperfection magnitude, the more rounded – over load versus displacement curve becomes.

While classical bifurcation buckling is an eigenvalue problem, the imperfect plate buckling is an equilibrium problem. The postbuckling paths can be determined with a nonlinear analysis.
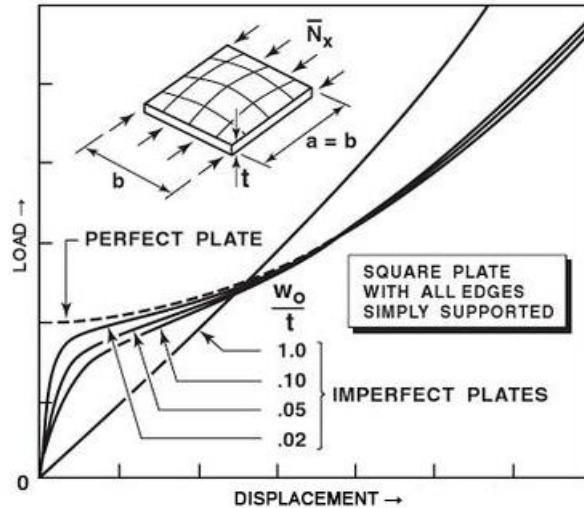
Figure 2.2.2 Buckling of a square plate with initial imperfections

As it can be seen from the figure 2.2.2 it is problematic to determine the critical load for an actual imperfect plate because of a rounded-over postbuckling path with no clear bifurcation point. It can also be noticed that when the magnitude of imperfection is very large then the curve becomes almost linear. In principle, an imperfect plate does not buckle; it begins with an initial bow which gradually increases without changing shape. Often large increase in transversal deformation occurs near the bifurcation load of a perfect plate. Next to that, a plate with initial out of plane deformation can buckle into a different shape at loads that are higher than the critical buckling load of a perfect plate. This effect is called secondary buckling.

Even though an imperfect plate does not have a clearly defined buckling load, there are methods to approximate this value for design purposes:

- strain-reversal method
- top-of-the-knee method.

In strain-reversal method two compressive strains in the x-direction are considered: on the concave side (ε_1) and on the convex side (ε_2) of the bowed plate. As the in-plane compressive load increases, so do the strains. At the critical stress strain ε_2 stops increasing and begins decreasing, this point is estimated as the buckling load. In top-of-the-knee method the portion of the postbuckling curve, where the rate of increase of out of plane deformation goes from low to high, is called "knee". The top of it corresponds to the approximate buckling load. Both methods are subjective as different observers might determine the load values slightly differently and become more difficult to apply as the magnitude of initial imperfection becomes larger.

A square composite plate that is clamped at all edges was researched in [12]. This paper presents finite element and experimental modelling of composite plates with initial transversal imperfection and finite element modelling of delaminated composite plates. The plate that is analysed is a part of a ship hull structure that is placed between two pairs of stiffeners. The plate has a square shape with the length of the side of 320 mm and thickness of 4.96 mm. Material that is used has the following properties:

$E_x = 46\ GPa, E_y = 13\ GPa, E_z = 13\ GPa, G_{xy} = 5\ GPa, G_{xz} = 5\ GPa, G_{yz} = 4.6\ GPa, \mu_{xy} = 0.3,$

$\mu_{yz} = 0.42, \mu_{xz} = 0.3,$ with $E_x/E_y = 3.54$

traction strengths $R_x = 1.062\ GPa, R_y = 0.031\ GPa$, compression strength $R_y = 0.118\ GPa$, shear strength $R_{xy} = 0.72\ GPa$.

The initial imperfection shape is the first buckling mode of the flat plate that is clamped at all sides.

Macro-layer	α	t [mm]
1	2x0⁰	0.62
	45⁰	0.31
	2×90⁰	0.62
	45⁰	0.31
	2x0⁰	0.62
2	2x0⁰	0.62
	45⁰	0.31
	2×90⁰	0.62
	45⁰	0.31
	2x0⁰	0.62
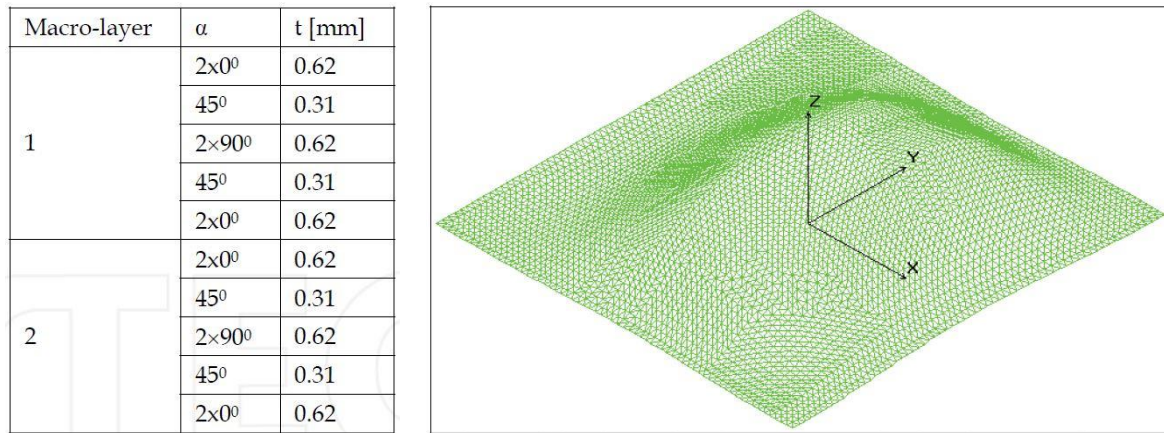
Figure 2.2.3 Plate layup and initial transversal deformation [12] p. 390, 393

The analysis is presented for the most usual imperfection magnitudes that is introduced after ship deck fabrication: $w_0 = 1.06\ mm, w_0 = 3.2\ mm, w_0 = 9.6\ mm$.

The finite element analysis was presented for the following cases: compressive buckling, shear buckling, mixed compressive and shear buckling. Only the first case is of interest for this research and, therefore, only this case will be described here.

The plate was modelled as clamped at all edges with the boundary conditions defined as (displacements u and rotations r):

- on the sides parallel with x-axis: $u_z = 0,\ r_x = 0,\ r_y = 0$
- on the sides parallel with y-axis:
    - clamped side: $u_x = 0, u_y = 0, u_z = 0,\ r_x = 0,\ r_y = 0,\ r_z = 0$
    - loaded side: $u_y = 0, u_z = 0,\ r_x = 0,\ r_y = 0,\ r_z = 0$

using shell elements and nonlinear analysis of the buckling behaviour.

The results are presented in a graph which shows the in-plane loading versus the transversal deformation of the midpoint of the plate. As it can be seen from this diagram the buckling load of a plate with initial transversal imperfection is difficult to determine since the curves do not have bifurcation points as in case of plates with perfect geometry. By drawing the asymptote to the curve where the slope changes almost suddenly the buckling load p_{cr}, is estimated to be between $140\ MPa < p_{cr} < 175\ MPa$.

These results were validated by the experiments. The tested plate has the initial transversal deformation of 9.6 mm. The measurements were done with the stretching machine, displacement transducer, strain gauge measurement system. A very rigid frame was used to assure the proper boundary conditions. The comparison is done in diagram in figure 2.13 and shows good agreement between the FEA and tests and demonstrates the behaviour described by theory.
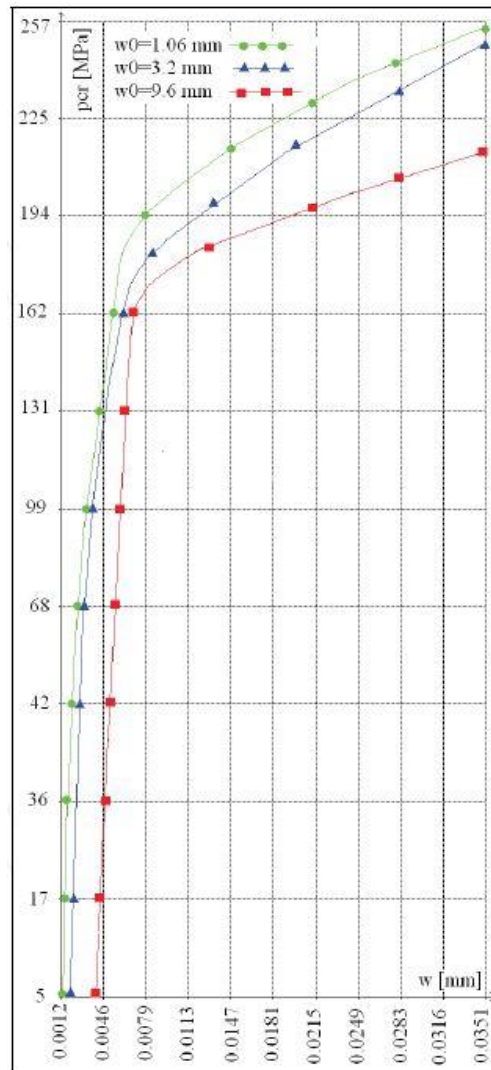
Figure 2.2.4 Buckling and post buckling behaviour of compression buckling of imperfect plate [12] p. 392
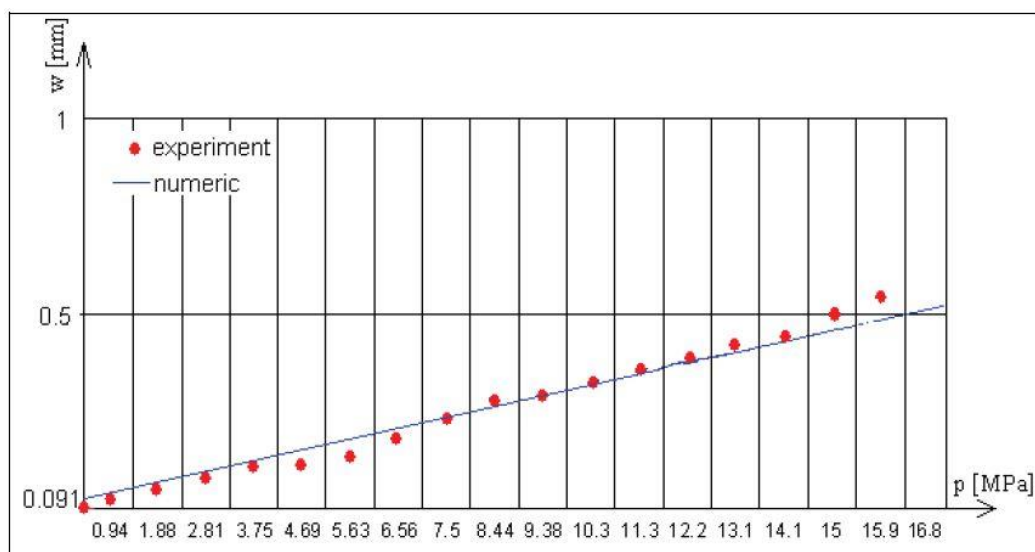
Figure 2.2.5 Variation of compression load versus displacement of the midpoint of the imperfect plate [12] p. 394

Experimental programme was presented by Czapski and Kubiak (2015) [13] for square hollow cross-section columns under concentric compression. Tests specimens were produced using autoclaving technique and have the dimensions shown in figure 2.2.6. The main aim of the tests to validate the FE model and study the influence of layer arrangement on buckling behaviour.
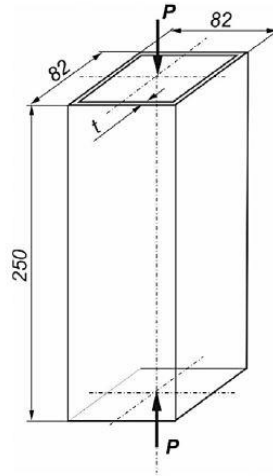
Figure 2.2.6 Geometry of the columns [13] p. 1161

Six different layups were considered of which three are symmetric and the other three are asymmetric:

- [45/-45/45/-45/-45/45/-45/45] - CS1;
- [45/-45/0/0/0/0/-45/45] – CS2;
- [45/-45/45/0/0/45/-45/45] – CS3;
- [45/-45/45/0/0/-45/45/-45] – CS4;
- [0/45/-45/45/-45/45/-45/0] – CS5;
- [-45/45/45/45/-45/-45/-45/45] – CS6.

The laminate properties:

$E_1 = 38.5\ GPa, E_2 = 8.1\ GPa, G_{12} = 2\ GPa, v_{xy} = 0.27, T_1 = 792\ MPa, T_2 = 39\ MPa,$

$S_{12} = 108\ MPa, C_1 = 679\ MPa, C_2 = 71\ MPa$

Each sample was loaded three times from 0 up to 150% of the critical load obtained with FEA, the fourth test was performed up to failure. In order to determine the deflection of the walls strain gauges and digital image correlation were used. After performing the tests buckling loads were obtained using two methods:

- load versus square of deflection $P - (\varepsilon_1 - \varepsilon_2)^2$ method M-1
- load versus deflection $P - (\varepsilon_1 - \varepsilon_2)$ curve inflection point method M-2

In the first method squared deflection becomes a straight line in the postbuckling state, which enables linear approximation of the curve. The point of intersection with the load axis is then assumed to be the critical force. In method M-2 the curve changes its concavity at the point called inflection point or "top of the knee". The vertical coordinate of this point is assumed to be the critical buckling load.

In numerical investigations both linear buckling and nonlinear static analysis were performed. The buckling mode of the magnitude $0.1t$, where t is thickness, was applied as initial imperfection in the nonlinear analysis. The boundary conditions of the column:

- at the unloaded side: $u_x = 0, u_y = 0, u_z = 0$
- at the loaded side where point force is applied: $u_x = 0, u_y = 0$

The comparison of the linear buckling analysis shows good agreement with the experimental data when the manufacturing imperfections, in this case variation in wall thickness, are taken into account.

As it can be seen from the graphs below the postbuckling curves obtained from the nonlinear static analysis are in general in good agreement with the test data (except case (e), when the specimen exhibited two modes; LBA critical buckling loads of these two mods were close together and the difference between experimental and numerical results were distinct). It can be seen that the experimental postbuckling paths of the symmetric layups are placed in between the FEA results; the paths for asymmetric layups determined experimentally are above those determined numerically.

In general, the FEA model gives a good prediction for the buckling behaviour of the hollow column with symmetric layups. The main conclusion was drawn that the problem lies in correct modelling of initial imperfections, and a future analysis investigating the influence of manufacturing imperfections on buckling load and postbuckling behaviour is necessary.
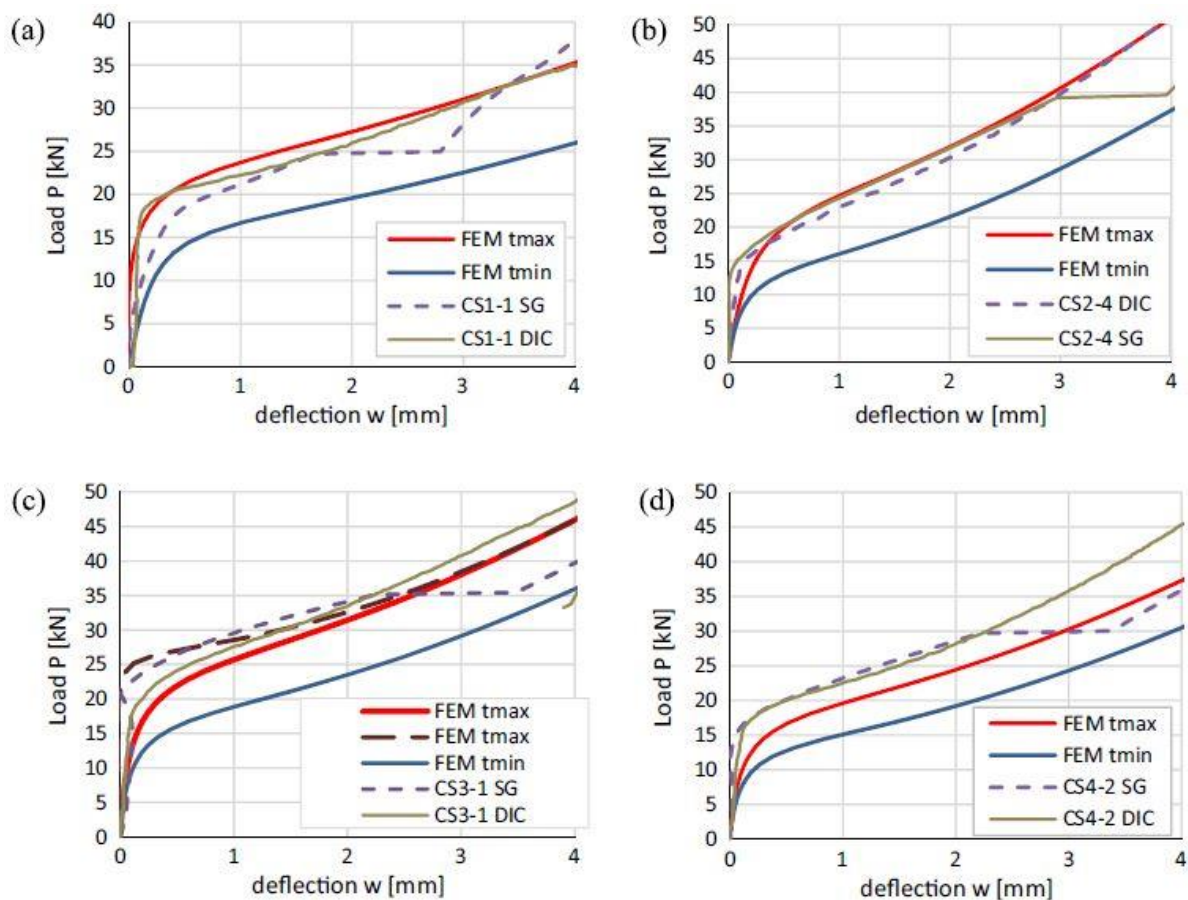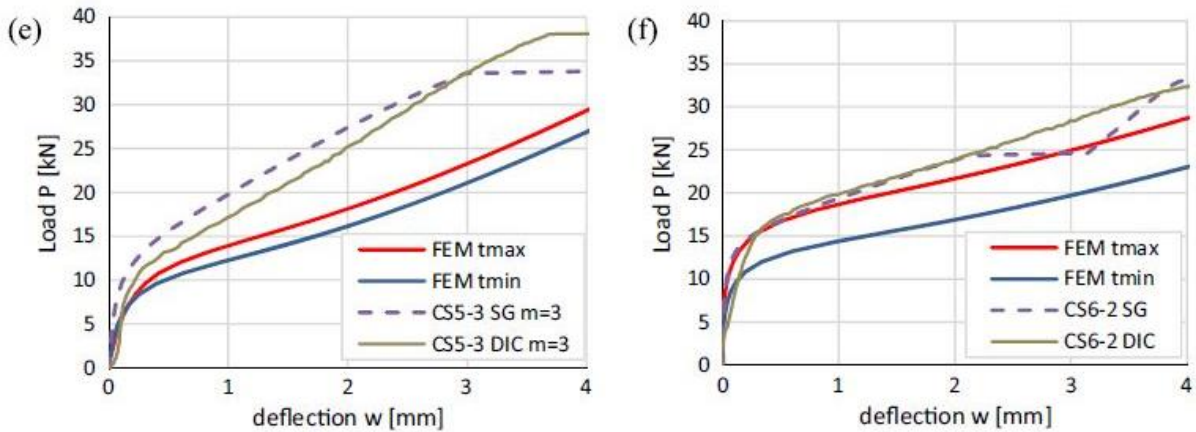
Figure 2.2.7 Numerical and experimental postbuckling curves [13] p. 1165

Barbero and Trovillion (1998) [14] performed experimental measurement on axially loaded columns where one of the points was to investigate the effect of damage accumulation. For that the columns that were already tested were loaded for the second time. It was found that when the initial test involved large postbuckling deflections the effect of damage was equal to magnification of the initial imperfections in the specimens. The buckling shape was identical but exhibiting more noticeable deflections under smaller load. However, the ultimate critical load was about the same as in the initial test (figure 2.2.8). It was therefore concluded that damage accumulated during the first loading has no effect on load carrying capacity of FRP element.
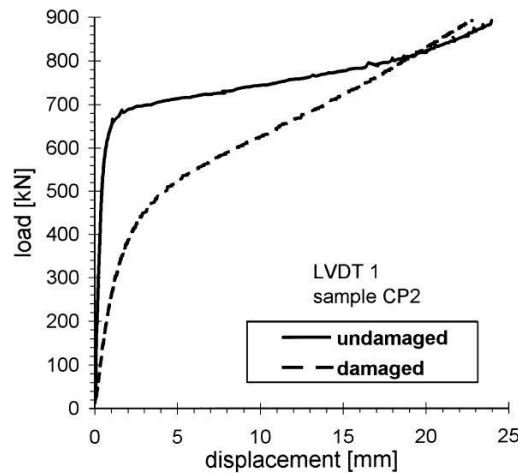
Figure 2.2.8 Effect of damage accumulation [14] p. 1339

2.2.2 APPLICATION OF IMPERFECTIONS IN STANDARDS

JRC

The influence of the imperfections on buckling is considered implicitly in the models given in JRC through considering the interaction between local and global buckling modes under axial compression. FRP material behaviour remains linear for large strains and because of that the local and the global buckling critical stress may be close to each other or coincide for columns of intermediate lengths. The interaction of the two buckling modes can lead to a combined buckling

mode, and it has been shown experimentally that the failure load is then lower than that predicted load for local or global buckling.
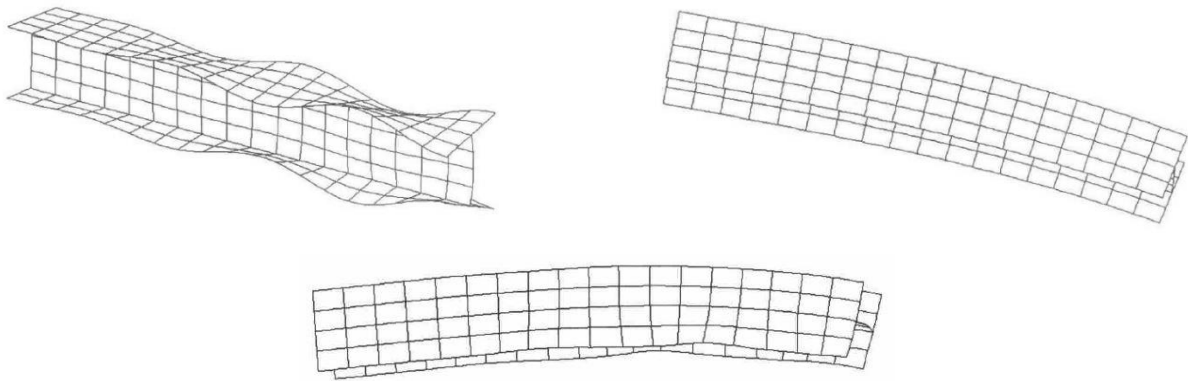
Figure 2.2.9 Local buckling mode (top left), global buckling mode (top right) and interactive buckling mode (bottom) [15] p. 270, 275

The postbuckling paths of local and global buckling are stable, but the one of the interaction mode is not with no load capacity after buckling. A column that buckles into an interactive buckling mode is imperfection-sensitive; this means that the failure load of such an element will be lower than the buckling mode of the perfect element.

In Barbero (2000) [15] an imperfection sensitivity study was made, considering three shapes of imperfections of local buckling mode shape, global buckling mode shape and the combination of both. The amplitude of imperfections ranged from $t/250$ to $t/2$, with t being the thickness of the column flange. The effect of the shape of imperfection is shown in figure 2.2.10 and the effect of amplitude of imperfection is shown in figure 2.2.11. The combined imperfection shape has a larger load reduction only because the combination of the two means a larger magnitude of imperfection, and so it was concluded that the magnitude rather than the shape of imperfection and slenderness has a significant influence on the behaviour of the column.
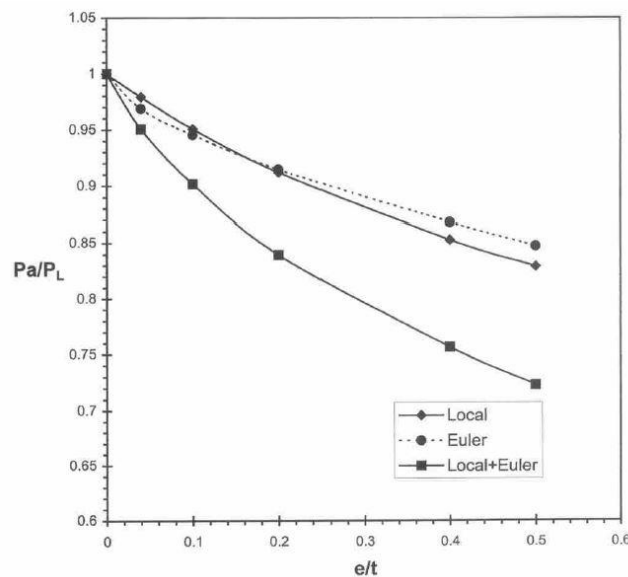
Figure 2.2.10 Effect of imperfection shape [15] p. 278
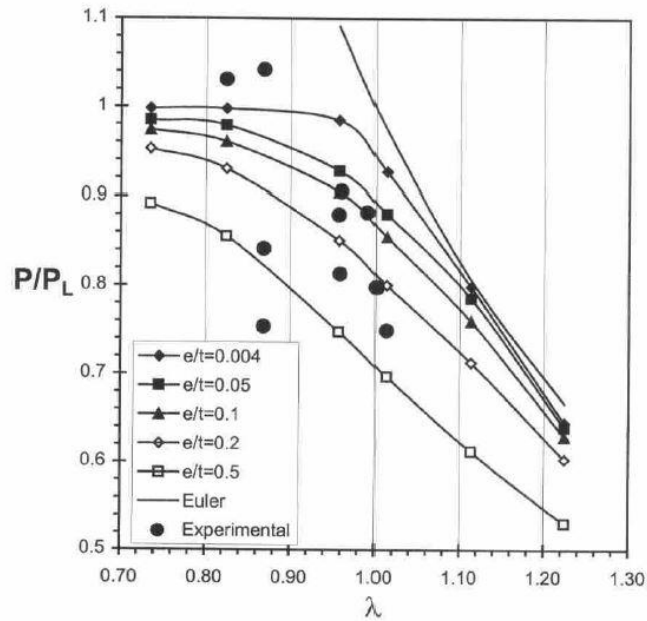
Figure 2.2.11 Effect of imperfection amplitude [15] p. 279

In design this behaviour is considered through an interaction constant c which is a function of geometry, material properties and initial imperfections.

The design force that causes instability of the element is given in JRC document by:

$$N_{Rd2,c} = \chi \cdot N_{loc,Rd}$$

(2.2.1)

where $N_{loc,Rd}$ is the design value of the compressive force that causes local instability of the element and was discussed in detail in the section 2.1.2.

χ is a reduction factor that takes into account the interaction between local and global buckling and is expressed as:

$$\chi = \frac{1}{c \cdot \lambda^2} \left(\Phi - \sqrt{\Phi^2 - c \cdot \lambda^2} \right)$$

(2.2.2)

with Φ being shape function and λ – slenderness;

c is taken equal to 0.65; and indicates the degree of interaction occurring between the two modes. $c = 1.0$ would represent the situation when mode interaction has no effect on the critical load.

The value $c = 0.65$ is based on experimental data provided by several researches: Barbero and Tomblin (1994) [17], Zureick and Scott (1997) [18], Barbero and Trovillion (1998) [14], Brown, Mottram and Anderson (1998) [19], and Barbero, Dede and Jones (1999) [20], and is a conservative estimation:
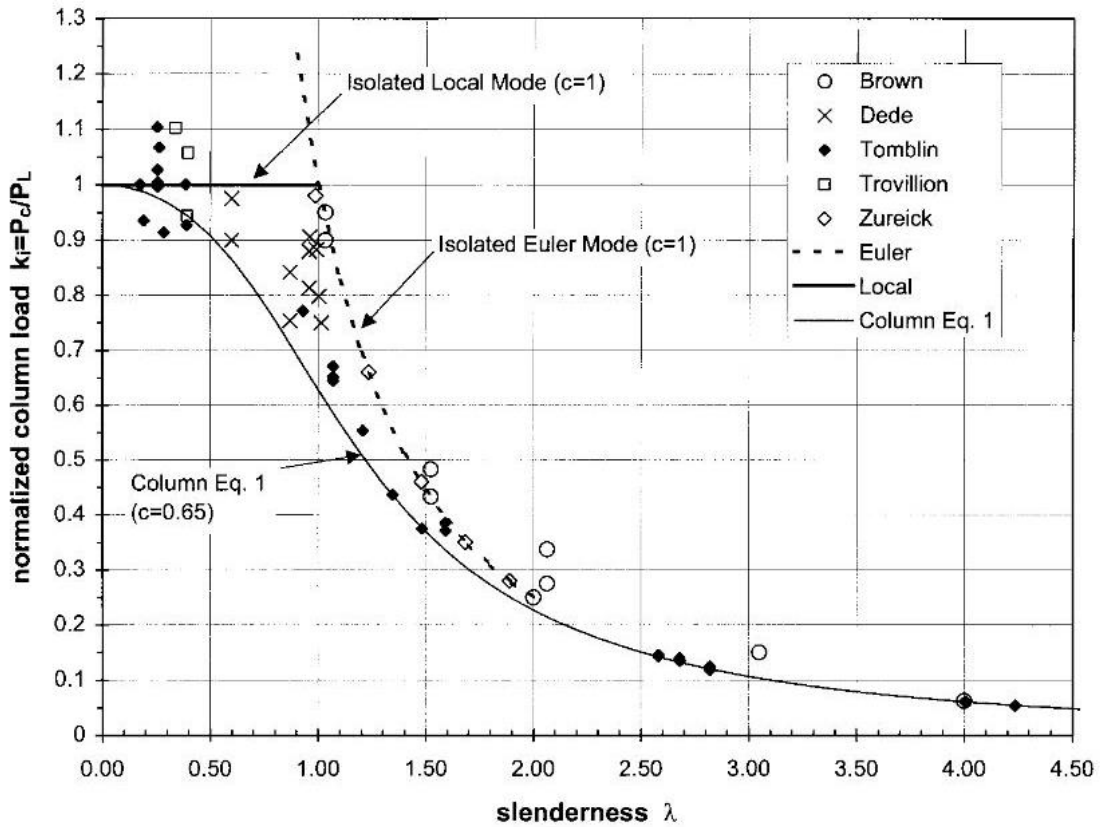
Figure 2.2.12 Comparison of the design equation and experimental results for buckling mode interaction [16] p. 186

CUR96

In CUR the imperfections factors are given global buckling and lateral torsional buckling.

Critical buckling force is given as:

$$N_{b,Rd} = \chi \cdot \frac{\eta_c \cdot A \cdot \rho \cdot f_{c,k}}{\gamma_M}$$

(2.2.3)

where χ is a reduction factor, A is area of cross-section, $f_{c,k}$ is characteristic compressive strength and

$$\rho = \frac{f_{c,stab,k}}{f_{c,k}} \leq 1$$

(2.2.4)

which is a reduction factor for local wrinkling and imperfections.

The expression for the reduction factor is

$$\chi = \frac{1}{\Phi + \sqrt{\Phi^2 - \bar{\lambda}^2}} \leq 1$$

<div align="right">(2.2.5)</div>

where the shape function depends on relative slenderness $\bar{\lambda}_f$, imperfection factor α_f and plateau length of buckling curve $\bar{\lambda}_{f,0}$:

$$\Phi = 0.5 \cdot \left(1 + \alpha_f \cdot \left(\bar{\lambda}_f - \bar{\lambda}_{f,0}\right) + \bar{\lambda}_f^2\right)$$

<div align="right">(2.2.6)</div>
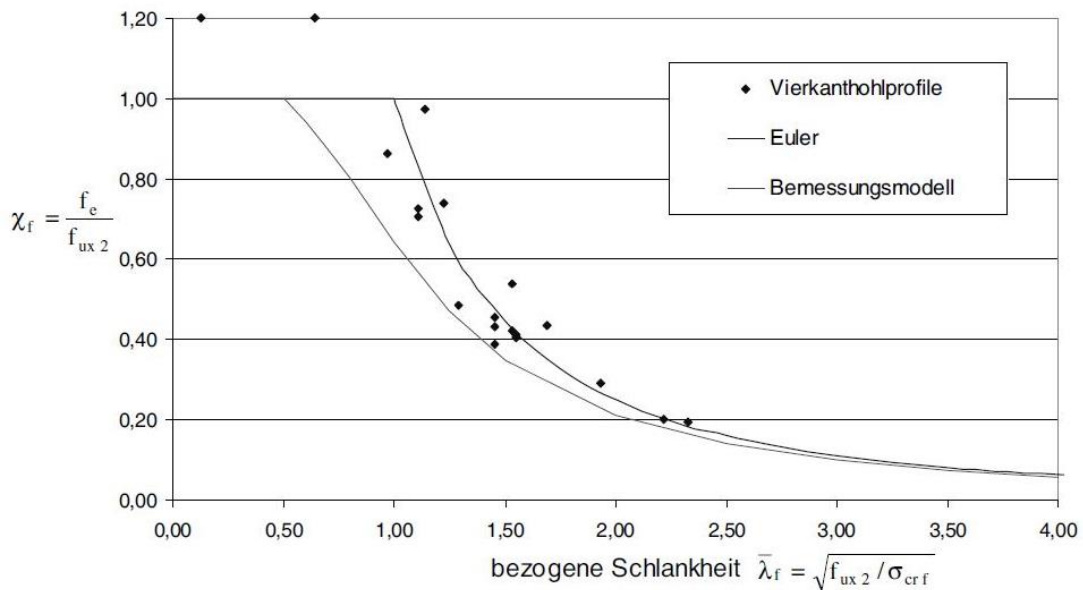
Figure 2.2.13 Buckling curves for a hollow profile [3] p. 152

Parameters α_f and $\bar{\lambda}_f$ depend on the shape of cross-sections and were determined experimentally and numerically [3]:

Cross-section	α_f	$\bar{\lambda}_{f,0}$
hollow	0.40	0.50
I-, U- (weak axis bending)	0.75	0.50
I-, U- (strong axis bending)	0.50	0.50

Table 2.5 α_f and $\bar{\lambda}_f$ for column buckling

A comparison between the design procedures given in JRC and CUR96 for column and lateral torsional buckling in given in Annex A.

In addition to column and lateral torsional buckling, CUR96 gives a guideline for buckling of plates as:

$$f_{x,Rd,c} = \alpha \cdot \frac{\eta_c \cdot \sigma_{cr,c}}{\gamma_M}$$

<div align="right">(2.2.7)</div>

where $\sigma_{cr,c}$ is critical buckling load that can be determined by plate formulas given in table 2.2 and α is the imperfection factor, which is not specified further; for a conservative estimation it can be taken as a maximum value of allowed bow imperfection of $L/125$, where L is the smallest value of width or length of the plate.

2.2.3 LIMITING VALUES

EN 13706-2:2002 [21] is a standard for Reinforced plastics composites – Specifications for pultruded profiles and Part 2 comprises test methods and general requirements.

ANNEX A lists visual defects with descriptions and acceptance levels, from which wrinkle depression is of interest for the scope of this research. Wrinkle depression is an undulation or series of undulations or waves on the surface of the pultruded profile and the dimensional tolerance is not greater than 20% of thickness or 1,5 mm out of its plane.

ANNEX B gives dimensional tolerances for pultruded profiles. These tolerances are shown in table 2.7. Among various deviations in geometry of profiles there is also a tolerance for initial transverse deflection of a flat plate, which is given as $F < 0.008 \cdot B$, where B is the width of the plate. This limiting value is basically the same as given in CUR96 with $L/125$ with L being the smallest dimension (length or width) of the plate.

The straightness tolerance for profiles in EN 13706-2 is given as a function of length and depends on cross-sectional dimensions. It is worth mentioning that ASTM Standard [22] specification for dimensional tolerance of thermosetting glass-reinforced plastic pultruded shapes gives a different limiting value for out-of-straightness $L/240$.

Zurieck and Scott [18] reported out-of-straightness measurements of I- and hollow section profiles. It was found that the imperfections were well within the tolerances allowed by ASTM. Their measured values were compared to the tolerances given in EN 13706-2 as:

- for I-columns and hollow columns VG13 to VG18: $D < 0.0005 \cdot L^2$
- for hollow columns VG19 to VG24: $D < 0.001 \cdot L^2$

These expressions provide much smaller values than those in ASTM and as a result not all the measured imperfections were within the acceptable limit given by EN 13706-2.

Property	Tolerance		
Wall thickness of open and closed profiles	Nominal dimensions (mm)		
	Thickness	T_1	T_2
	0 to 2	± 0,15	± 10 %
	2 to 5	± 0,20	with
	5 to 10	± 0,35	minimum
		± 0,45	of ± 0,30
Flatness in transverse direction	Tolerance $F < 0,008 \times B$ mm		
Profile height and width of flange	Nominal dimensions (mm) B and H: ± 0,5 % with minimum ± 0,20 mm and maximum ± 0,75 mm		
Size of angle	Tolerance Y ± 1,5 °		
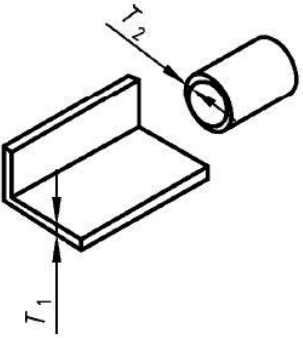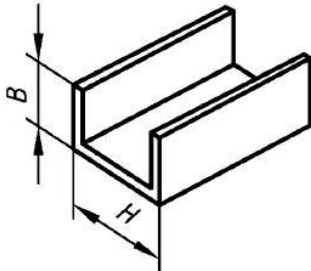
Straightness	Tolerance (B and H are overall breadth and height dimensions)
	$D < 0{,}002 \times L^2$ for sections with B or $H < 50$ mm $D < 0{,}001 \times L^2$ for sections with B or $H \geq 50$ and < 100 mm $D < 0{,}000\,5 \times L^2$ for sections with B or $H \geq 100$ mm where D and L are in metres.
Twist	Tolerance
	$V < 1{,}5°$ per metre maximum for thickness < 5 mm $V < 1{,}0°$ per metre maximum for thickness ≥ 5 mm
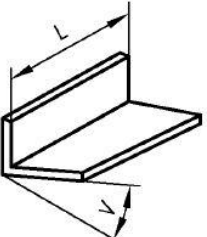
Table 2.7 Dimensional tolerances for pultruded profiles [21] p. 12-13

Laudiero, Minghini and Tullini (2014) [23] presented an extended study of I-section profile subjected to pure compression with three types of geometric imperfections verifying the limiting values given in standards and found in literature [24].

The three shapes of imperfections are:

- uniform bending in the minor axis plane (S)
- sinusoidal imperfection of web and flanges similar to the first local buckling mode (L)
- non-orthogonality between the planes of the web (A)

The two sets of imperfection values were evaluated:

- S: $L/240$ and $L/4500$
- L: $8 \cdot 10^{-3} \cdot b_f$ and $2 \cdot 10^{-5} \cdot b_f$
- A: $1.5°$ and $0°$

The first limiting value for S-imperfection corresponds to the out-of-straightness imperfection given by ASTM, while the first limiting value for L-imperfection is that of provided in EN for plate flatness. For the first set of imperfection amplitudes in stocky columns it was found that the S-imperfection and the superposition of S- and L-imperfections have the most detrimental influence on the behaviour of the element. The A-imperfections turned out to be ineffective and the curve representing the superposition of S- and A-imperfections just slightly differs from the curve of S-imperfections acting alone (figure 2.2.14). Moreover, the numerical results did not agree with previously obtained experimental data [25].
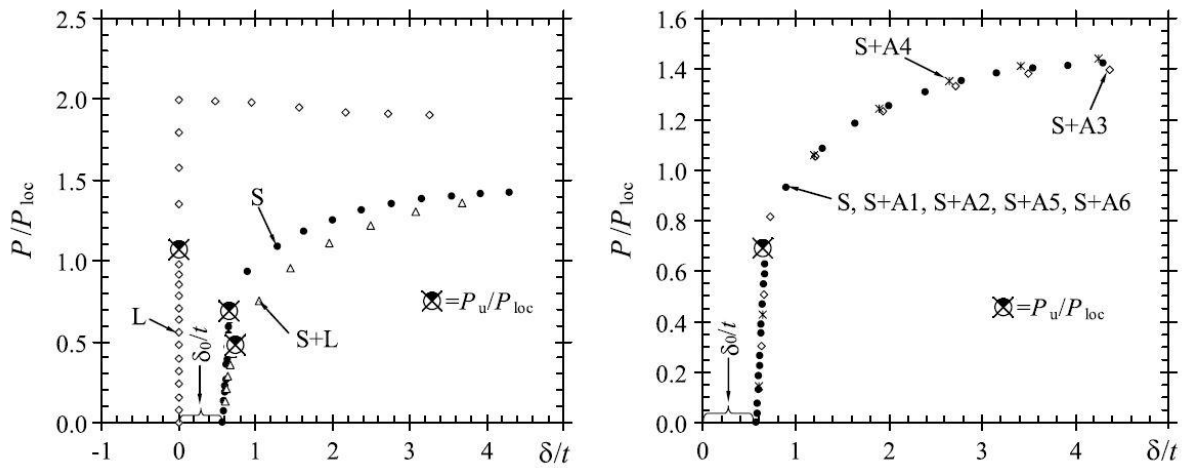
Figure 2.2.14 Numerical results for the first set of imperfection amplitudes [23]

With the reduced magnitudes of imperfections (second set) higher ultimate loads were obtained and the results were in good agreement with test data. For L-imperfections of original amplitude the ratio between the ultimate load and local buckling load was 1.07 and for the second set of amplitudes 1.27.
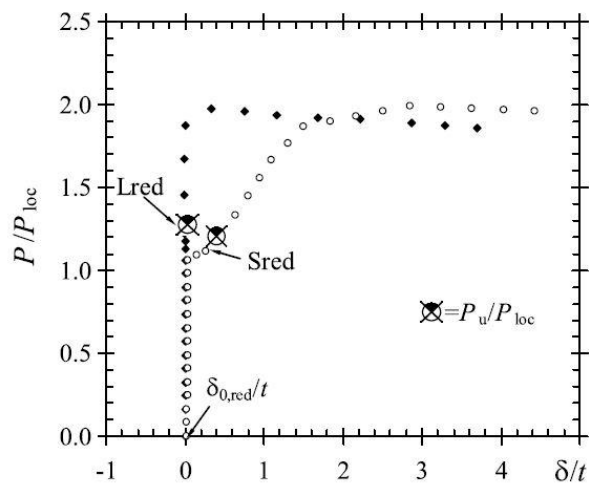
Figure 2.2.15 Numerical results for the reduced set of imperfection amplitudes [23]

Thus, it was concluded that the limiting amplitudes were unrealistic and resulted in the failure modes and ultimate loads that did not comply with experimental results.

This is in contradiction to what was concluded by Barbero and Trovillion [14].

2.3 CHAPTER SUMMARY

Analytical models for plates and profiles were discussed in this chapter. While plate expressions based on idealized boundary conditions, the plates which are a part of a profile are considered with rotational restraints. This means that the interaction between web and flanges as to be taken into account. Two approaches for that were described: JRC with Kollar's work as a background and CUR96 that is based on research by Barbero and Qiao.

JRC's method takes into account the differences between material properties and thickness of webs and flanges, while CUR96 does not. The difference in material properties can be taken into consideration by using the expanded formula given in the CUR's background document Step-by-Step design equations [11], the thickness of the web however is only considered when calculating the axial or bending stiffness of the element and therefore is not present in the expression of critical buckling stress.

The approach for modelling local buckling behaviour of H. Trumpf is similar to the one that is used for steel plates with effective cross-section and considering idealized boundary conditions, providing plate buckling coefficients calculated only for certain material properties.

The analytical formulas for plates with idealized boundary conditions and for profiles do not account for initial geometric imperfections. The plate whose geometry deviates from the intended one in a form of initial transverse deflection shows a different buckling behaviour than a perfect plate. This behaviour can be studied by performing a nonlinear analysis. The main difference is observed around the Euler's buckling load: while a perfect plate has a bifurcation point, the imperfect plate does not. Because of the rounded-over load – deflection curve it is difficult to estimate critical buckling load of an imperfect plate, however, because the postbuckling path is known it is possible to estimate ultimate loads. In a study on effect of damage accumulation [14] it was found that the presence of initial deformations did not degrade the load carrying capacity.

The influence of initial geometric imperfections is considered in JRC through the global and local buckling modes interaction: for columns of intermediate length the two modes can be close or even coincide forming a new unstable buckling mode. In this case a structural element is considered imperfection-sensitive and its imperfections' magnitude and not the shape has the biggest influence of the behaviour. CUR96 provides imperfection coefficients for column buckling, the influence of imperfections on the local buckling behaviour is not quantified but should be taken into account. The buckling mode interaction is not a part of CUR96's procedure for stability.

Dimensional tolerances are provided for pultruded profiles in EN 13706-2:2002, and give smaller allowable levels than ASTM. The limiting values given in standards were concluded by some authors [23] to be unrealistic compared to the actual measured imperfections and gave rise to results that did not match the experimental data. The smaller magnitudes of initial imperfections resulted in higher ultimate loads and matched the test results, which contradicts the conclusion that was drawn in [14] based on the study on the effect of damage accumulation.

For a large part the research in local buckling of FRP structural elements is made for pultruded profiles. No experimental or numerical data was found for VARTM-produced plates, columns or beams. The imperfection-sensitivity analysis is mostly performed using the buckling modes obtained from the linear analysis and focuses on mode interaction and influence of layer arrangement.

3. PLATE BUCKLING ANALYSIS

The goal of the plate buckling analysis is to study buckling behaviour of orthotropic plates and to establish what effect shape and amplitude of initial imperfection has on the buckling behaviour, and the role of geometry and material properties in buckling behaviour of perfect and imperfect plates. Several magnitudes of initial geometric imperfections including the limiting value provided in EN 13706-2 and vales found in literature will be examined.

3.1 EFFECT OF SHAPE AND MAGNITUDE OF IMPERFECTION

Both linear buckling analysis and geometrically nonlinear static analysis will be performed to investigate buckling behaviour of plates with initial out of plane deformation. Linear buckling analysis (LBA) will be used to obtain buckling modes of a plate and the results will be compared to analytical solutions. In the geometrically nonlinear analysis four shapes of imperfections are analysed. Three arbitrary amplitudes - $B/3000, B/1000, B/300$ - of imperfections are considered to establish the sensitivity to the magnitude of initial deviations; fourth value $B/125$ is the limiting value from the standard.

3.1.1 MODEL

The following model is used:

Rectangular plate with width $B = 300 \ mm$, length $L = \ 900 \ mm$, and thickness $t = 4 \ mm$

Layup I: $[0_2/45_2/-45_2/90_2/0_2]_s$ with ply thickness is $0.2 \ mm$ (figure 3.1.1)

$0° - 40\%; \ 45° - 20\%; \ -45° - 20\%; \ 90° - 20\%$
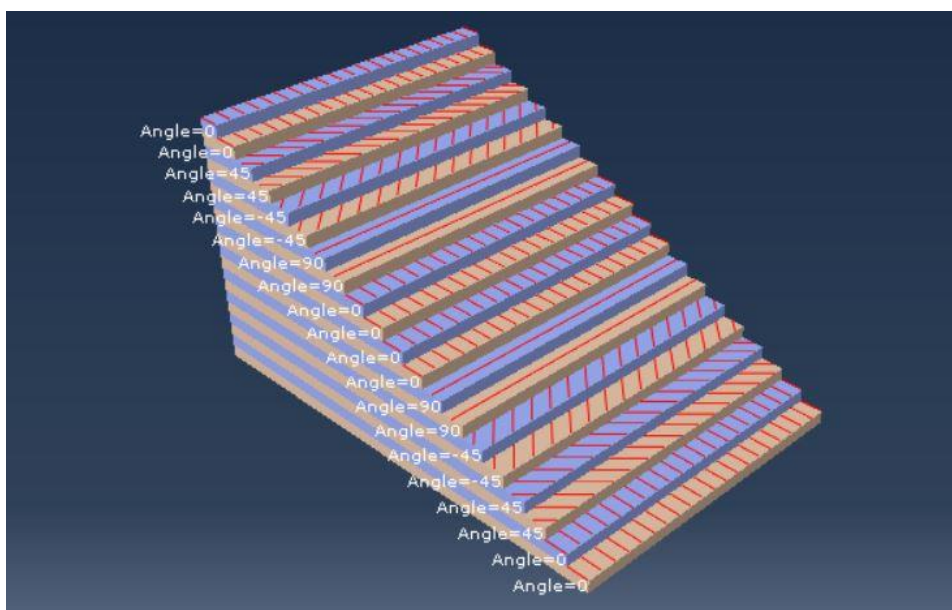
Figure 3.1.1 Ply stack plot layup I (E_x/E_y = 1.27), t = 4 mm

The properties of the ply are calculated using strain limits for E-glass / Polyester UD ply given in table 3.1 and stiffness properties given in table 3.2:

Rekken		E-Glas Polyester	HS-Carbon Epoxy	VVK-type R-Glas Epoxy	IM-Carbon Epoxy	HM-Carbon Epoxy
		Karakteristieke waarden [%]	Karakteristieke waarden [%]	Richtwaarden [%]	Richtwaarden [%]	Richtwaarden [%]
Trek	$\varepsilon_{1t,Rk}$	2,0	1,3	3,1	1,2	0,7
	$\varepsilon_{2t,Rk}$	0,2	0,3	0,4	0,7	0,4
Druk	$\varepsilon_{1c,Rk}$	1,2	0,7	1,8	0,7	0,5
	$\varepsilon_{2c,Rk}$	0,9	1,3	0,9	2,3	2,1
Afschuiving	$\gamma_{12,Rk}$	1,9	2,5	1,5	1,7	1,8

Table 3.1 UD ply strain limits [2] p. 45

V_f	E_1 [kN/mm^2]	E_2 [kN/mm^2]	G_{12} [kN/mm^2]	ν_{12}
40 %	30,4	8,9	2,7	0,30
45 %	33,8	10,1	3,0	0,29
50 %	37,2	11,4	3,4	0,29
55 %	40,5	12,9	3,8	0,28
60 %	43,9	14,6	4,3	0,27
65 %	47,3	16,8	5,0	0,27
70 %	50,7	19,4	5,8	0,26

Table 3.2 UD ply stiffness properties [2] p. 43

Taking into account $V_f = 50\%$:

$f_{1t} = E_1 \cdot \varepsilon_{1t} = 744\ MPa$ – tensile strength in the longitudinal direction

$f_{1c} = E_1 \cdot \varepsilon_{1c} = 446.4\ MPa$ – compressive strength in the longitudinal direction

$f_{2t} = E_2 \cdot \varepsilon_{2t} = 22.8\ MPa$ – tensile strength in the transversal direction

$f_{2c} = E_2 \cdot \varepsilon_{1c} = 102.6\ MPa$ – compressive strength in the transversal direction

$f_{12} = G_{12} \cdot \gamma_{12} = 64.6\ MPa$ – in-plane shear strength

The resulting axial stiffness properties of the laminate are:

$E_x = 22.56\ GPa\ E_y = 17.71\ GPa;\ G_{xy} = 6.35\ GPa;\ \nu_{xy} = 0.323;\ \nu_{yx} = 0.257$

The stiffness ratio of axial moduli of elasticity in longitudinal and transverse direction: $E_x/E_y = 1.27$

Calculation of the equivalent laminate properties is presented in Annex B.

Boundary conditions:

- along all edges $u_z = 0$
- at $x = 450; y = 150$ (midpoint of the plate) $u_x = 0; u_y = 0$
- at $x = 900; y = 150\ u_y = 0$

The load is applied to a point at each side of the plate and is rigidly coupled to the loaded edges.
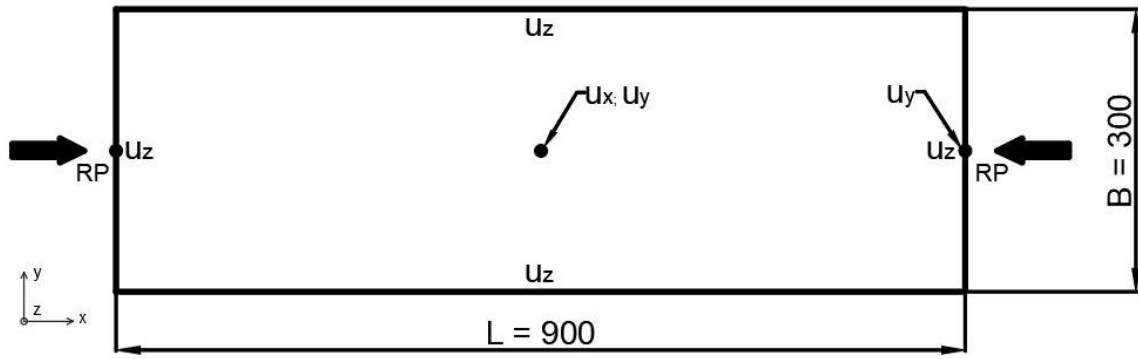
Figure 3.1.2 Plate geometry, boundary and loading conditions for buckling analysis

The plate was modelled in Abaqus software. The element type used is S4R, with size of $18.75 \times 19.57 \ mm$ (16 elements in y and 46 elements in x direction of the plate).

3.1.2 LINEAR BUCKLING ANALYSIS

The first six buckling modes obtained from the linear buckling analysis are presented in figure 3.1.3.
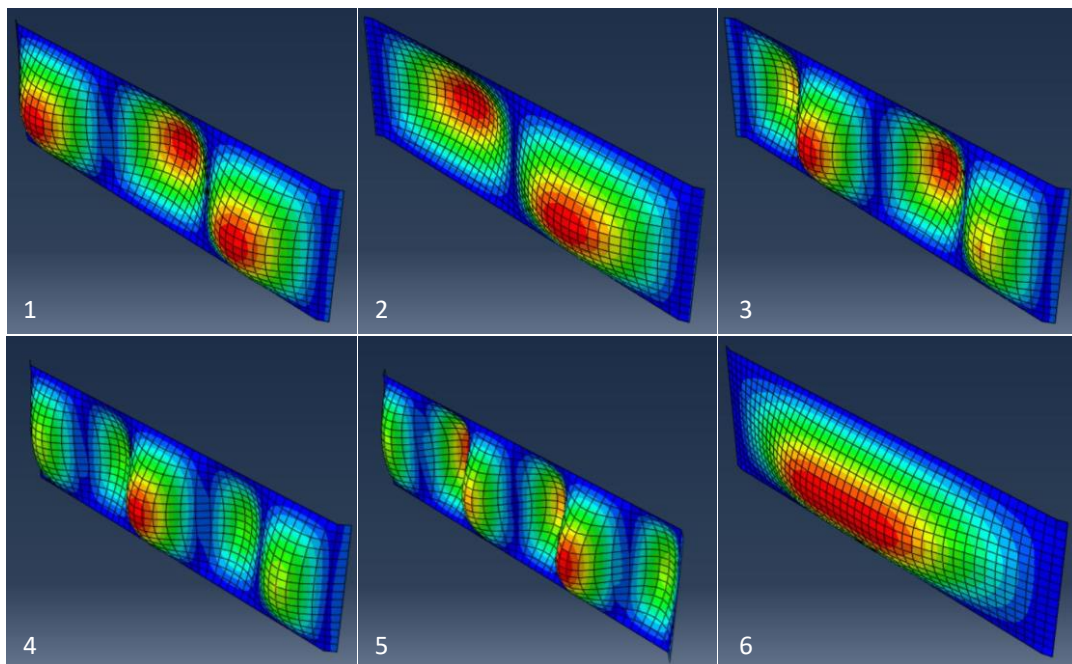
Figure 3.1.3 The first six buckling modes of the plate of layup I and t = 4 mm

Using the analytical expression for a simply supported plate from table 2.1 the buckling loads were calculated for the given plate geometry and number of halfwaves in the direction of the load (m). The resulting values and the difference with the values from the finite element analysis are shown below (table 3.3). The first number in the mode column relates to the number of the mode, the value of m shows the number of halfwaves in corresponding buckling mode. For example, the first buckling mode (1) has 3 halfwaves ($m = 3$).

mode	force FEA, N	force analytical, N	difference, %
1; m=3	14696	14648.78	-0.3
2; m=2	15047	15439.69	2.5
3; m=4	17412	17183.06	-1.3
4; m=5	21744	21440.25	-1.4
5; m=6	27532	27024.97	-1.9
6; m=1	29234	3256.31	10.2

Table 3.3 Comparison of the critical loads obtain from the analytical formula and FEA
(layup I, t = 4 mm)

The load values from FEA and the analytical formula are within 3% from each other, except for the critical load for buckling mode 6, where the difference is about 10%, which is still within acceptable limits. The plus sign in the difference column in the table 3.3 means that the result obtained with FEA gives a lower value of the critical load compared to the analytical result. This happens in two cases: for $m = 2$ (buckling mode 2) and $m = 1$ (buckling mode 6). The largest difference in analytical and FEA solutions is observed for $m = 1$; in this case the length of the halfwave (buckling length) is the largest compared to all the other cases. In figure 3.1.4 it can be seen that the blue curve for $m = 1$ intersects with the vertical dashed line $AR = 3$ with the ascending branch of the curve. This also happens for $m = 2$, but the intersection point's ordinate is a lot closer to the minimum critical load value, than in case of $m = 1$ and could be the reason for better agreement between the results.
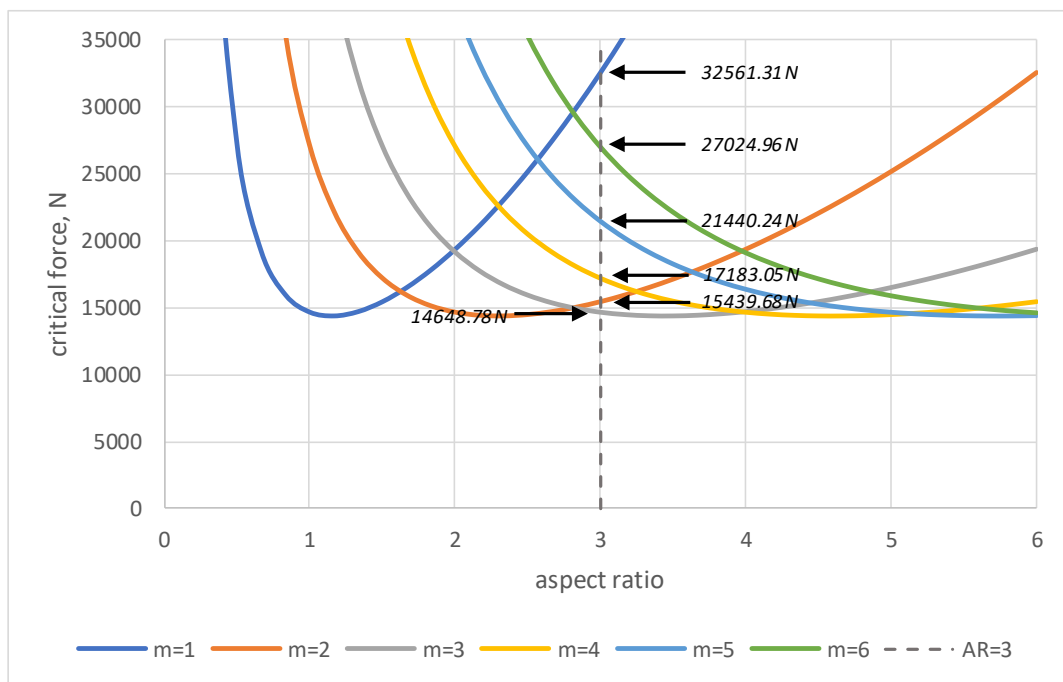
Figure 3.1.4 Visualization of the analytical results for the plate of layup I and t = 4 mm
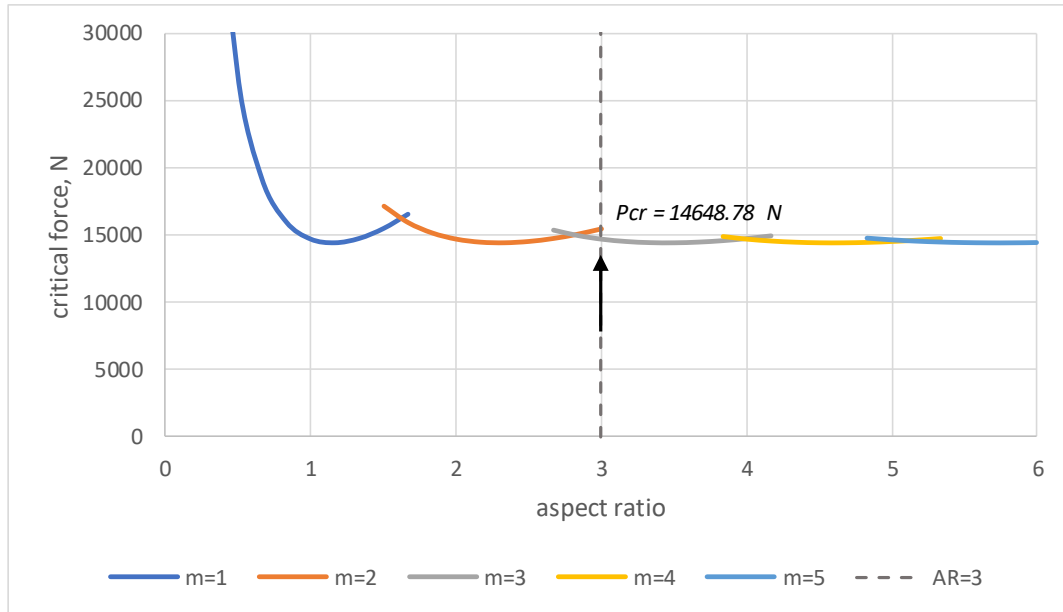
Figure 3.1.5 Dependence of buckling load and mode on plate aspect ratio for the plate of layup I and t = 4 mm

Figure 3.1.5 shows the dependence of the buckling mode and load on plate aspect ratio. From the graph it is visible that plates with aspect ratio larger than 3 will buckle at almost the same load level into corresponding buckling modes, which is represented by grey, yellow and blue curves that become more linear with the increase of the aspect ratio. In case of a homogeneous plate (e.g. steel), the minimum of the parabola (minimum critical load) for a given buckling mode coincides exactly with the corresponding aspect ratio. In other words, a plate with $AR = 3$ will buckle into a buckling mode $m = 3$ and the minimum of the buckling mode curve will be exactly at $AR = 3$. This is not the case for an orthotropic plate, since the plate has different bending stiffness in longitudinal and transverse directions $(D_{11}/D_{22} \neq 1)$. For $m = 3$, according to figure 3.1.5, the minimum buckling load will correspond to aspect ratio of ≈ 3.4; it is determined by the measure $AR \cdot \sqrt[4]{D_{11}/D_{22}}$. So, the minimum of curve $m = 3$ is located at $3 \cdot \sqrt[4]{146.48/84.34} = 3.44$; $m = 2$: $\sqrt[4]{146.48/84.34} = 2.30$, etc.

3.1.3 GEOMETRICALLY NONLINEAR ANALYSIS

Geometrically nonlinear analysis considers the presence of initial out of plane deformations of the plate. The shape of the geometric initial imperfection is introduced to the non-linear model through *IMPERFECTION command in Abaqus. The applied force is about 3 times higher than the critical buckling load that was obtained in the linear buckling analysis.

In the geometrically nonlinear analysis several types of imperfections are considered:

- in the shape of the first buckling mode from the linear buckling analysis – type 1;
- in the shape of the second buckling mode – type 2;
- in the shape of a single half-wave (buckling mode 6) – type 3;
- wrinkle imperfection – type 4

Four magnitudes of imperfections are considered for the nonlinear analysis:
$B/3000, B/1000, B/300, B/125$, where B is the width of the plate. For a plate with the width of
$B = 300\ mm$, the values of the imperfections are $0.1; 0.3; 1;\ 2.4\ mm$. The last amplitude is the
limiting value given in EN 13706-2.
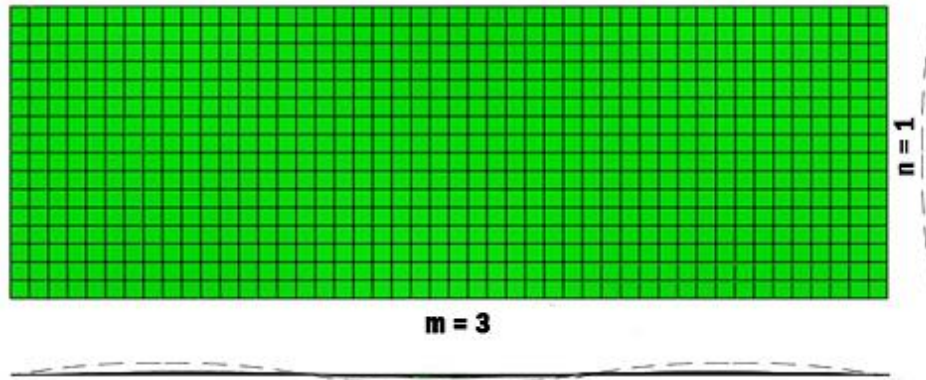
Figure 3.1.6 Plate with initial imperfection in the shape of the first buckling mode (m=3)

FIRST BUCKLING MODE – TYPE 1

The initial and final shape of the plate at the first load increment $P = 50\ N$ and at the maximum
load $P = 50000\ N$ respectively with the initial imperfection of the amplitude $B/125$ is shown in the
figure 3.1.7. The plate with the imperfection type 1 has the same general initial shape and assumes
the same shape at the maximum value of the load for all magnitudes of imperfection; only the
values of the out of plane deformations differ depending on the imperfection amplitude.
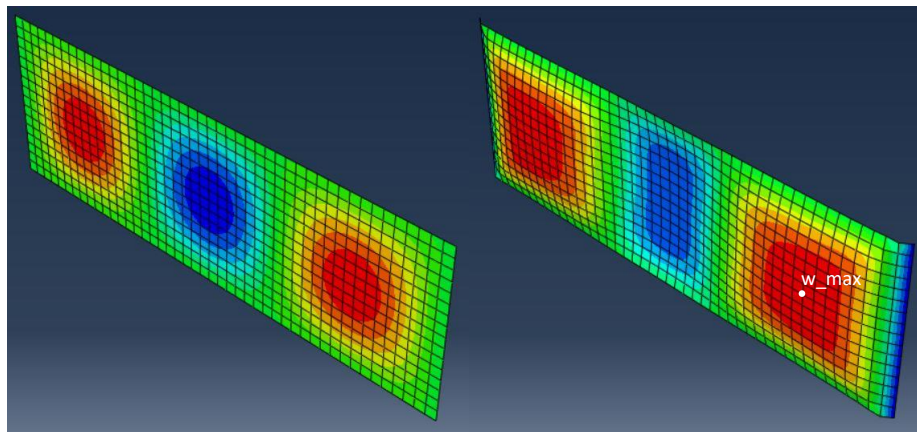
Figure 3.1.7 Initial and final shapes of the imperfect plate type 1

The imperfection magnitude also affects how the plate assumes the buckled shape. To illustrate that
the contour plots (figure 3.1.8) of the plate displacements are shown at different load values for a
very small imperfection amplitude $B/300000$; intermediate amplitude $B/1000$ and the maximum
amplitude $B/125$. First the displacements are shown for the first increment at which $P = 50\ N$;
increments 34 and 35 correspond to the values of $P = 14589.1\ N$ and $P = 15089.1\ N$ and the last
increment is the maximum load of $P = 50000\ N$. The increments 34 and 35 are chosen because
they correspond to the load levels just before and after the buckling of the plate without initial
imperfections occurs. By selecting to view the magnitude of the displacement in Abaqus, the
contour plot will show the largest values of the displacement out of three directions (x, y, z).

For the imperfection magnitude $B/300000$ it can be seen from the figure 3.1.8 that initially the displacements of the plate are governed by the shortening of the plate (increment 1 and 34). However, at the load just above the critical value the out of plane deflection increased rapidly. This shows that between $P = 14589.1\ N$ and $P = 15089.1\ N$ the buckling occurred.

The plate with the initial imperfection of $B/1000$ already shows noticeable out of plane deformation compared to the shortening in the first increment of the analysis, which continue to grow with the load increase. There is no sudden increase of the out of plane deformation as in previous case.

For the imperfection amplitude of $B/125$ the out of plane deflection is the governing displacement on every stage of the analysis. Compared to the previous case ($B/1000$) larger deflections occur under lower load values. At $P = 50\ N$ the out of plane deflection repeats the buckling mode 1, showing three locations of the maximum deflection (red areas). As the load increases the more prominent increase of the deformation is seen at the red areas at the edges of the plate.
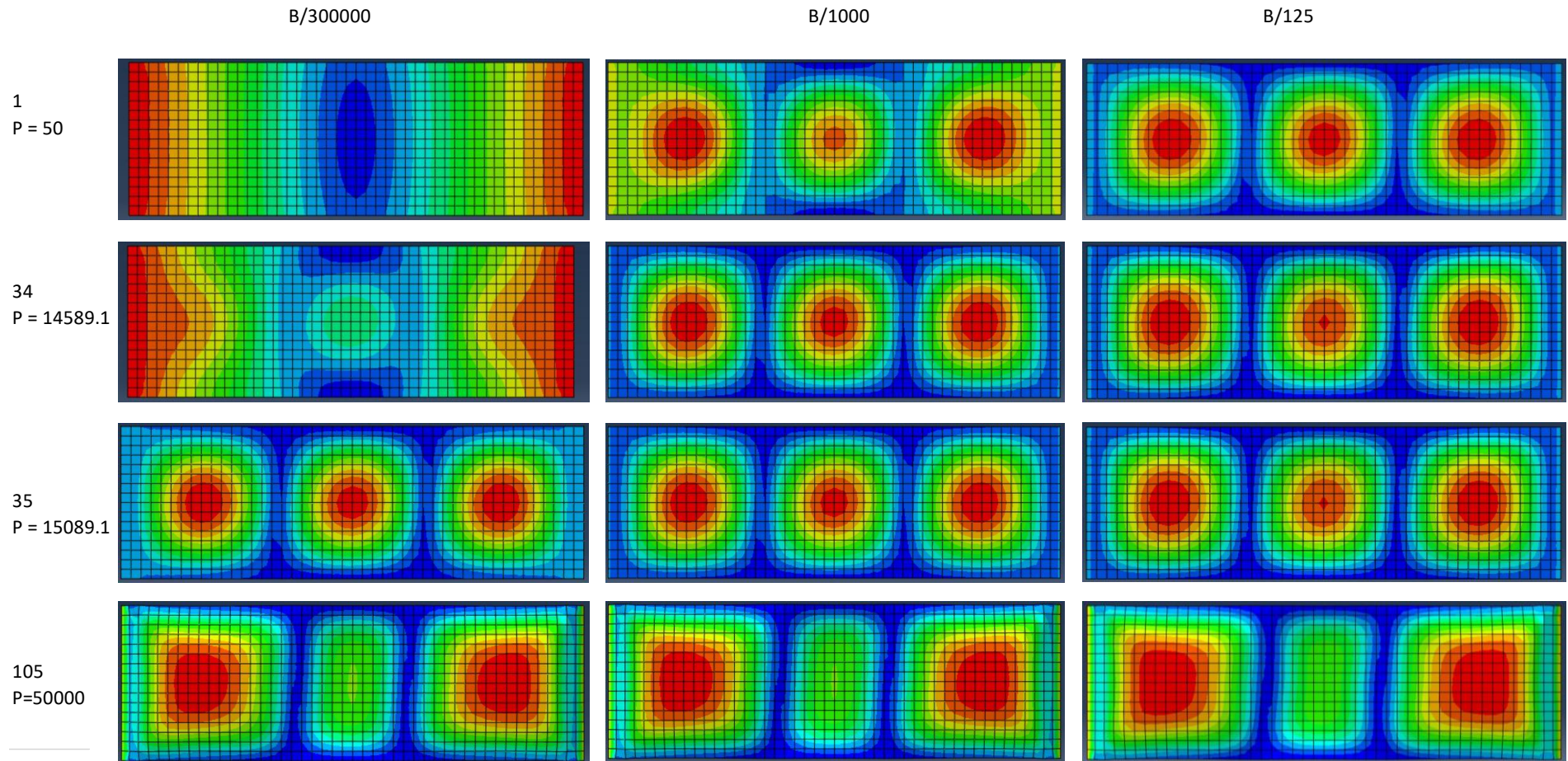
Figure 3.1.8 Displacements of the imperfect plate at different load levels (based on the absolute values)

Figure 3.1.9 shows the force-deflection curves for a plate with initial geometric imperfection in a shape of the first buckling mode. The transverse deflection is measured in the point of the maximum deflection (shown with w_max in figure 3.1.7) at the final force increment. The dashed line represents the Euler critical load obtained from the linear buckling analysis. The grey curve represents the plate with a very small imperfection $B/300000$ to demonstrate that the behaviour is very close to that of a perfect plate – the curve has a bifurcation point at the load level close to the critical buckling load of the perfect plate. As expected, the larger the imperfection the bigger the effect on the buckling behaviour. At $B/125$ the curve becomes very rounded over, which corresponds to what was shown in figure 3.1.8 and indicates that the plate with an imperfection of this magnitude does not buckle suddenly. For the intermediate magnitudes of $B/300$ and $B/1000$ there is no bifurcation buckling, but the transverse deflection grows slowly in the first part of the graph, around the critical buckling load there is a knee in the curve after which the deflections increase at a higher rate. Overall, the graph is very similar to the one in figure 2.2.2 and follows the behaviour that is known from theory and practice.
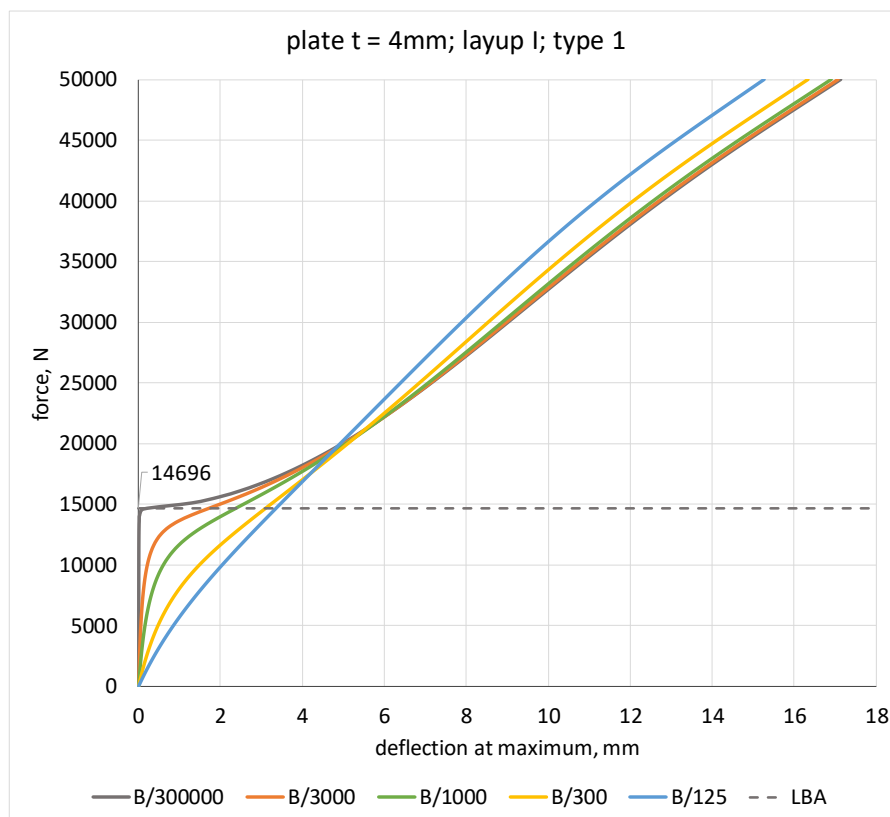
Figure 3.1.9 Force – deflection at maximum curves for a plate with the imperfection in the shape of the first buckling mode

Based on these graphs it can be concluded that for a plate with given geometry the bifurcation buckling does not occur when the values of initial imperfection are $B/300$ and $B/125$. For lower amplitudes the buckling load can be approximated, since it is possible to distinct two regions of the curves with different rate of change in out of plane deformation.
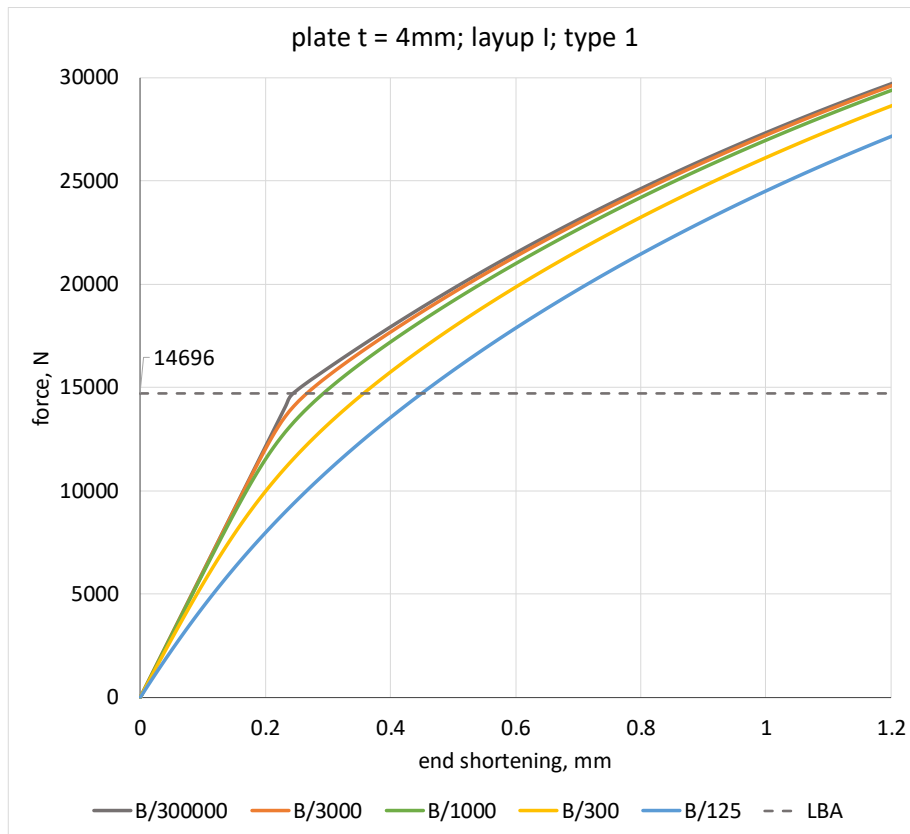
Figure 3.1.10 Force – end shortening curves for a plate with the imperfection in the shape of the first buckling mode

Figure 3.1.10 shows the axial displacement of the plate. From these plots it can be seen that the curves corresponding to the imperfection magnitudes of $B/3000$ and $B/1000$ almost coincide with the curve of $B/300000$, which means that the initial "apparent" or equivalent stiffness of the plate is the same in these three cases and begins to reduce around the critical buckling load. The reduction is sudden in case of $B/300000$ and more gradual for the other two imperfection amplitudes. For $B/300$ and $B/125$ there is a noticeable reduction in initial stiffness of the plate almost from the start of loading. In relation to initial modulus of elasticity $E_x = 22.56\ GPa$ the reduction of apparent stiffness will be approximately 0.4% for $B/1000$, 9.6% for $B/300$ and 30% for $B/125$ at $P = 6089.06\ N$ This is not the actual stiffness reduction, but the effect of additional bending moment that results from the initial out of plane deformation. For loads higher than the linear critical load the apparent stiffness for all imperfection magnitudes seem to be the same – the curves are almost parallel to each other.

SECOND BUCKLING MODE – TYPE 2

The initial and final shapes of the plate with the imperfection type 2 are shown in the figure below. As in the case of the imperfection type 1 the general buckled shape of the plate is the same for all imperfection magnitudes.
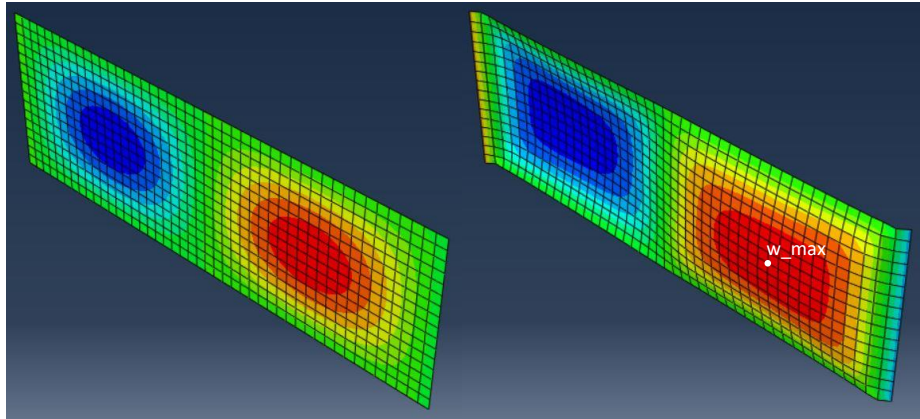
Figure 3.1.10 Initial and final shapes of the imperfect plate type 2

In general, the effect of imperfection in the shape of the second buckling mode is similar to the first buckling mode. Plots for out of plane and axial deflections of the plate with initial imperfection type 2 can be found in Annex C.1, figures C.1.1 and C.1.2.

Figure 3.1.11 shows the comparison of out of plane deformations measured at maximum (w_max) for imperfection amplitudes $B/1000$ and $B/125$.
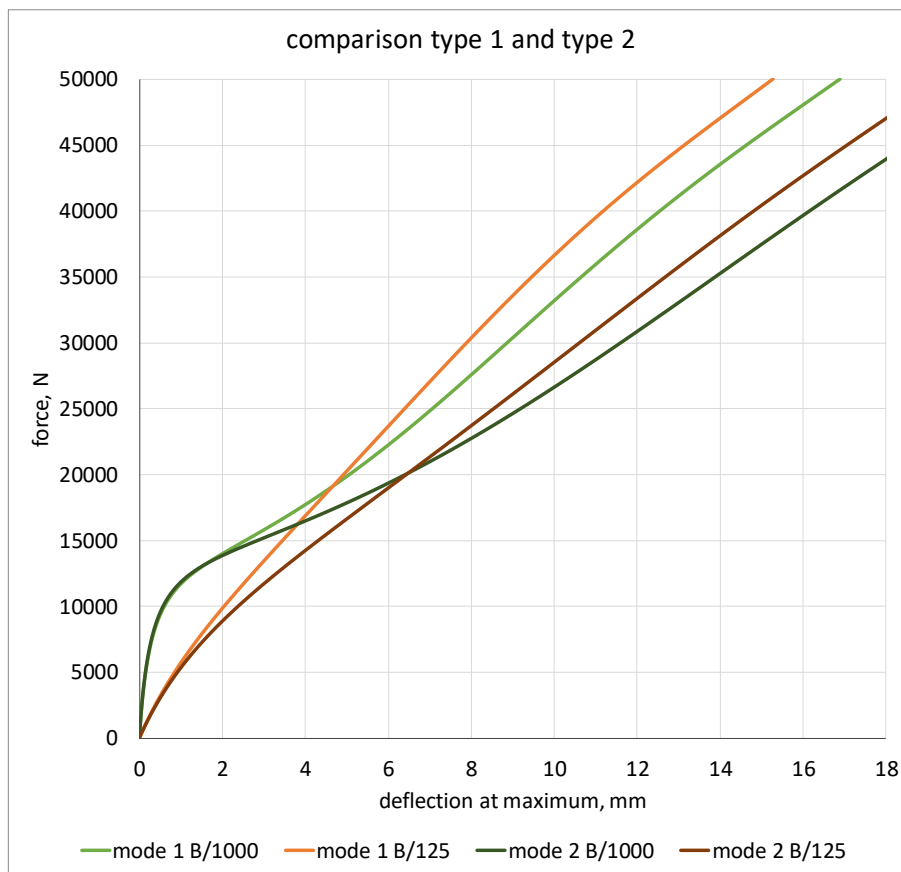
Figure 3.1.11 Comparison of imperfection shape type 1 and type 2 on out of plane deformations

At the beginning of loading the deflections coincide in both cases; after a certain level the deflections in the plate with the imperfection type 2 (second buckling mode) increase faster than in the plate with the imperfection type 1. In the geometrically linear analysis it was determined that the first buckling mode of the plate has 3 halfwaves, and in the second buckling mode – halfwaves,

therefore, the length of the halfwaves is different for type 1 and type2. For type 1 it is $L/m = 300\ mm$ (L is the length of the plate and m is the number of halfwaves) and $450\ mm$ for type 2.
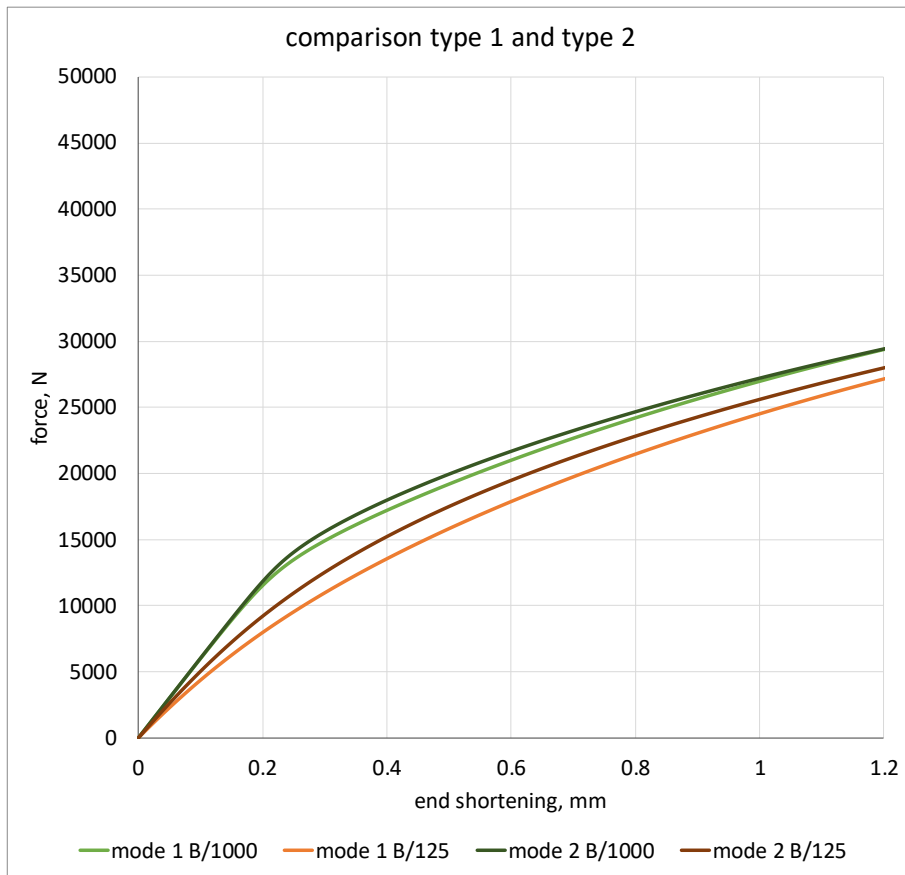
Figure 3.1.12 Comparison of imperfection shape type 1 and type 2 on end shortening

In 3.1.12 it is seen that for $B/1000$ mode 1, the initial apparent stiffness is the same as for mode 2, but for $B/125$ plate with imperfection type 1 has larger axial displacement than plate with imperfection type 2.

ONE HALFWAVE (SIXTH BUCKLING MODE) – TYPE 3

In contrast with two previous cases, the plate with the imperfection in the shape of one halfwave over the whole length of the plate shows different behaviour for different amplitudes of imperfection. This is illustrated in figures 3.1.13 to 3.1.15.
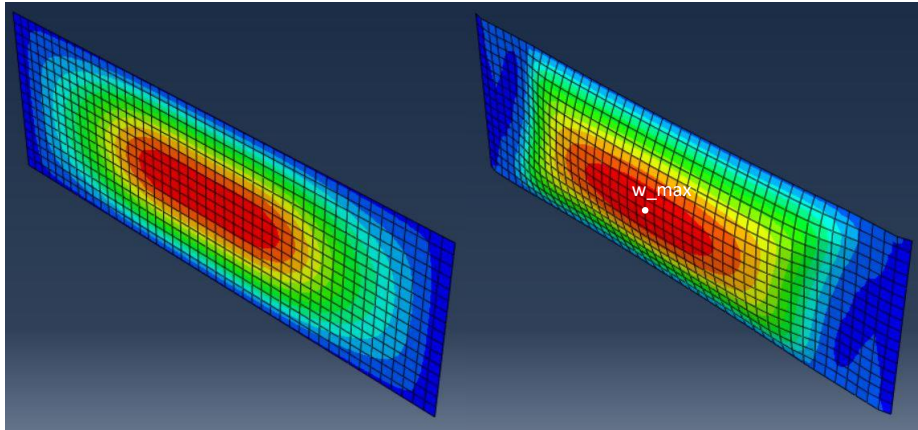
Figure 3.1.13 Initial and final shapes of the imperfect plate for B/3000 and B/1000 type 3

Figure 3.1.13 shows that for smaller amplitudes of imperfection ($B/3000$ and $B/1000$) the plate gradually bends in the shape that is determined by the shape of initial imperfection – one halfwave (buckling mode 6).
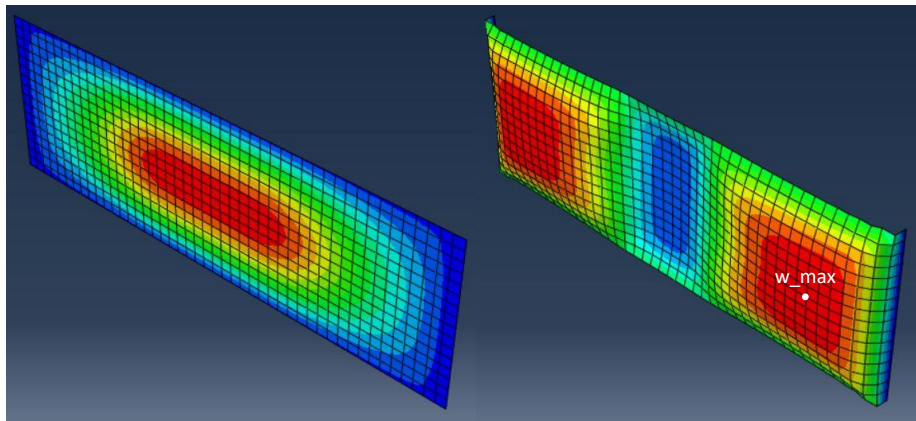
Figure 3.1.14 Initial and final shapes of the imperfect plate for B/300 and B/125 type 3

Figure 3.1.14 shows that for imperfections with amplitudes $B/300$ and $B/125$ the initial imperfection shape has one halfwave but the final shape of the plate has three halfwaves, which corresponds to initial imperfection in the shape of the first buckling mode ($m = 3$).
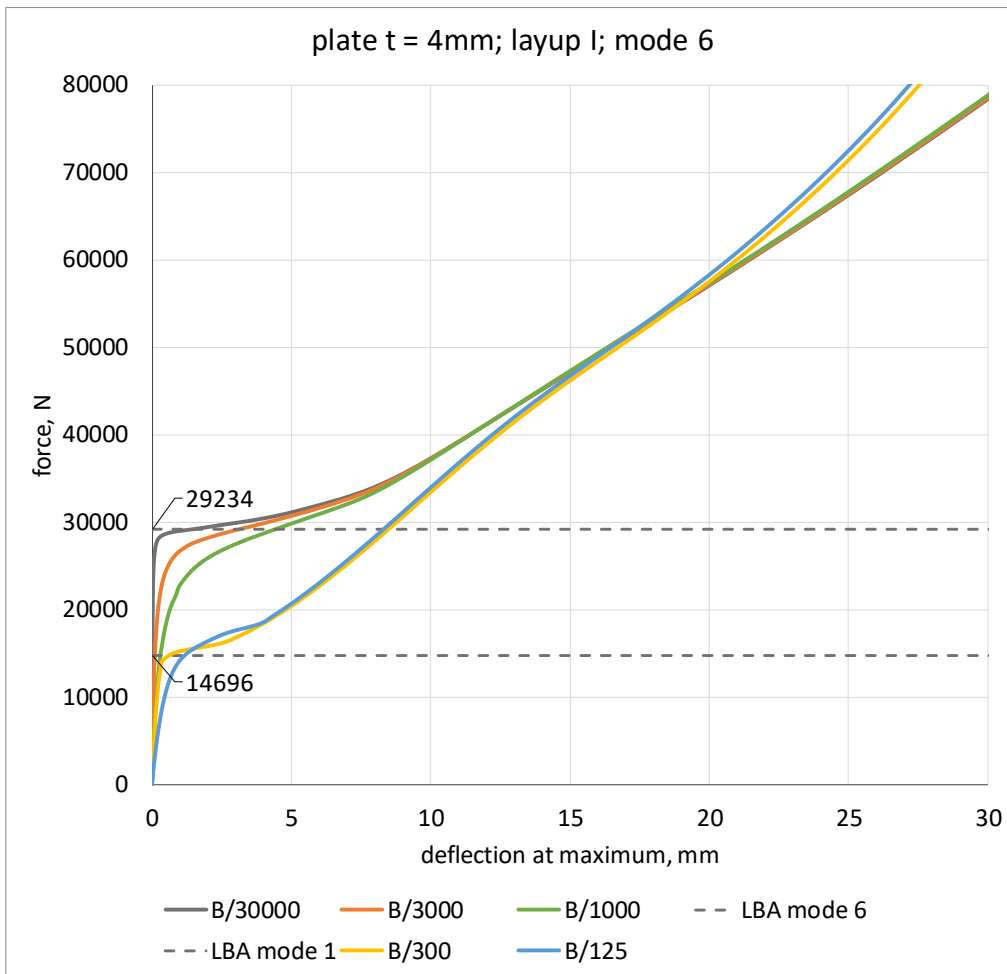
Figure 3.1.15 Force – deflection at maximum curves for a plate with the imperfection in the shape of the sixth buckling mode

Plot in figure 3.1.15 shows the force – deflection curves of the plate for the imperfection amplitudes measured at the maximum of the final buckled shape (for $B/30000$, $/3000$ and $B/1000$ corresponding to the point w_max in figure 3.1.12 and for $B/300$ and $B/125$ - w_max in 3.1.13). As is seen in the plot, the plate with smaller amplitudes of imperfection ($B/30000$, $/3000$ and $B/1000$) buckles around the critical load corresponding to buckling mode 6, while imperfection $B/300$ and $B/125$ causes plate to buckle around critical load of the first buckling mode (the theoretical buckling load is slightly higher for $B/125$ than $B/300$).
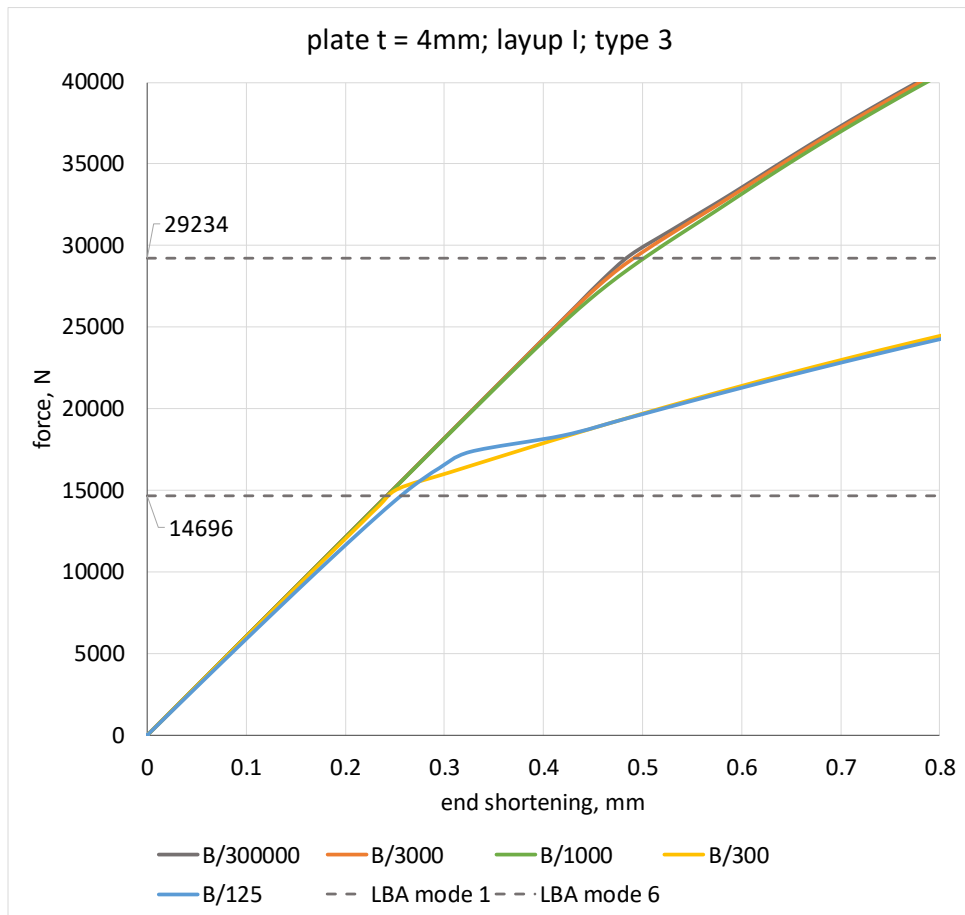
Figure 3.1.16 End shortening of a plate with the imperfection in the shape of the sixth buckling mode

The plots in figure 3.1.16 show the end shortening of the plate with the imperfection of one halfwave. These correspond to previous observations: for lower amplitudes of the imperfection the plate buckles around the load corresponding to the mode 6 and for higher amplitudes – around the critical buckling load of mode 1 (for $B/125$ the kink in the curve (blue) appears at the value that is a little higher, around $17000\ N$).

The contour plots in figure 3.1.17 show step by step buckling of the plate for $B/3000$ and $B/125$ to illustrate the change from the initial shape to the final buckled shape. As is seen, the plate with imperfection $B/3000$ continuously bends in the shape of the buckling mode 6 ($m = 1$), first having small out of plane deflections which then increase around critical load of the fist buckling mode. The plate with imperfection $B/125$ begins with the imperfection with one halfwave and then changes into shape with three halfwaves. Between $P = 15338.1\ N$ and $P = 17338.1\ N$ the plate with imperfection $B/125$ changes shape from one halfwave to two halfwaves and at $P = 18338.1\ N$ it shows three halfwaves. Because of this change from the shape of one halfwave into the two halfwaves and eventually into three halfwaves, the theoretical critical load does not really correspond exactly to any one the buckling modes critical loads.
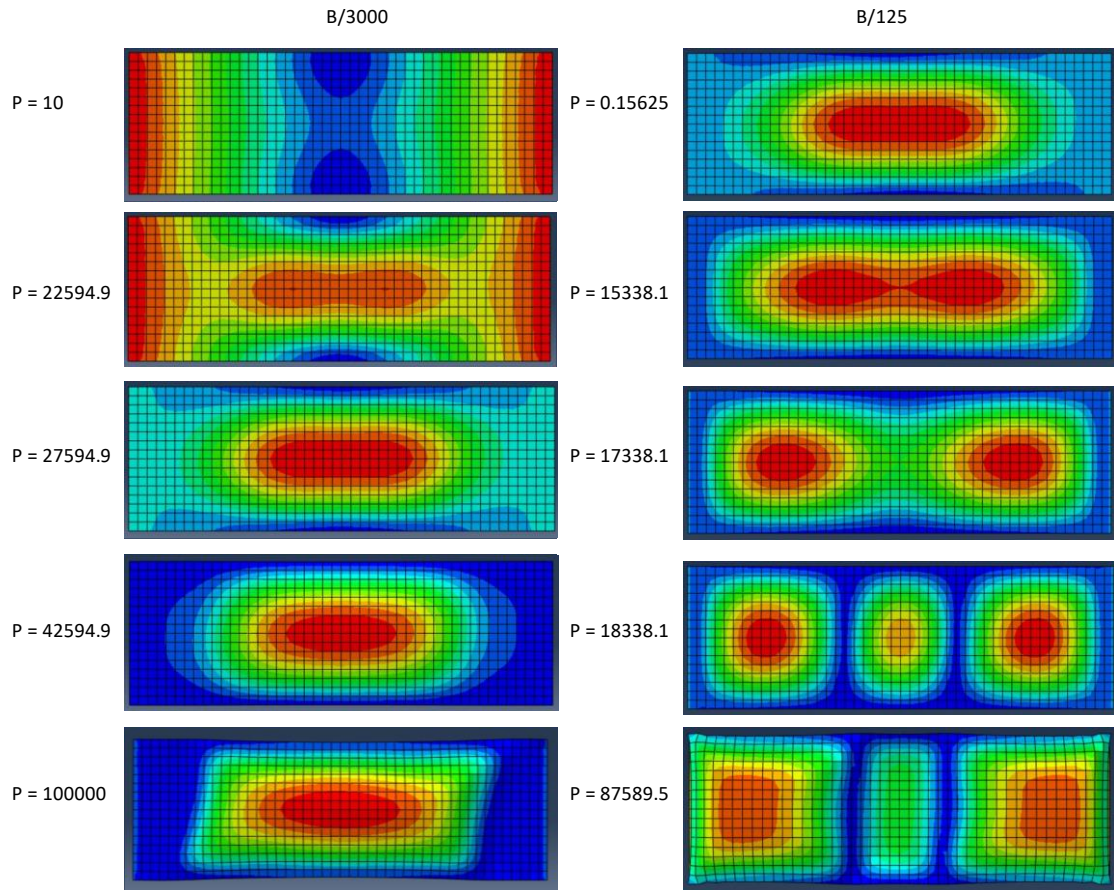
Figure 3.1.17 Buckling of the plate with imperfection type 3 with B/300 and B/125 (based on the absolute values)

WRINKLE IMPERFECTION – TYPE 4

The wrinkle imperfection's width is $19.57\ mm$ (width of one element). In the preliminary analysis of plate buckling behaviour with a wrinkle imperfection, it was established that a plate buckles into the first buckling mode, with the maximum deflection at the point denoted as w_max in figure 3.1.18:
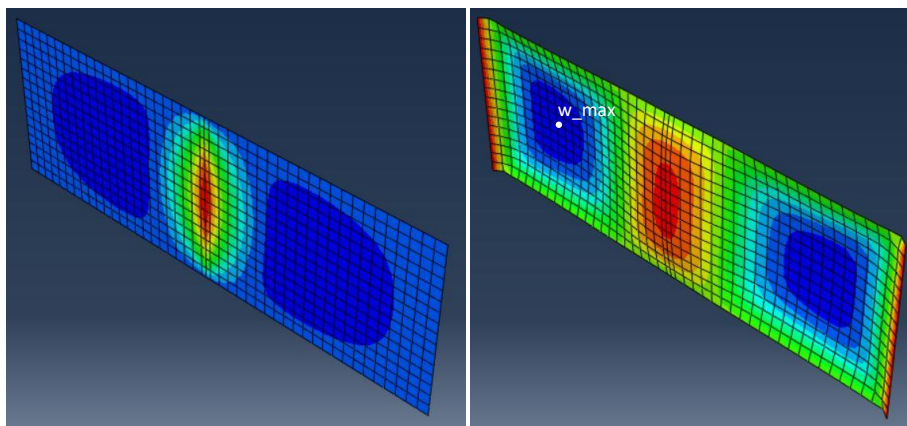
Figure 3.1.18 Initial and final shapes of the imperfect plate with a single wrinkle in the middle

Therefore, the for more detailed analysis the two locations of the wrinkle imperfection were chosen; assymetric (wrinkle 1) and symmetric (wrinkle 2):
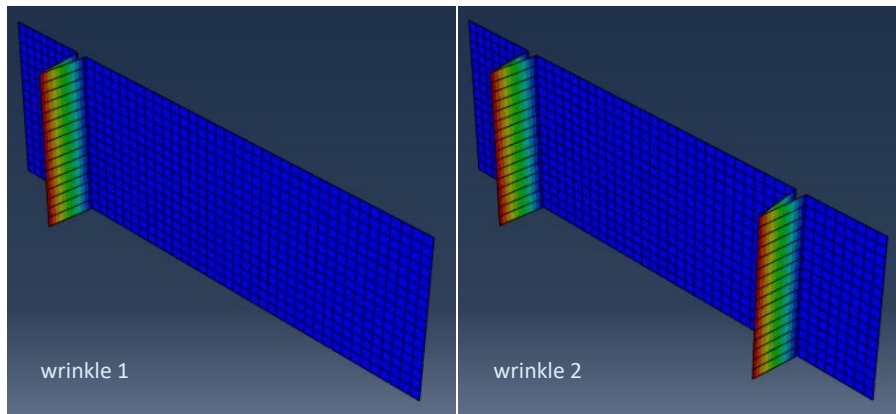
Figure 3.1.19 Locations of the wrinkle imperfection

In both cases for all imperfection amplitudes the buckled shapes are similar to each other having three halfwaves in longitudinal direction. In case of the asymmetric wrinkle imperfection the buckled shape is also slightly asymmetric as expected; the two outside halfwaves are not equal and the maximum deflection occurs at the point where the initial imperfection is applied (figure 3.1.20). For symmetric wrinkle imperfection the buckled shape is symmetric, with maximum deflection occurring at points denoted as w_max (figure 3.1.21).
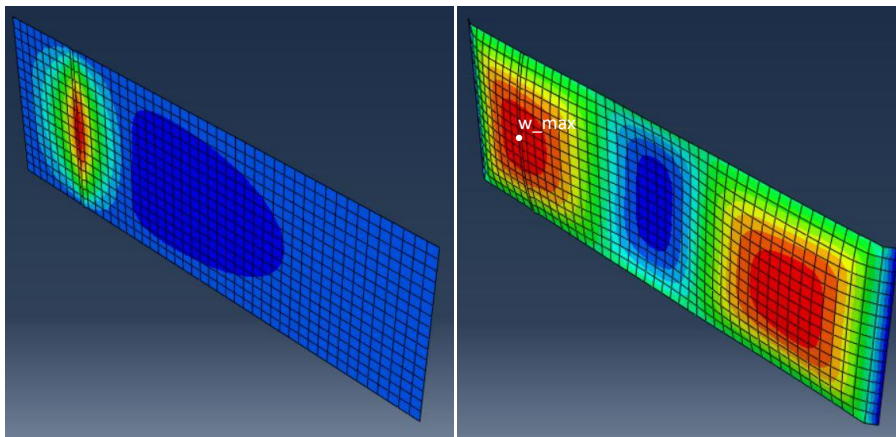
Figure 3.1.20 Initial and final shapes of the plate with asymmetric wrinkle imperfection
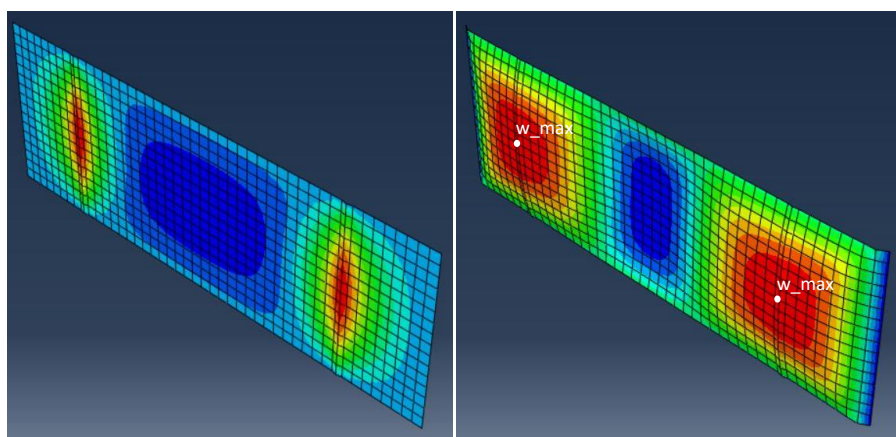
Figure 3.1.21 Initial and final shapes of the plate with symmetric wrinkle imperfection

plate t = 4mm; layup I; wrinkle asymmetric

14696

B/3000   B/1000   B/300   B/125   – – LBA
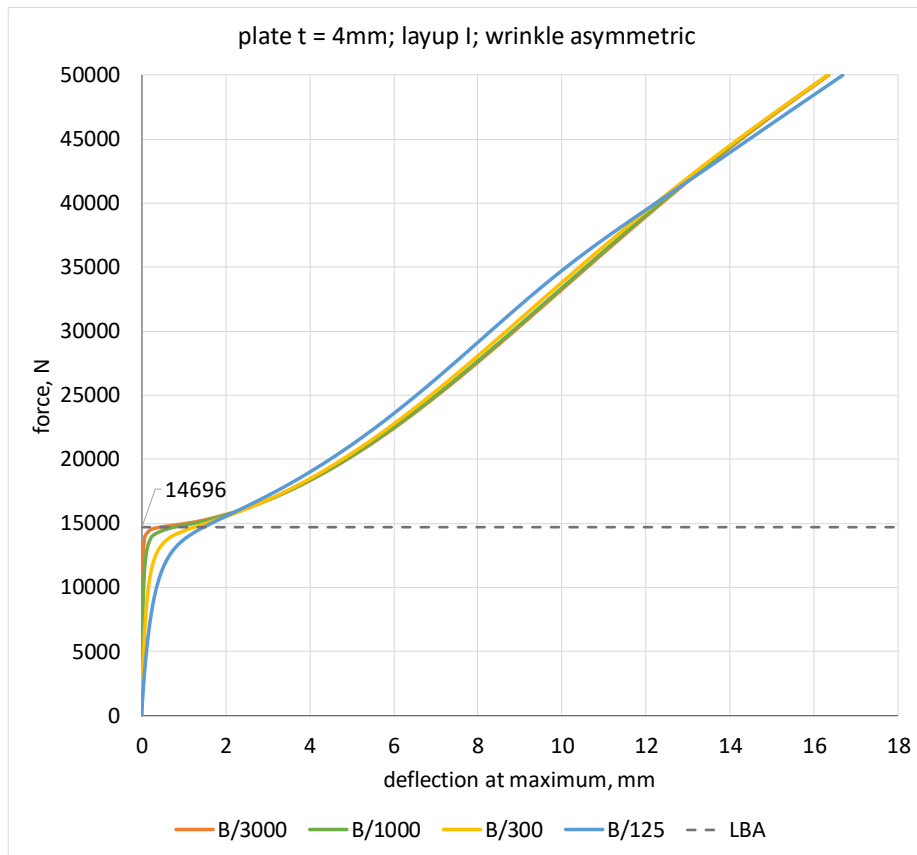
Figure 3.1.22 Force – deflection curves for a plate with the asymmetric wrinkle imperfection

plate t = 4mm; layup I; wrinkle symmetric

14696

B/3000   B/1000   B/300   B/125   – – LBA
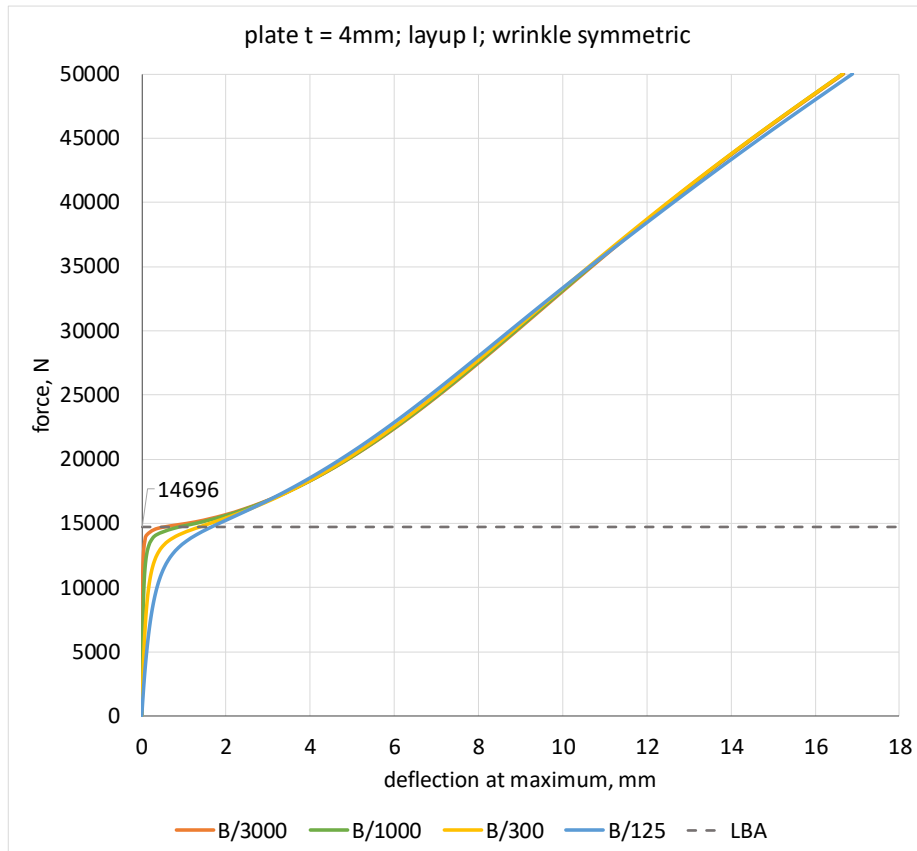
Figure 3.1.23 Force – deflection curves for a plate with the symmetric wrinkle imperfection

From the plots in figures 3.1.22 and 3.1.23 it can be concluded that the influence of this type of imperfection is not as severe as previously investigated shapes. While buckled plate shapes are similar to those observed for imperfection in the shape of the first buckling mode, the behaviour is different. There is a clear change in the slope of the load – deflection curves in case of wrinkle imperfection for all imperfection amplitudes.

COMPARISON

After studying the effect of various shapes on plate's behaviour the following can be summarized:

- the imperfections in the shape of the first and the second buckling mode have a similar effect on the behaviour of the plate, the critical loads for these two buckling modes are close and the difference lies in number and, therefore, length of one halfwave;

- the imperfection in the shape of the sixth buckling mode triggers different behaviour depending on the imperfection amplitude: for $B/3000$ and $B/1000$ plate bends into the shape determined by the shape of initial imperfection (one halfwave), but for $B/300$ and $B/125$ the final buckled shape has three halfwave which is similar to the first buckling mode;

- plate with wrinkle imperfection buckles into the shape corresponding to the first buckling mode.

Since there are three cases in which the plate buckles in the shape of the first buckling mode, it makes sense to further compare these three situations.
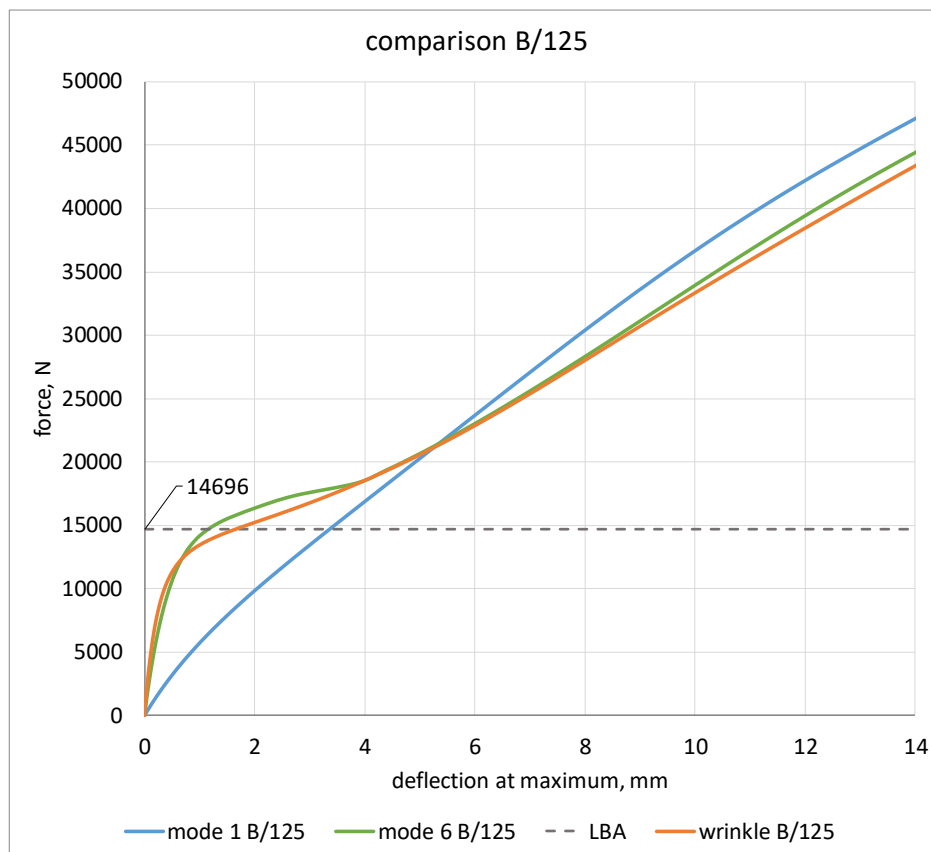
Figure 3.1.24 Effect of various imperfection shapes on out of plane deformation

Figure 3.1.24 illustrates the effect of the imperfection shape. In all the three cases the plate buckles into the shape corresponding to the first buckling mode ($m = 3$). The most pronounce effect is seen when an imperfection in the shape of the first buckling mode is applied. In this case, the plate gradually bends into the predetermined shape, and the largest effect is seen in the prebuckling region (loads below the critical load of a perfect plate), in which the curve is almost linear compared to two other imperfection shapes. In two other case, the shape of initial imperfection was either wrinkle or one halfwave (buckling mode 6). In case of the wrinkle imperfection (orange curve) the growth of out of plane deformations is a lot slower compared to type 1 imperfection; there is still no bifurcation point but there is a knee in the force – deflection curve around the critical buckling load. In case of the imperfection in the shape of the buckling mode 6, the plate begins bending into the shape determined by the initial imperfection but at approximately around critical buckling load (the load level is a little higher, since the shape changes from one halfwave into two halfwaves and only then into three halfwaves) of the first buckling mode it changes shape. As is seen in the graph the postbuckling response corresponding to these two shapes (buckling mode 6 and wrinkle imperfection) is somewhat similar.
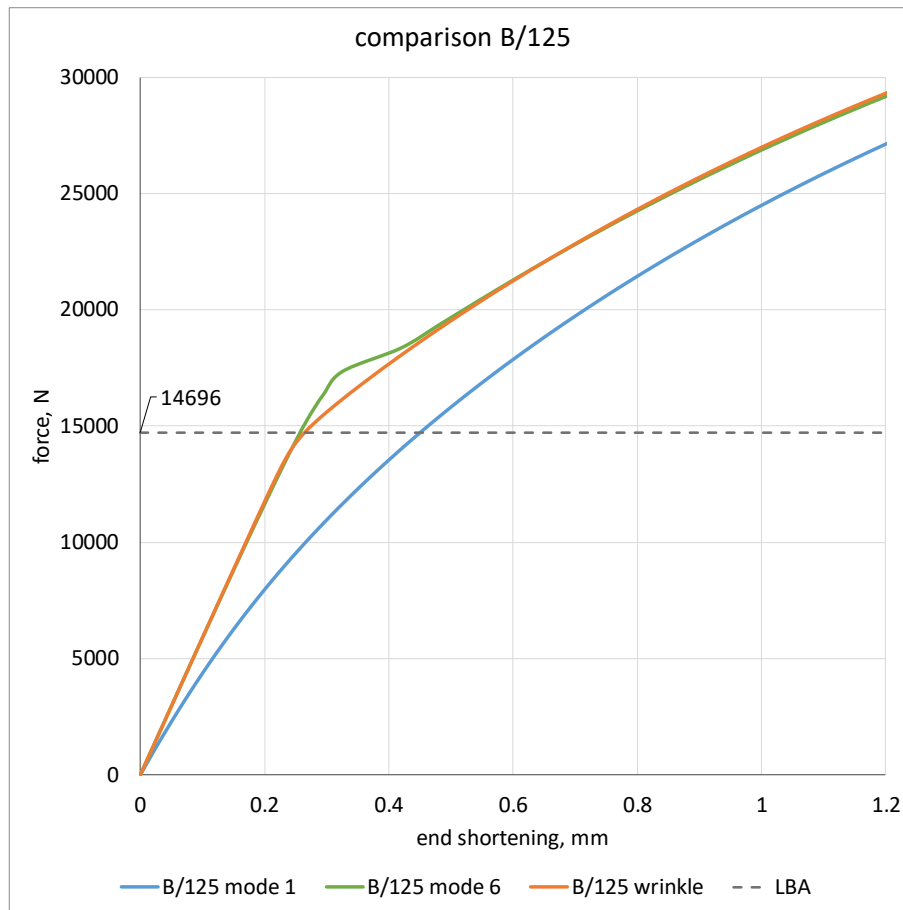
Figure 3.1.25 Effect of various imperfection shapes on plate's end shortening

Figure 3.1.25 show the effect of imperfection shape on the reduction of the equivalent stiffness of the plate. Again, the largest axial displacements are in a plate with initial imperfection in the shape of the first buckling mode. The response of the pate with wrinkle imperfection and imperfection in the shape of the buckling mode 6 is similar, apart from the area just above the critical buckling load.

From the studying the effect of different imperfection shapes, the imperfection type 1 seems to be the most significant, as it coincides with the fundamental buckling mode of a plate. It was shown

that plates with other imperfection shapes can also buckle into the first buckling mode, but since in case of imperfection shape type 1 the initial shape of plate and buckled shape coincide, it has a much noticeable effect than imperfection type 3 (6th buckling mode) and wrinkle imperfection.

3.2 PARAMETER STUDY

The effect of different plate parameters on the nonlinear buckling behaviour is studied. Three variables are considered: plate thickness, aspect ratio and layup. For each case linear buckling analysis and geometrically nonlinear analysis will be employed. The imperfection is taken in the shape of the first buckling mode.

3.2.1 THICKNESS

MODEL

To investigate the influence of laminate thickness a plate of $t = 8\ mm$ was modelled. The width and the length stay the same ($300\ \times 900\ mm$), so do the laminate elastic properties ($E_x/E_y = 1.27$)

LINEAR BUCKLING ANALYSIS

The first six buckling shapes of the plate with thickness of 8 mm are similar to those of the plate with thickness $t = 4\ mm$, and are shown in figure 3.2.1.
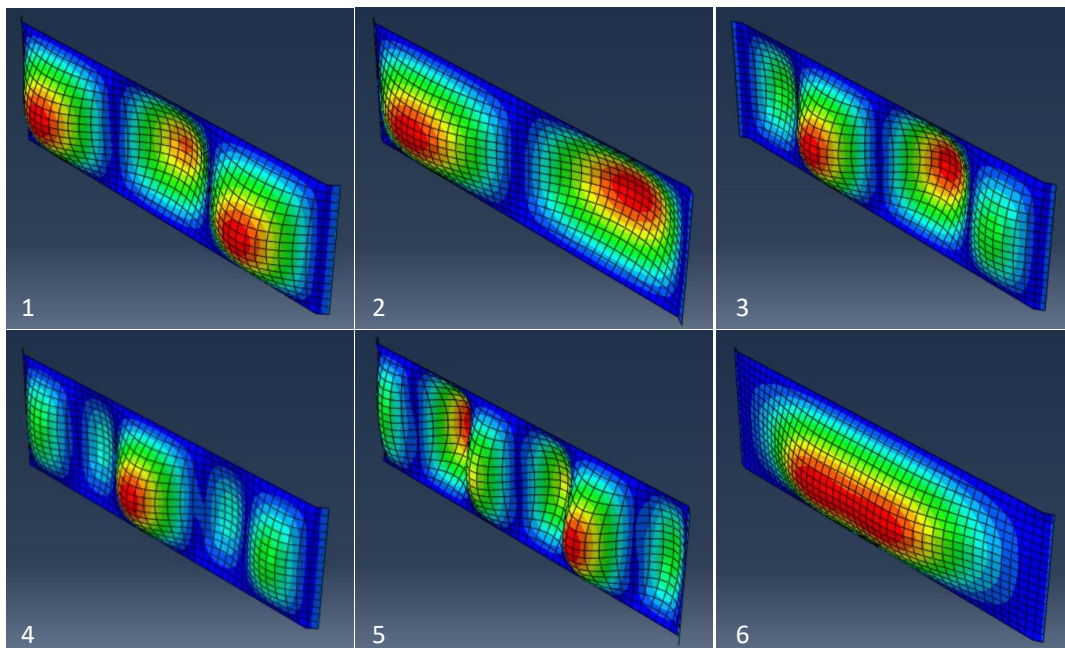
Figure 3.2.1 The first six buckling modes of the plate of layup I and t = 8 mm

The comparison of the results from finite element analysis and analytical expression is presented in table 3.4.

mode	force FEA, N	force analytical, N	difference, %
1; m=3	112736	117194.97	3.8
2; m=2	114594	123520.2	7.2
3; m=4	134939	137472.87	1.8
4; m=5	166832	171535.29	2.7
5; m=6	212114	216219.18	1.9
6; m=1	219916	260495.78	15.6

Table 3.4 Comparison of the critical loads obtain from the analytical formula and FEA (layup I, t = 8 mm)

In general, the results from analytical expression gives slightly higher results than FEA. The largest differences between the analytical and FEA results are observed for $m = 2$ (second buckling mode) and $m = 1$ (sixth buckling mode) which are 7.23% and 15.58%, respectively. In figure 3.2.2, it can be seen that the vertical line representing aspect ratio under consideration AR = 3 crosses the ascending parts of curves $m = 2$ and $m = 1$. The same observation was made in case of the $t = 4\ mm$ plate and it seems that the difference between analytical and FEA results have to do with a halfwave's length.
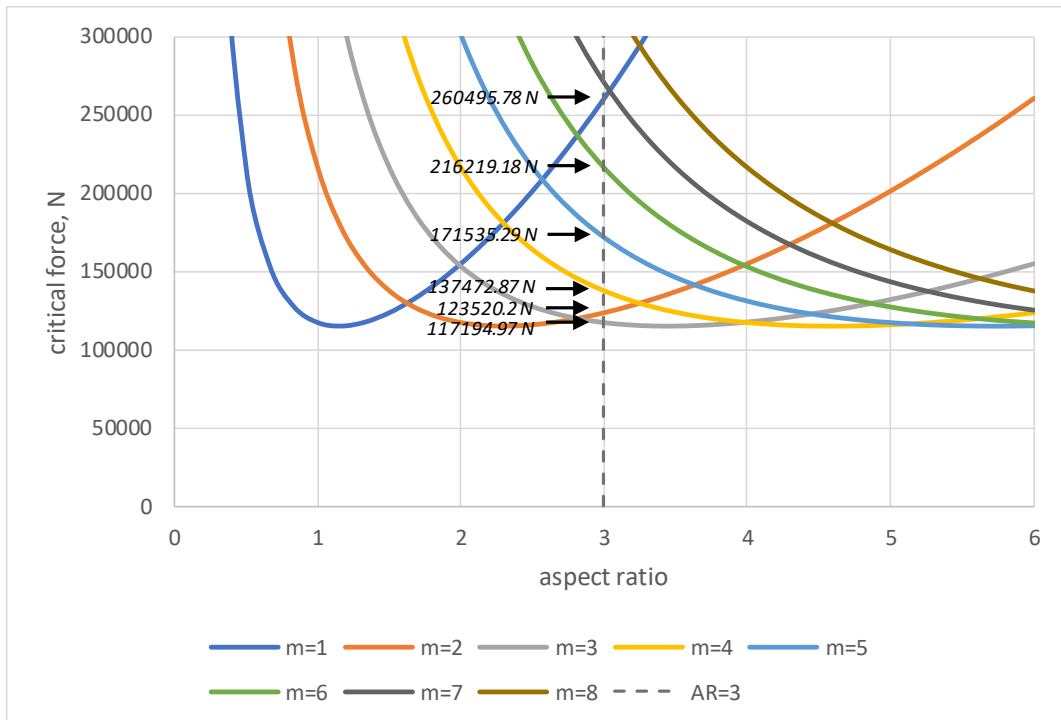
Figure 3.2.2 Visualization of the analytical results for the plate of layup I and t = 8 mm

Figure 3.2.3 illustrates the dependence of critical load and buckling mode on orthotropic aspect ratio. The position of the minimal critical load corresponding to $m = 3$ is again determined by $AR \cdot \sqrt[4]{D_{11}/D_{22}}$. For plate thickness $t = 8\ mm$ it will be at the same aspect ratio value of 3.44 as for plate $t = 4\ mm$, since the layup is the same in both cases.
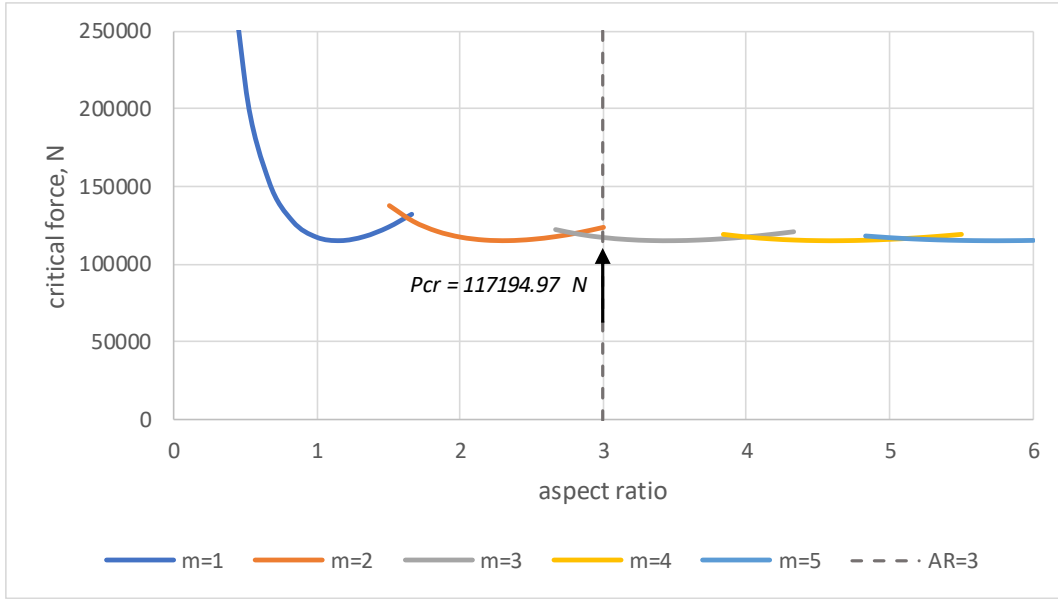
Figure 3.2.3 Dependence of buckling load and mode on plate aspect ratio for the plate of layup I and t = 8 mm

GEOMETRICALLY NONLINEAR ANALYSIS

The buckling behaviour and therefore the plots of the plate with a larger thickness are in general very similar to those of the plate with $t = 4\ mm$. The force – out of plane deflection and force – end shortening diagrams for imperfection type 1 is given in Annex C.1, figures C.1.3. and C.1.4. Here the comparison between plates with $t = 4\ mm$ and $t = 8\ mm$ will be shown.

As is known from theory, buckling strength relates to bending stiffness of a laminate. The bending stiffness parameters of orthotropic material are calculated as $D_{ij} = 1/3 \sum_{k=1}^{n} (\bar{Q}_{ij})_k (h_k^3 - h_{k-1}^3)$ with h being the vertical position of the ply from the midplane. Axial stiffness is defined as $A_{ij} = \sum_{k=1}^{n} (\bar{Q}_{ij})_k (h_k - h_{k-1})$. Therefore, a plate with thickness $t = 8\ mm$ has a higher bending and axial stiffness. Based on that, it is expected that the influence of initial imperfections will be less on a thicker plate.

Figure 3.2.4 and 3.2.5 shows the comparison of out of plane deflections and axial displacements in plates with thickness $t = 4\ mm$ and $t = 8\ mm$ for imperfection amplitudes $B/1000$ and $B/125$. As expected, both out of plane and in plane deflections in the thicker plate are smaller at a certain load level compared to deflections in the thinner plate. Since the critical load does not occur, exact influence of the initial imperfection

68
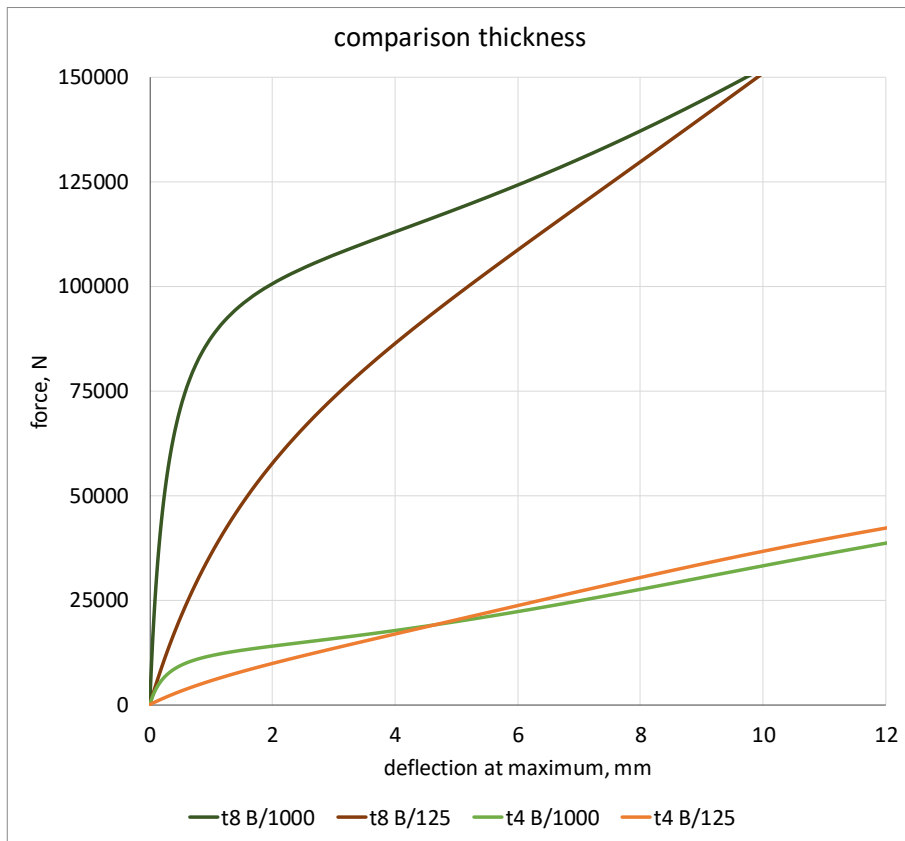
Figure 3.2.4 Comparison of thickness effect on out of plane deformation
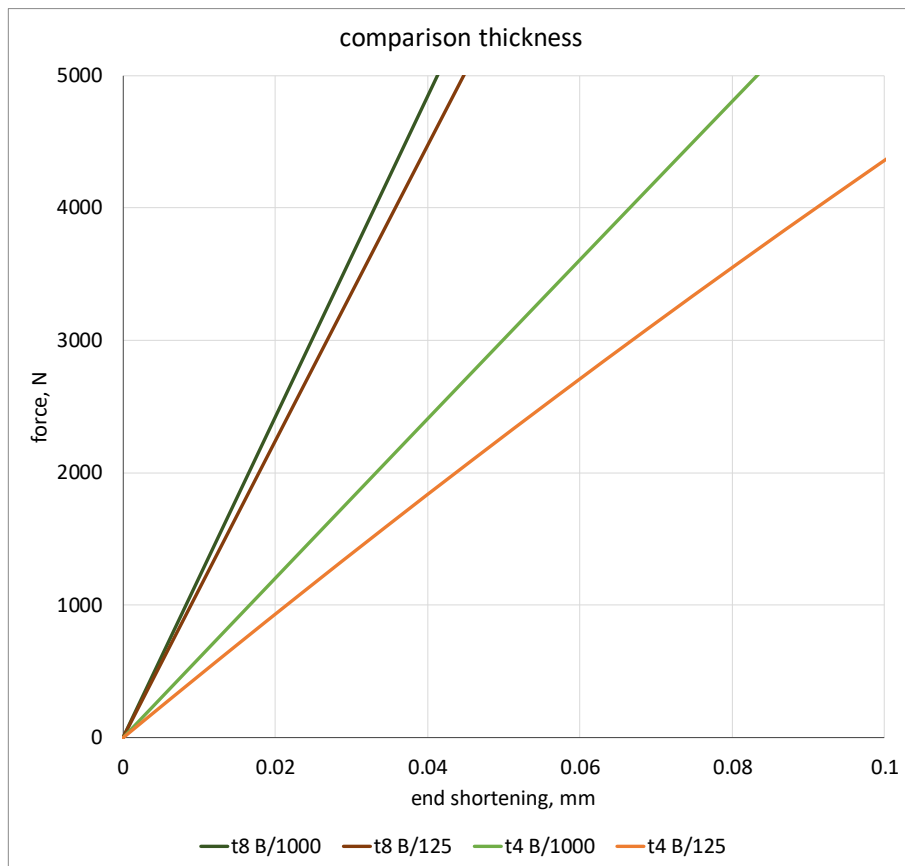
Figure 3.2.5 Comparison of thickness effect on axial displacement

3.2.2 ASPECT RATIO

MODEL

To investigate the influence of aspect ratio a plate AR = 5 was modelled. The width and the length are $300 \times 1500 \ mm$, $t = 8 \ mm$ and the laminate elastic properties are such that $E_x/E_y = 1.27$ (layup I). The element size is $25 \times 25 \ mm$ (12 elements in y and 60 elements in x direction of the plate).

LINEAR BUCKLING ANALYSIS

The first six buckling modes are shown in figure 3.2.6. In comparison to the plate with AR = 3, one thing is immediately visible: the fully developed halfwaves (coloured red at the tips) all have about the same length in longitudinal direction. The halfwaves corresponding to buckling modes 1, 2 and 4 are slightly longer in comparison to the other three. From the theory it is known that the longer the plate is, the less influence aspect ratio has on the critical load, and for plates with AR > 5, the aspect ratio and the number of halfwaves is excluded from the expressions for the critical load (expressions in table 2.2). Therefore, it is expected that the critical loads for different number of halfwaves will be closer to each other than in case of AR = 3. It is also expected that the critical load for buckling mode 2 with $m = 5$ will be the same as the critical load for buckling mode 1 ($m = 3$) of a plate with aspect ratio 3, since in both cases the length of one halfwaves are the same:

AR = 3: $L = 900 \ mm$, $m = 3$; $L_{buc} = L/m = 300 \ mm$

AR = 5: $L = 1500 \ mm$, $m = 5$; $L_{buc} = L/m = 300 \ mm$
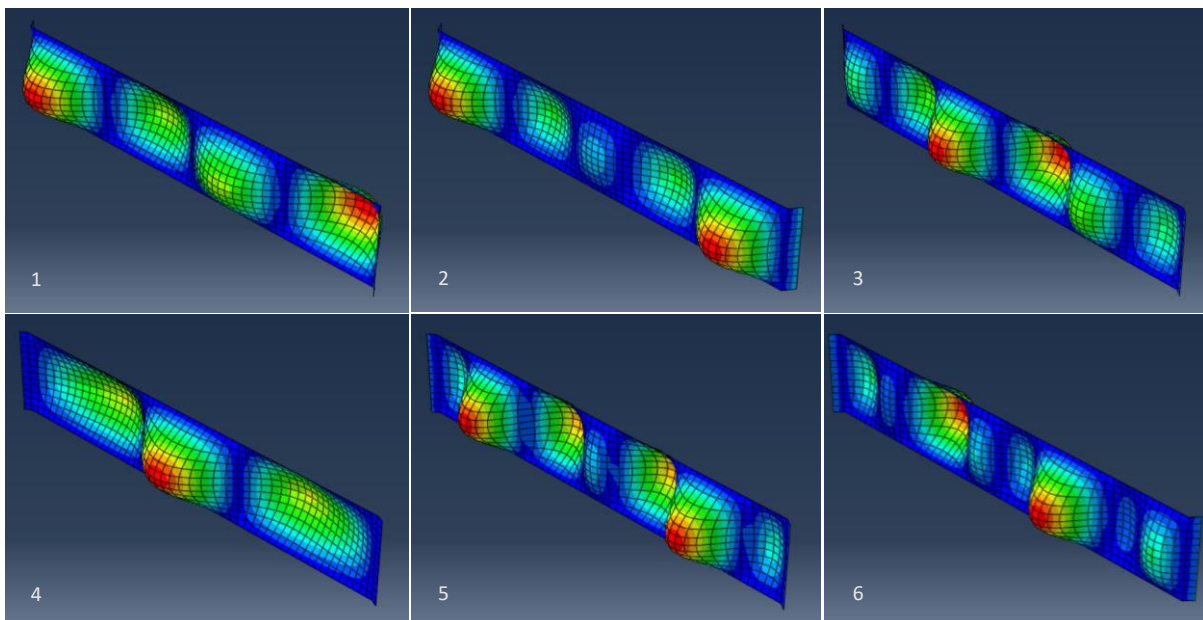
Figure 3.2.6 The first six buckling modes of the plate of layup I and AR = 5

The comparison of analytical solutions for plates AR = 3 and AR = 5 are shown in figure 3.2.7.
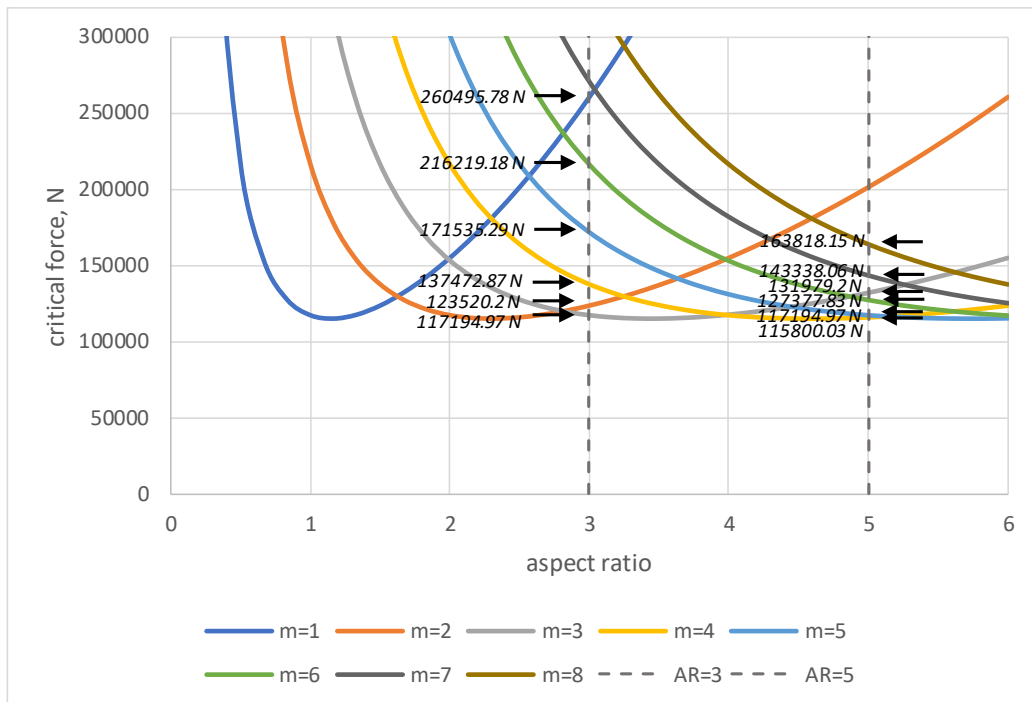
Figure 3.2.7 Comparison of the analytical results for the plate with AR = 3 and AR = 5

As is seen, the values for critical loads corresponding to various buckling modes for plate AR = 5 are indeed are closer to each other, compared to plate AR = 3. Also, the critical load for the first buckling load AR = 3 ($m = 3$) equals to the critical load for the second buckling load AR = 5 ($m = 5$): $P = 117194.97\ N$.

mode	force FEA, N	force analytical, N	difference, %
1; m=4	107988	115800.03	6.8
2; m=5	109804	117194.97	6.3
3; m=6	123797	127377.83	2.8
4; m=3	123919	131979.20	6.1
5; m=7	140971	143338.06	1.7
6; m=8	158857	163818.15	3.0

Table 3.5 Comparison of the critical loads obtain from the analytical formula and FEA (layup I, AR = 5)

The differences of 6.75%, 6.31% and 6.11% between analytical and FEA solutions are obtained for buckling modes 1, 2 and 4, respectively (table 3.5). The theoretical lengths of halfwaves in these cases are the longest; in previous cases the biggest differences were also found for the longest buckling lengths. For buckling modes 1 and 4 ($m = 4$ and $m = 3$; AR = 5) also the observation as in previous cases applies: the critical buckling load lies on the ascending branches of the curves. For $m = 5$, which is buckling mode 2, this is not the case. The conclusion therefore is: the largest difference between FEA and analytical solutions for layup I is found for the buckling modes in which the length of a halfwave is longest (lowest m).

GEOMETRICALLY NONLINEAR ANALYSIS

The applied imperfection is in the shape of the first buckling mode, the final shape of the plate is determined by the shape of initial imperfection (figure 3.2.8):
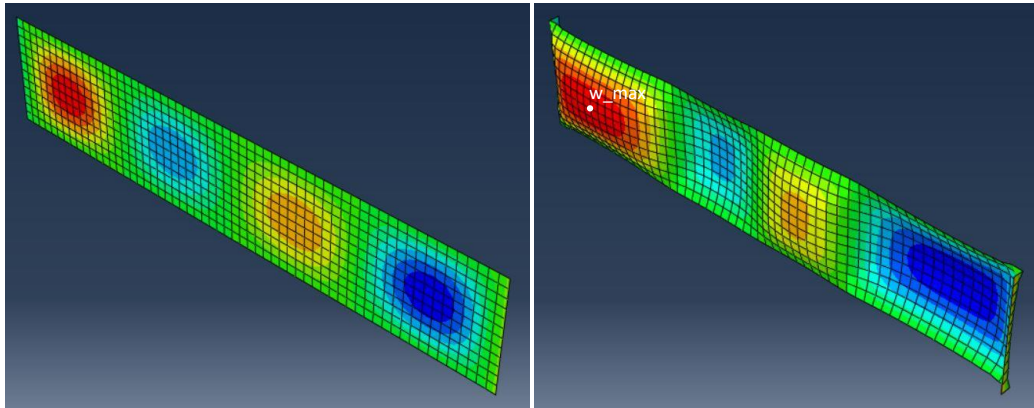
Figure 3.2.8 Initial and final shapes of the plate AR = 5 with imperfection type 1

The length of the halfwave in the first buckling mode theoretically is $L/m = 375 \ mm \ (m = 4)$ for plate with AR = 5; for the plate with AR = 3 and $m = 3$ it is $300 \ mm$. In the comparison of the effect of imperfection type 1 and type 2 (3.1.3) larger out of plane deflections were found for larger halfwave length and larger axial displacement for smaller number of halfwaves. In this case, it is therefore expected that the out of plane deformations and axial displacements will be higher for plate with aspect ratio 5, since in this case the length and the number of halfwaves is larger.

The force – out of plane deflection and force – end shortening diagrams for imperfection type 1 is given in Annex C.1, figures C.1.5 and C.1.6. The diagrams in figures 3.2.9 and 3.2.10 show the comparison of out of plane deflections and plate end shortening for two plates with different aspect ratios and imperfection amplitudes of $B/1000$ and $B/125$.
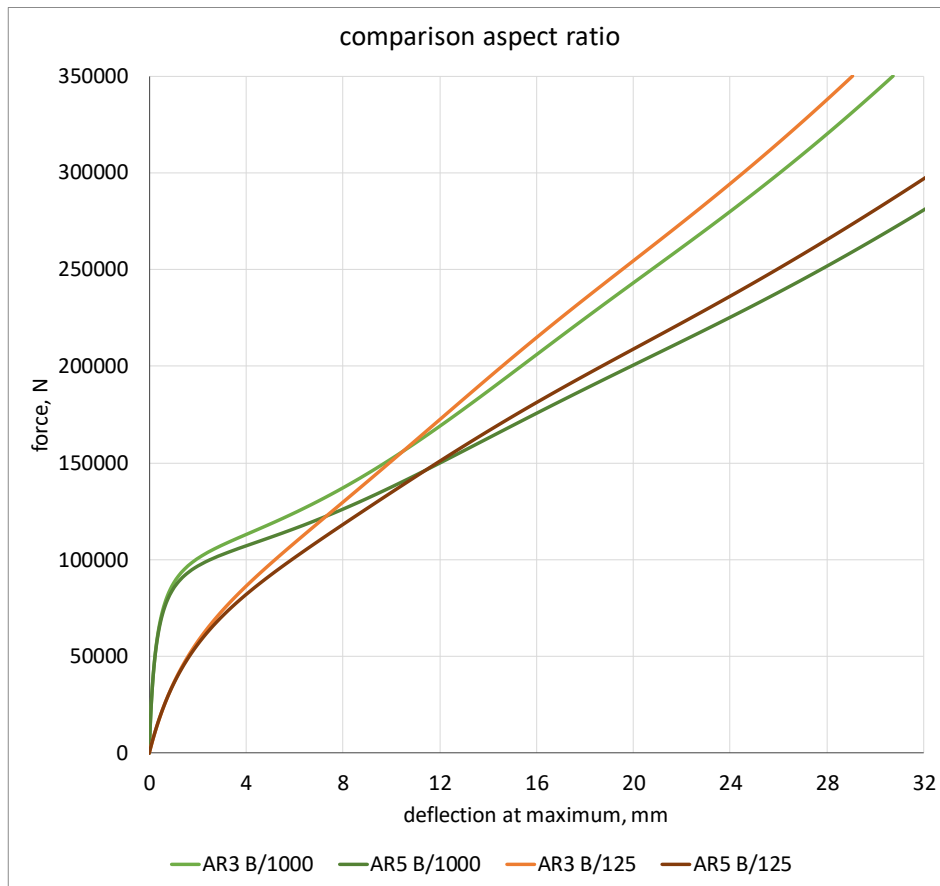
Figure 3.2.9 Comparison of out of plane deflections for plates with AR = 3 and AR = 5

In the beginning of loading the out of plane deflections are almost the same in both cases but shortly after they begin increase faster for AR = 5, as expected (figure 3.2.9).

In figure 3.2.10 it can be seen that the axial displacement is also larger for plate with aspect ratio 5. Based on these comparisons it is concluded that for the same material properties the presence of initial out of plane deformations has a more negative impact on the plate with AR = 5.
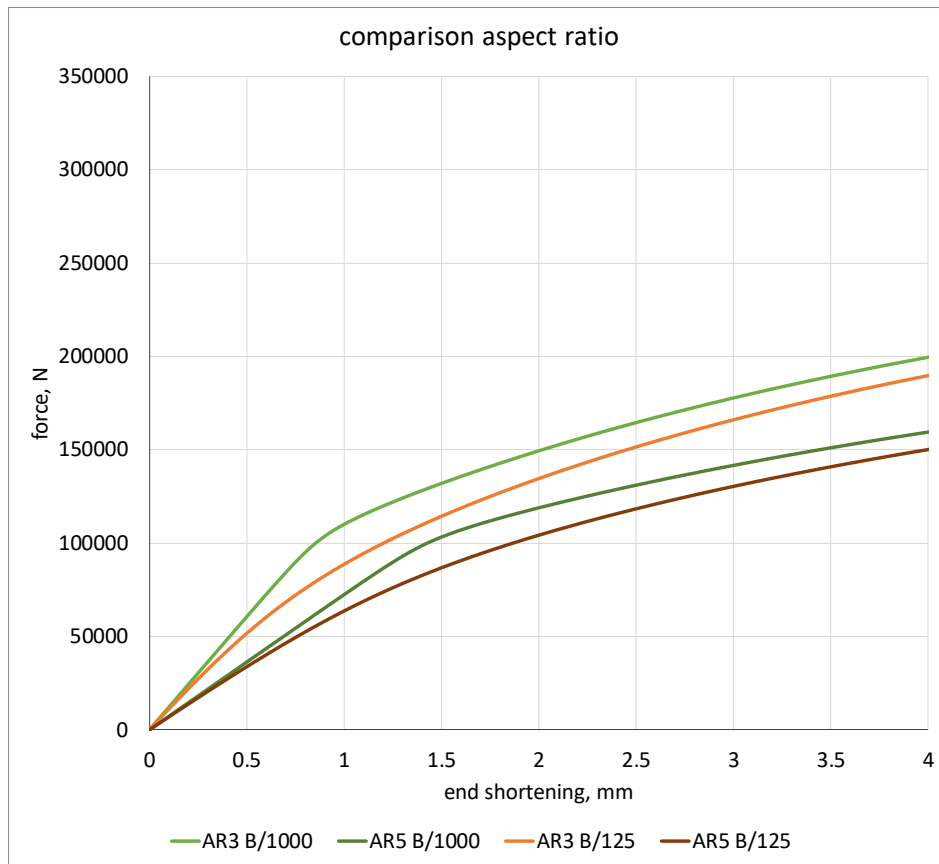
Figure 3.2.10 Comparison of end shortening for plates with AR = 3 and AR = 5

3.2.3 LAYUP

MODEL

To examine the effect of different stiffness ratio on the buckling behaviour of a plate, the following layup is considered:

Layup II: $[0_3/45/-45/90/0_2]_s$; ply thickness is $0.25\ mm$ (figure 3.2.11)

$0° - 62.5\%;\ 45° - 12.5\%;\ -45° - 12.5\%;\ 90° - 12.5\%;$

The equivalent laminate axial stiffness properties:

$E_x = 28.06\ GPa;\ E_y = 15.57\ GPa;\ G_{xy} = 5.24\ GPa;\ \nu_{xy} = 0.318;\ \nu_{yx} = 0.176$

The stiffness ratio of axial moduli of elasticity in longitudinal and transverse direction: $E_x/E_y = 1.80$

Calculation of the equivalent laminate properties is presented in Annex B.

The geometry ($300 \times 900\ mm, t = 4\ mm$), boundary and loading conditions remain the same as reported in §3.1.1.
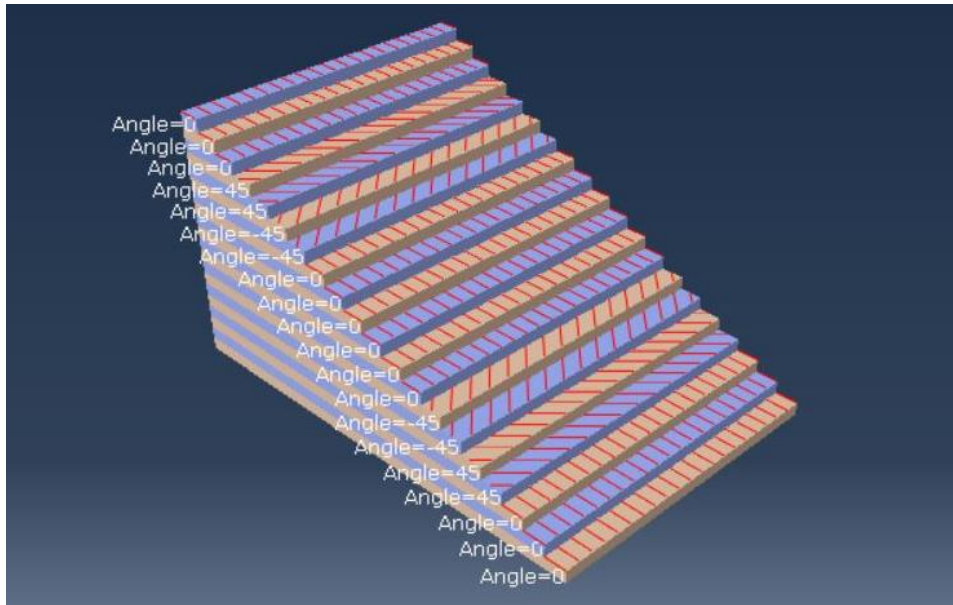
Figure 3.2.11 Ply stack plot layup II (E_x/E_y = 1.80), t = 4 mm

LINEAR BUCKLING ANALYSIS

The first six buckling modes obtained from the linear buckling analysis are presented in figure 3.2.12.
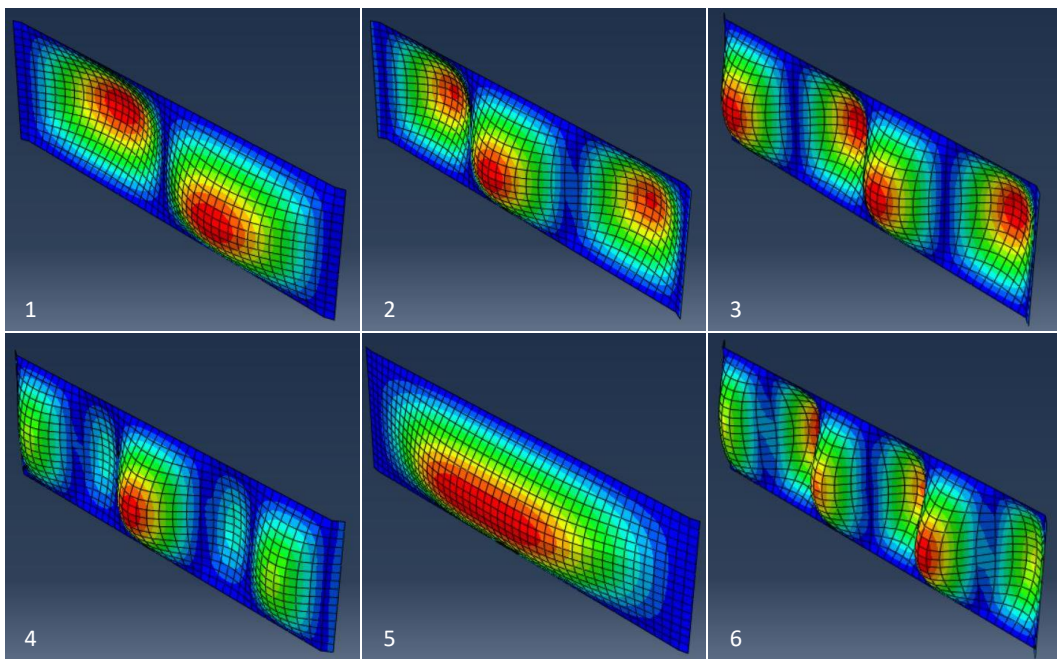
Figure 3.2.12 The first six buckling modes of the plate of layup II and t = 4 mm

The comparison of the results from finite element analysis and analytical expression is presented in table 3.5.

mode	force FEA, N	force analytical, N	difference, %
1; m=2	13248	13107.31	-1.1
2; m=3	13867	13320.7	-4.1
3; m=4	17534	16799.12	-4.4
4; m=5	22966	22143.51	-3.7
5; m=1	25351	27514.94	7.9
6; m=6	30066	29008.65	3.6

Table 3.6 Comparison of the critical loads obtained from the analytical formula and FEA (layup II, t = 4 mm)

In terms of the difference between the FEA and analytical results for layup II the following observations are made. The largest difference is seen for buckling mode 5 ($m = 1$); in figure 3.2.13 the corresponding point of intersection lies on the ascending part of the $m = 1$ curve. This also happens in case of the first buckling mode ($m = 2$) but the difference between the FEA and analytical results is only 1.1%. It can also be concluded for layup II, that the largest difference between the results is seen for the longest halfwave length.
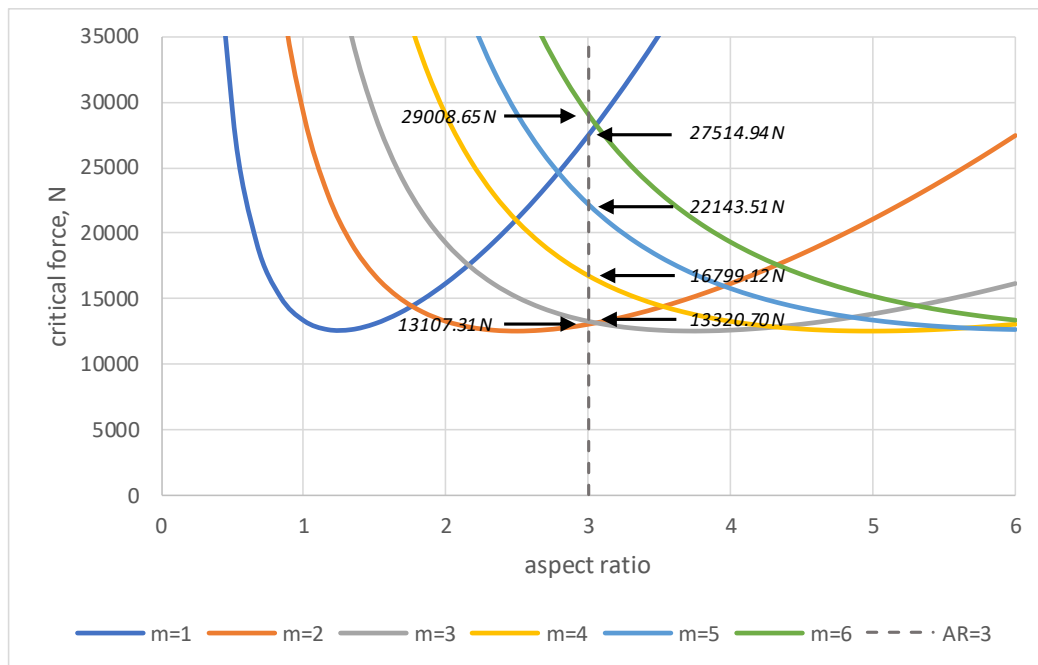
Figure 3.2.13 Visualization of the analytical results for the plate of layup II and t = 4 mm

Since the layup II has different stiffness properties, the behaviour in terms of buckling is also different. The shift of the minimum of the buckling mode curve depends on the stiffness ratio D_{11}/D_{22}. For layup I $D_{11}/D_{22} = 1.15$, for layup II $D_{11}/D_{22} = 1.25$. The comparison is made between layup I and layup II for $m = 1, m = 2$ and $m = 3$ (table 3.7):

mode	layup I	layup II
m=1	1.15	1.25
m=2	2.30	2.49
m=3	3.44	3.74

Table 3.7 Effect of orthotropy on buckling of perfect plates

As is seen from the comparison, the shift of the minimum value compared to the isotropic material is larger for layup II. Layup I has less 0° fibres and more 90° fibres in comparison with layup II, and therefore is "less orthotropic" (smaller ratio between stiffnesses in two directions).
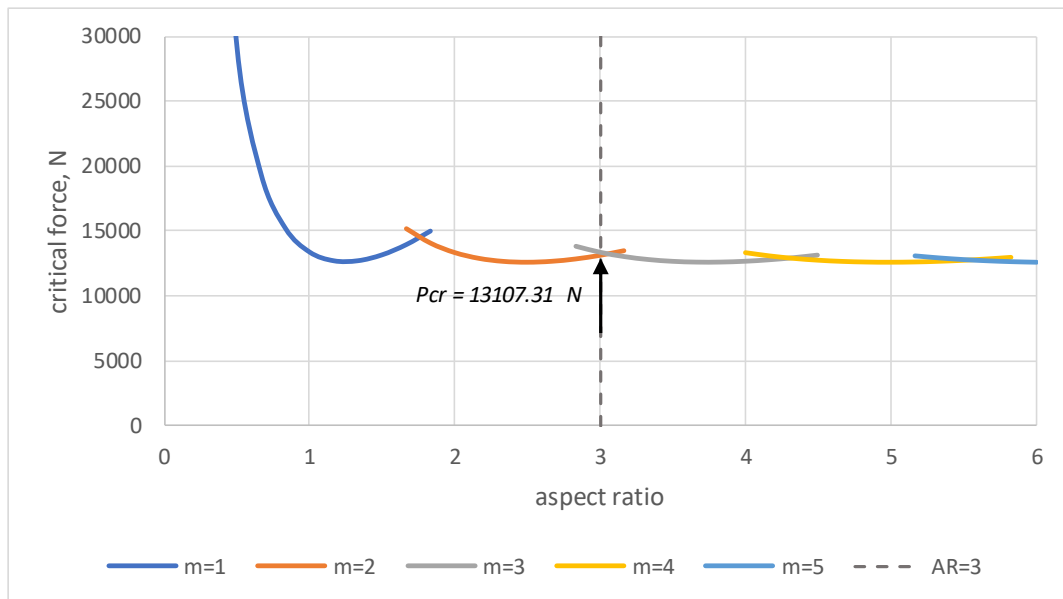
Figure 3.2.14 Dependence of buckling load and mode on plate aspect ratio for the plate of layup II and t = 4 mm

GEOMETRICALLY NONLINEAR ANALYSIS

The two first buckling modes of layup II is swapped compared to layup I. Therefore, the imperfection type 1 for layup II corresponds to the second buckling mode ($m = 3$).

The force deflection diagrams for layup II are presented in Annex C.1, figures C.1.7 to C.1.10. The conclusions drawn for layup I are also true for layup II:

- the largest out of plane deflections depend on the halfwave buckling length; plate with the imperfection in the shape of the first buckling mode (type 2, $m = 2$: $L/m = 450\ mm$) has larger out of plane deflections than a plate with imperfection in the shape of the second buckling mode (type 1, $m = 3$, $L/m = 300\ mm$);

- the largest axial displacements depend on the number of halfwaves in the imperfection shape; plate with the imperfection in the shape of the first buckling mode (type 2, $m = 2$) has smaller end shortening compared to a plate with imperfection in the shape of the second buckling mode (type 1, $m = 3$);

In general, the behaviour of an imperfect plate with layup II is similar to the behaviour of a plate with layup I. Since a plate with layup II has higher axial and bending stiffness in the longitudinal direction, for the same plate geometry and the shape of initial imperfection it is expected that the out of plane deflection and plate's end shortening will be larger for layup I. Figures 3.2.15 and 3.2.16 prove that. The "prebuckling" out of plane deflections almost coincide for layup I and II, and gradually becoming larger in plate of layup I. Much more noticeable difference in layups is seen in apparent stiffness, with plate of layup I having larger in plane deflection.
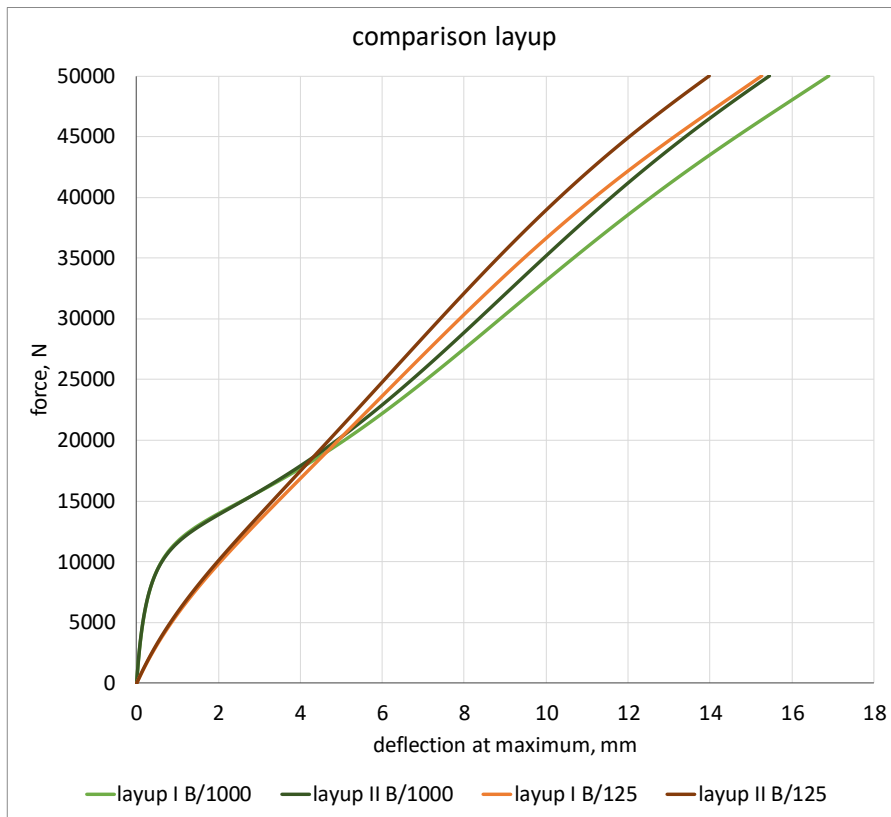
Figure 3.2.15 Comparison of out of plane deflection for plates with layup I and layup II
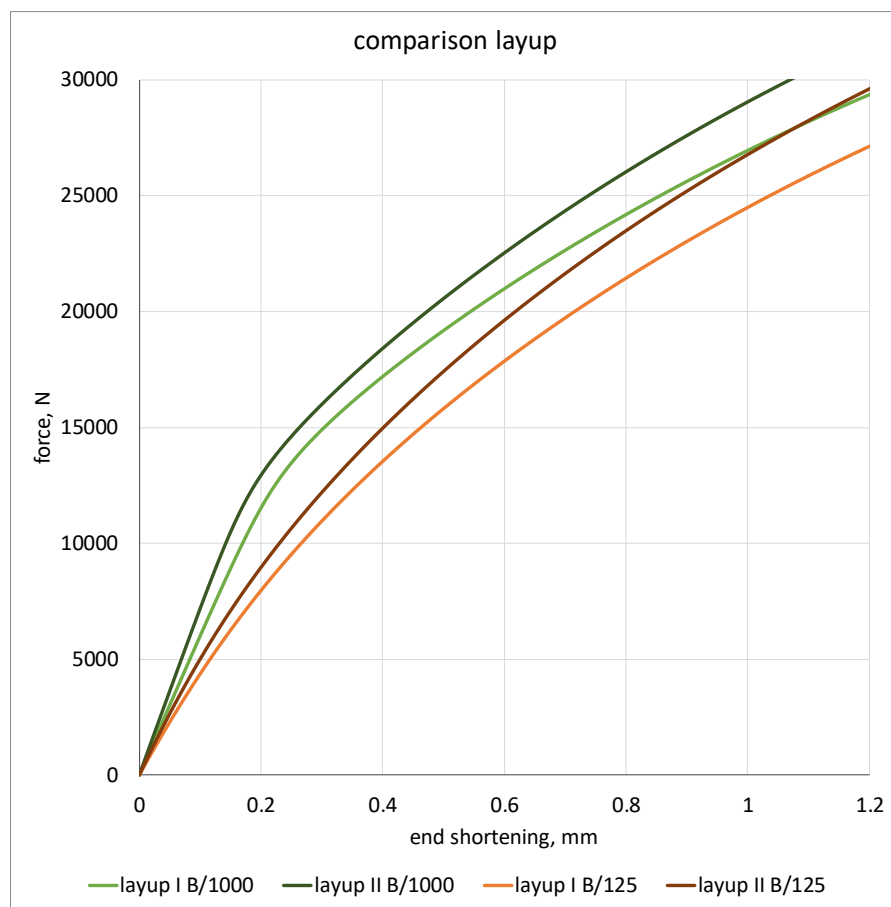
Figure 3.2.16 Comparison of end shortening for plates with layup I and layup II

3.3 CHAPTER SUMMARY

The buckling behaviour of perfect and imperfect plates was studied and a comparison between the effect of different imperfection shapes was made.

The difference between plate buckling of an isotropic and orthotropic material was established; in case of orthotropic plates not only aspect ratio but also bending stiffness ratio plays a role in buckling behaviour.

With geometrically nonlinear analysis it was shown that critical load only occurs for perfectly flat plates. In an imperfect plate no bifurcation point occurs and instead of suddenly changing shape, a plate with initial imperfection gradually bends (bows). The presence of initial out of plane deformations results in additional bending moments, which means that an imperfect plate is loaded both by uniform axial compression and bending moment. The effect of this additional bending moment can be described as apparent stiffness reduction, because under the same compression load level an imperfect plate will have much larger axial deflection. This apparent stiffness reduction is influenced by shape and amplitude of initial imperfection. It was determined, that an imperfection in the shape of plate's buckling mode have the most negative effect and the shape of the fundamental buckling mode is the most significant. Additionally, plate properties such as thickness, aspect ratio and layup also influence imperfect plate's structural behaviour.

Since there are many variables that contribute to the way plate with initial out of plane deformations behaves, it is necessary to classify plates based on their properties. The measure that ties together plate material and geometric properties and relates compression strength to buckling strength is plate slenderness. Since there is dependence of the plate response on the number and length of halfwaves of the buckling mode, it is important to use the full analytical formula to determine the critical load (table 2.1) taking those parameter into account. Once plate slenderness and failure criterion are defined, the effect of initial out of plane deformations can be quantified for plates of various geometries and certain layups. This means that materially nonlinear analysis has to be employed to determine the failure loads of plates with initial imperfections.

4. PLATE FAILURE ANALYSIS

In this chapter plate slenderness, failure criteria and the relation between slenderness and failure load reduction due to initial out of plane deformation determined. The objective is to derive buckling curves that can be used for buckling design of fibre reinforced polymer plates with initial imperfections.

4.1 PLATE SLENDERNESS

It was shown in chapter 3 that imperfect plates of different layups, aspect ratio and thickness show similar buckling behaviour, but the exact influence of initial imperfections depending on these properties was not determined. Plates with different geometric and material properties can be classified by defining plate slenderness λ. The plate slenderness is a parameter that ties together plate strength, stiffness and geometry and is defined as:

$$\lambda = \sqrt{\frac{f_{ult}}{\sigma_{cr}}}$$

(4.1.1)

where f_{ult} is the strength of a perfect plate under uniform compressive load (depending on the considered failure criterion) and σ_{cr} is the critical buckling load of a perfect plate. When $\lambda = 1$, this means that the compressive and critical loads coincide. The slenderness relates to a plate without any imperfections and can be derived analytically, meaning that no nonlinear finite element analysis is necessary.

When the failure criterion is defined, the fail load of a plate with initial imperfection f_{fail} can be determined from finite element analysis. The failure load f_{fail} will be lower than the compressive strength f_{ult} because in case of an imperfect plate, next to axial load, a plate is loaded by bending moments that result from the eccentricities cause by the transverse deflections of the plate, which increase as the applied axial load increases.

With known buckling strength a reduction factor ρ can be derived as:

$$\rho = \frac{f_{fail}}{f_{ult}}$$

(4.1.2)

Once reduction factors are derived it is possible to construct buckling curves similar to the buckling curves derived for steel. The horizontal axis will correspond to plate slenderness and the vertical axis – to reduction factor.

4.2 FAILURE CRITERIA

As said, the compressive strength relates to the chosen failure criterion. Commonly, there are a few failure criteria that are used in the analysis of the laminate strength.

Due to their simplicity the maximum stress and maximum strain theories are often used. For a failure to occur according to the maximum stress theory one of the conditions has to be met:

$$f_{1c} < \sigma_1 < f_{1t};$$

$$f_{2c} < \sigma_2 < f_{2t};$$

$$-f_{12} < \tau_{12} < f_{12}$$

The maximum strain criterion reads as:

$$\varepsilon_{1c} < \varepsilon_1' < \varepsilon_{1t};$$

$$\varepsilon_{2c} < \varepsilon_2' < \varepsilon_{2t};$$

$$-\gamma_{12} < \gamma_{12}' < \gamma_{12}$$

The maximum stress and maximum strain theories yield different results because the strains in a ply coordinate system include the Poisson's ratio. These results in general are not very accurate and do not take interaction into account. One of the examples of the interaction-based theories is Tsai-Hill, which is included in CUR96:

$$\left[\frac{\sigma_1}{f_1}\right]^2 - \left[\frac{\sigma_1 \sigma_2}{f_1^2}\right] + \left[\frac{\sigma_2}{f_2}\right]^2 + \left[\frac{\tau_{12}}{f_{12}}\right]^2 < 1$$

where

$$f_1 = f_{1t} \text{ if } \sigma_1 \geq 0 \text{ (tension); } f_1 = f_{1c} \text{ if } \sigma_1 < 0 \text{ (compression);}$$

$$f_2 = f_{2t} \text{ if } \sigma_2 \geq 0; f_2 = f_{2c} \text{ if } \sigma_2 < 0$$

This failure theory does not distinguish between the compressive and tensile strengths, and it will not indicate the mode of failure unlike the maximum stress / strain theories. Other ply failure theories based on stress interactions such as Tsai-Wu and Puck are allowed by CUR96 as well.

The mentioned above failure criteria are applicable to a ply. However, a first ply failure is usually a conservative criterion, since a laminate consists of multiple plies with fibres in all direction and a failure of one ply does not necessary mean a failure of the whole laminate. To have a more realistic prediction of a laminate strength a progressive failure analysis has to be performed. Progressive failure analysis involves a gradual reduction of stiffness properties of a laminate. When one of the plies is considered failed according to one of the failure theories, its stiffness is fully or partially reduced, then the laminate is loaded again up to the failure of the next ply [28]. This process is repeated until no plies are left. Alternatively, CUR96 gives a simple failure strain limit for a laminate: 1.2% for longitudinal tension and compression and 1.6% for shear

In this study, the following four criteria will be considered to describe the influence of initial imperfection on the structural behaviour of a plate. In paragraphs 4.4 to 4.7 these failure criteria will be considered in more detail.

CRITICAL LOAD

Critical load is one of the failure criterion that is currently used in design codes. It was shown that for an imperfect plate the determination of the critical buckling load is a difficult task, especially for larger amplitudes of imperfections, since bifurcation buckling does not take place. However, there are methods to approximate the buckling loads.

In the paper by Czapski and Kubiak [13] two ways of approximating critical buckling load of imperfect plates were briefly described. More detailed descriptions of various methods are presented in "Selected Problems of Determining Critical Loads in Structures with Stable Post-Critical Behaviour" by the same authors [26]. Out of all described methods, the $P - w^2$ method was chosen as the most suitable one to attempt to approximate the buckling loads of the imperfect plates.
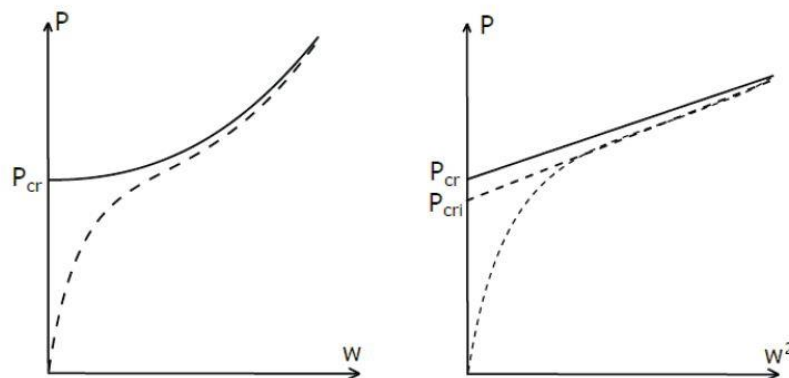
Figure 4.2.1 Determination of the critical load with P-w² method [26] p.84

In $P - w^2$ method square root of deflection plotted versus the load. In this case the postbuckling part of the curve can be approximated with a straight line as shown in figure 4.2.1. The intersection of this line with the load axis is considered as the critical load. The result obtained with this method depends on which region of the curve is considered and is only an approximation.

HASHIN PROGRESSIVE FAILURE

Hashin progressive failure analysis is suitable for multiaxial stress situations and considers four failure mechanisms: fibre failure in tension and compression and matrix failure in tension and compression. The onset of damage takes place when one of these criteria is reached:

- fibre rupture in tension ($\sigma_{11} \geq 0$);

$$F_f^t = \left(\frac{\sigma_{11}}{f_{1t}}\right)^2 + \left(\frac{\tau_{12}}{f_{12}}\right)^2$$

(4.1.3)

- fibre buckling and kinking in compression ($\sigma_{11} < 0$);

$$F_f^c = \left(\frac{\sigma_{11}}{f_{1c}}\right)^2$$

(4.1.4)

- matrix cracking under transverse tension and shearing ($\sigma_{22} \geq 0$);

$$F_m^t = \left(\frac{\sigma_{22}}{f_{2t}}\right)^2 + \left(\frac{\tau_{12}}{f_{12}}\right)^2$$

(4.1.5)

- matrix crushing under transverse compression and shearing ($\sigma_{22} < 0$);

$$F_m^c = \left(\frac{\sigma_{22}}{2f_{12}}\right)^2 + \left[\left(\frac{f_{2c}}{2f_{12}}\right)^2 - 1\right] \cdot \frac{\sigma_{22}}{f_{2c}} + \left(\frac{\tau_{12}}{f_{12}}\right)^2$$

(4.1.6)

Abaqus finite element analysis software offers a progressive damage model for fibre reinforced composites. Damage is defined by the degradation of material stiffness. The initiation of damage corresponds to the Hashin's failure modes. Once one of the four criteria is reached in one of the plies in an certain element, the software will reduce the stiffness of the material until the ply in the element is failed. As load increases more plies in more elements will fail until the load cannot be increased any longer due to the severity of damage in a laminate. The rate at which the material properties are reduced depends on damage evolution parameters input [29]. The maximum load that can be applied to the plate will be considered to be the failure load.

Hashin damage model does not consider delamination failure mode, it is therefore will be important to investigate whether or not the onset of delamination occurs before or after one of the Hashin failure modes.

SERVICEABILITY LIMIT STATE STRAIN

SLS ply strain limit refers to the strain at which the cracks appear in the resin of the laminate. The formation of cracks in resin by itself does not necessary lead to a failure in a laminate but the onset of cracks can eventually lead to other failure modes and the stiffness reduction of the material. Depending on the severity of cracks, this failure mechanism can lead to seepage of fluids through the laminate or fracture. [27].

The strain limit for the matrix cracking in tension is 0.2%. This criterion is assumed to be satisfied when the strain limit is reached in one of the plies, in other words this is a first ply failure criterion.

DELAMINATION

Delamination is a failure mode of composite materials which is characterized by separation of layers in the laminate. Once delaminations are initiated they start to grow gradually. The onset of delamination is difficult to predict, but it is known that there will be no initiation of delamination before the cracks are formed in resin [27].

CUR96 provides the interlaminar shear stress limits for three kinds of matrix: polyester, vinylester and epoxy. Once this limit is reached, cracks between plies initiate. The material that is considered in this research is polyester and the interlaminar stress strength is given as $f_{ILSS} = 20 \, N/mm^2$.

Harstype van het GVK-laminaat	Interlaminaire afschuifsterkte ILSS [N/mm^2]
Polyesterhars	20
Vinylesterhars	25
Epoxyhars	30

Table 4.1 Interlaminar shear stress limits [2] p. 49

When the interlaminar shear stress value of $20\ N/mm^2$ is reached anywhere in a laminate, the failure criterion is fulfilled.

4.3 MODEL

To investigate the influence of initial out of plane deformations the plate of layup I ($E_X/E_y = 1.27$), length $L = 900\ mm$, width $B = 300\ mm$ is used. To obtain various plate slenderness values only the plate thickness is changed.

The shape of initial imperfection is the shape of the first buckling mode. Two imperfection amplitudes were considered: $B/1000$ and $B/125$. $B/1000$ is an arbitrary value of an imperfection magnitude, $B/125$ is the limiting value suggested in the design code CUR96 in case no information on initial imperfection tolerances is available.

The boundary conditions were modified; the linear buckling analysis results stay almost the same as in case of original boundary conditions reported in 3.1.1, but for the geometrically and materially nonlinear analysis the modified boundary conditions reduce the peak values that were found in the model with the original boundaries. The detailed description is given in annex D.
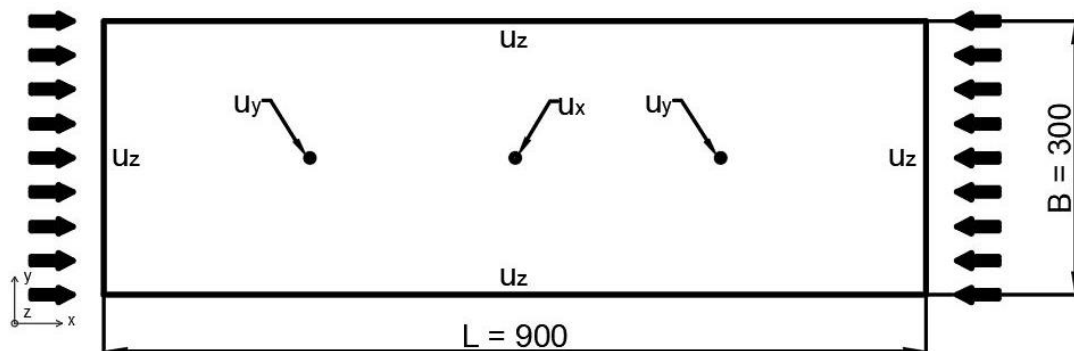
Figure 4.3.1 Plate geometry, boundary and loading conditions for failure analysis

Figure 4.3.1 shows the boundary and loading conditions used for plate failure analysis.

Boundary conditions:

- along all edges $u_z = 0$
- at $x = 450; y = 150$ (midpoint of the plate) $u_x = 0$
- at $x = 225; y = 150$ and $x = 675; y = 150$ $u_y = 0$

Initial displacement was applied in x direction at the plate edges $x = 0$ and $x = 900$.

The element type used is S4R (uses thick shell theory as the shell thickness increases and become discrete Kirchhoff thin shell elements as the thickness decreases; the transverse shear deformation

becomes very small as the shell thickness decreases [29]), with size of $18.75 \times 19.57 \ mm$ (16 elements in y and 46 elements in x direction of the plate).

The determination of the ply properties for damage initiation is given in 3.1.1.

The values for damage evolution should be determined experimentally but due to absence of test data for E-glass polyester laminates, the values for fracture energies based on data for E-glass epoxy laminate are used [30]:

- longitudinal tensile: 12
- longitudinal compressive: 12
- transverse tensile: 1
- transverse compressive: 1

A sensitivity study of transverse tensile and compressive energies influence on fail load showed that these parameters do not have a large effect. More details can be found in annex E.

4.4 CRITICAL LOAD CRITERION

It was decided to use the $P - w^2$ method to attempt to approximate the buckling loads of the imperfect plates $f_{fail,crit}$. The more or less linear postbuckling region of the force - deflection^2 graph was approximated with linear trendline. Setting $x = 0$, the y-coordinate was obtained from the equation of the trendline, which according to the method's description is the critical load.

Figures 4.4.1 and 4.4.2 show the application of P-w2 method to the plates with imperfection $B/1000$ and $B/125$.
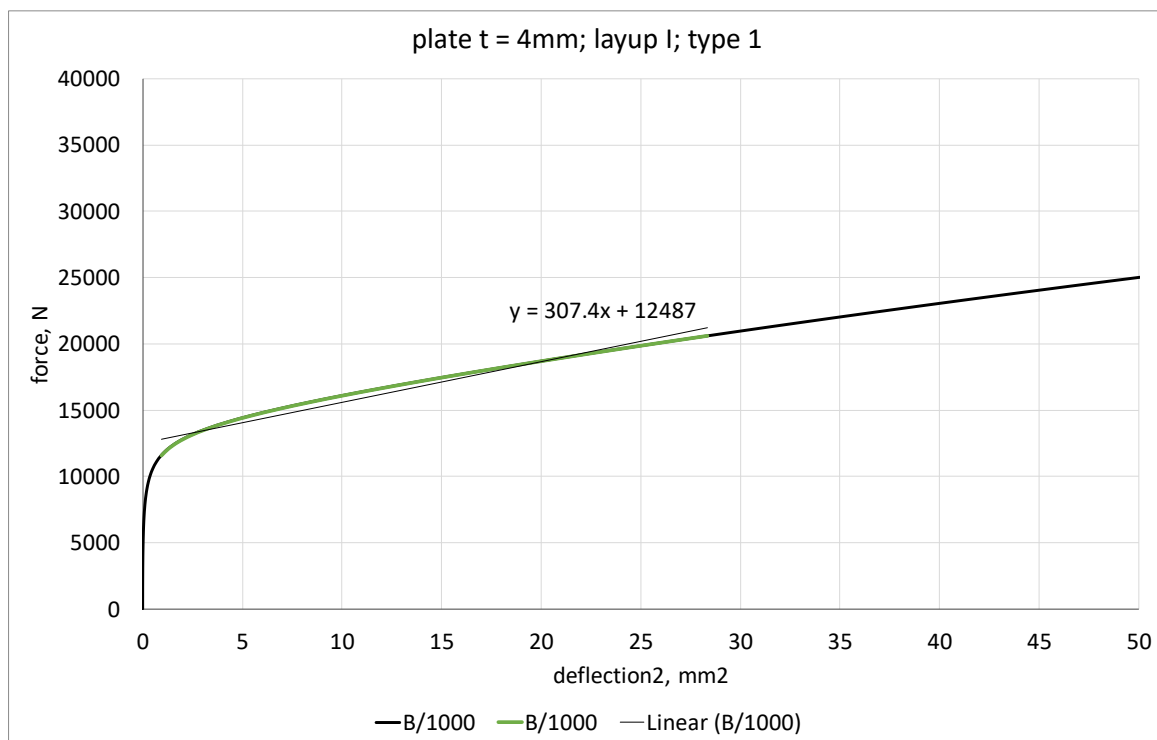
Figure 4.4.1 Determination of the critical load of the imperfect plate B/1000
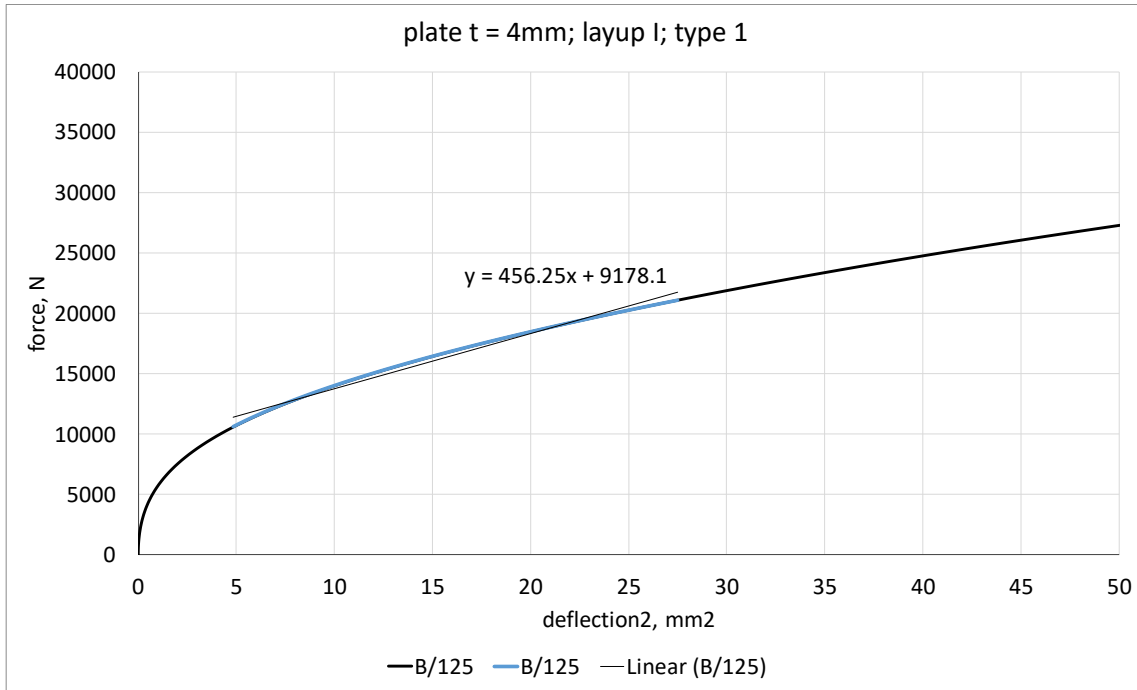
Figure 4.4.2 Determination of the critical load of the imperfect plate B/125

	f_fail,crit, N	reduction, %
B/1000	12487	15.0
B/125	9178.1	37.5

Table 4.2 Approximated fail loads $f_{fail,crit}$

Table 4.2 shows the obtained forces for the plate with imperfections. As it can be seen, the reduction of the buckling force is 37.5% for $B/125$, which is significant. It has to be mentioned, that it was very difficult to decide which part of the curve to approximate, especially in case of a larger amplitude of imperfection. This observation brings up a question about the applicability and physical meaning of the P-w^2 method.

When the imperfection has a small amplitude ($> B/1000$) or when the imperfection itself is small (for example, a wrinkle imperfection considered in 3.1.3) then the two regions in load – deflection diagram can be distinguished:

- the prebuckling region when the growth of out of plane deformations is slow
- the postbuckling region when the growth of out of plane deformations is a lot faster than in the prebuckling region;

in between these two regions the load – deflection diagram has a rounded over part ("knee") instead of a bifurcation point. In this case applying P-w^2 method makes sense.

For large imperfections that coincide with the shape of plate's buckling mode, it was shown that no clear change in growth of deformations can be seen for larger imperfection amplitudes, e.g. the behaviour of an imperfect plate is very different from that of a perfect plate. For that reason, it is concluded that a different failure criterion should be applied to quantify the influence of initial imperfections considered in this study.

4.5 HASHIN PROGRESSIVE FAILURE CRITERION

4.5.1 GEOMETRICALLY LINEAR PROGRESSIVE FAILURE ANALYSIS

The ultimate compressive load ($f_{ult,Hashin}$) of a flat laminate was determined by performing geometrically linear (no initial out of plane deformations present) and materially nonlinear analysis (Abaqus Hashin progressive damage model). A perfectly flat plate loaded by uniform axial compression was modelled, no imperfection was included to avoid buckling. The typical load – end shortening curve is shown in figure 4.5.1.

As it can be seen, the curve has three peak values at 218.6; 229.09 and 208.56 N/mm^2, which represent the ply-by-ply failure loads. These results were checked using elamX[2] software.
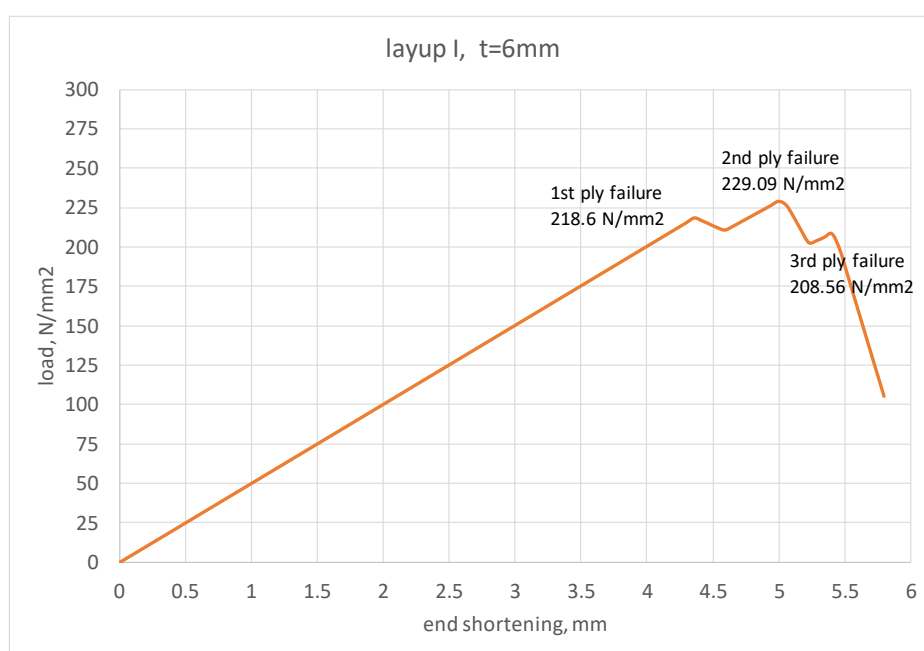
Figure 4.5.1 Load – end shortening for Hashin damage criterion curve of a perfectly flat plate

First, the first ply failure and failure mode were determined, after which the stiffness of the failed ply was reduced and the load that causes the second and the third ply failure respectively is found. Since the first and second plies (90º and ±45º) fail due to matrix compressive failure, the transverse modulus of elasticity (E_y) of a ply was reduced to zero, the rest of the properties were left unchanged.

The table below shows the failure loads obtained from FEA and CLT, which are in good agreement with each other:

	FEA, N/mm2	CLT, N/mm2
1st ply 90º	218.6	218.62
2nd ply ±45º	229.09	229.72
last ply 0º	208.56	208.98

Table 4.3 Comparison of failure loads obtained from FEA and CLT

After the initial first ply (all the 90° plies) failure at 218.6 MPa, the remaining ±45° and 0° can still be loaded up to 229.09 MPa. After the ±45° plies fail, the remaining 0° plies can only withstand 208.56 MPa. Therefore, the maximum compressive load that can be applied to the laminate is 229.09 MPa. Almost the same ultimate load was determined for all plate thicknesses, in reality this is not necessarily the case.

The longitudinal strain at the maximum load (corresponding to the second ply failure) has value of $1.11 \cdot 10^{-2}$. However, this value relates to the reduced stiffness properties of the laminate, since the 90° plies have already failed. Relating the ultimate load to the initial stiffness of the material, the strain in the laminate is:

$$\varepsilon_x = \frac{\sigma_{ult}}{E_{x,initial}} = 1.02 \cdot 10^{-2}$$

which is a lower value than 1.2% given in CUR96 for laminates with have at least 12.5% fibres in each direction (0°, 45°, -45° and 90°). Since the 1.2% strain limit is based on test data it is concluded that the result obtained from FEA is conservative.

4.5.2 GEOMETRICALLY NONLINEAR PROGRESSIVE FAILURE ANALYSIS

The geometrically nonlinear progressive damage analysis was performed to determine the ultimate load of the plate with initial imperfections due to buckling ($f_{fail,Hashin}$).
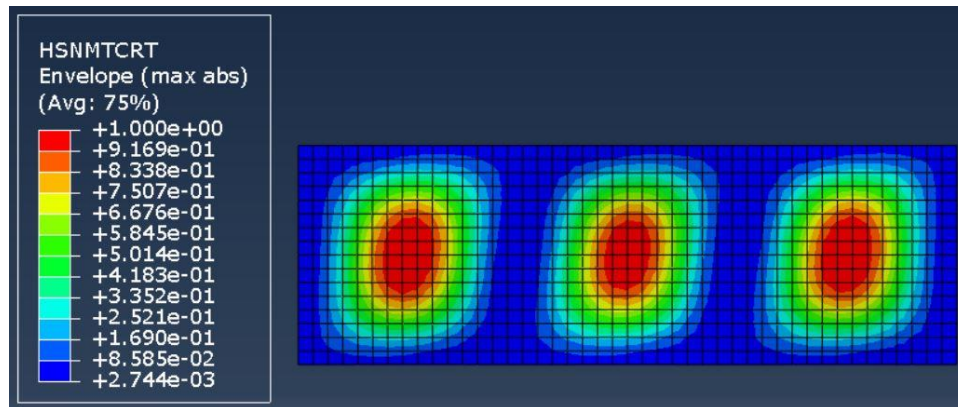
Figure 4.5.1 Damage initiation matrix tension in a plate with initial imperfection

Figure 4.5.1 depicts the damage initiation in matrix due to transverse tension. The areas in which damage initiates are coloured red. Matrix cracking due to transverse tension is described by equation 4.1.5:

$$F_m^t = \left(\frac{\sigma_{22}}{f_{2t}}\right)^2 + \left(\frac{\tau_{12}}{f_{12}}\right)^2$$

When damage is initiated it means that:

$$F_m^t = 1$$

The corresponding transverse (σ_{22}) and shear (τ_{12}) stresses are shown in figures 4.5.2 and 4.5.3.
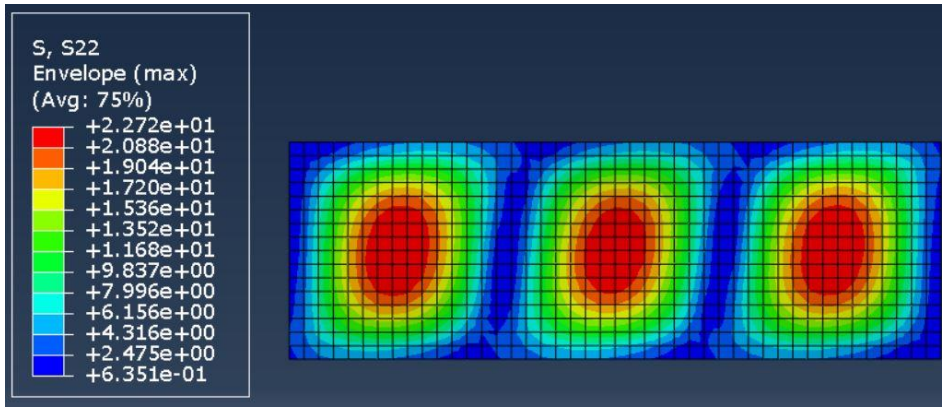
Figure 4.5.2 Transverse tensile stresses in the plate with initial imperfection at damage initiation
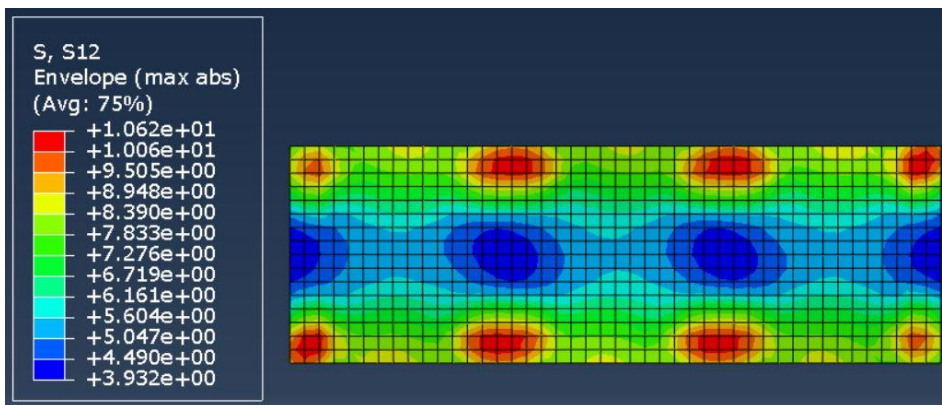
Figure 4.5.3 Shear stresses in the plate with initial imperfection at damage initiation

The stress values from figures 4.5.2 and 4.5.3 in the areas were damage is initiated are:

$$\sigma_{22} = 22.72 \ N/mm^2$$

$$\tau_{12} = 5.60 \ N/mm^2$$

Substituting these values and the ply strength properties given in 3.1.1 to equation for matrix cracking initiation:

$$F_m^t = \left(\frac{22.72}{22.8}\right)^2 + \left(\frac{5.6}{64.6}\right)^2 = 1.0$$

From this point on the software will start reducing the stiffness properties of the laminate. Figure 4.5.4 shows the comparison of materially linear and materially nonlinear behaviour of a plate:
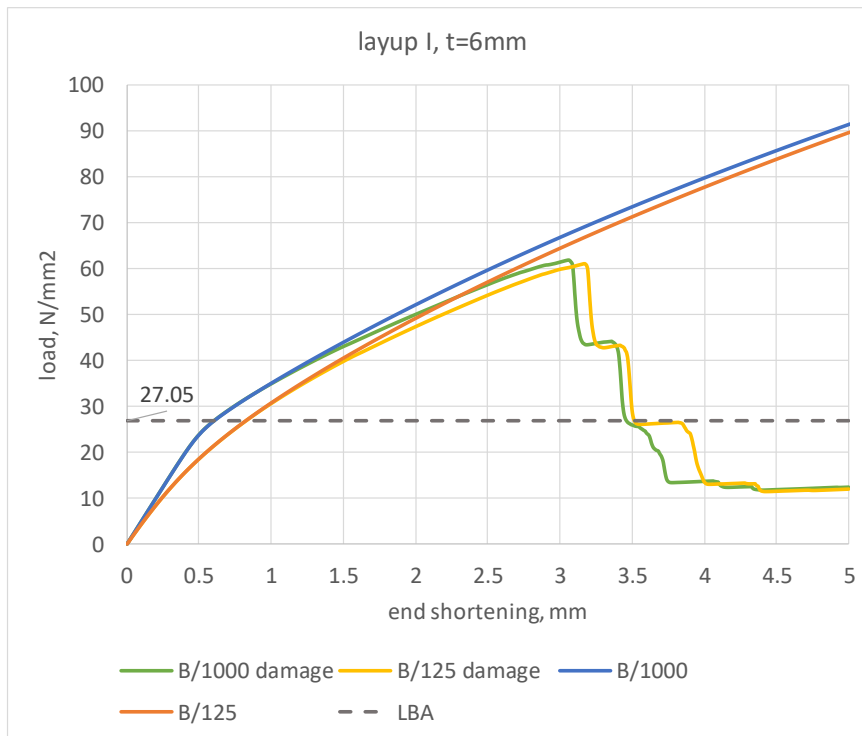
Figure 4.5.4 Materially linear and nonlinear behaviour of a plate

The green and yellow curves correspond to the progressive failure analysis of a plate with thickness $t = 6\ mm$ and two magnitudes of imperfection $B/1000$ and $B/125$, the blue and orange curves are based on the materially linear analysis. The horizontal dashed line represents the critical load of a perfect plate.

From this plot it can be seen that the stiffness reduction for the plate with initial out of plane deformation begins at the load level around $\sim 30 - 35\ N/mm^2$ and from this point the curves associated with materially nonlinear analysis start to deviate from the curves that represent materially linear analysis, which means stiffness reduction takes place.
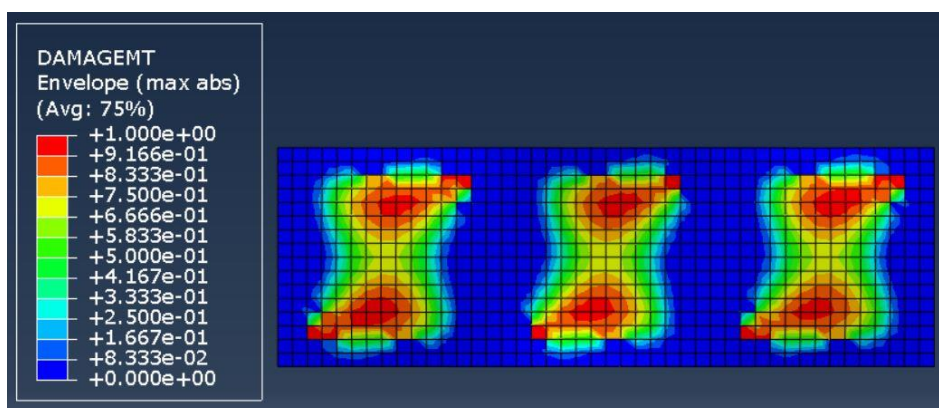
Figure 4.5.5 Damaged elements occurrence in the plate

Eventually the parameters will be reduced to a point that the element is considered damaged (figure 4.5.5), after that the number of damaged elements will be growing until the load can no longer be increased. The maximum load that a plate is able to carry is considered the failure load. Figure 4.5.6 shows damage in the plate at failure.
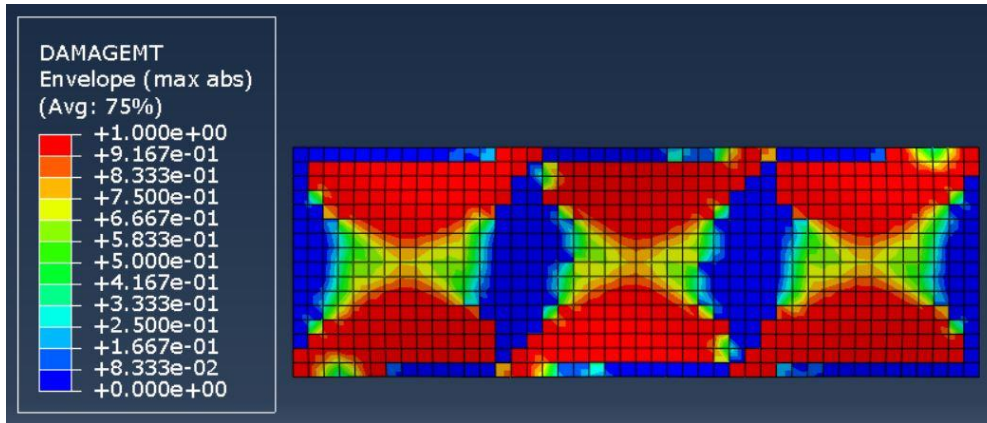
Figure 4.5.6 Damaged elements in the plate at failure

Plots in figures 4.5.7 and 4.5.8 show load – end shortening of a plate $t = 6\ mm$ with imperfection amplitude $B/1000$ and $B/125$ and damage initiation / evolution values.
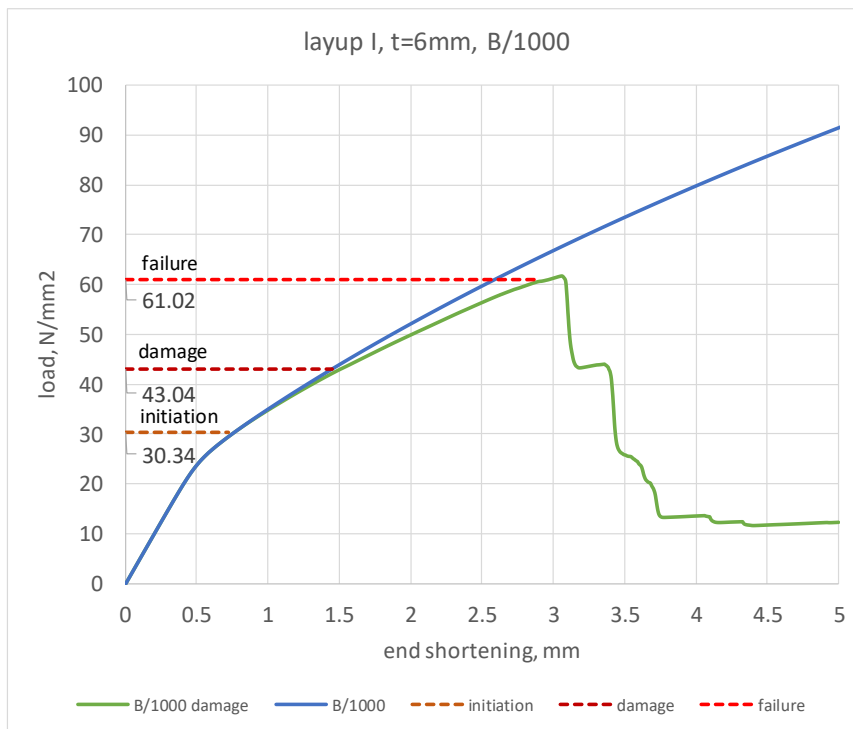
Figure 4.5.7 Progressive failure analysis of a plate t = 6 mm with imperfection B/1000

In case of $B/1000$ before damage initiation there is a slope change in the graph which occurs around the critical load value of a perfect plate ($27.05\ N/mm^2$) and failure of the plate occurs at the load level almost two times higher then the critical load. For $B/125$ the slope is not a straight line but it is difficult to determine where the change takes place because due to a large amplitude of initial imperfection plate very gradually bends into the shape prescribed by the initial imperfection.
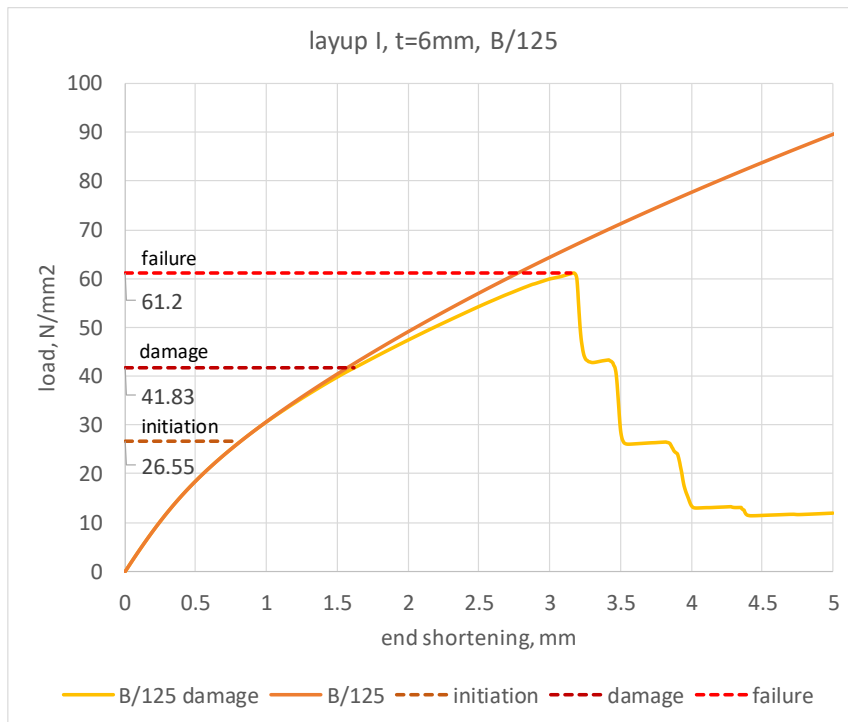
Figure 4.5.8 Progressive failure analysis of a plate t = 6 mm with imperfection B/125

It is seen that the damage initiation and occurrence (denoted by horizontal dashed lines named 'initiation' and 'damage') take place at slightly lower load levels for the plate with imperfection amplitude $B/125$ compared to the plate with imperfection $B/1000$. The failure load however is not influenced by imperfection magnitude and is the same in both cases.

Figures 4.5.9 and 4.5.10 show behaviour of a thicker plate ($t = 24\ mm$).
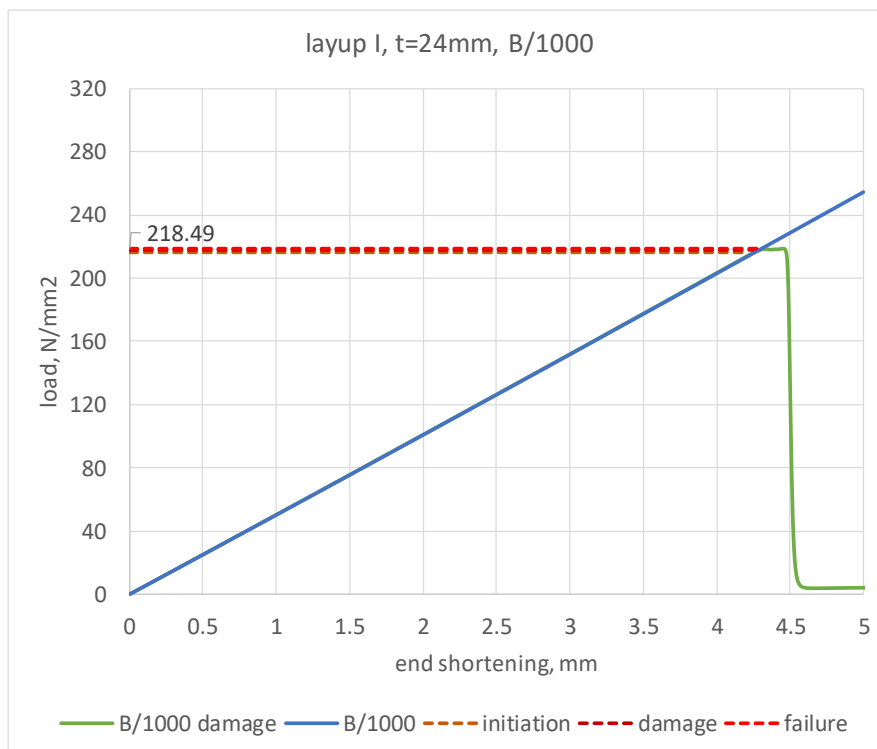
Figure 4.5.9 Progressive failure analysis of a plate t = 24 mm with imperfection B/1000
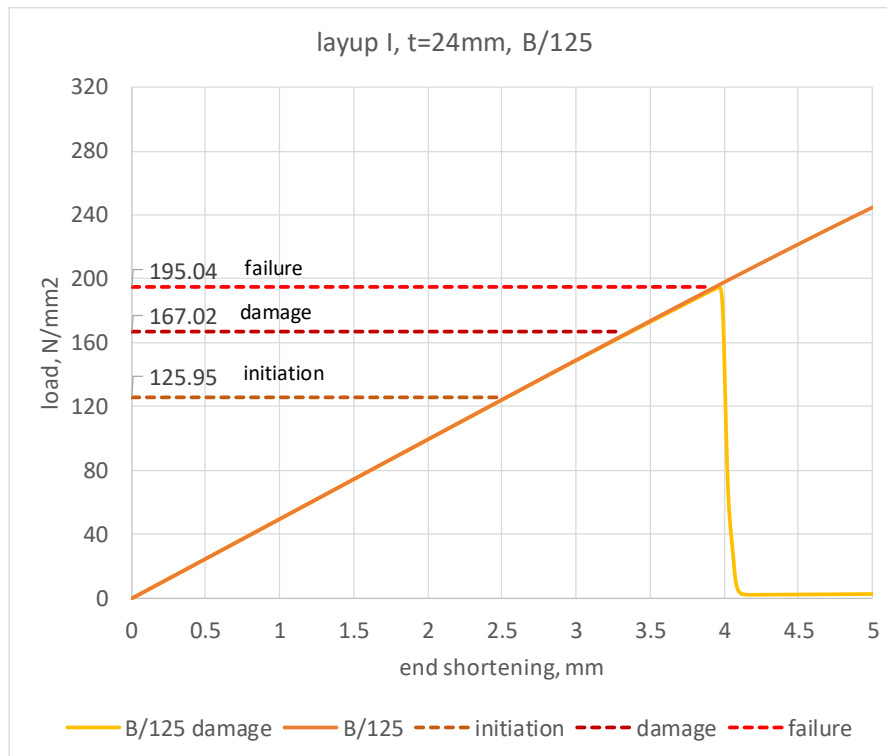
Figure 4.5.10 Progressive failure analysis of a plate t = 24 mm with imperfection B/125

In case of a thicker plate, there is a noticeable difference in behaviour depending on the amplitude of the applied initial imperfection. Not only damage initiation and evolution occur at a noticeably lower load levels for imperfection magnitude $B/125$, but also the failure load is ~11% lower compared to imperfection $B/1000$. It should also be noted that for $B/1000$ the damage initiation, occurrence and failure loads are much closer together than in case of $B/125$. In the plate with imperfection $B/1000$ damage is due to matrix crushing, while in the plate with imperfection $B/125$ the failure mode is matrix cracking(as in case of plate $t = 16\ mm$). The critical load in case of a plate with thickness $t = 24\ mm$ is above the failure load ($\sigma_{cr} = 380.19\ N/mm^2$ and therefore the curves based on linearly and materially nonlinear analysis (green curve for $B/1000$ and yellow curve $B/125$) almost fully coincide with the curves based on materially linear analysis and the slight deviation is only seen after damage initiated in the plate with imperfection amplitude $B/125$.

From this study it can be concluded that there are two effects that have influence on the structural behaviour of plates: additional bending moment due to initial imperfections that changes the apparent stiffness of the material and the actual change in stiffness that is caused by material degradation. In case of thinner plates, the amplitude of initial out of plane deformation has a little effect on damage and failure load, in case of thicker plate the effect increases and there is a significant difference for plate behaviour between imperfection amplitude $B/1000$ and $B/125$.

4.5.3 BUCKLING CURVES

The buckling curves for Hashin progressive failure are constructed by varying the thickness of a plate of $300\ \times 900\ mm$ to quantify the effect of initial imperfections depending on the plate slenderness. Six different plate slenderness values corresponding to thicknesses $4, 6, 8, 12, 16, 24$ and $54\ mm$ and two magnitudes of initial imperfections are considered - $B/1000 = 0.3\ mm$ and $B/125 = 2.4\ mm$.

Table 4.4 lists all the loads found for the plates of various thicknesses of a layup I. Figure 4.5.11 shows the derived buckling curves.

t, mm	σcr, N/mm2	fult, N/mm2	λ	ffail, N/mm2 B/1000	ffail, N/mm2 B/125	ρ Hashin B/1000	ρ Hashin B/125	ρ, linear buckling
4	12.13	229.17	4.35	45.53	45.44	0.20	0.20	0.05
6	27.05	229.09	2.91	61.81	61.20	0.27	0.27	0.12
8	47.59	229.33	2.20	78.15	74.36	0.34	0.32	0.21
12	104.53	229.33	1.48	115.14	106.97	0.50	0.47	0.46
16	180.67	229.33	1.13	168.12	141.02	0.73	0.61	0.79
24	380.19	228.00	0.77	218.49	195.04	0.96	0.86	1.67
54	1381.7	229.33	0.41	220.5	214.84	0.96	0.94	

Table 4.4 Plate slenderness and load reduction factors for Hashin damage criterion
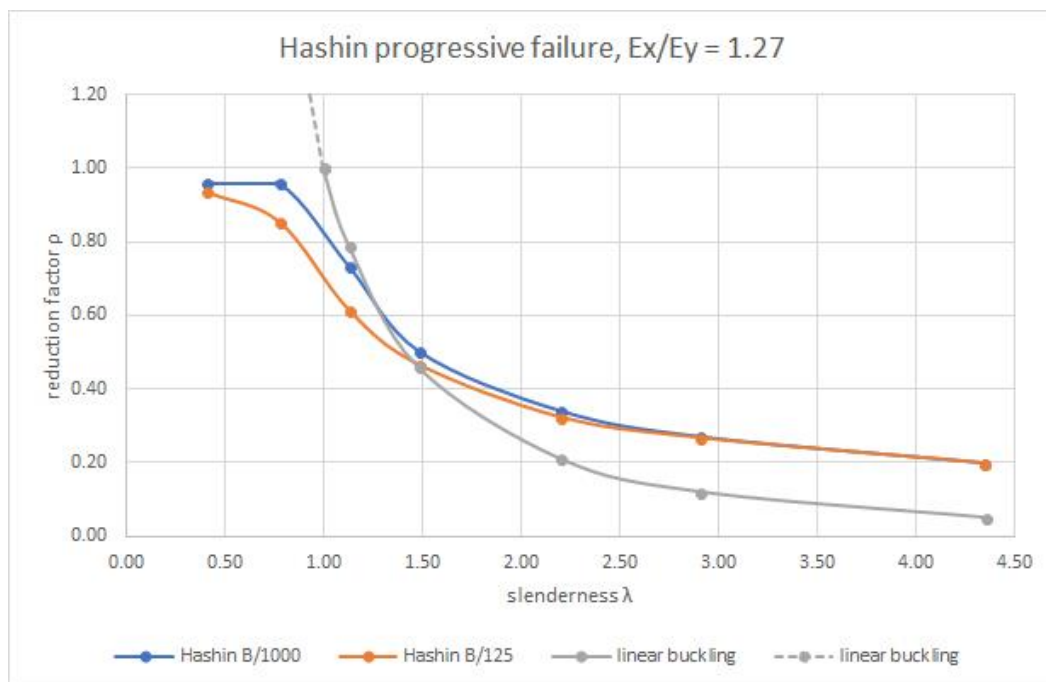
Figure 4.5.11 Buckling curves for Hashin progressive failure criterion for Ex/Ey = 1.27

In the figure above the blue curve corresponds to the plate with an initial imperfection of amplitude $B/1000$ and the orange curve to the plate with an initial imperfection of $B/125$. The grey curve represents the failure mode corresponding to buckling of a flat plate without initial imperfections. The dashed part of the grey curve relates to reduction factors > 1 (in fact it is not a reduction factor anymore), it means that for ideal plates with $\lambda > 1$ the compressive failure will occur sooner than buckling and so no reduction due to buckling is necessary ($\rho = 1$).

For thin plates ($\lambda > 2.5$) the curves representing different values of imperfection amplitude almost coincide, which means that the failure load is independent of the magnitude of initial out of plane deformation and the reduction factor has (almost) the same value for imperfection $B/1000$ and $B/125$.

For thicker plates ($\lambda \leq 2.5$) the effect of imperfection amplitude becomes more pronounced as slenderness becomes smaller, i.e. the larger the thickness becomes the larger is the difference between the reduction for imperfection amplitude $B/1000$ and $B/125$. For example, a plate of

layup I and $\lambda = 1.13$ there is 16% difference between the failure load associated with imperfection $B/1000$ and $B/125$.

However, for $\lambda = 0.41$ the difference between reduction factor for $B/1000$ and $B/125$ becomes smaller again. The failure mode in case of plate $t = 54\ mm$ for both amplitudes of imperfection and in case of plate $t = 24\ mm$ with imperfection $B/1000$ is matrix crushing in compression and shearing. It can be seen from the buckling curves that in these three cases the reduction factor is close to 1 ($0.94 - 0.96$), therefore, it can be concluded that for plate slenderness $\lambda = 0.41$ with imperfection up to $B/125$ and for slenderness $\lambda = 0.77$ with imperfection up to $B/1000$ the effect of initial imperfection is insignificant and will not cause plate to buckle but fail in compression.

Comparing the buckling curves derived for plates with imperfection (blue and orange, figure 4.5.11) to buckling curve based on critical load criterion for flat plates (grey, figure 4.5.11) it can be seen that the plates with slenderness $\lambda > 1.50$ have load bearing capacity above the theoretical critical load. For example, for layer I for a plate with $\lambda = 2.20$ the failure load is 39% higher for $B/1000$ and 36% for $B/125$ than the critical load. While in case of $\lambda = 1.13$ the critical load is higher than the failure load by 7% for $B/1000$ and 22% for $B/125$.

Therefore, for plates with slenderness $\lambda > 1.50$ and imperfection amplitudes up to $B/125$ the critical load criterion (related to ideal plates, disregarding initial imperfections) would give conservative results. The Hashin progressive failure buckling curves for plates with slenderness $\lambda < 1.50$ are below the critical load buckling curve, so, for imperfect plates with $\lambda < 1.50$ the critical load criterion overestimates the plate buckling strength. At slenderness value $\lambda = 1$ this would mean that the critical load would be 30% higher for a plate with imperfection $B/1000$ and 18% for $B/125$ than the plate failure load.

4.5.4 VALIDATION OF SLENDERNESS

The buckling curves in 4.5.3 were derived for various slenderness values based on different plate thickness. As a check of the relation between plate slenderness and reduction factor two plates of different dimensions were modelled:

- 400×600; (AR = 1.5) which leads to initial imperfection amplitudes of $B/1000 = 0.4\ mm$ and $B/125 = 3.2\ mm$ and plate slenderness $\lambda = 2.41$
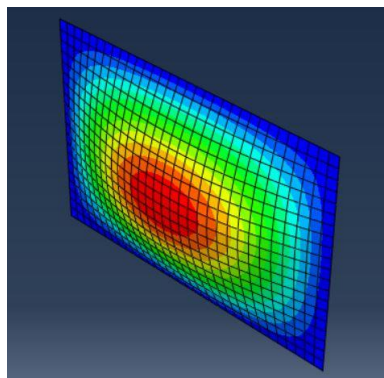
Figure 4.5.12 First buckling mode of the plate λ = 2.41

- 700 × 1600; (AR = 2.29) which leads to initial imperfection amplitudes of $B/1000 = 0.7\ mm$ and $B/125 = 5.6\ mm$ and plate slenderness $\lambda = 1.07$
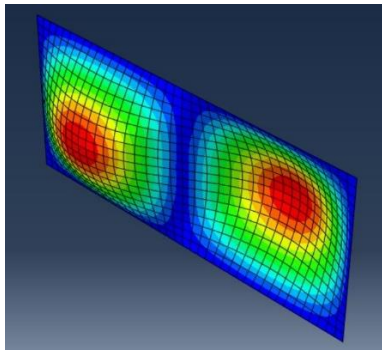
Figure 4.5.13 First buckling mode of the plate λ = 1.07

Four additional points were obtained and plotted over the buckling curve. Figure 4.5.14 shows that the reduction factors for plates with slenderness $\lambda = 2.41$ and $\lambda = 1.07$ are in line with the derived buckling curves.
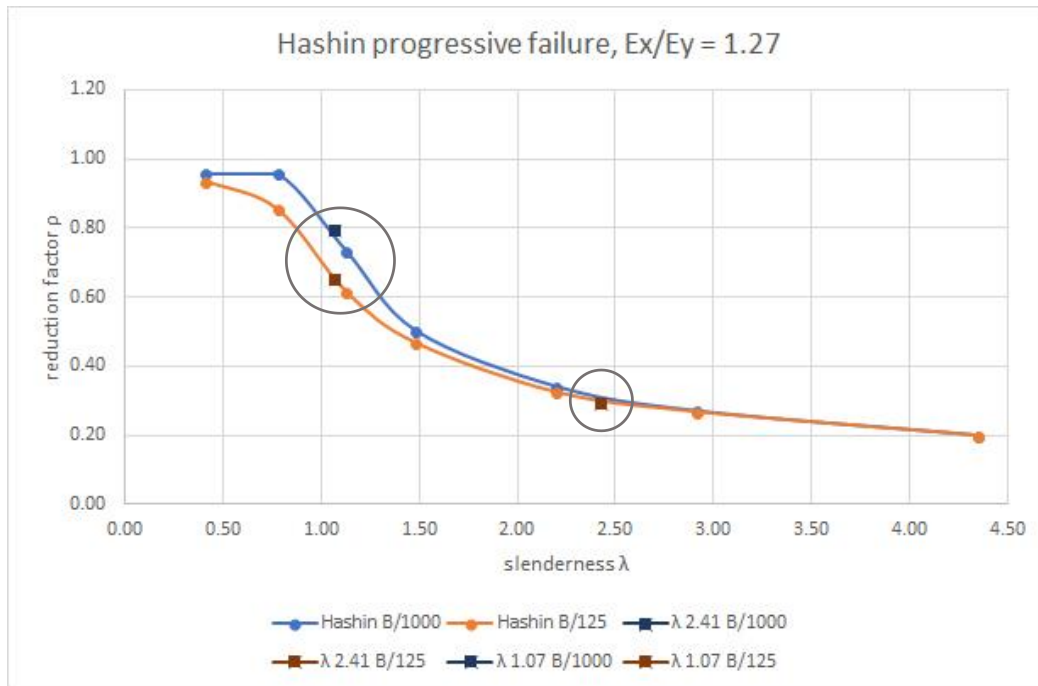
Figure 4.5.14 Slenderness validation for buckling curves for Hashin progressive failure criterion

4.6 SERVICEABILITY LIMIT STATE STRAINS CRITERION

4.6.1 GEOMETRICALLY LINEAR MATERIALLY NONLINEAR ANALYSIS

For this criterion both longitudinal and transverse strains are checked. The ultimate compressive load $(f_{ult,SLSstrain})$ is obtained by checking the positive values of longitudinal and transverse strains. Once the strain value reaches $\sim 0.2 \cdot 10^{-2}$, the corresponding load level is registered.

The limit is reached both for longitudinal (90° ply) and transverse (0°) strain at the same load level of approximately 137.0 N/mm^2 (the exact value is given for each plate in 4.6.2 and 4.6.3 in tables 4.5 and 4.6).

The obtained values were checked with elamX[2] software (see figure 4.6.1). As seen the values of $0.2 \cdot 10^{-2}$ are obtained simultaneously for longitudinal (ε_{1t}) and transverse (ε_{2t}) strains in 90° and 0° plies, respectively. Dividing the applied distributed load by the laminate thickness the compressive stress is obtained:

$$f_{ult} = 137.58 \ N/mm^2$$

which is very close to the values found with finite element analysis.

	$nm_{mech.}$	+	$nm_{hygrotherm.}$	=		ABD-Matrix					*	$\varepsilon\kappa$	
n_x =	-825.48		0.0		147847.3	38060.0	0.0	-0.0	-0.0	0.0		-0.006098	= ε_x
n_y =	0.0		0.0		38060.0	116068.3	0.0	-0.0	-0.0	0.0		0.002	= ε_y
n_{xy} =	0.0		0.0		0.0	0.0	38099.3	0.0	0.0	-0.0		-0.0	= γ_{xy}
m_x =	0.0	+	0.0	=	-0.0	-0.0	0.0	494372.4	120551.8	17160.7	*	-0.0	= κ_x
m_y =	0.0		0.0		-0.0	-0.0	0.0	120551.8	284630.8	17160.7		0.0	= κ_y
m_{xy} =	0.0		0.0		0.0	0.0	-0.0	17160.7	17160.7	120669.5		0.0	= κ_{xy}

No.	Name	Angle	$z_{m,i}$	z_i	$\varepsilon_\parallel$	$\varepsilon_\perp$	$\gamma_{\parallel\perp}$
1	0	0.0	2.85	3.0	-0.006098	0.002	0.0
				2.7	-0.006098	0.002	0.0
2	0	0.0	2.55	2.7	-0.006098	0.002	0.0
				2.4	-0.006098	0.002	0.0
3	45	45.0	2.25	2.4	-0.002049	-0.002049	0.008098
				2.1	-0.002049	-0.002049	0.008098
4	45	45.0	1.95	2.1	-0.002049	-0.002049	0.008098
				1.8	-0.002049	-0.002049	0.008098
5	-45	-45.0	1.65	1.8	-0.002049	-0.002049	-0.008098
				1.5	-0.002049	-0.002049	-0.008098
6	-45	-45.0	1.35	1.5	-0.002049	-0.002049	-0.008098
				1.2	-0.002049	-0.002049	-0.008098
7	90	90.0	1.05	1.2	0.002	-0.006098	0.0
				0.9	0.002	-0.006098	0.0
8	90	90.0	0.75	0.9	0.002	-0.006098	0.0
				0.6	0.002	-0.006098	0.0
9	0	0.0	0.45	0.6	-0.006098	0.002	0.0
				0.3	-0.006098	0.002	-0.0
10	0	0.0	0.15	0.3	-0.006098	0.002	-0.0
				-0.0	-0.006098	0.002	-0.0

Figure 4.6.1 First ply failure determination for ideal plate t = 6 mm

4.6.2 LONGITUDINAL STRAIN ε_{1t}

Geometrically and materially nonlinear analysis was used to obtain failure loads of plates with initial imperfections with amplitudes of $B/1000$ and $B/125$. Typical contour plot of longitudinal strains is shown in figure 4.6.2.

Different plate slenderness values were obtained by varying plate thickness: $3, 4, 6, 8, 12, 16, 24$ and $54\ mm$. The values of pate slenderness (calculated using expression 4.1.1), loads of imperfect plates at which longitudinal tensile strain reaches the limit value and reduction factors (calculated using expression 4.1.2) are shown in table 4.5 and the associated buckling curves are presented in figure 4.6.3.
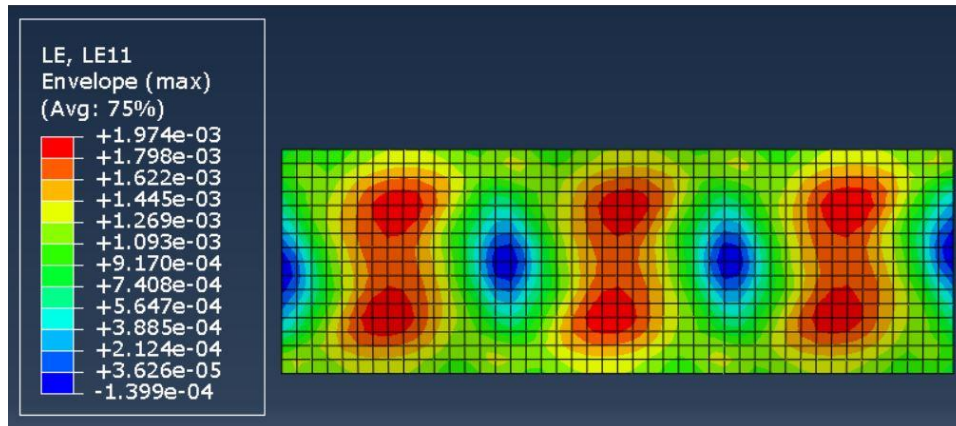
Figure 4.6.2 Longitudinal tensile strain contour plot (t = 6 mm)

t, mm	σcr, N/mm2	fult, N/mm2	λ	ffail, N/mm2 B/1000	ffail, N/mm2 B/125	ρ SLS εₜₜ B/1000	ρ SLS ε1t B/125
3	6.85	137.19	4.48	23.26	22.90	0.17	0.17
4	12.13	137.19	3.36	29.04	28.17	0.21	0.21
6	27.05	137.19	2.25	39.29	36.60	0.29	0.27
8	47.59	136.26	1.69	52.63	46.71	0.39	0.34
12	104.53	136.26	1.14	95.15	67.15	0.70	0.49
16	180.67	136.26	0.87	124.65	86.96	0.91	0.64
24	380.19	137.08	0.60	135.15	108.59	0.99	0.79
54	1381.7	136.26	0.31	138.34	125.74	1.02	0.92

Table 4.5 Plate slenderness and load reduction factors for SLS longitudinal strain criterion
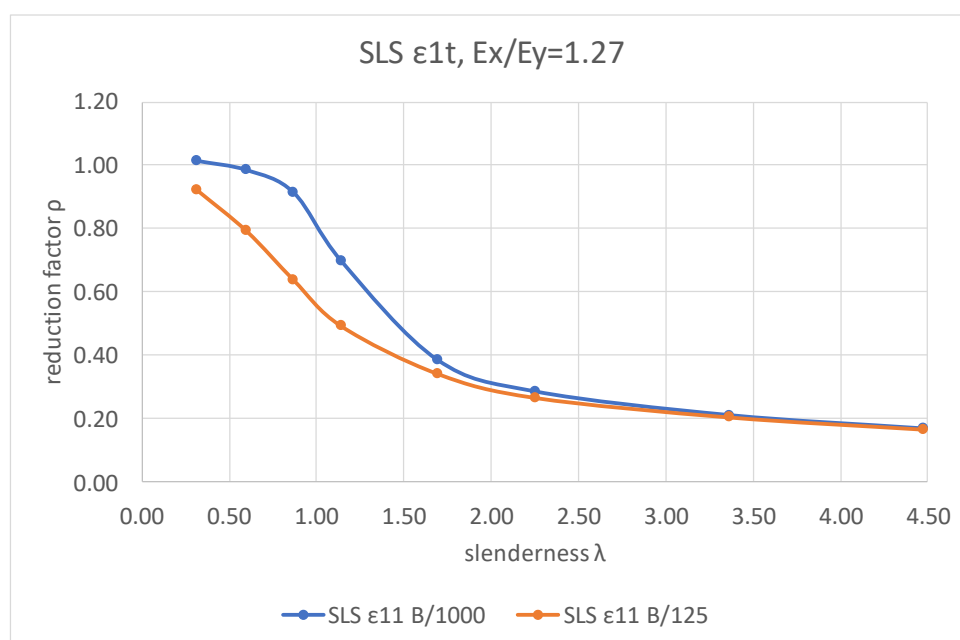
Figure 4.6.3 Buckling curves for SLS longitudinal strain criterion

The plot in figure 4.6.3 shows two curves. The orange curve is for a plate with an initial imperfection with magnitude of $B/125$ and the blue curve is for a plate with an initial imperfection with magnitude of $B/1000$.

The same trend as in case of Hashin progressive failure criterion can be seen in figure 4.6.3. For plates with slenderness $\lambda > 2.5$ (thin plates) the amplitude of imperfection has no or very little effect on load reduction factor. For plates with slenderness $\lambda \leq 2.5$ the reduction factor depends on the amplitude of the imperfection: for amplitude $B/1000$ the reduction of plate capacity will be smaller (larger value of the imperfection factor ρ), for amplitude $B/125$ the reduction will be larger (smaller value of the imperfection factor ρ). The difference between reduction factors for plates with imperfection $B/1000$ and $B/125$ increases as plate slenderness decreases up to $\lambda \approx 0.87$, after which the difference starts to become smaller.

4.6.3 TRANSVERSE STRAIN ε_{2t}

Table 4.6 shows the data necessary for constructing the buckling curve for the transverse strain limit criterion (figure 4.6.4).

t, mm	σcr, N/mm2	fult, N/mm2	λ	ffail, N/mm2 B/1000	ffail, N/mm2 B/125	ρ SLS ε2t B/1000	ρ SLS ε2t B/125
3	6.85	137.19	4.48	17.50	17.03	0.13	0.12
4	12.13	137.19	3.36	21.88	19.83	0.16	0.14
6	27.05	137.19	2.25	30.34	27.68	0.22	0.20
8	47.59	136.26	1.69	46.57	34.13	0.34	0.25
12	104.53	136.26	1.14	84.59	50.68	0.62	0.37
16	180.67	136.26	0.87	112.51	64.65	0.83	0.47
24	380.19	137.08	0.60	128.01	84.23	0.93	0.61
54	1381.7	136.26	0.31	134.25	109.50	0.99	0.80

Table 4.6 Plate slenderness and load reduction factors for SLS transverse strain criterion
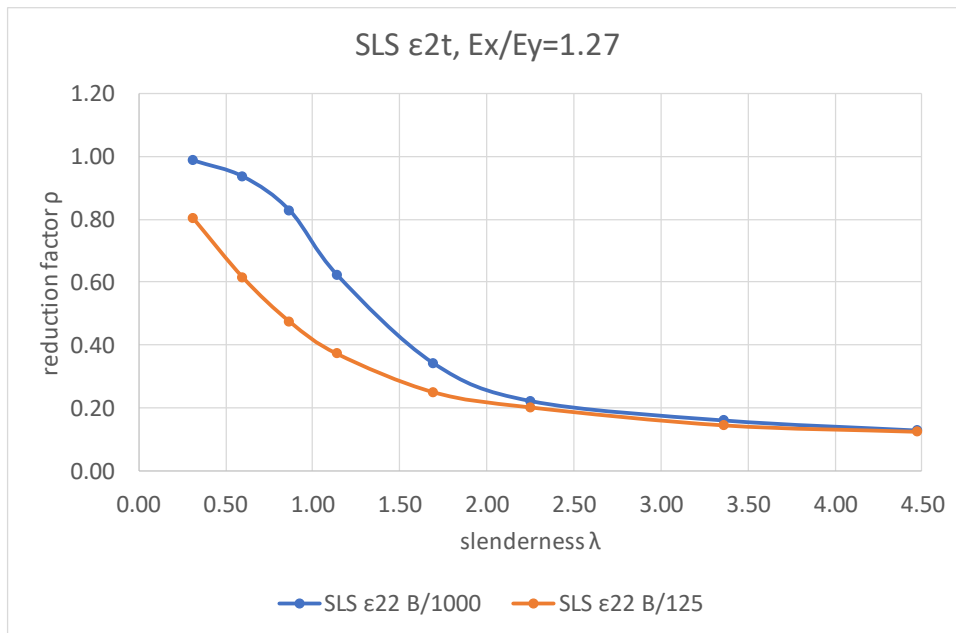
Figure 4.6.4 Buckling curves for SLS transverse strain criterion

As is seen in figure 4.6.4, for thin plates ($\lambda > 2.5$) according to serviceability limit state criterion for transverse strains there is a slight difference between the reduction factor for imperfection amplitudes $B/1000$ and $B/125$. However, it is much smaller than in case of thicker plates with $\lambda > 2.5$.
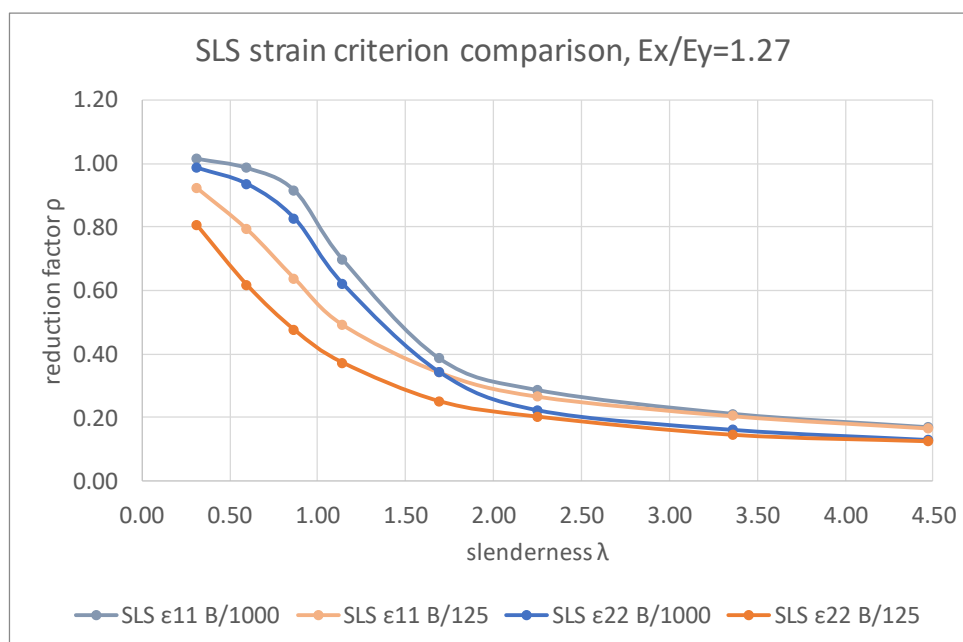
Figure 4.6.5 Comparison between the buckling curves for longitudinal and transverse strains

Figure 4.6.5 shows the comparison between the SLS longitudinal and transverse strains criteria. The largest reduction (lowest values of reduction factors ρ) are obtained in case of the SLS transverse strain criterion, which means that the cracks in the resin will occur due to tensile strains in the transverse direction faster than in longitudinal direction. It can also be seen that the transverse strains are more sensitive to amplitude of imperfection; e.g. for $\lambda = 1.14$ according to SLS longitudinal strain (ε_{1t}) criterion reduction factors are as follows:

- for $B/1000$: $\rho_{\varepsilon 1} = 0.70$
- for $B/125$: $\rho_{\varepsilon 1} = 0.49$

and according to SLS transverse strain criterion (ε_{2t}):

- for $B/1000$: $\rho_{\varepsilon 2} = 0.62$
- for $B/125$: $\rho_{\varepsilon 2} = 0.37$

So, the difference in case of SLS longitudinal strain criterion associated with different imperfection amplitude is 30%, and 40% in case of SLS transverse strain criterion.

4.7 DELAMINATION

As the last failure criterion, delamination is considered. This criterion is considered to be fulfilled when the interlaminar shear stress has reached the value of $20 \ N/mm^2$ anywhere in the laminate. Since the Hashin progressive failure model does not consider delamination failure mode, the interlaminar shear stresses values were checked and compared with the critical value given in CUR96 to determine if delamination might occur before the failure load of a plate.

Figure 4.7.1 shows the contour plot of interlaminar shear stresses in a flat plate under uniform axial compression from geometrically and materially linear analysis at ultimate load level (for a plate $t = 6 \ mm \ f_{ult} = 229.09 \ N/mm^2$).
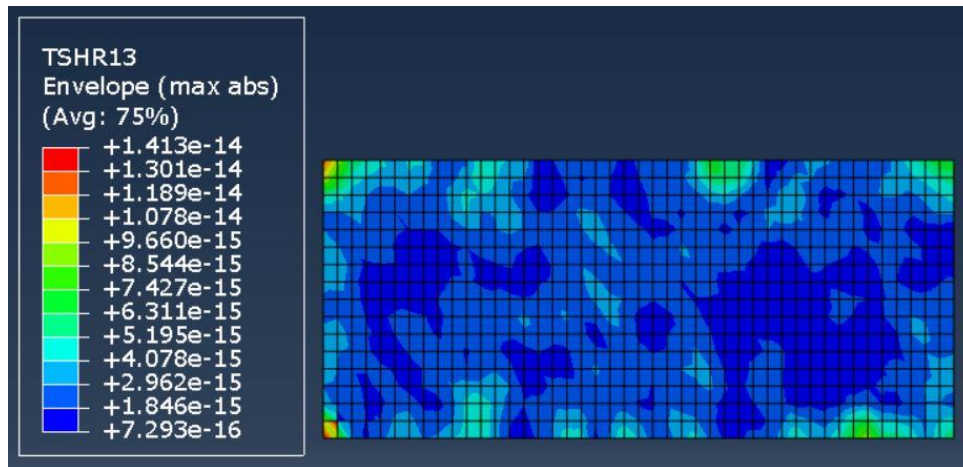
Figure 4.7.1 ILSS at ultimate load in an ideal plate

The interlaminar shear stresses are very low, with the maximum value of $1.41 \cdot 10^{-14} \ N/mm^2$ which is much less than the critical value of $20 \ N/mm^2$.
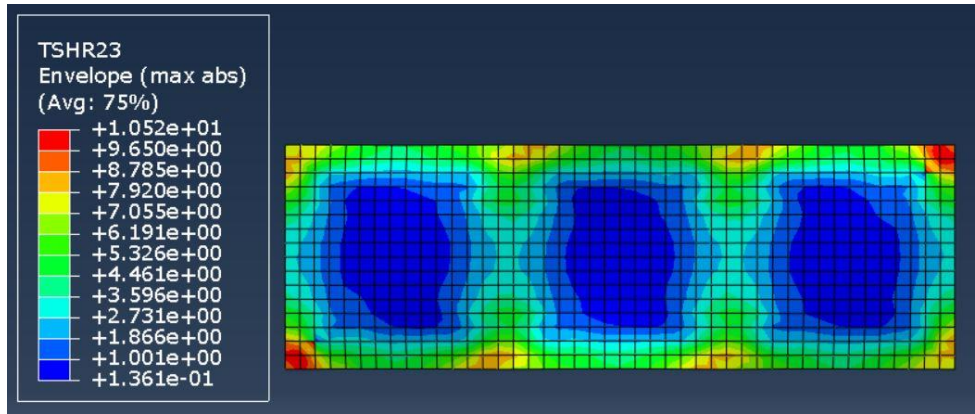
Figure 4.7.2 ILSS at failure load in an imperfect plate

In figure 4.7.2 the contour plot of interlaminar shear stresses in a plate ($t = 6\ mm$) with initial out of plane deformation is shown. The maximum value ($10.50\ N/mm^2$) is almost two times lower than the critical value.

The table 4.7 shows the maximum values of ILSS that occur in plates of various thicknesses obtained both from geometrically linear (flat plates) and nonlinear analysis (plates with initial imperfection).

t, mm	geom. linear		B/1000		B/125	
	Hashin, N/mm2	ILSS, 10^(-14) N/mm2	Hashin, N/mm2	ILSS, N/mm2	Hashin, N/mm2	ILSS, N/mm2
3	229.09	0.68	35.48	10.4	34.03	9.09
4	229.17	1.48	45.53	11.4	45.44	11.57
6	229.09	141	61.81	10.52	61.2	10.32
8	229.33	4.77	78.15	13.4	74.36	12.28
12	229.33	4.67	115.14	18.01	106.97	17.33
16	229.33	6.69	168.12	13.11	141.02	17.53
24	228	2.39	218.49	3.13	195.04	10.3
54	229.33	17.3	220.5	0.87	214.84	6.64

Table 4.7 ILSS values for ideal and imperfect plates

In all of the cases the values are below the critical value $f_{ILSS} = 20\ N/mm^2$.

Since from the interlaminar shear stresses check it was found that the values do not reach the critical value of $20\ N/mm^2$, it is concluded that delamination will not occur before the failure according to Hashin progressive damage model.

4.8 COMPARISON FAILURE CRITERIA

Four failure criteria were considered. The critical load criterion is not applicable in case of imperfect plates, since a plate with initial out of plane deformation does not have bifurcation buckling behaviour. Delamination criterion was checked against progressive failure model and it was shown that interlaminar shear stresses are below the critical value of $20\ N/mm^2$ specified in the design code CUR96 for polyester resin. This leaves two failure criteria: Hashin progressive failure and serviceability strain limit criterion, which includes longitudinal and transverse strain limits, and therefore three sets of buckling curves were derived.

To compare the buckling curves corresponding to the Hashin progressive failure and SLS strain limit criteria, one plate slenderness definition is used:

$$\lambda = \sqrt{\frac{f_{ult,Hashin}}{\sigma_{cr}}}$$

(4.8.1)

The reduction factors are calculated as:

- Hashin progressive failure: $\rho_{Hashin} = f_{fail,Hashin}/f_{ult,Hashin}$
- SLS longitudinal limit strain: $\rho_{SLS\varepsilon1} = f_{fail,SLS\varepsilon1}/f_{ult,Hashin}$
- SLS transverse limit strain: $\rho_{SLS\varepsilon2} = f_{fail,SLS\varepsilon2}/f_{ult,Hashin}$

(4.8.2)

This allows to obtain the same plate slenderness values for all the criteria and the reduction factor in relation to the failure load of the plate. The buckling curves related to a plate with initial imperfection of magnitude $B/1000$ is shown in figure 4.8.1 and with initial imperfection of magnitude $B/125$ in figure 4.8.2. The blue curve shows reduction factor according to Hashin progressive failure criterion, green curve – SLS longitudinal strain criterion and orange curve – SLS transverse strain criterion.
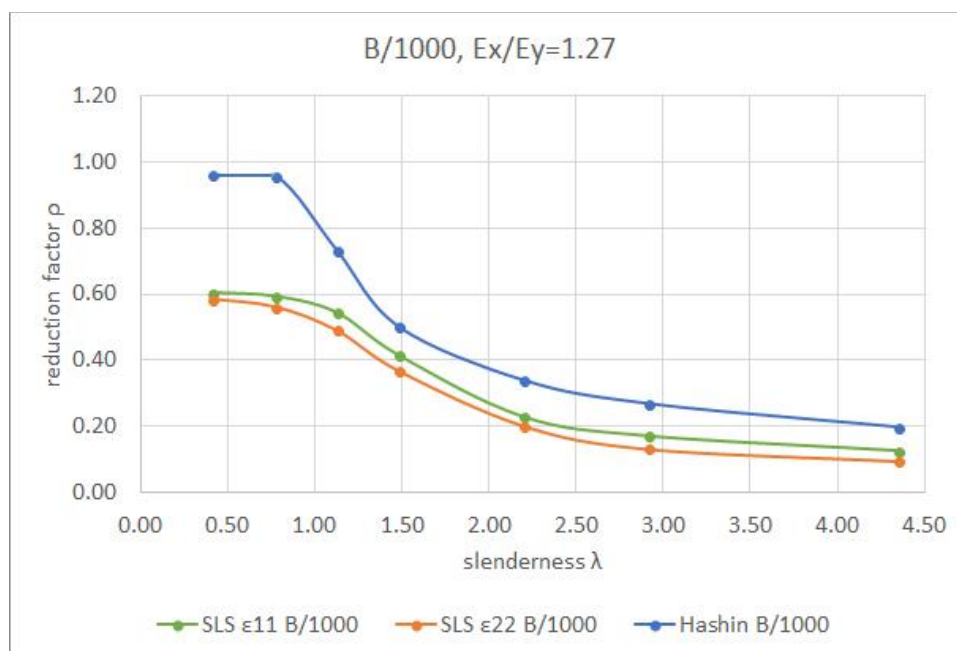
Figure 4.8.1 Comparison of failure criteria for imperfection amplitude B/1000
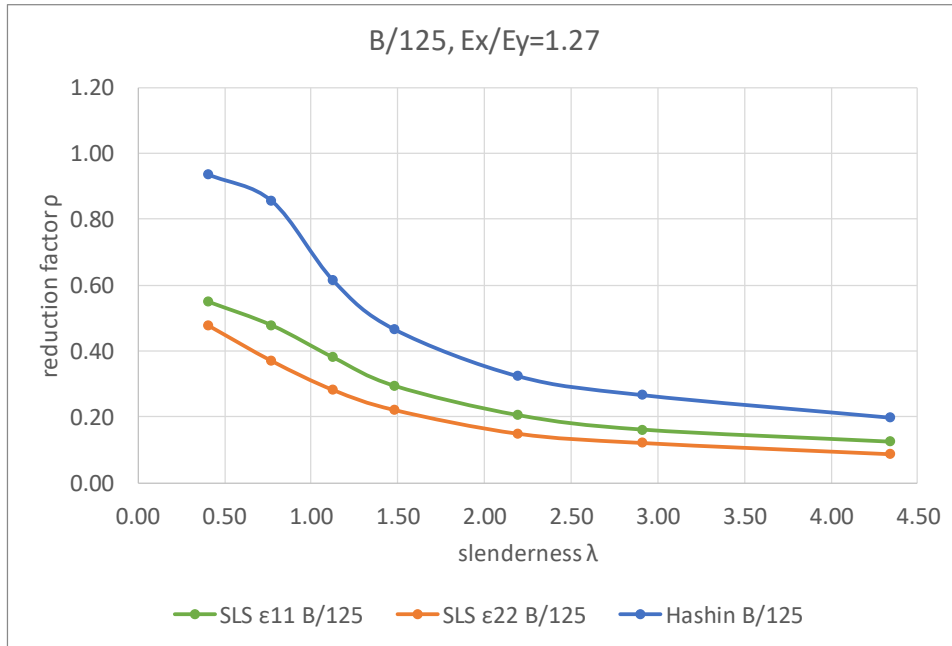
Figure 4.8.2 Comparison of failure criteria for imperfection amplitude B/125

For both magnitudes of imperfection, the buckling curve associated with Hashin progressive failure fits above the SLS strain limit curves. That makes sense and is explained by the fact that the SLS strain limit criterion is a first ply failure and will occur at lower load levels than a failure of a laminate as a whole. Out of three buckling curves the one related to SLS transverse strains gives the largest reduction of ultimate load, so in case of serviceability limit state loads this would be the governing buckling curve.

4.9 EFFECT OF ORTHOTROPY

Since plate slenderness defined as a square root of compressive strength to critical load ratio, it is expected that for different layups different values of reduction factor ρ in relation to slenderness will be derived.

To compare the buckling curves for Hashin progressive failure criterion for plates with different material properties, two layups are considered:

- layup II: 0⁰ -62.5%, 45⁰ -12.5%, -45⁰ -12.5%, 90⁰ -12.5%
- layup III: 0⁰ -25%, 45⁰ -25%, -45⁰ -25%, 90⁰ -25%

which are often used in practice.

Figure 4.9.1 shows critical loads for the three layups for the first four buckling modes for laminate thickness $t = 6\ mm$. The longitudinal and transverse moduli of elasticity ratio and strength values are as follows:

- layup I: $E_{cx}/E_{cy} = 1.27$; $D_{11}/D_{22} = 1.74$; $f_{ult} = 229.09\ N/mm^2$
- layup II: $E_{cx}/E_{cy} = 1.80$; $D_{11}/D_{22} = 2.41$; $f_{ult} = 298.59\ N/mm^2$
- layup III: $E_{cx}/E_{cy} = 1.0$; $D_{11}/D_{22} = 1.45$; $f_{ult} = 182.78\ N/mm^2$

Layup III is quasi isotropic, which means that the axial stiffness in both directions is the same. The bending stiffness in two directions however is not necessarily the same, although it can be achieved. If $D_{11}/D_{22} = 1.0$, then the material behaviour will be similar to isotropic and the critical stress value for AR = 3 will be lower, since there will be no shift and the minimum value will be located at $AR = m$. In this study, however, the influence of stack sequence of a laminate is not considered further.
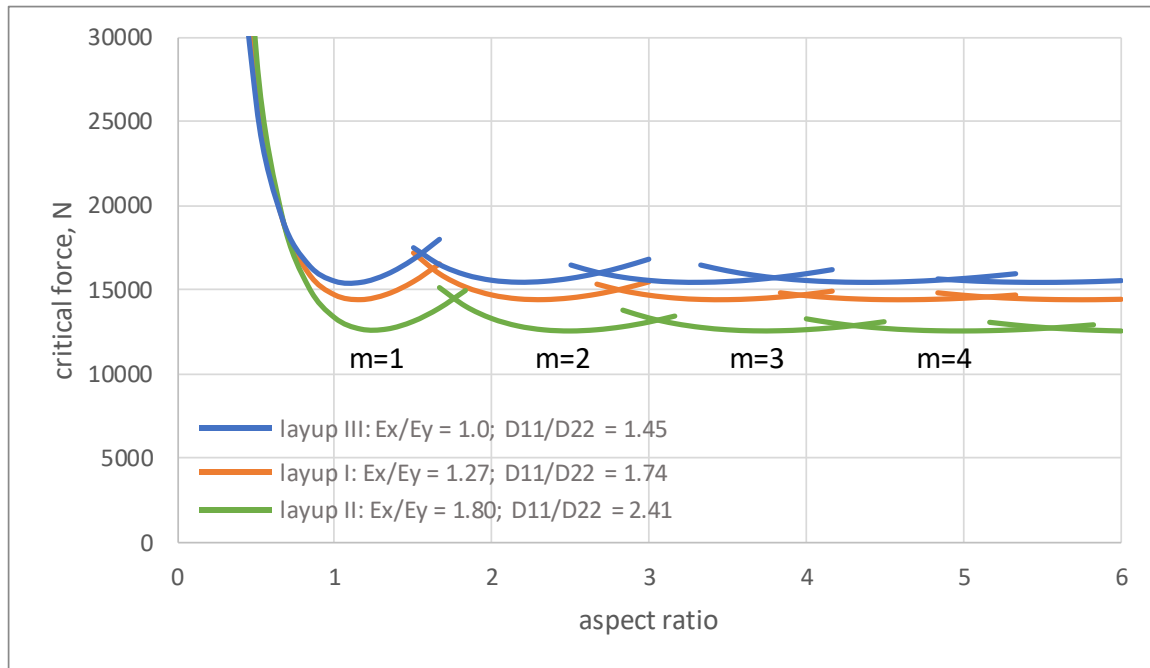
Figure 4.9.1 Ideal plate's critical forces

The highest critical loads are obtained for plates of layup III (lowest E_{cx}/E_{cy} ratio), at the same time this layup has the lowest strength, determined by Hashin progressive damage analysis. The lowest critical loads correspond to layup II (highest E_{cx}/E_{cy} ratio), which has the highest strength. It should also be noted that for layups II and III the strain in the laminated related to initial modulus of elasticity is 1.07% and 0.97%, respectively, which is again lower than 1.2%, and is a conservative result, since the strain limit for failure of the laminate 1.2% is based on experimental data.

Based on these observations, it is clear that different reduction factors will be obtained for plates with different laminates, since plate slenderness relates to both ultimate and buckling strengths. It is expected that the lowest reduction factors will be obtained for layup II and the highest for layup III. Below the slenderness values, failure loads and buckling curves for layups II and III are presented.

t, mm	σcr, N/mm2	fult, N/mm2	λ	ffail, N/mm2 B/1000	ffail, N/mm2 B/125	ρ Hashin B/1000	ρ Hashin B/125	ρ, linear buckling
4	10.94	298.91	5.23	43.60	43.68	0.15	0.15	0.04
6	24.48	298.59	3.49	58.65	58.58	0.20	0.20	0.08
8	43.23	298.91	2.63	74.45	73.97	0.25	0.25	0.14
12	95.80	298.89	1.77	105.23	102.56	0.35	0.34	0.32
16	167.31	298.90	1.34	149.35	135.44	0.50	0.45	0.56
24	356.15	298.90	0.92	272.61	207.42	0.91	0.69	1.19
54	1329.59	298.90	0.47	301.57	286.13	1.00	0.96	

Table 4.8 Plate slenderness and load reduction factors for Hashin damage criterion for layup II
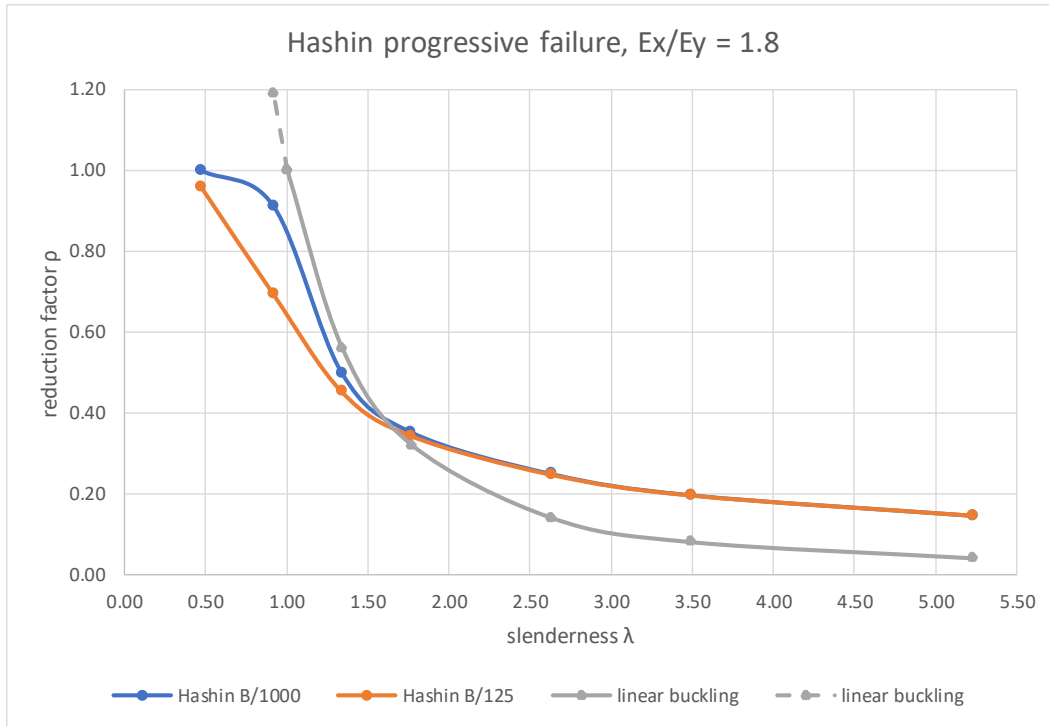
Figure 4.9.2 Buckling curves for Hashin damage criterion for layup II

t, mm	σcr, N/mm2	fult, N/mm2	λ	ffail, N/mm2 B/1000	ffail, N/mm2 B/125	ρ Hashin B/1000	ρ Hashin B/125	ρ, linear buckling
3	7.20	182.78	5.04	33.45	30.20	0.17	0.17	0.04
4	12.75	182.78	3.79	42.34	42.34	0.23	0.23	0.07
6	28.39	182.78	2.54	57.80	57.09	0.32	0.31	0.16
8	49.88	182.78	1.91	72.76	71.75	0.40	0.39	0.27
12	109.23	182.78	1.29	112.25	102.66	0.61	0.56	0.60
16	188.19	182.78	0.99	168.82	134.76	0.92	0.74	1.03
24	393.63	182.78	0.68	183.63	171.90	1.00	0.94	2.15

Table 4.9 Plate slenderness and load reduction factors for Hashin damage criterion for layup III
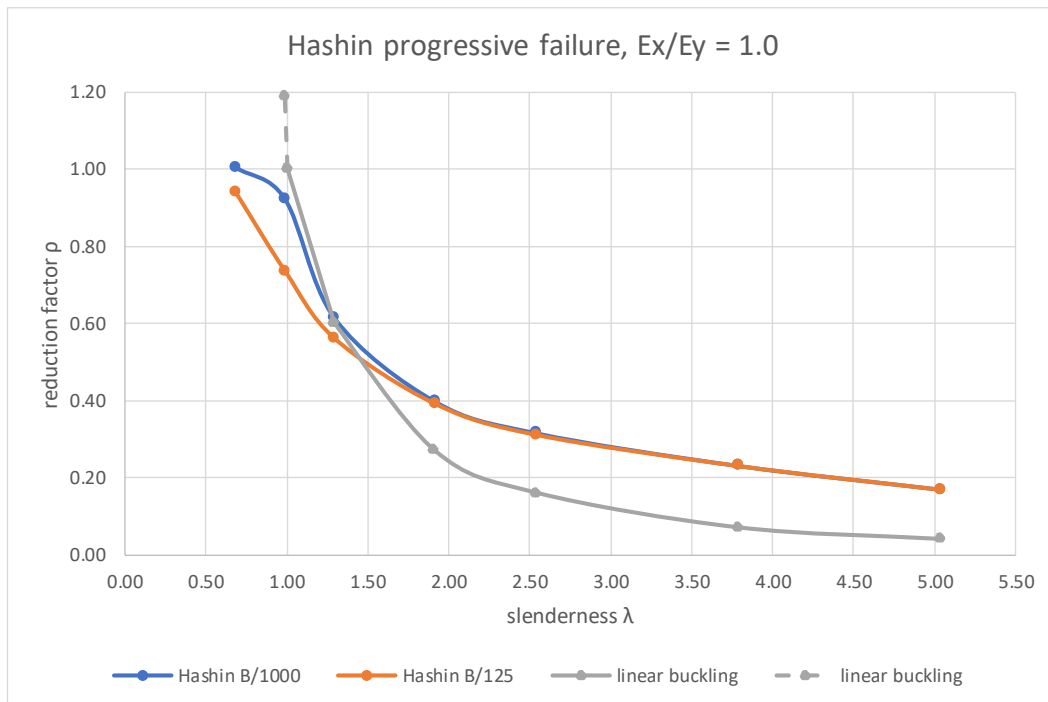
Figure 4.9.3 Buckling curves for Hashin damage criterion for layup III

In general, the shape of the curves for layup II and layup III are very similar to each other and the general trends are the same. For thin plates with slenderness $\sim\lambda > 2.5$ the magnitude of initial imperfection does not play a role for reduction of strength: the curves for $B/1000$ and $B/125$ almost coincide and the reduction factor has the same value. As plate becomes stockier ($\lambda < 2.5$) the influence of the imperfection amplitude becomes more pronounced but decreases at $\lambda = 0.47$ for layup II and $\lambda = 0.68$ for layup III, when the reduction factor is $\cong 1$.

In terms of comparison with the ideal plate buckling curve, plates with slenderness $\lambda > 1.77$ (layup II) and $\lambda > 1.50$ (layup III) have capacity that exceeds the critical load of equivalent ideal plate (no initial out of plane deformations present), so using critical load as failure criterion for these plates would be conservative.

It can also be noticed that in case of layup II (more orthotropic, larger E_x/E_y ratio) the influence of the amplitude of initial imperfection is more pronounced for stockier plates ($\sim\lambda < 1.3$) and less pronounced for layup III (quasi isotropic, $E_x/E_y = 1$).

Figures 4.9.4 and 4.9.5 show the comparison in terms of slenderness of buckling curves for three different layups for imperfection amplitude $B/1000$ and $B/125$. The goal is to compare the reduction of compressive strength that corresponds to a certain slenderness value of plates of three different layups (i.e. for $\lambda = 2.5$ $\rho_{layupI} = 0.31$, $\rho_{layupI} = 0.3$, $\rho_{layupII} = 0.23$ and $\rho_{layupIII} = 0.31$).
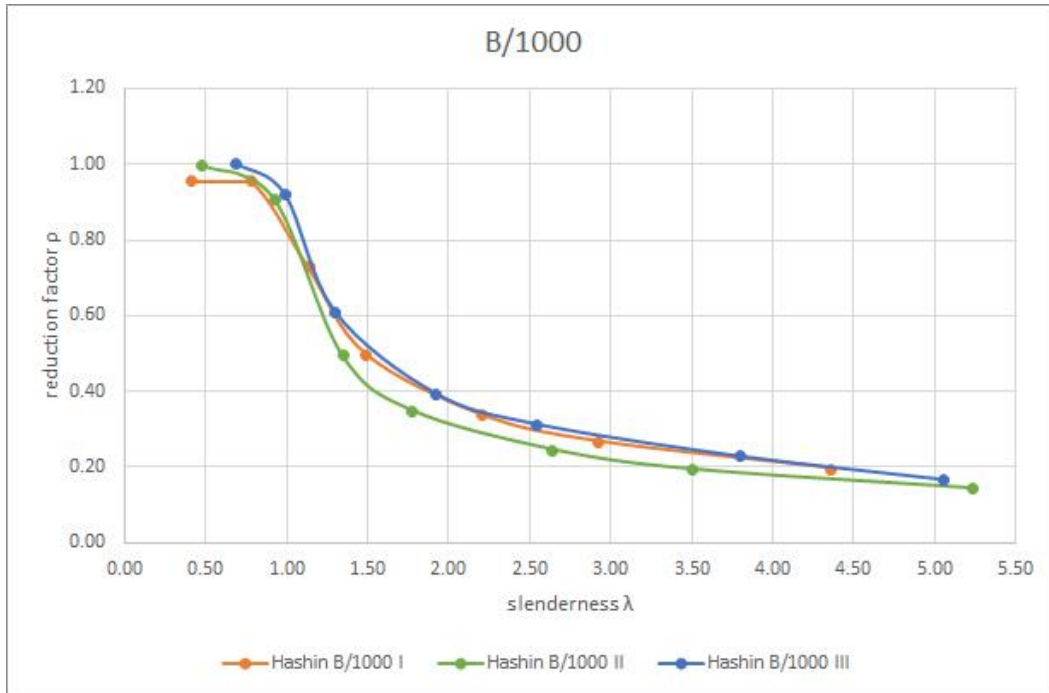
Figure 4.7.6 Buckling curves comparison for imperfection B/1000
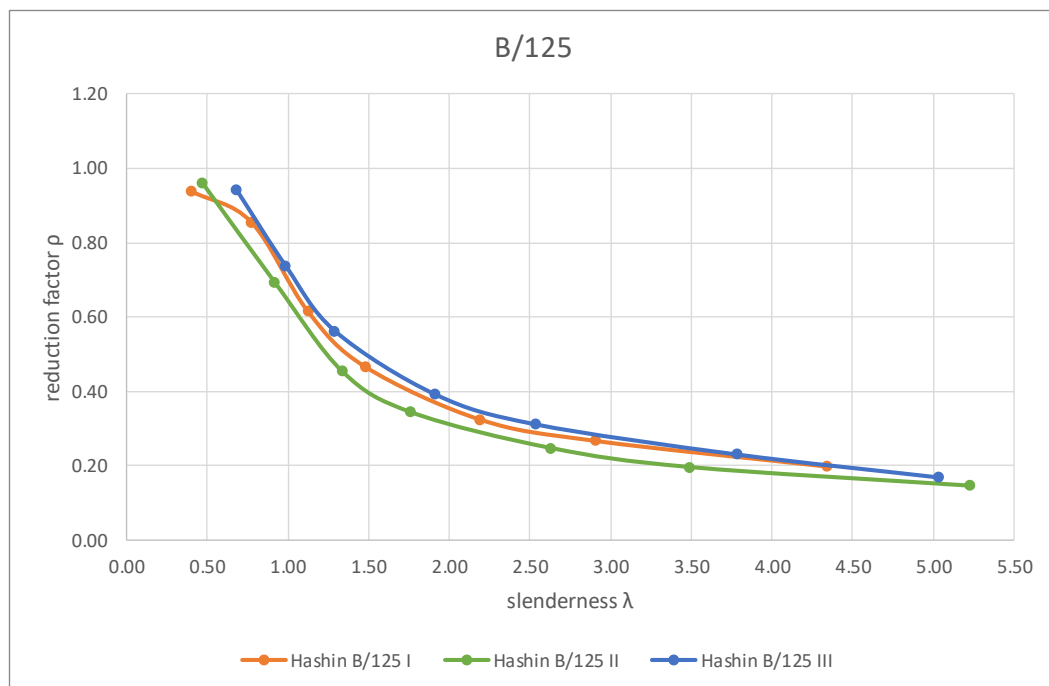
Figure 4.7.7 Buckling curves comparison for imperfection B/125

From the comparison diagrams it can be seen that the curves associated with layup I and layup III do not differ that much. The buckling curve associated with layup II shows larger reduction of compression strength compared to buckling curves of layup I and III. As was reported, layup I and layup III have 40% and 50% of fibres in 0° direction and layup III – 62.5%. This suggests that in terms of design for buckling the larger stiffness ratio has a negative effect on carrying capacity of plates.

5. NUMERICAL EXAMPLE

To demonstrate how the derived buckling curves might be used in design of plated fibre reinforced polymer structures, and to compare it with existing analytical models a numerical example is presented.

This example shows the calculation of local buckling strength of a hollow profile under uniform axial compression according to

- JRC/Kollar method
- CUR96 method
- Buckling curves method

5.1 INPUT DATA

The geometry of the cross-section is shown in figure 5.1.1
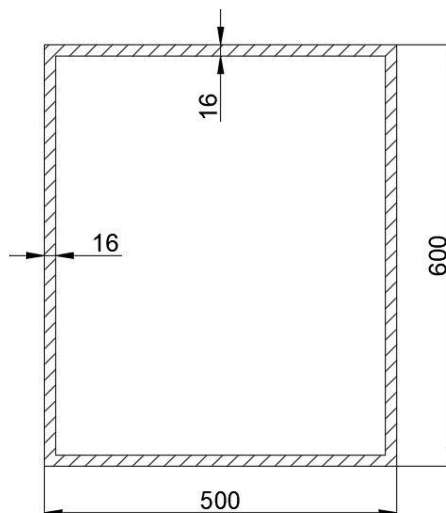
Figure 5.1.1 Cross-section geometry

The length of the profile is chosen $L = 3000\ mm$;

$B_f = 484\ mm$ $\qquad\qquad t_f = 16\ mm$

$B_w = 584\ mm$ $\qquad\qquad t_w = 16\ mm$

Layup II (with 62.5% fibres in the longitudinal direction, $E_x/E_y = 1.8$) is used in this profile, with the following equivalent bending stiffness properties:

$E_x = 31.78\ GPa$ $\qquad\qquad G_{xy} = 4.81\ GPa$

$E_y = 13.11\ GPa$ $\qquad\qquad \nu_{xy} = 0.356$

Bending stiffness parameters obtained with CLT:

$D_{11} = 11351152.9\ MPa \cdot mm^3$ $\qquad\qquad D_{22} = 4712867.1\ MPa \cdot mm^3$

$$D_{12} = 1640113.6 \; MPa \cdot mm^3 \qquad\qquad D_{66} = 1642346.5 \; MPa \cdot mm^3$$

The geometry and material properties are chosen such, so that the webs and the flanges have the same layup and thickness but different width, resulting in lower critical stress in the webs (vertical plates in the cross-section drawing). In this case:

- according to JRC/Kollar method the flanges will give additional support to the webs, so the increase of critical stress has to be calculated;
- method described in CUR96 can be applied directly, since both webs and flanges have the same thickness.

5.2 JRC/KOLLAR METHOD

Since JRC method does not directly give the design procedure for hollow profiles, the extended Kollar procedure is used. The necessary equations are given in table 2.3.

Step 1: determine the critical stress in webs and flanges assuming simply supported boundary conditions.

Flange:

$$(f_{loc,k}^{axial})_f^{SS} = \frac{\pi^2}{t_f b_f^2}\left\{2\sqrt{(D_{11})_f (D_{22})_f} + 2\left[(D_{12})_f + 2(D_{66})_f\right]\right\} = 64.46 \; MPa$$

Web:

$$(f_{loc,k}^{axial})_w^{SS} = \frac{\pi^2}{t_w b_w^2}\left\{2\sqrt{(D_{11})_w (D_{22})_w} + 2\left[(D_{12})_w + 2(D_{66})_w\right]\right\} = 44.27 \; MPa$$

Since $(f_{loc,k}^{axial})_f^{SS} > (f_{loc,k}^{axial})_w^{SS}$, the increase of the critical stress of the web will be considered through the interaction with the flange.

Step 2: determine stiffness of the rotational spring provided by the flange.

$$\tilde{k}_f = \frac{2(D_{22})_f}{b_f}\left[1 - \frac{(f_{loc,k}^{axial})_w^{SS}(E_{Lc})_f}{(f_{loc,k}^{axial})_f^{SS}(E_{Lc})_w}\right] = 6098.46 \; N$$

Step 3: recalculate "improved" critical stress of the web.

$$\zeta = \frac{(D_{22})_w}{\tilde{k}_f b_w} = 1.323$$

$$\xi = \frac{1}{1 + 10\zeta} = 0.070$$

$$\begin{aligned}(f_{loc,k}^{axial})_w = \frac{\pi^2}{t_w b_w^2}&\left\{2\sqrt{1 + 4.139\xi}\sqrt{(D_{11})_w (D_{22})_w} + (2 + 0.62\xi^2)\left[(D_{12})_w + 2(D_{66})_w\right]\right\}\\ &= 47.90 \; MPa\end{aligned}$$

By considering the interaction between webs and flanges, the critical stress of the web is increased by 7.6%.

5.3 CUR96 METHOD

Step 1: determine the critical load of the flange.

$$\xi = \frac{b_w}{b_f} = 1.207$$

$$b = B_f = 484 \ mm$$

$$p = 2.0 + \frac{0.002}{\xi - 1.3} = 1.979$$

$$q = 1.0 + \frac{0.08}{\xi + 0.2} = 1.057$$

$$f_{c,stab,k,f} = \frac{\pi^2}{12} \cdot \left(\frac{t_f}{b}\right)^2 \cdot \left[\sqrt{q} \cdot \left(2 \cdot \sqrt{E_x \cdot E_y}\right) + p \cdot (y \cdot v_{xy} + 2 \cdot G_{xy})\right] = 63.13 \ MPa$$

Step 2: determine the critical load of the web.

$$f_{c,stab,k,w} = \frac{\pi^2}{t_w \cdot b_w^2} \cdot \left(2 \cdot \sqrt{D_{11,w} \cdot D_{22,w}} + 2 \cdot (D_{12,w} + 2D_{66,w})\right) = 44.27 \ MPa$$

As it can be seen in the CUR96 method, the web is calculated using formula for a simply supported plate. However, in case of a hollow section it is unclear which plates are webs and which are flanges. By swapping the widths and taking $B_f = 584 \ mm$ and $B_w = 484 \ mm$, the following results are obtained:

$$f_{c,stab,k,f} = \frac{\pi^2}{t_f \cdot b_f^2} \cdot \left(2 \cdot \sqrt{D_{11,f} \cdot D_{22,f}} + 2 \cdot (D_{12,f} + 2D_{66,f})\right) = 64.46 \ MPa$$

$$f_{c,stab,k,w} = \frac{\pi^2}{12} \cdot \left(\frac{t_w}{b}\right)^2 \cdot \left[\sqrt{q} \cdot \left(2 \cdot \sqrt{E_x \cdot E_y}\right) + p \cdot (y \cdot v_{xy} + 2 \cdot G_{xy})\right] = 43.77 \ MPa$$

Since the difference is small, the first definition of the webs (vertical plates with reference to figure 5.1.1, same as in JRC/Kollar method) is adopted.

5.4 BUCKLING CURVES METHOD

Step 1: determine the compressive strength of the web and flange.

Both plates have the same layup and therefore $f_{ult,f} = f_{ult,w}$. Using eLamX software and Hashin failure criterion, the strength of the laminate is determined as described in 4.5.1: first, the first ply failure is determined, then the transverse elastic modulus is reduced to zero in the failed ply, and the second ply failure is calculated, which is the maximum load that the plate can carry.

$$f_{ult,f} = f_{ult,w} = 298.94 \ MPa$$

Step 2: determine the critical load of the web and flange.

The critical loads were already calculated in 5.2:

Flange:

$$(f_{loc,k}^{axial})_f^{SS} = 64.46 \ MPa$$

Web:

$$(f_{loc,k}^{axial})_w^{SS} = 44.27 \ MPa$$

These values were obtained using the simplified formula (table 2.2) for plates whose aspect ratio is larger than 5 (AR > 5). For shorter plates, the relation between the number of halfwaves and aspect ratio becomes important, and the full formula has to be used (table 2.1). Alternatively, eLamX can be used to determine the critical load of the plate taking into account aspect ratio:

$$\sigma_{cr,f} = 64.42 \ MPa$$

$$\sigma_{cr,w} = 44.29 \ MPa$$

Step 3: calculate slenderness of the web and the flange.

Flange:

$$\lambda_f = \sqrt{\frac{f_{ult,f}}{\sigma_{cr,f}}} = 2.15$$

Web:

$$\lambda_w = \sqrt{\frac{f_{ult,w}}{\sigma_{cr,w}}} = 2.60$$

Step 4: determine the failure load of the web and the flange using buckling curves.

From the buckling curves for layup II the reduction factors are obtained and the failure loads are calculated:
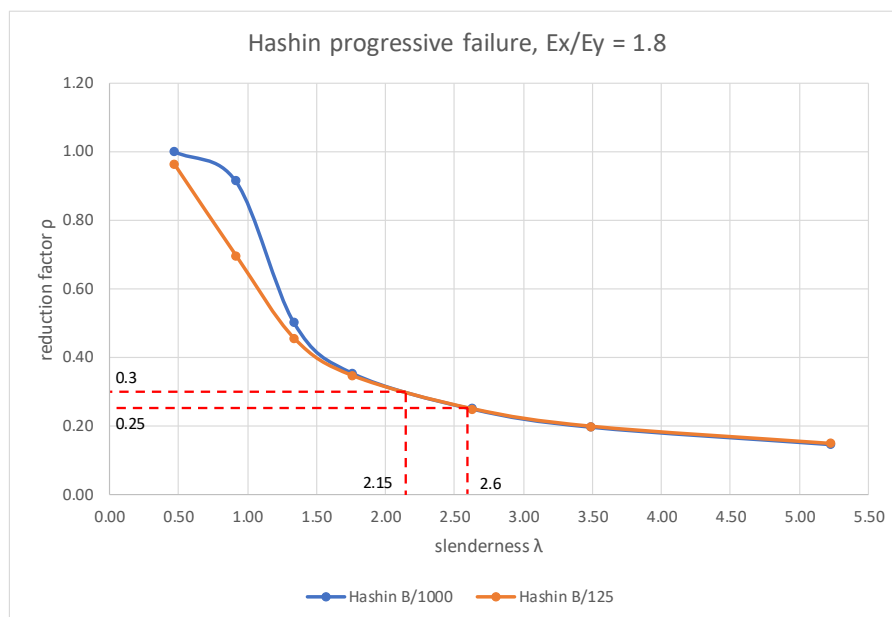
Figure 5.4.1 Determination of reduction factors

112

Flange:

$$\rho_f = 0.30 \qquad\qquad f_{fail,f} = \rho_f \cdot f_{ult,f} = 89.68\ MPa$$

Web:

$$\rho_w = 0.26 \qquad\qquad f_{fail,w} = \rho_w \cdot f_{ult,w} = 74.74\ MPa$$

Since both flange and web are rather slender, the reduction factors for imperfection amplitude $B/1000$ and $B/125$ are almost the same. As it can be seen, by using failure load instead of critical load, the carrying capacity of the flange is increased by 28% and the web by 40%.

5.5 DISCUSSION OF RESULTS

Table 5.1 shows the comparison of the results obtained by JRC/Kollar method, CUR96 method and buckling curves method. Also, the results from finite element analysis are presented. All the values given in [MPa].

	JRC/ Kollar	CUR96	buckling curves	FEA
flange	64.46	63.13	89.68	94.39 / 93.29
web	47.9	44.27	74.74	79.43 / 79.30

Table 5.1 Results obtained from four different methods

The first that can be noticed is that the results obtained with JRC/Kollar method and CUR96 method give load values that are close to each other. The difference is that in JRC/Kollar the flange and the web are first evaluated to determine which plate will buckle first, and then the restraining plate (the one that buckles later) will provide additional strength to the plate that already buckled. In CUR96 the formula that takes into account interaction between the web and the flange is given only for flanges, while for webs an analytical formula for a simply supported plate is used, which gives a conservative result.

The buckling curves method gives higher load values both for the flange and the web because this method considers not critical load but failure load. It was shown that thin plates have "postbuckling" capacity and therefore can carry loads higher than critical load. For the flange, the failure load obtained with buckling curves method gives a value that is 28% higher than the value obtained with JRC/Kollar method and 29% higher than the value obtained with CUR96 method. For the web the difference is 36% and 40%. The larger difference in case of the web is based on the fact that web has a higher plate slenderness than the flange and is in line with what was described in chapter 4.

The results that were obtained with finite element analysis (the two values correspond to plates with two different imperfection amplitudes $B/1000$ / $B/125$) are slightly higher the values obtained with buckling curves. The difference is about 5% for the flange and 6% for the web.

Below the table that shows the difference between the obtained loads is given. The values obtained with the three methods: JRC/Kollar, CUR96 and buckling curves are compared to the results taken directly from the finite element analysis.

	JRC/ Kollar, %		CUR96, %		buckling curves, %	
	B/1000	B/125	B/1000	B/125	B/1000	B/125
flange	32	31	33	29	5	4
web	40	40	44	44	6	6

Table 5.2 Comparison of results obtained from design procedures and FEA

The largest difference of 44% relates to the critical load of the web calculated with the analytical formula for a simply supported plate in CUR96 method for both imperfection values. This difference means that the plate with slenderness $\lambda_w = 2.60$ can carry load almost two times the critical load. The buckling strength of the flange according to the JRC/Kollar method is also calculated using formula for a simply-supported plate but the difference with the failure load is 32% and 31%, since slenderness of the flange has a lower value $\lambda_f = 2.15$ than slenderness of the web. The load calculated by considering interaction between webs and flanges gives a difference of 33% and 29% for $B/1000$ and $B/125$, respectively.

This example shows that by using the failure load that can be estimated from the buckling curves the carrying capacity of the slender plates ($\lambda > 2.5$) can be improved significantly.

6. CONCLUSION

6.1 CONCLUSIONS BASED ON THE RESULTS

Behaviour of orthotropic plates was studies using geometrically and materially nonlinear finite element analysis. Various shapes and amplitudes of imperfections were considered, and plate geometric and material parameters were studied. The following conclusions were made based on the analysis.

- Orthotropic materials have different linear buckling behaviour than isotropic materials.

In case of an isotropic material (for example, steel) the relation between pate aspect ratio and buckling mode (number of halfwaves m) reads as: $AR = m$; and the minimum critical stress corresponds to plates, in which aspect ratio is such that the length of one halfwave equals exactly to the width of the plate. For an orthotropic material, the difference in stiffness in longitudinal and transverse directions has to be taken into consideration. The relation between aspect ratio and number of halfwave is given as: $AR = m\sqrt[4]{D_{11}/D_{22}}$, which means that the minimal critical stress of a certain buckling mode will no longer only depend on the aspect ratio but also on the bending stiffness ratio.

- Critical load only occurs in plates with no initial out of plane deformations.

The load – deflection diagram of a perfect plate has a bifurcation point, which ordinate gives plate's critical load. Until that point there is only increase of load and no increase of out of plane deformation. In an imperfect plate the out of plane deflections begin to increase as soon as load increases and instead of a bifurcation point there is a rounded over "knee" in the diagram, which means that a critical load value is difficult to determine. So, in other words, an imperfect plate gradually bends or bows, rather than suddenly changes shape.

- Relating the limiting value of imperfection only to plate width might result in very large initial out of plane deformations in relation to plate thickness.

When constructing buckling curves, plates of $300 \times 900 \ mm$ with various thicknesses were analysed. So, for plate thickness $t = 3 \ mm$ the limiting value of initial imperfection is $B/125 = 2.4 \ mm$, which is almost equal to thickness and is unlikely to happen in practice. Relating the limiting value of imperfection to both width and thickness (slenderness) would be more sensible.

- Small imperfection (single / double wrinkle) causes plate buckling in the first buckling mode, large imperfection (imperfection in the shape of one of the buckling mode) causes plate buckling into the shape that coincides with the shape of initial imperfection.

When a single or a double wrinkle imperfection is present in a plate, the plate will buckle into the first buckling mode and will show small increase of initial out of plane deformations at the load levels below the theoretical critical load. Imperfection in the shape of the first buckling mode also causes plate buckling in the first buckling mode shape but with a larger out of plane deformations compared to the plate with wrinkle imperfection. Imperfections in the shape of the second buckling mode causes the plate to buckle into the second buckling mode, etc.

- There are two effects that account for strength reduction of a composite plate with initial geometric imperfections.

The first effect is due to additional bending moment that results from eccentricities caused by initial out of plane deformations. The degree of this effect depends on plate thickness, aspect ratio and layup. The other effect is due to material degradation. According to Hashin progressive failure analysis, the governing failure mode is matrix cracking in tension. However, for very stocky plates ($\lambda \sim 0.41 - 0.7$, depending on the layup and the amplitude of imperfection) the failure mode becomes matrix crushing.

- Initial imperfection amplitude does not have an effect on failure load of thin plates with slenderness $\sim \lambda > 2.5$.

In case of imperfect plates of slenderness approximately $\lambda > 2.5$, the reduction factor ρ does not depend on the imperfection amplitude, meaning that the same values of ρ are to be applied to plates with imperfection $B/1000$ and $B/125$.

However, as the pate slenderness decreases the failure load starts to depend on the amplitude of initial imperfection: larger magnitude of initial deformation associates with lower failure load and smaller magnitude of initial deformation associates with higher failure load of a plate with a certain slenderness.

- Slender plates with initial imperfections can carry load higher than the critical load of an ideal plate with the same geometric and material properties.

Slender plates ($\lambda > 1.50$ for layup I and III; $\lambda > 1.77$ for layup II) have "postbuckling" capacity (load levels higher than the critical load associated with a perfect plate). That means that the critical buckling load criterion (disregarding presence of initial imperfections) for slender plates will give conservative results.

In case of stocky plates ($\lambda \leq 1.50$ for layup I and III; $\lambda \leq 1.77$ for layup II) the critical load criterion will be an overestimation of carrying capacity and can give results up to 18% and 30% higher for plate of layup I with imperfection $B/1000$ and $B/125$, respectively. This difference varies depending on material properties of a plate (layup II: 38% and 18%; layup III: 28% and 8%).

- The design procedures described in JRC/Kollar and CUR96 documents relate to critical load.

It was shown through a numerical example for a profile with a specific geometry and material properties that the analytical models described in JRC/Kollar and CUR96 taking into account web / flange interaction can give the buckling strength up to 40% less than the results obtained from the finite element analysis. It also means that for stocky plates ($\lambda \leq 1.50$ for layup I and III; $\lambda \leq 1.77$ for layup II) these design procedures might overestimate the buckling strength.

6.2 RECOMMENDATION FOR FURTHER RESEARCH

While reviewing the literature on the topic, it was suggested in one of the papers that the limiting value of imperfections give unrealistic results. It should be noted that this limiting value is given for pultruded structural elements. It was also difficult to find information in literature on the measured initial out of plane deformations of the test specimens. To evaluate the sensibility of the purposed limiting values given in standard, it would be good to have some statistics on the actual imperfections that occur in the elements produced by VARTM.

Another point of attention would be the research data for material properties required for progressive damage analysis. In this research the values calibrated for E-glass / epoxy laminate were used in the absence of information for E-glass / polyester laminates. In addition, test data for VARTM produced elements would be helpful to verify the results obtained from finite element analysis.

Next to geometric imperfections the fibre reinforced composites can have material imperfections such as wrinkling of fabric. The influence of material imperfections was not a part of this thesis but such imperfections could also influence the behaviour of FRP plates.

LIST OF FIGURES

LIST OF TABLES

REFERENCES

1. EUR 27666 EN "Prospect for New Guidance in the Design of FRP", Joint Research Centre, European Union 2016

2. CUR-Aanbeveling 96:2017 "Vezelversterkte kunststoffen in bouwkundige en civieltechnische draagconstructies"

3. Trumpf, H. 2006, "Stabilitätsverhalten ebener Tragwerke aus pultrudierten faserverstärkten Polymerprofilen", PhD thesis, Rheinisch-Westfälischen Technischen Hochschule Aachen, Aachen, Germany

4. Jones, R. M. 2006, "Buckling of Bars, Plates and Shells", Bull Ridge Publishing, Blacksburg, Virginia

5. Erklig, A., 05.02.2018 < http://slideplayer.com/slide/2389089/8/images/20/Coordinate+Locations+of+Plies+in+a+Laminate.jpg>

6. Kassapoglou, C. 2013, "Design and Analysis of Composite Structures", Wiley, Chichester, United Kingdom

7. Lekhnitskii, S. G. 1968, "Anisotropic Plates", Gordon and Breach, New York

8. Leissa, A. W. 1985, "Buckling of Laminated Composite Plates and Shell Panels", The Ohio State University Research Foundation, Columbus, Ohio

9. Trajan, G., Sapkas, A., Kollar, L. P. 2010, "Stability Analysis of Long Composite Plates with Restrained Edges Subjected to Shear and Linearly Varying Loads", Budapest University of Technology and Economics, Budapest, Hungary

10. Kollar, L. P. 2003, "Local Buckling of Fiber Reinforced Plastic Composite Structural Members with Open and Closed Cross Sections", *Journal of Structural Engineering*, vol. 129(11), pp. 1503-1513

11. Davalos, J. F, Barbero, E. J., Qiao, P. 2002, "Step-by-Step Engineering Design Equations for Fiber-reinforced Plastic Beams for Transportation Structures", West Virginia Department of Transportation, Charleston, West Virginia

12. Beznea, E. – F., Chirica, I. 2011, "Buckling and Post-Buckling Analysis of Composite Plates, Advances in Composite Materials - Ecodesign and Analysis", InTech

13. Czapski, P., Kubiak, T. 2015, "Numerical and Experimental Investigations of the Post-Buckling Behaviour of Square Cross-section Composite Tubes", *Composite Structures*, vol. 132, pp. 1160-1167

14. Barbero, E. J., Trovvilion, J. 1998, "Prediction and Measurement of the Post-Critical Behavior of Fiber-Reinforced Composite Columns", *Composites Science and Technology,* vol. 58, pp. 1335-1341

15. Barbero, E. J. 2000, "Prediction of Buckling-Mode Interaction in Composite Columns", *Mechanics of Composite Materials and Structures*, vol. 7, pp. 269-284

16. Barbero, E. J., DeVivo, L. 1999, "Beam-Column Design Equations for Wide-Flange Pultruded Structural Shapes", *Journal of Composites for Construction*, vol. 3, pp. 185-191

17. Barbero, E. J., Tomblin, J. 1994, "A Phenomenological Design Equation for FRP Columns with Interaction between Local and Global Buckling", *Thin-Walled Structures*, vol. 18, pp. 117-131

18. Zureick, A., Scott, D. 1997, "Short-Term Behaviour and Design of Fiber-Reinforced Polymeric Slender Members under Axial Compression", *Journal of Composites for Construction*, vol. 1, pp. 140-149

19. Brown, N. D., Mottram, J. T., and Anderson, D. 1998, ''The Behaviour of Columns for the Design of Pultruded Frames: Tests on Isolated Centrally Loaded Columns'', Proceedings of 2nd International Conference on Composites in Infrastructure, pp. 248–260

20. Barbero, E. J., Dede, E., and Jones, S. 2000 ''Experimental Verification of Buckling Mode Interaction in Intermediate Length Composite Columns'', *International Journal of Solids and Structures*, vol. 37, 3919-3934

21. NEN-EN 13706-2 "Reinforced Plastics Composites – Specifications for Pultruded Profiles - Part 2: Methods of Test and General Requirements", Nederlands Normalisatie-instituut, Delft, November 2002

22. ASTM, "Standard specification for dimensional tolerance of thermosetting glass-reinforced plastic pultruded shapes" D3917-08, West Conshohocken, 2008

23. Laudiero, F., Minghini, F., Tullini, N. 2014, "Buckling and Postbuckling Finite-Element Analysis of Pultruded FRP Profiles under Pure Compression", *Journal of Composites for Construction,* vol. 18

24. Mottram, J. T., Brown, N. D., Anderson, D. 2003, "Physical testing for concentrically loaded columns of pultruded glass fibre reinforced plastic profile", Proceedings of the Institution of Civil Engineers, pp. 205-219

25. Turvey, G. J., and Zhang, Y. 2006b, "A Computational and Experimental Analysis of the Buckling, Postbuckling and Initial Failure of Pultruded GRP Columns", *Computers & Structures*, 84, 1527–1537

26. Czapski, P., Kubiak, T. 2016, "Selected Problems of Determining Critical Loads in Structures with Stable Post-Critical Behaviour", *Mechanics and Mechanical Engineering*, vol. 20, pp 79-95

27. Offshore Standard DNV-OS-C501 "Composite Components", Det Norske Veritas AS, Oslo, November 2013

28. Datoo, H. H. 1991, "Mechanics of Fibrous Composites", Elsevier Science Publishers LTD, Essex, England

29. Smith, M. 2009, ABAQUS/Standard User's Manual, Version 6.9. Simulia, Providence, Rhode Island

30. Xin, H., Mosallam, A., Liu, Y., Wang, C., Zhang, Y. 2017, "Analytical and experimental evaluation of flexural behavior of FRP pultruded composite profiles for bridge deck structural design", Construction and Building Materials, 150, 123-149

31. Pavlovic, M. 2016, "Introduction to FRP structures"

32. Tromp, L. 2016, "Development of Design Guidance FRP: Opportunities and Challenges"

ANNEX

A. DESIGN FOR BUCKLING ACCORDING TO JRC AND CUR96

The equations for column and lateral-torsional buckling according to JRC and CUR96 are listed in the table below.

JRC	CUR96
Column Buckling	
$N_{Rd2,c} = \chi \cdot N_{loc,Rd}$	$N_{b,Rd} = \chi \cdot \dfrac{\eta_c \cdot A \cdot \rho \cdot f_{c,k}}{\gamma_M}$
$\chi = \dfrac{1}{c \cdot \lambda^2} \left(\Phi - \sqrt{\Phi^2 - c \cdot \lambda^2} \right)$	$\chi = \dfrac{1}{\Phi + \sqrt{\Phi^2 - \bar{\lambda}^2}} \leq 1$
$\Phi = \dfrac{1 + \lambda^2}{2}$	$\Phi = 0.5 \cdot \left(1 + \alpha_f \cdot \left(\bar{\lambda}_f - \bar{\lambda}_{f,0} \right) + \bar{\lambda}_f^2 \right)$
$\lambda = \sqrt{\dfrac{N_{loc,Rd}}{N_{Rd,E}}}$	$\bar{\lambda}_f = \sqrt{\dfrac{A \cdot \rho \cdot f_{c,k}}{N_{cr}}}$
Lateral (Flexural) Torsional Buckling	
$M_{Rd,2} = \chi_{FT} \cdot M_{loc,Rd}$	$M_{b,Rd} = \chi_{LT} \cdot \dfrac{\eta_c \cdot W_y \cdot \rho \cdot f_{b,c,k}}{\gamma_M}$
$\chi_{FT} = \dfrac{1}{c \cdot \lambda_{FT}^2} \left(\Phi_{FT} - \sqrt{\Phi_{FT}^2 - c \cdot \lambda_{FT}^2} \right)$	$\chi_{LT} = \dfrac{1}{\Phi_{LT} + \sqrt{\Phi_{LT}^2 - \bar{\lambda}_{LT}^2}} \leq 1$
$\Phi_{FT} = \dfrac{1 + \lambda_{FT}^2}{2}$	$\Phi_{LT} = 0.5 \cdot \left(1 + 0.75 \cdot \alpha_f \cdot \left(\bar{\lambda}_{LT} - \bar{\lambda}_{LT,0} \right) + \bar{\lambda}_{LT}^2 \right)$
$\lambda_{FT} = \sqrt{\dfrac{M_{loc,Rd}}{M_{Rd,FT}}}$	$\bar{\lambda}_{LT} = \sqrt{\dfrac{W_y \cdot \rho \cdot f_{b,c,k}}{M_{cr}}}$

Table A.1 Design procedures for buckling according to JRC and CUR96

The general procedure is very similar in both methods: the buckling resistance equals to the multiplication of the reduction factor and the local buckling resistance. If the expression of $N_{b,Rd}$ given in CUR96 is rearranged, it will coincide with $N_{Rd2,c}$ given in JRC:

$$N_{b,Rd} = \chi \cdot \frac{\eta_c \cdot A \cdot \rho \cdot f_{c,k}}{\gamma_M} = \chi \cdot \frac{\eta_c \cdot A \cdot \frac{f_{c,stab,k}}{f_{c,k}} \cdot f_{c,k}}{\gamma_M} = \chi \cdot \frac{\eta_c \cdot A \cdot f_{c,stab,k}}{\gamma_M} = \chi \cdot N_{c,stab,Rd}$$

<div align="right">(A.1)</div>

The buckling reduction factor χ in JRC procedure takes into account the interaction of global and local bucking modes of a profile. This is reflected in the interaction factor c which is a function of geometry, material properties and initial imperfections. For column buckling $c = 1.0$. In CUR96 the buckling reduction factor depends on the shape function and the slenderness.

In both design codes the definition of slenderness is actually the same:

$$\bar{\lambda}_f = \sqrt{\frac{A \cdot \rho \cdot f_{c,k}}{N_{cr}}} = \sqrt{\frac{A \cdot \frac{f_{c,stab,k}}{f_{c,k}} \cdot f_{c,k}}{N_{cr}}} = \sqrt{\frac{N_{c,stab,k}}{N_{cr}}}$$

<div align="right">(A.2)</div>

$N_{cr} = N_{Rd,E}$, in both methods it is a critical value of buckling load.

The parameter Φ in JRC is a function of slenderness; in CU96 it depends on slenderness, imperfection factor α_f and plateau length of buckling curve $\bar{\lambda}_{f,0}$. The two latter factors depend on the shape of cross-section. Their values were determined experimentally and numerically and are given in table A.2 (2.5).

Cross-section	α_f	$\bar{\lambda}_{f,0}$
hollow	0.40	0.50
I-, U- (weak axis bending)	0.75	0.50
I-, U- (strong axis bending)	0.50	0.50

<div align="center">*Table A.2 α_f and $\bar{\lambda}_f$ for column buckling*</div>

The difference in design for lateral torsional buckling is similar as for column buckling with an exception of different values of c, α_f and $\bar{\lambda}_{f,0}$. In case of lateral torsional buckling $c = 0.7$ and imperfection factor and plateau length is given in table A.2.

Cross-section	α_f	$\bar{\lambda}_{f,0}$
all (weak axis bending)	0.50	0.50

<div align="center">*Table A.3 α_f and $\bar{\lambda}_{LT,0}$ for lateral torsional buckling*</div>

The derivation of imperfection factors and the plateau lengths of the buckling curves can be found in the work by H. Trompf [3].

The procedure given in JRC is focused on the interaction between the global and local buckling modes. In this case the imperfections are considered implicitly through the interaction constant c. The interaction constant is introduced in the expression of the reduction factor χ. If the global buckling is prevented, then the buckling resistance will be equal to local buckling resistance, since $\chi = 1.0$.

The buckling resistance In CUR96 is expressed in the same way as in JRC. However, the imperfections are considered explicitly through the imperfection factors α. The imperfection factors together with the lengths of horizontal lines in the buckling curve diagrams (plateau lengths) are included in the expression of the shape functions Φ. The mode interaction is not a part of this design procedure.

B. LAMINATE STIFFNESS MATRICES

B.1 CLASSICAL LAMINATION THEORY CALCULATIONS

1. The reduced stiffness matrix of a unidirectional ply - describes the elastic behaviour of the material

$$Q_{ij} = \begin{bmatrix} Q_{11} & Q_{12} & 0 \\ Q_{12} & Q_{22} & 0 \\ 0 & 0 & Q_{66} \end{bmatrix}$$

with

$$Q_{11} = \frac{E_1^2}{E_1 - v_{12}^2 \cdot E_2}$$

$$Q_{12} = \frac{v_{12} \cdot E_1 \cdot E_2}{E_1 - v_{12}^2 \cdot E_2}$$

$$Q_{22} = \frac{E_1 \cdot E_2}{E_1 - v_{12}^2 \cdot E_2}$$

$$Q_{66} = G_{12}$$

2. The transformed reduced stiffness matrix – takes into account fibre orientation in each ply

$$\overline{Q_{ij}} = \begin{bmatrix} \overline{Q_{11}} & \overline{Q_{12}} & \overline{Q_{16}} \\ \overline{Q_{12}} & \overline{Q_{22}} & \overline{Q_{26}} \\ \overline{Q_{16}} & \overline{Q_{26}} & \overline{Q_{66}} \end{bmatrix}$$

with

$$\overline{Q_{11}} = Q_{11} \cdot (\cos\theta)^4 + 2(Q_{12} + 2Q_{66}) \cdot (\cos\theta)^2 \cdot (\sin\theta)^2 + Q_{22} \cdot (\sin\theta)^4$$

$$\overline{Q_{12}} = \overline{Q_{21}} = Q_{12} \cdot ((\cos\theta)^4 + (\sin\theta)^4) + (Q_{11} + Q_{22} - 4Q_{66}) \cdot (\cos\theta)^2 \cdot (\sin\theta)^2$$

$$\overline{Q_{16}} = \overline{Q_{61}} = (Q_{11} - Q_{12} - 2Q_{66}) \cdot (\cos\theta)^3 \cdot \sin\theta - (Q_{22} - Q_{12} - 2Q_{66}) \cdot \cos\theta \cdot (\sin\theta)^3$$

$$\overline{Q_{22}} = Q_{11} \cdot (\sin\theta)^4 + 2(Q_{12} + 2Q_{66}) \cdot (\cos\theta)^2 \cdot (\sin\theta)^2 + Q_{22} \cdot (\cos\theta)^4$$

$$\overline{Q_{26}} = \overline{Q_{62}} = (Q_{11} - Q_{12} - 2Q_{66}) \cdot \cos\theta \cdot (\sin\theta)^3 - (Q_{22} - Q_{12} - 2Q_{66}) \cdot (\cos\theta)^3 \cdot \sin\theta$$

$$\overline{Q_{66}} = (Q_{11} + Q_{22} - 2Q_{12} - 2Q_{66}) \cdot (\cos\theta)^2 \cdot (\sin\theta)^2 + Q_{66} \cdot ((\cos\theta)^4 + (\sin\theta)^4)$$

3. A_{ij}, B_{ij} and D_{ij} matrices of the laminate

The extensional stiffness matrix:

$$A_{ij} = \sum_{k=1}^{n} (\overline{Q}_{ij})_k (h_k - h_{k-1})$$

The strain-curvature coupling stiffness matrix:

$$B_{ij} = \frac{1}{2} \sum_{k=1}^{n} (\overline{Q}_{ij})_k (h_k^2 - h_{k-1}^2)$$

The bending stiffness matrix:

$$D_{ij} = \frac{1}{3}\sum_{k=1}^{n}(\bar{Q}_{ij})_k\left(h_k^3 - h_{k-1}^3\right)$$

with h being the vertical position of the ply from the midplane
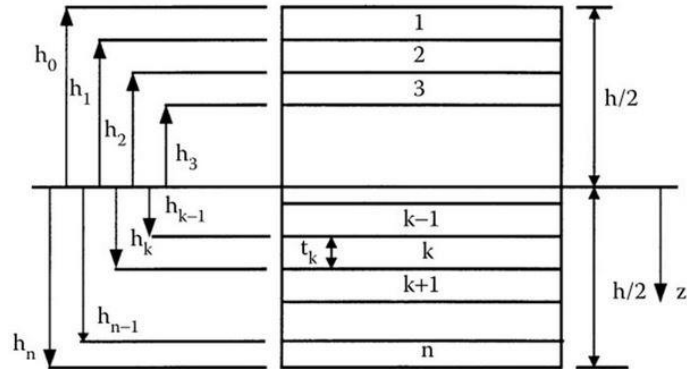
Figure B.1 Laminate with n plies [5]

4. Equivalent stiffness properties of the laminate

Axial:

$$E_x = 1/(ta_{11})$$

$$E_y = 1/(ta_{22})$$

$$G_{xy} = 1/(ta_{66})$$

$$v_{xy} = -a_{12}/a_{11}$$

$$v_{yx} = -a_{12}/a_{22}$$

Flexural:

$$E_x = 12/(t^3 d_{11})$$

$$E_y = 12/(t^3 d_{22})$$

$$G_{xy} = 12/(t^3 d_{66})$$

$$v_{xy} = -d_{12}/d_{11}$$

$$v_{yx} = -d_{12}/d_{22}$$

Where a_{ij} and d_{ij} are the values from the inverse of A or D matrices, and t is thickness of a laminate.

B.2 LAYUP AND MATERIAL PROPERTIES

Laminate properties are computed for three layups:

- layup I: 0⁰ -40%, 45⁰ -20%, -45⁰ -20%, 90⁰ -20%
- layup II: 0⁰ -62.5%, 45⁰ -12.5%, -45⁰ -12.5%, 90⁰ -12.5%
- layup III: 0⁰ -25%, 45⁰ -25%, -45⁰ -25%, 90⁰ -25%

LAYUP I

| 0° |
| 0° |
| 45° |
| 45° |
| -45° |
| -45° |
| 90° |
| 90° |
| 0° |
| 0° |

2 mm

LAYUP II

| 0° |
| 0° |
| 0° |
| 45° |
| -45° |
| 90° |
| 0° |

0.2 mm

LAYUP III

| 0° |
| 45° |
| 45° |
| -45° |
| -45° |
| 90° |
| 90° |
| 0° |

0.25 mm

0.25 mm

line of symmetry
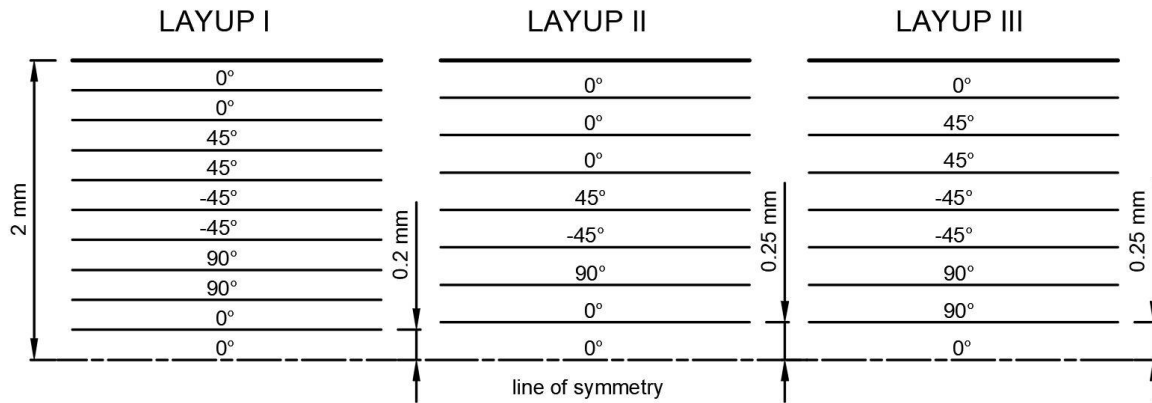
Figure B.2 Ply sequence for layup I and II

Laminate properties are calculated based on the indicative values given in table 3.6 [2] p. 43.

B.3 A, B AND D MATRICES

Layup I

$$A = \begin{bmatrix} 98.56 & 25.37 & 0 \\ 25.37 & 77.38 & 0 \\ 0 & 0 & 25.4 \end{bmatrix} GPa \cdot mm$$

$$B = \begin{bmatrix} 0 & 0 & 0 \\ 0 & 0 & 0 \\ 0 & 0 & 0 \end{bmatrix}$$

$$D = \begin{bmatrix} 146.48 & 35.72 & 5.08 \\ 35.72 & 84.34 & 5.08 \\ 5.08 & 5.08 & 35.75 \end{bmatrix} GPa \cdot mm^3$$

Layup II

$$A = \begin{bmatrix} 118.88 & 20.95 & 0 \\ 20.95 & 65.91 & 0 \\ 0 & 0 & 20.97 \end{bmatrix} GPa \cdot mm$$

$$B = \begin{bmatrix} 0 & 0 & 0 \\ 0 & 0 & 0 \\ 0 & 0 & 0 \end{bmatrix}$$

$$D = \begin{bmatrix} 177.36 & 25.63 & 1.66 \\ 25.63 & 73.64 & 1.66 \\ 1.66 & 1.66 & 25.66 \end{bmatrix} GPa \cdot mm^3$$

Layup III

$$A = \begin{bmatrix} 85.02 & 28.32 & 0 \\ 28.32 & 85.02 & 0 \\ 0 & 0 & 28.35 \end{bmatrix} GPa \cdot mm$$

$$B = \begin{bmatrix} 0 & 0 & 0 \\ 0 & 0 & 0 \\ 0 & 0 & 0 \end{bmatrix}$$

$$D = \begin{bmatrix} 128.62 & 42.37 & 8.28 \\ 42.37 & 88.89 & 8.28 \\ 8.28 & 8.28 & 42.41 \end{bmatrix} GPa \cdot mm^3$$

B.4 EQUIVALENT LAMINATE PROPERTIES

Layup I

$$A^{-1} = \begin{bmatrix} 0.0111 & -0.0036 & 0 \\ -0.0036 & 0.0141 & 0 \\ 0 & 0 & 0.0394 \end{bmatrix} 1/(GPa \cdot mm)$$

$$D^{-1} = \begin{bmatrix} 0.0076 & -0.0032 & -0.0006 \\ -0.0032 & 0.0133 & -0.0014 \\ -0.0006 & -0.0014 & 0.0283 \end{bmatrix} 1/(GPa \cdot mm^3)$$

Axial:

$E_x = 22.56 \; GPa$

$E_y = 17.71 \; GPa$

$G_{xy} = 6.35 \; GPa$

$\nu_{xy} = 0.323$

$\nu_{yx} = 0.257$

Flexural:

$E_x = 24.67 \; GPa$

$E_y = 14.10 \; GPa$

$G_{xy} = 6.63 \; GPa$

$\nu_{xy} = 0.421$

$\nu_{yx} = 0.241$

Layup II

$$A^{-1} = \begin{bmatrix} 0.0055 & -0.0017 & 0 \\ -0.0017 & 0.0157 & 0 \\ 0 & 0 & 0.0477 \end{bmatrix} 1/(GPa \cdot mm)$$

$$D^{-1} = \begin{bmatrix} 0.0059 & -0.0021 & -0.0003 \\ -0.0021 & 0.0143 & -0.0008 \\ -0.0003 & -0.0008 & 0.0390 \end{bmatrix} 1/(GPa \cdot mm^3)$$

Axial:

$E_x = 28.06 \; GPa$

Flexural:

$E_x = 31.78 \; GPa$

$$E_y = 15.57 \ GPa \qquad\qquad\qquad E_y = 13.11 \ GPa$$

$$G_{xy} = 5.24 \ GPa \qquad\qquad\qquad G_{xy} = 4.81 \ GPa$$

$$\nu_{xy} = 0.318 \qquad\qquad\qquad\qquad \nu_{xy} = 0.356$$

$$\nu_{yx} = 0.176 \qquad\qquad\qquad\qquad \nu_{yx} = 0.147$$

Layup III

$$A^{-1} = \begin{bmatrix} 0.0132 & -0.0044 & 0 \\ -0.0044 & 0.0132 & 0 \\ 0 & 0 & 0.0353 \end{bmatrix} 1/(GPa \cdot mm)$$

$$D^{-1} = \begin{bmatrix} 0.0093 & -0.0043 & -0.0010 \\ -0.0043 & 0.0135 & -0.0018 \\ -0.0010 & -0.0018 & 0.0241 \end{bmatrix} 1/(GPa \cdot mm^3)$$

Axial: Flexural:

$$E_x = 18.90 \ GPa \qquad\qquad\qquad E_x = 20.24 GPa$$

$$E_y = 18.90 \ GPa \qquad\qquad\qquad E_y = 13.91 \ GPa$$

$$G_{xy} = 7.09 \ GPa \qquad\qquad\qquad G_{xy} = 7.77 \ GPa$$

$$\nu_{xy} = 0.333 \qquad\qquad\qquad\qquad \nu_{xy} = 0.467$$

$$\nu_{yx} = 0.333 \qquad\qquad\qquad\qquad \nu_{yx} = 0.321$$

C. LOAD – DEFLECTION DIAGRAMS
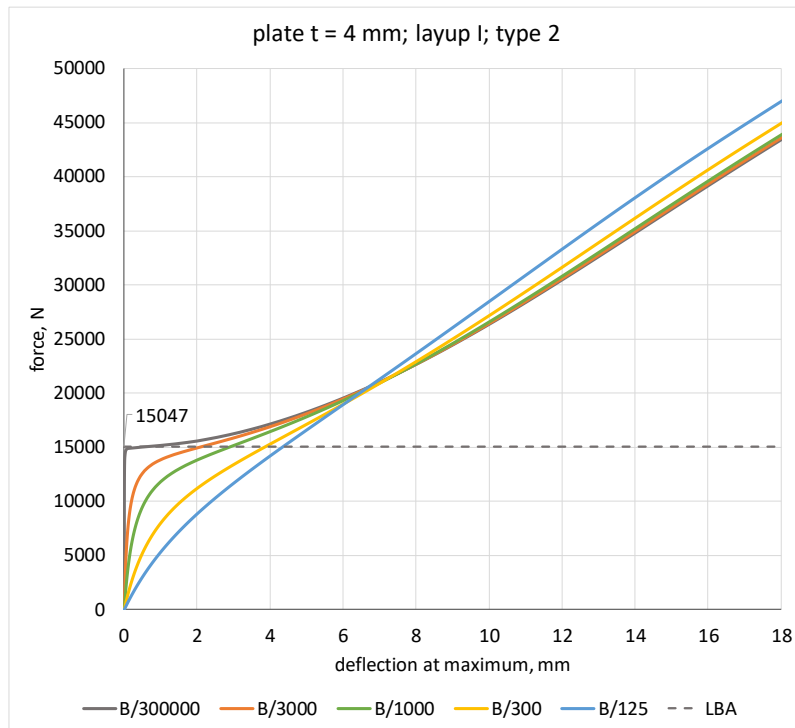
Figure C.1.1 Force – deflection at maximum curves for a plate t = 4 mm with the imperfection in the shape of the second buckling mode
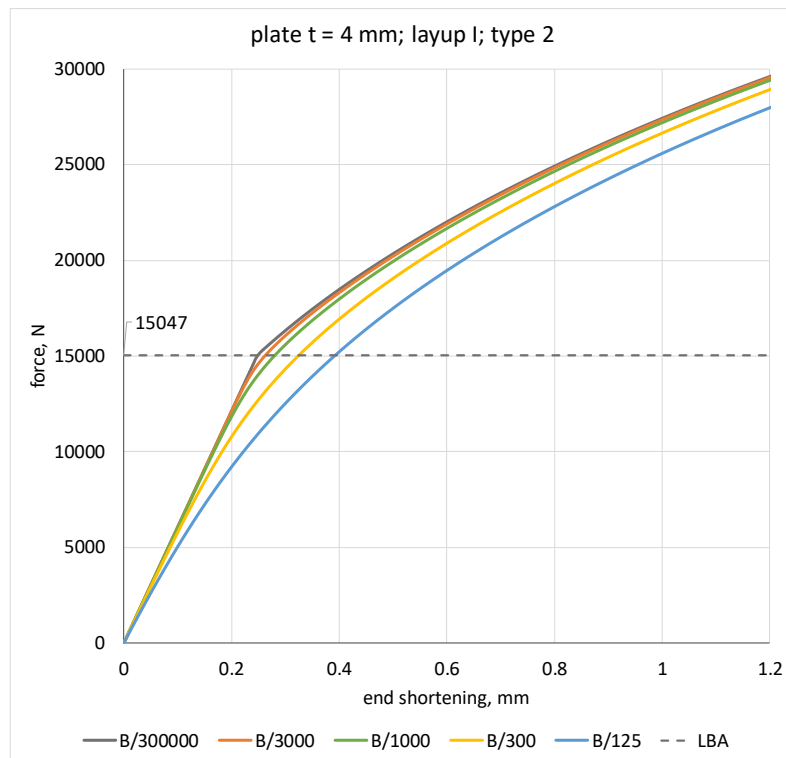
Figure C.1.2 End shortening of a plate t = 4 mm with the imperfection in the shape of the second buckling mode
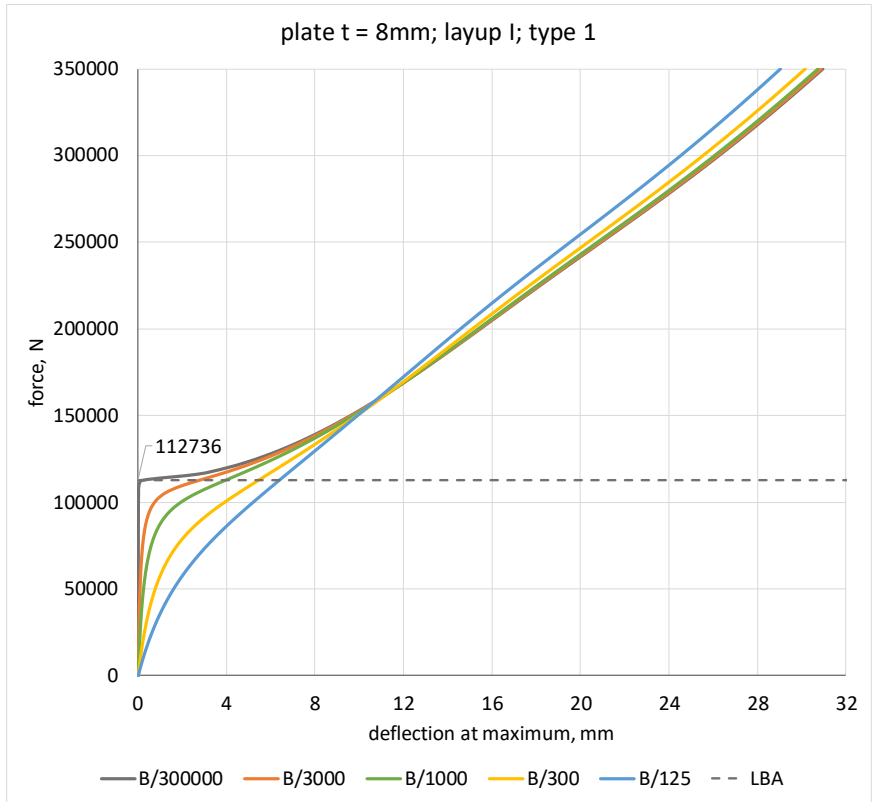
Figure C.1.3 Force – deflection at maximum curves for a plate t = 8 mm with the imperfection in the shape of the first buckling mode
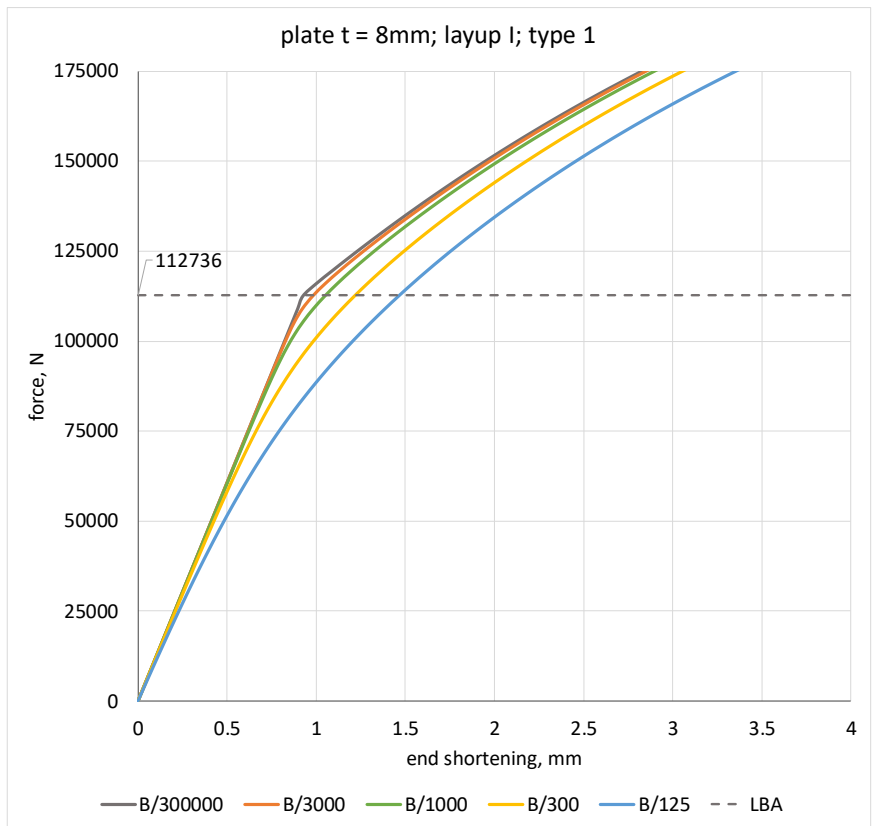
Figure C.1.4 End shortening of a plate t = 8 mm with the imperfection in the shape of the first buckling mode
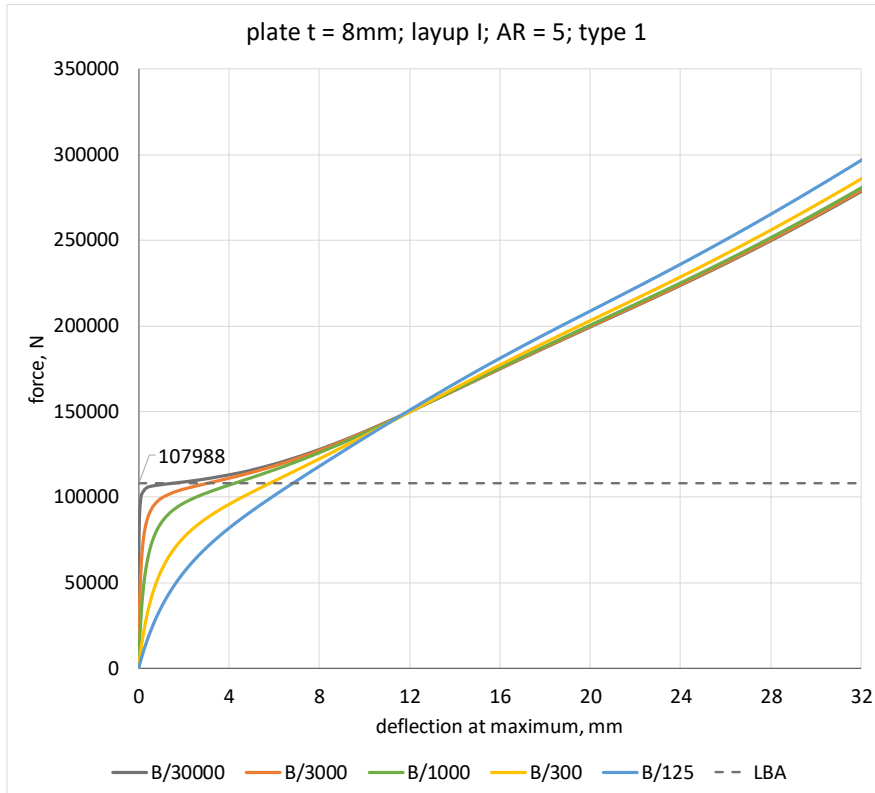
Figure C.1.5 Force – deflection at maximum curves for a plate AR = 5 with the imperfection in the shape of the first buckling mode
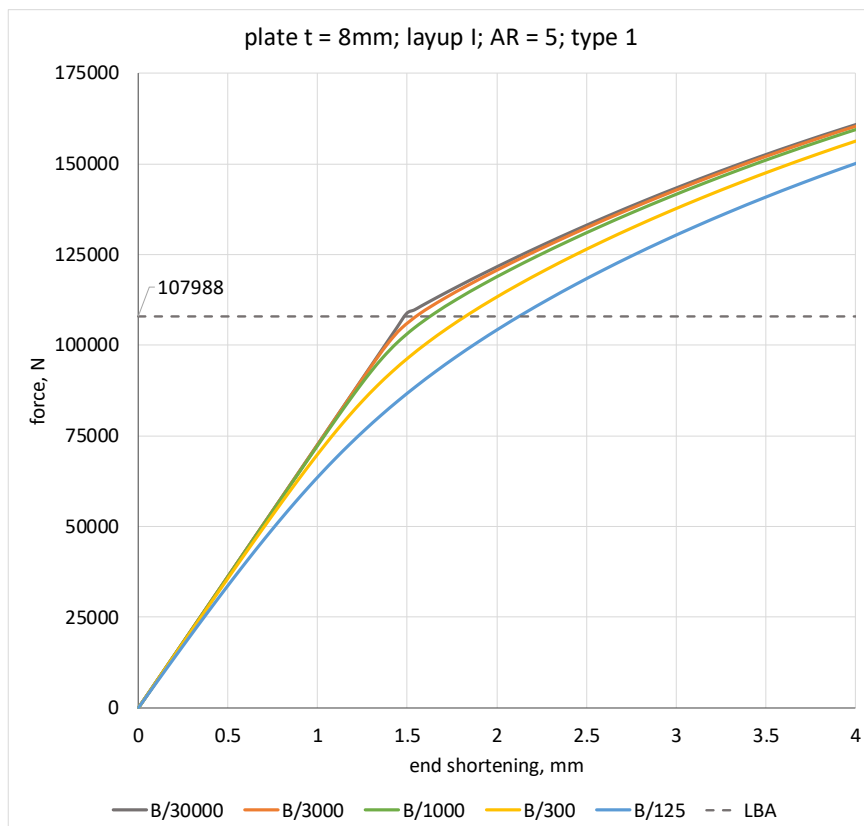
Figure C.1.6 End shortening of a plate AR = 5 with the imperfection in the shape of the first buckling mode
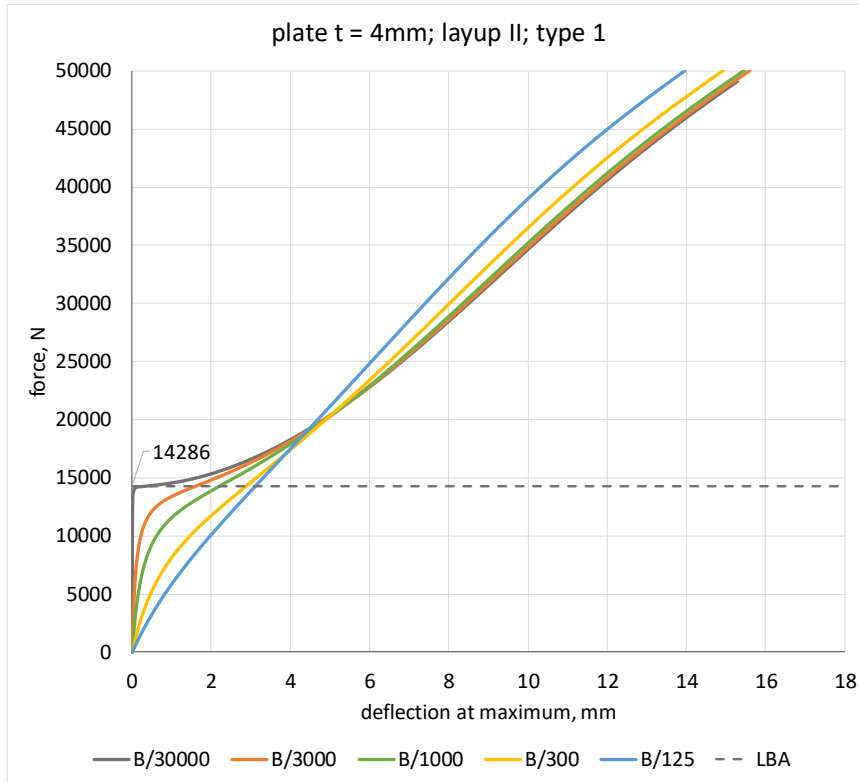
Figure C.1.7 Force – deflection at maximum curves for a plate layup II with the imperfection in the shape of the second buckling mode
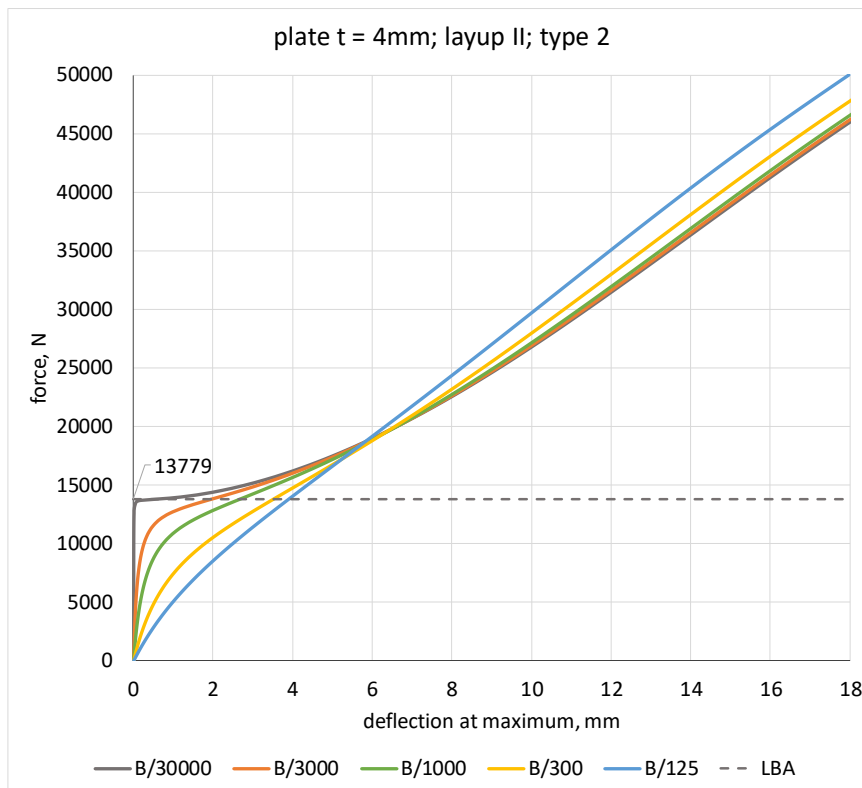
Figure C.1.8 Force – deflection at maximum curves for a plate layup II with the imperfection in the shape of the first buckling mode
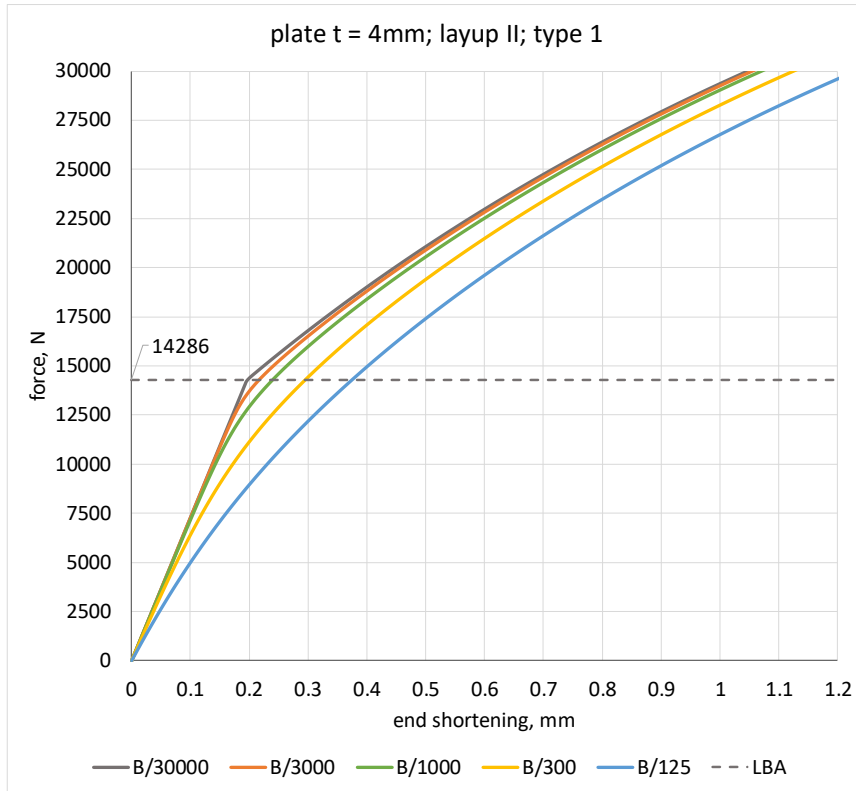
Figure C.1.9 End shortening of a plate with the imperfection in the shape of the second buckling mode
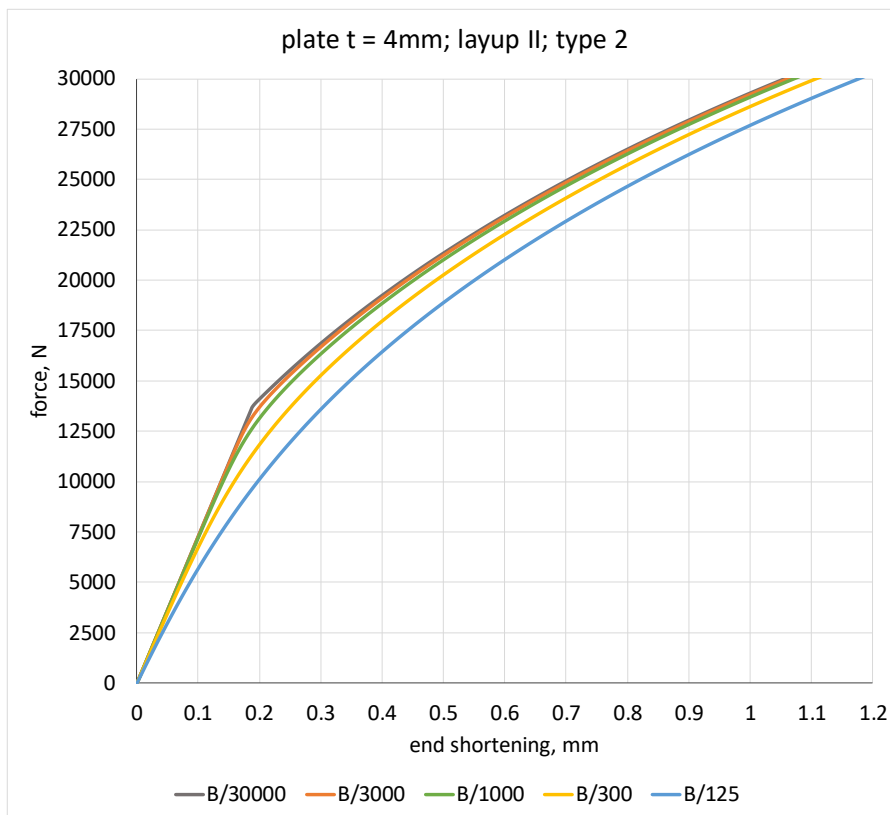
Figure C.1.10 End shortening of a plate with the imperfection in the shape of the first buckling mode

D. BOUNDARY CONDITIONS

When analysing the plates for transverse shear stresses, very high localized stress values (red areas) compared to the rest of the plate were observed in the corner elements:
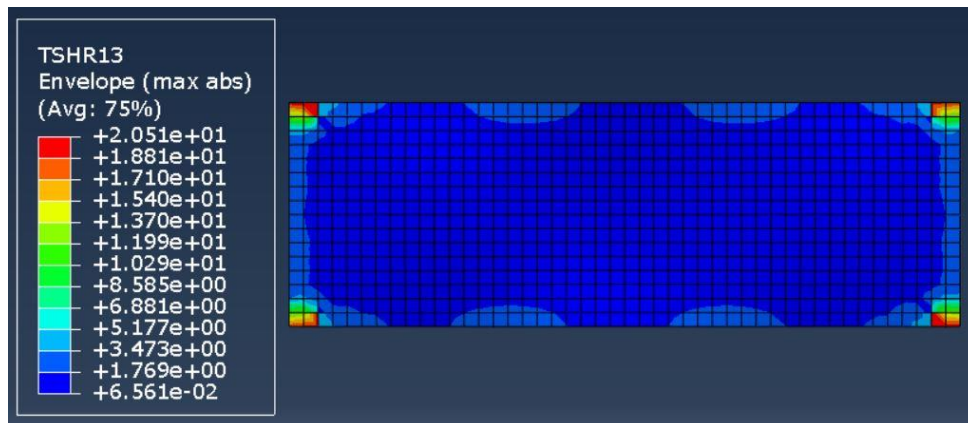
Figure D.1 Transverse shear stresses contour plot

A question which arises is whether this caused by the unrealistically rigid boundary conditions or if delamination can initiate and propagate from the corners of the plate. In order to attempt to answer this question alternative boundary conditions were modelled.
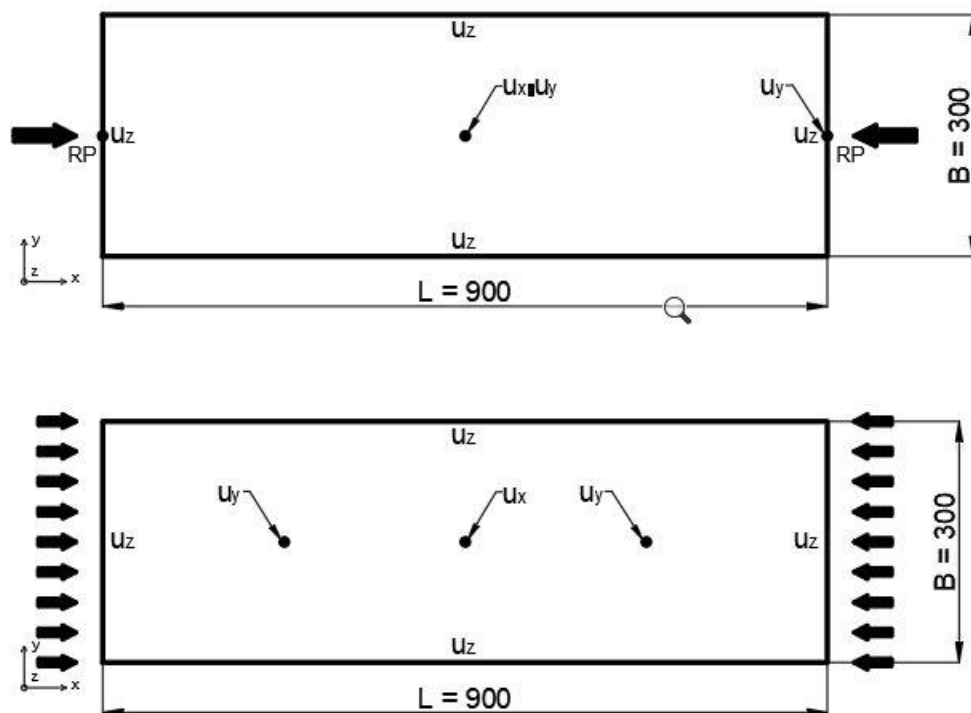
Figure D.2 Original (top) and alternative (bottom) boundary conditions

The main difference is that in the original boundary conditions a concentrated force was applied to a reference point that was rigidly coupled to a plate's edge. In the new boundary conditions instead of the concentrated force initial axial displacement was applied in the x direction and the rigid coupling was removed, making the plate edge unrestrained.

Further the study of the effect of the boundary conditions is presented. The investigated plate has thickness of $6\ mm$. The initial imperfection amplitude is taken as $B/125 = 2.4\ mm$. Geometrically and materially nonlinear model is used.

EFFECT OF BOUNDARY CONDITIONS ON INTERLAMINAR SHEAR STRESSES

Since the goal is to establish whether delamination might occur before Hashin failure, the ultimate Hashin progressive failure load was determined first. In case of the original boundary conditions: $P_{ult,or} = 67.95\ kN$, and for the alternative boundary conditions: $P_{ult,al} = 107.9\ kN$. The interlaminar shear stresses for a plate with original boundary conditions are shown in the contour plot in figure D.3 and with alternative boundary conditions in figure D.4.
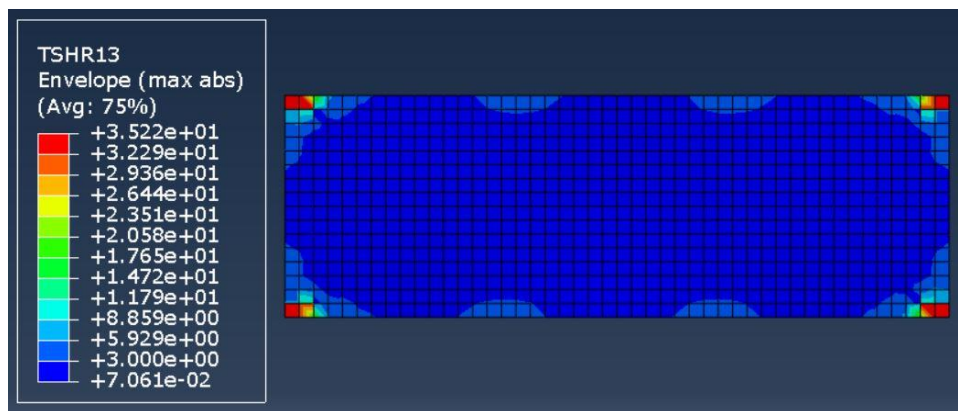
Figure D.3 Interlaminar shear stresses in the plate with original boundary conditions at P$_{ult,or}$

Very high interlaminar stresses are seen in the corner of the plates of $35.22\ MPa$ and much lower values elsewhere in the plate $\sim 3.0\ MPa$.

For the plate with alternative boundary conditions for the same load level lower values of interlaminar shear stresses were found:
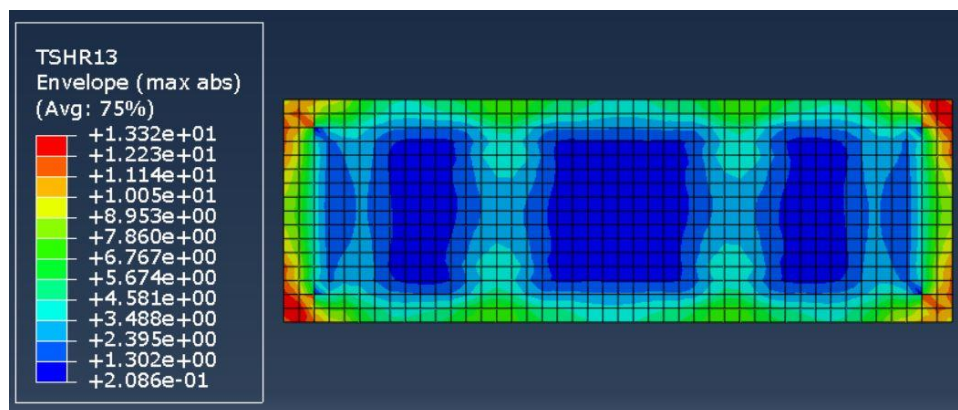
Figure D.4 Interlaminar shear stresses in the plate with modified boundary conditions at P_{ult,al}

Peak values are 13.32 MPa, and general distribution of interlaminar shear stresses is more uniform than in case of the original boundary conditions.

Since it was discovered that the ultimate Hashin progressive failure load values also differ depending on the boundary conditions, it was decided to look closer how they influence the results.

EFFECT OF BOUNDARY CONDITIONS ON HASHIN PROGRESSIVE FAILURE

The difference between the ultimate Hashin progressive failure loads is ~35%. In both cases governing failure mode is matrix cracking:
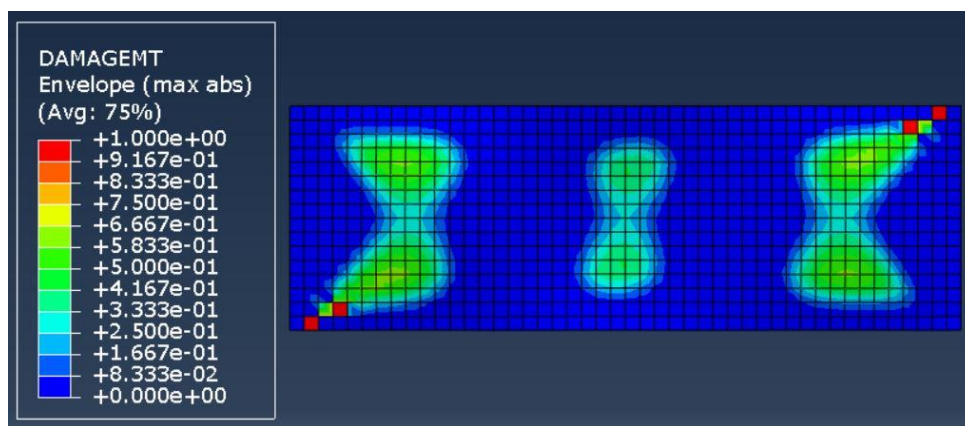
Figure D.5 Damage in the plate with original boundary conditions
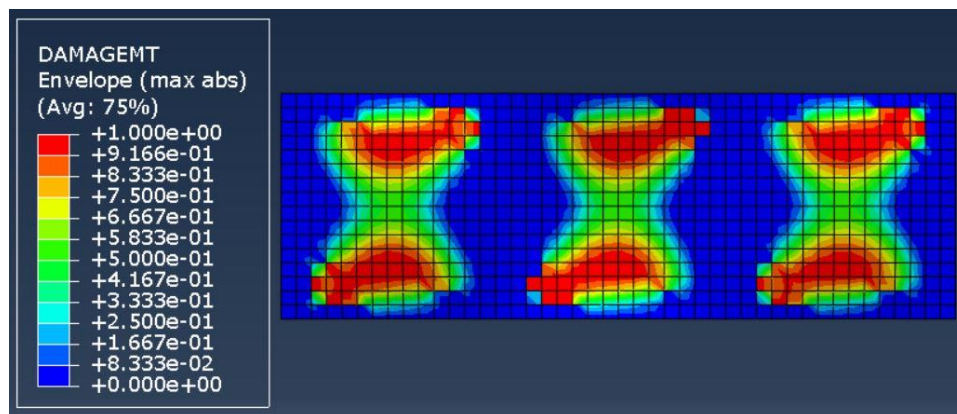
Figure D.6 Damage in the plate with modified boundary conditions

As seen in the figures above, in the original plate the critical points are close to the corners, while the alternative plate does not have them. The damage in the original situation occurs at lower load levels than in the plate with modified boundary conditions at $P = 58.04\ kN$ and $P = 77.07\ kN$. So, the software will start reducing stiffness of the laminate sooner and the ultimate strength of the plate will be lower. The plot below shows the load – end shortening curves comparison between a plate with original and alternative boundary conditions with imperfection amplitude $B/1000$ and $B/125$, where it can be seen that in case of the original boundary conditions the reduction and the failure of the laminate occurs sooner than for the alternative situation.
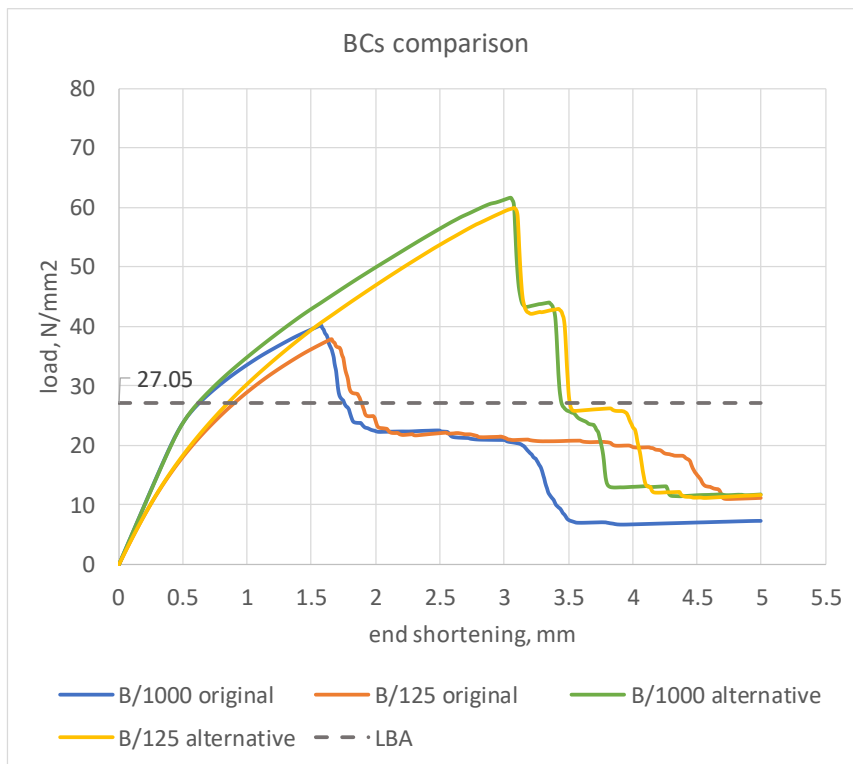
Figure D.7 Load – end shortening curves for the original and modified boundary conditions

CONCLUSIONS

The effect of boundary conditions and load introduction on the interlaminar shear stresses and the progressive damage analysis was presented.

It was found that when a reference point that is rigidly coupled to the plate's edge is used, very high localized transverse shear stresses occur in the plate's corners. In case of modified boundary conditions, when the load is introduced directly to the plate's edge, the maximum values also occur at the edges, however, they are much lower for the same load level.

The boundaries also have an effect on the ultimate progressive damage analysis load. In the original situation with the plate edge being rigidly coupled to the reference point, damage occurs in the corner area of the plate at the lower load compared to the modified constraints. Higher ultimate loads were obtained for the plate with alternative boundary: 35% higher.

Based on these results, it is concluded that the high localized transverse shear stresses are caused by the rigid constraint of the plate's edge. The alternative boundary conditions reduce these high values and prevent the damage evolution at the points close to the plate's corners in the progressive analysis. The linear buckling analysis results with the alternative boundary conditions stay almost unchanged compared to the results obtained with the original boundary conditions. It is therefore decided to continue analysis with the alternative boundary conditions.

E. DAMAGE EVOLUTION PARAMETERS

A small sensitivity analysis was performed to see the influence of the fracture energy parameters. The damage initiates due to matrix cracking. The fracture energy values are given for E-glass epoxy, but the resin under consideration is polyester. Therefore, the transverse tensile and compressive fracture energies were varied.

The model used for this study is of a plate with layup I ($E_X/E_y = 1.27$), $t = 6\ mm$, $L = 900\ mm$, $B = 300\ mm$ and alternative boundary conditions as reported in 4.3.

Figure 4.5.1 shows the load – end shortening curves for a plate with two different amplitudes of imperfection and three difference values for transverse tensile and compressive fracture energies, denoted as 1/1 (the original values for E-glass / epoxy laminate), 0/0 and 4/4.
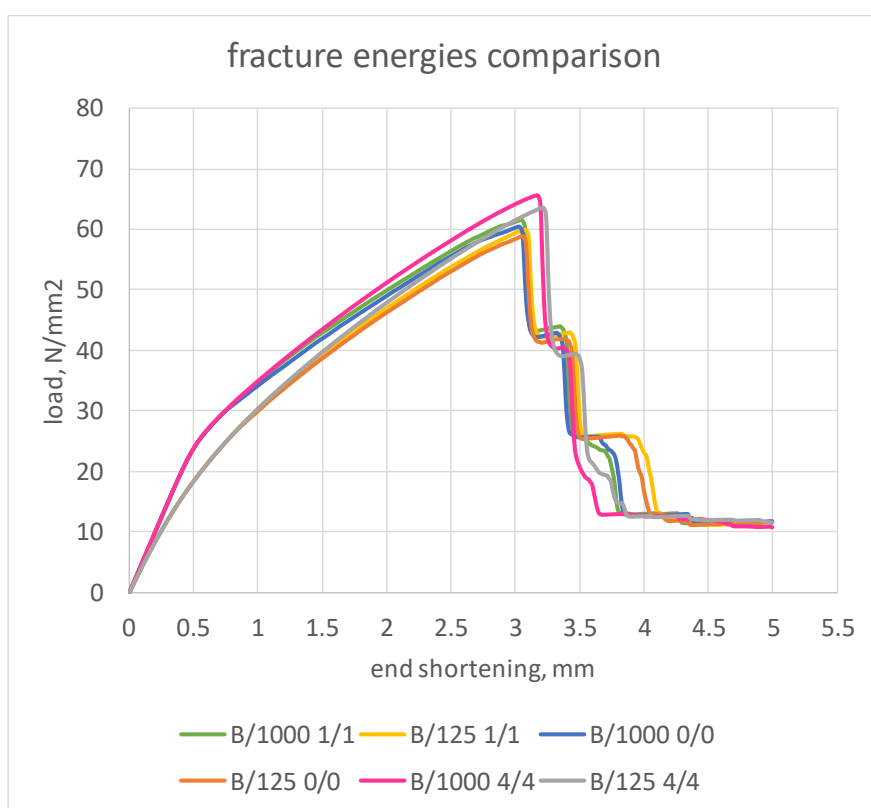
Figure E.1 Effect of transverse fracture energies input values

	B/1000	B/125
1/1	61.61 N/mm2	59.93 N/mm2
0/0	60.52 N/mm2	58.8 N/mm2
4/4	65.57 N/mm2	63.62 N/mm2

Table E.1 Failure loads corresponding to different values of transverse fracture energies

As expected, the largest difference in ultimate loads is between the 1/1 and the 4/4 values; around 6% increase for $B/1000$ and $B/125$. The reduction of material stiffness is more pronounced in case of transverse energies being set to zero, and the least reduction can be observed for fracture energies in transverse direction set to 4. Since the fracture energy properties for transverse tension

and compression do not seem to have a large influence on the ultimate load, it is decided to use the values available for E-glass epoxy laminate.

F. MODEL VALIDATION

Buckling curves for FRP plates were derived by H. Trumpf [3] based on FEA simulations and experimental results.
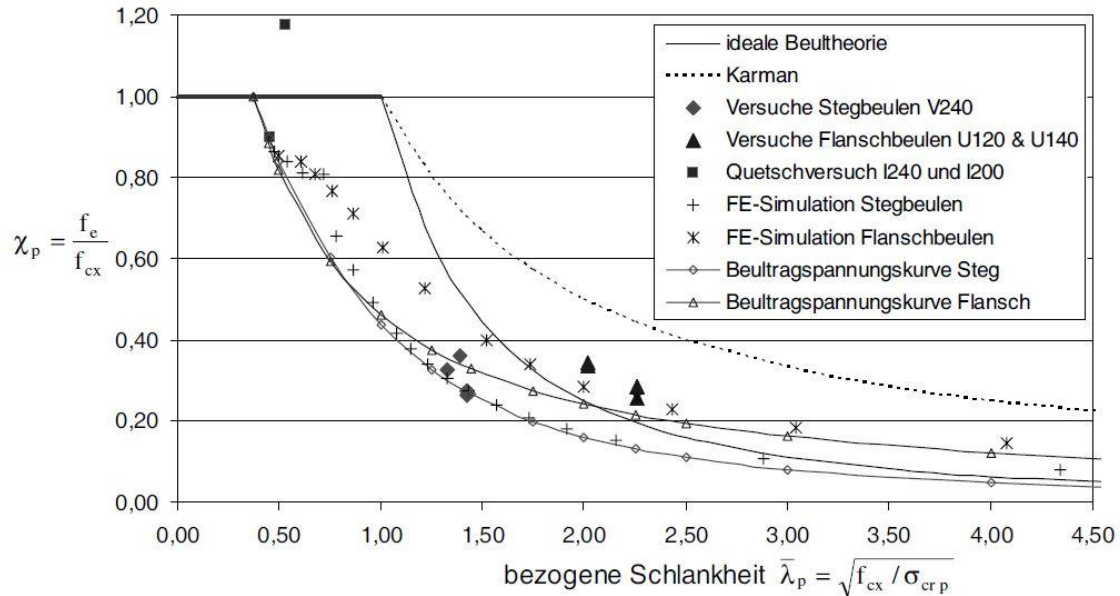
Figure 4.7.1 Buckling curves for plates with various supports [3] p. 141

The curve that corresponds to the simply supported boundary conditions is denoted as Beultragspannungskurve Steg and experimental results Versuche Stegbeulen V240. The material properties of the laminate are such that $E_{cx}/E_{cy} = 2.45$. As it can be seen the derived buckling curve is below the curve that is based on the perfect plate buckling theory (ideale Beultheorie), even for large values of plate slenderness, unlike what was observed in the analysis in chapter 4.

The material properties for layup I result in much lower ratio between longitudinal and transverse modulus of elasticity $E_{cx}/E_{cy} = 1.27$, compared to the values from Trumpf's work. The exact layup from [3] is not known, but the slenderness corresponding to experimental results is $\lambda = 1.45$. To match slenderness and ratio between moduli of elasticity in two directions the following layup was used:
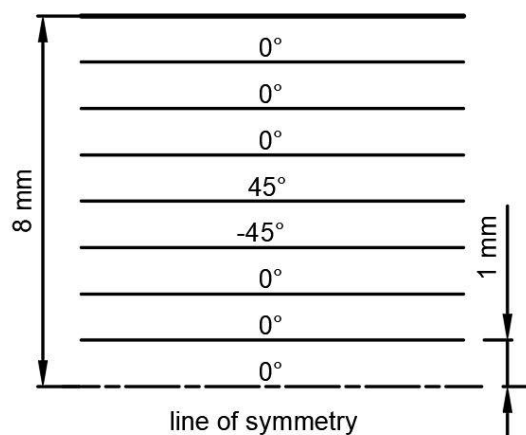
Figure 4.7.2 Layup for model validation

145

Which results in $E_{cx}/E_{cy} = 2.51$ and for a plate with dimensions $300 \times 900, t = 16 \ mm$ slenderness is $\lambda = 1.46$. Two amplitudes of imperfections were considered $B/1000$ and $B/125$. The resulting reduction factors are shown over the results from [3]:
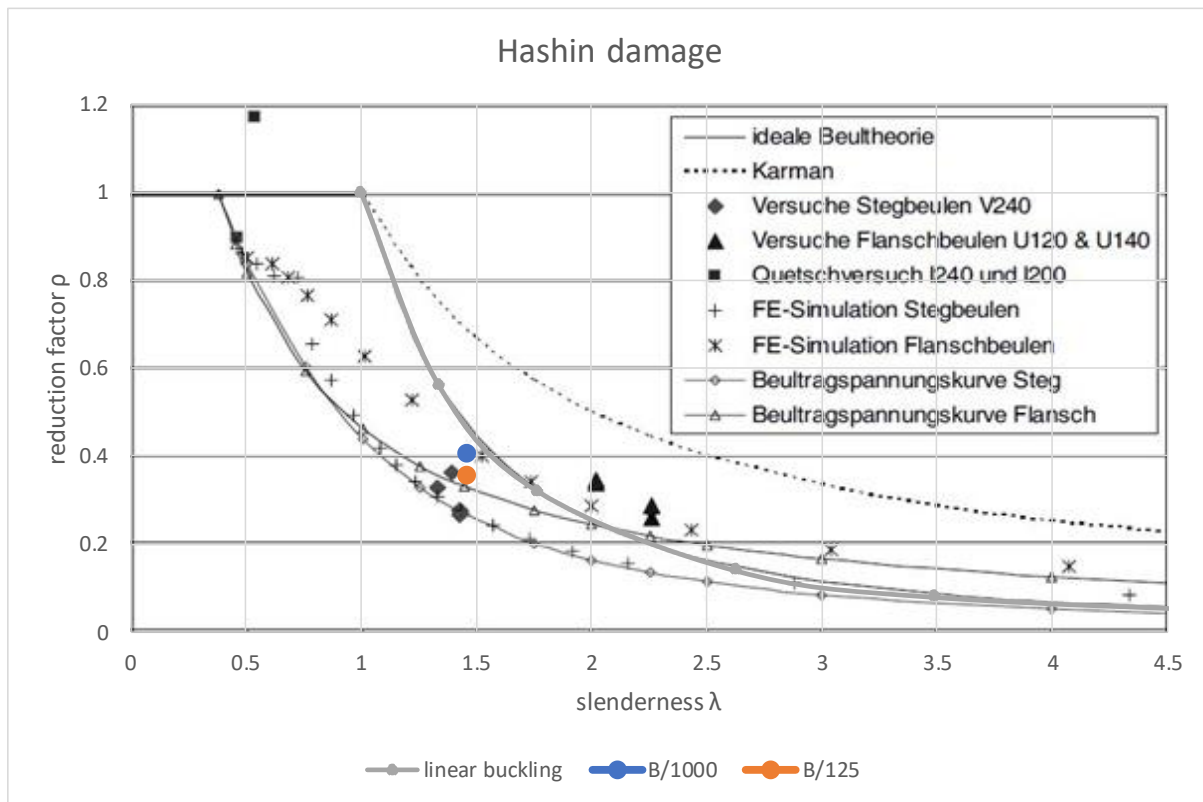
Figure 4.7.3 Comparison of FEA with experimental results

For given slenderness the results obtained from the finite element model are slightly optimistic compared to the test results. This could be due to uncertainties in modelling the laminate: ply properties and layup had to be assumed. Also, there is uncertainty in terms of the failure load determined experimentally. According to [3] the drop of the load was considered as failure, which in case of plate with very small imperfection can also mean critical load.

G. PROGRESSIVE DAMAGE DIAGRAMS

The following load – end shortening diagrams are derived for plates of layup I ($E_x/E_y = 1.27$).

Slenderness $\lambda = 4.35$
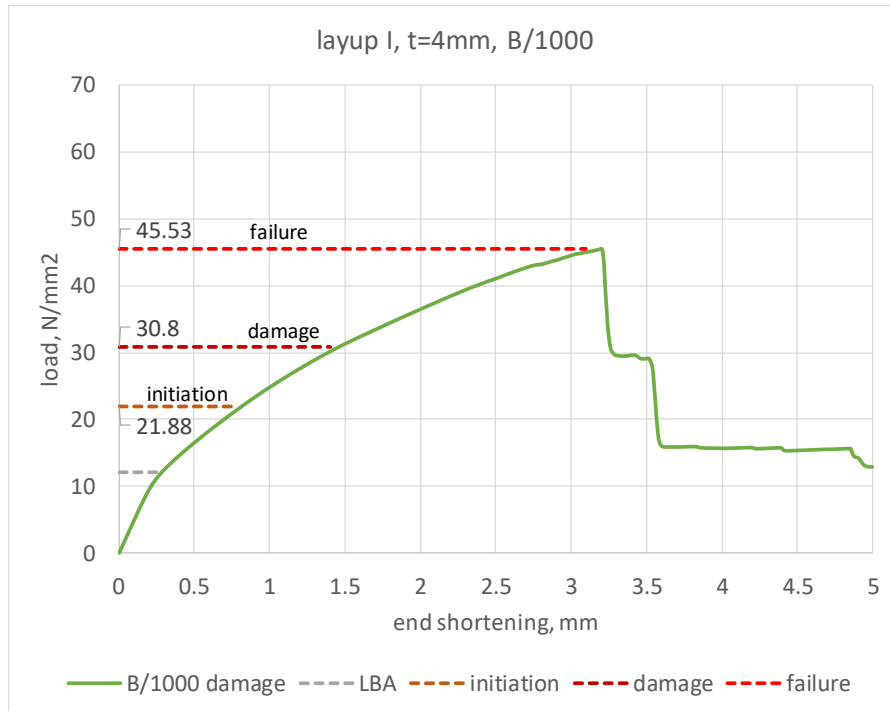
Figure G.1 Load – end shortening diagram, λ = 4.35 B/1000
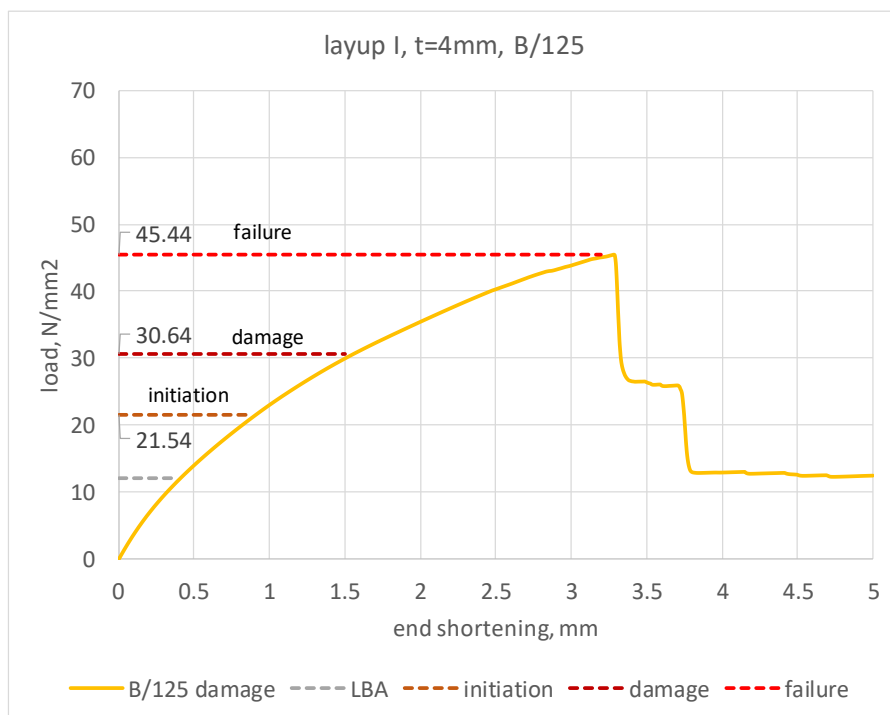
Figure G.2 Load – end shortening diagram, λ = 4.35 B/125

Slenderness $\lambda = 2.91$
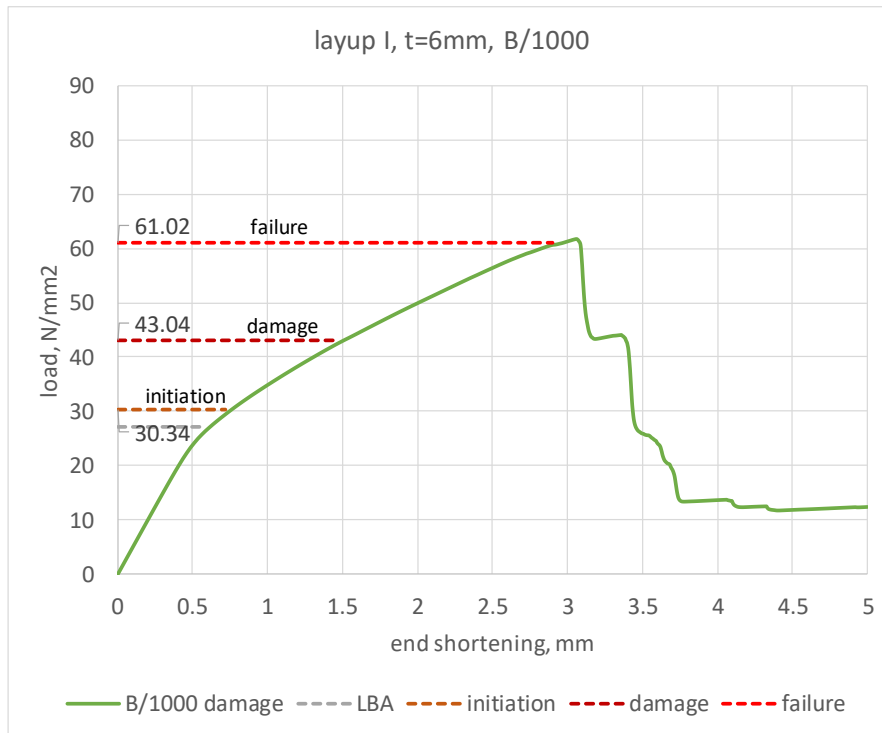
Figure G.3 Load – end shortening diagram, λ = 2.91 B/1000
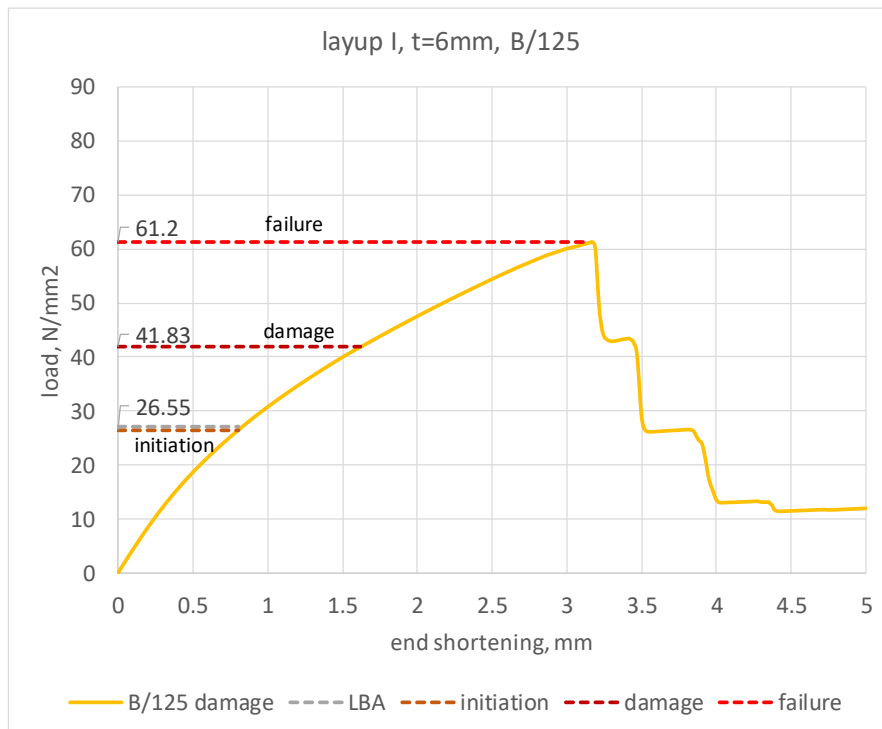
Figure G.4 Load – end shortening diagram, λ = 2.91 B/125

Slenderness $\lambda = 2.20$
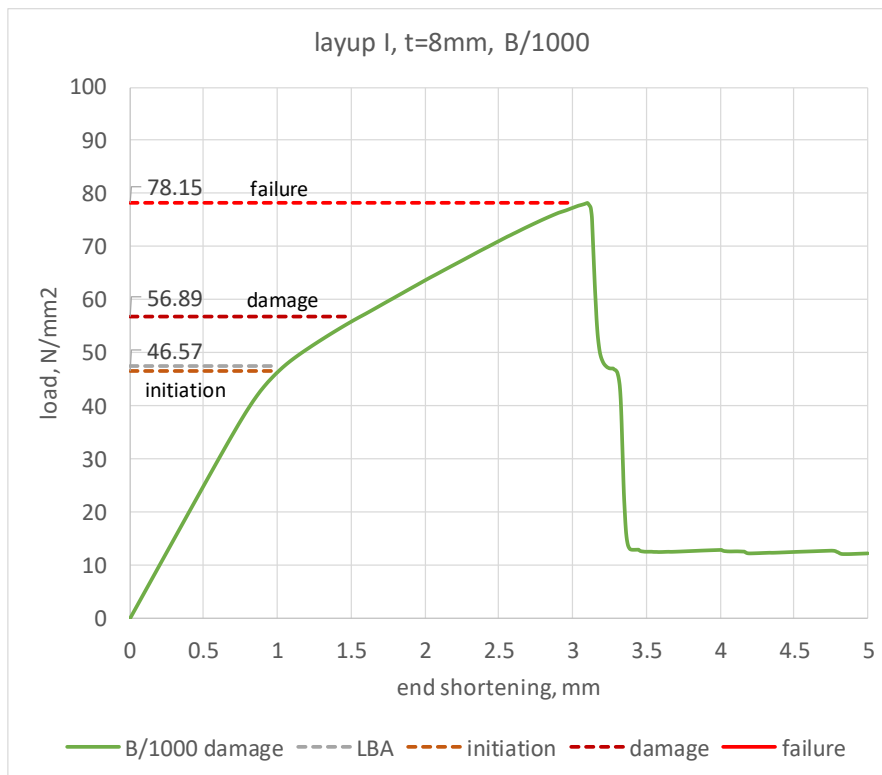
Figure G.5 Load – end shortening diagram, λ = 2.20 B/1000
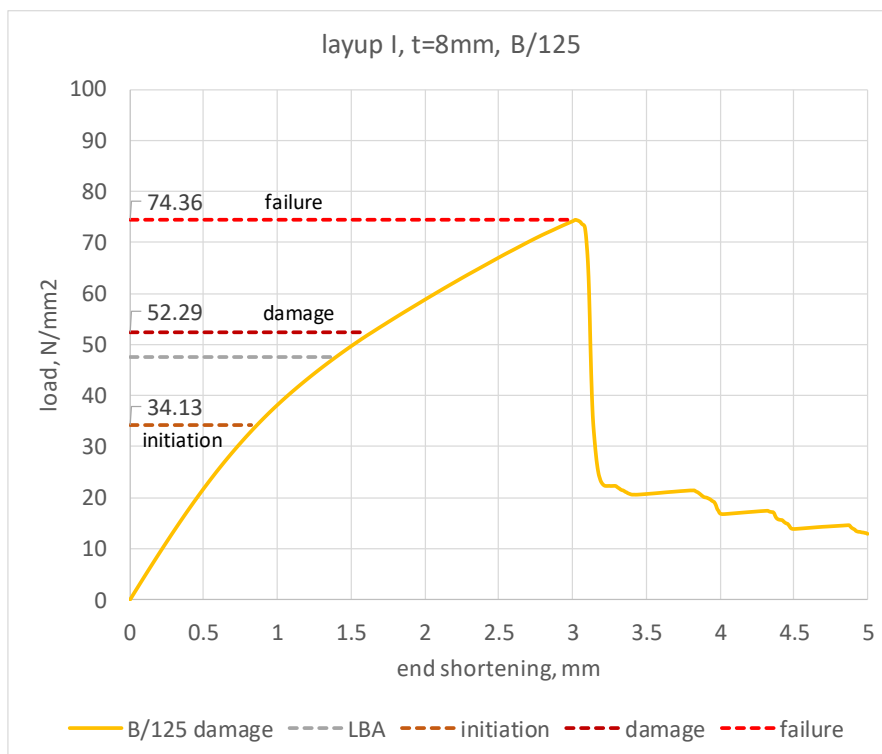
Figure G.6 Load – end shortening diagram, λ = 2.20 B/125

Slenderness $\lambda = 1.48$
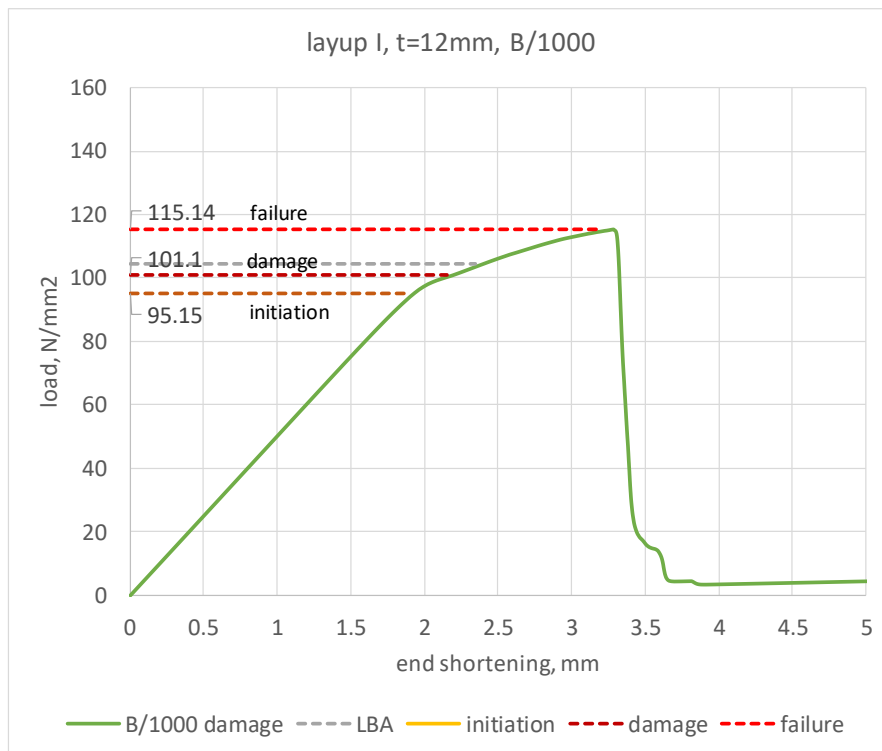
Figure G.7 Load – end shortening diagram, λ = 1.48 B/1000
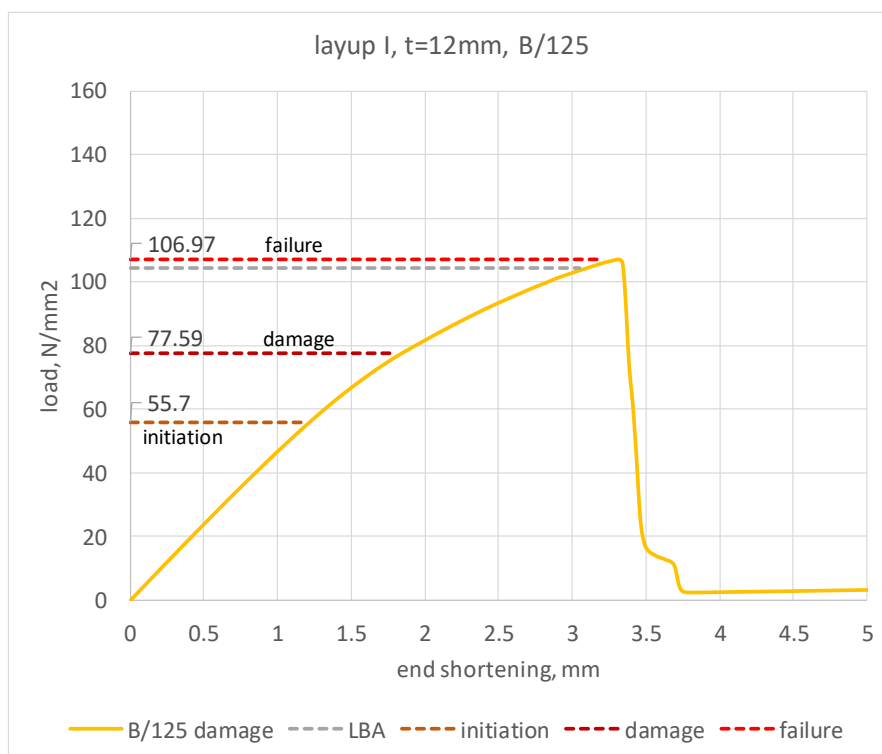
Figure G.8 Load – end shortening diagram, λ = 1.48 B/125

Slenderness $\lambda = 1.13$
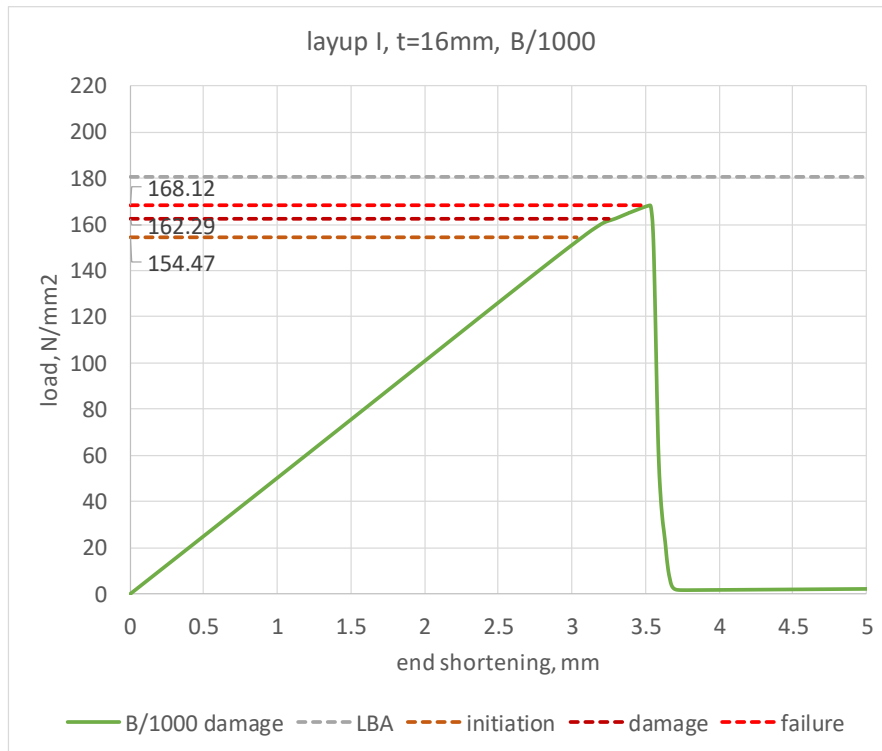
Figure G.9 Load – end shortening diagram, λ = 1.13 B/1000
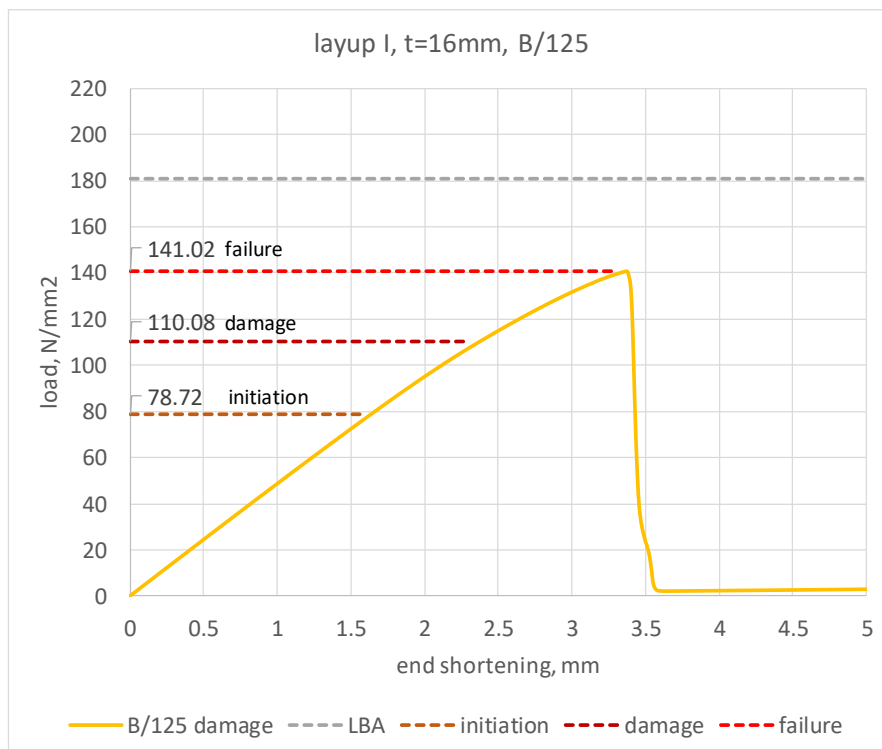
Figure G.10 Load – end shortening diagram, λ = 1.13 B/125

Slenderness $\lambda = 0.77$
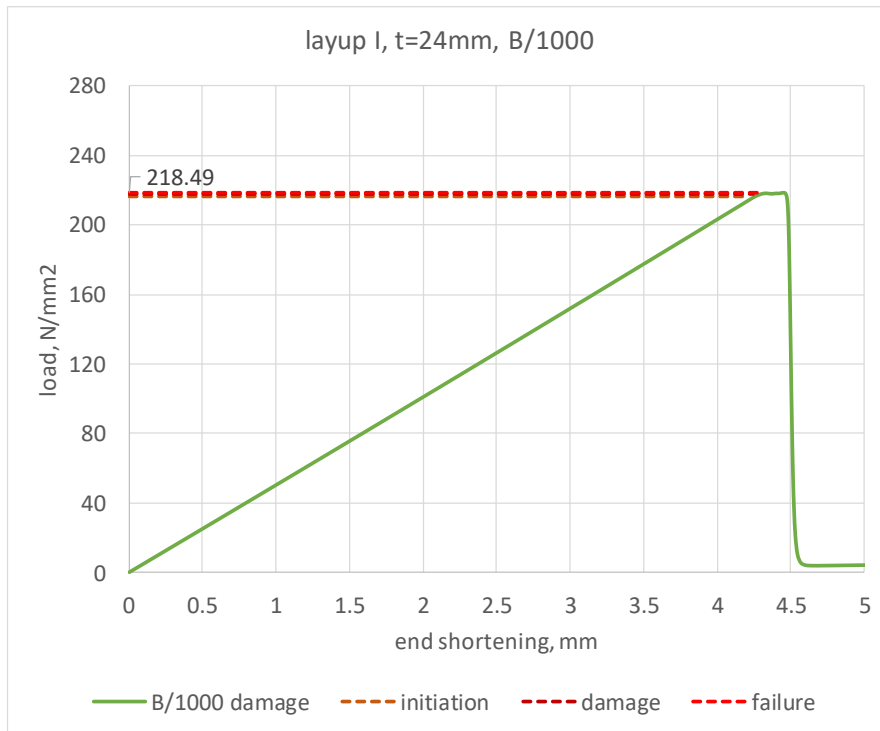
Figure G.11 Load – end shortening diagram, λ = 0.77 B/1000
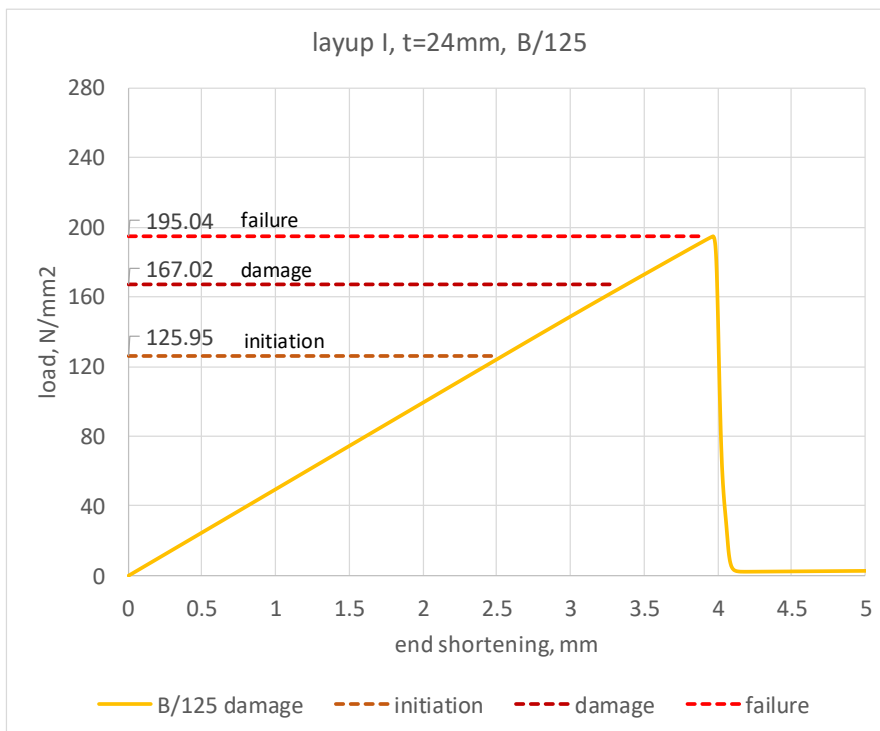
Figure G.12 Load – end shortening diagram, λ = 0.77 B/125

Slenderness $\lambda = 0.41$

layup I, t=54mm, B/1000

220.5
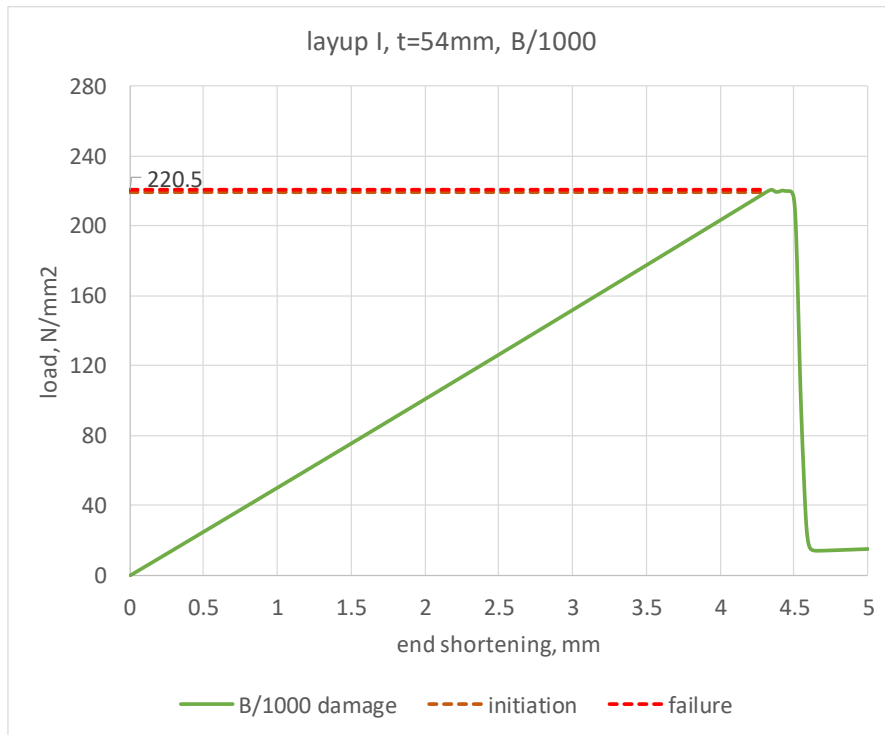
Figure G.13 Load – end shortening diagram, λ = 0.41 B/1000

layup I, t=54mm, B/125

214.84   initiation   damage   failure
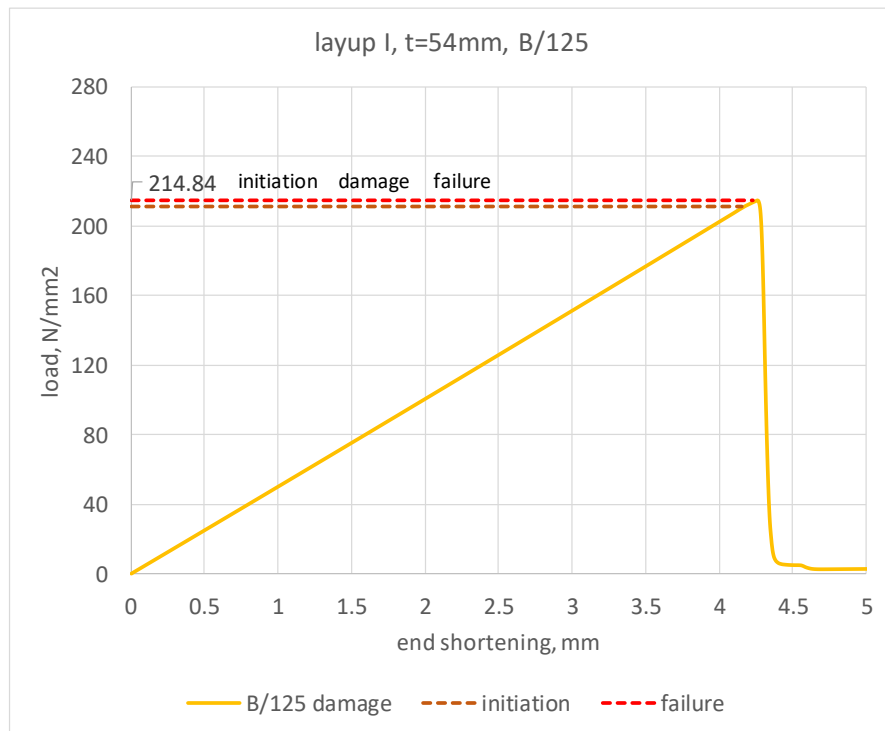
Figure G.14 Load – end shortening diagram, λ = 0.41 B/125